Machine-vision based Phenotyping and Competition Effects of Individual Ryegrass Plants

Saba Rabab

Bachelor of Science in Electronic Engineering, 2011 Islamic University

Master of Science in Electrical Engineering, 2015 Military College of Signals

A thesis submitted in total fulfilment of the requirements for the degree of

Doctor of Philosophy

School of Applied Systems Biology

College of Science, Health and Engineering

La Trobe University

Victoria, Australia

July 2021

Table of Contents

List of Figures

List of Tables

List of Algorithms

Abstract

This thesis focused on developing methods for the extraction of plant phenomics characteristics from high-resolution images of perennial ryegrass and the analysis of competition effects between plants with genomics enabled mixed linear models common in genomic selection. A first crucial step in digital phenotype development is the identification of regions of interest on the image (e.g., crop rows, individual plants). A template-free crop row detection algorithm was developed to identify perennial ryegrass plant rows in a field trial. The accuracy of the proposed algorithm was 87.5% and 84% for our field trial and a public data set, respectively. A subsequent study proposed a new method to extract of individual plant phenomics from images and validated the results by correlation to plant fresh biomass. Assuming that ryegrass plants were generally circular, the method identified the centre points and radii of individual plants to quantify plant areas and NDVI intensity. The Pearson correlation between plant area and fresh weights ranged between 0.63 to 0.75 across four time points. Perennial ryegrass is grown in pastures where plants are in close proximity. The impact of a plant on its neighbours has been shown to be partly influenced by genetics in other species but has not been investigated in pasture grasses. Individual plant phenomics and genetic markers were used to determine whether these impacts were positive (beneficial) or negative (competitive) through the estimation of indirect genetic effects. Our investigation of four ryegrass populations across 9 time points indicated that indirect genetic effects were present and were negatively correlated with direct effects, showing that ryegrass plants do exhibit competitive behaviour. The phenomics algorithms developed are general and applicable for the extraction of forage phenomics for other plant species. Our results on

ryegrass indirect genetic effects form a basis for understanding competition among forage plants.

Statement of Original Authorship

This thesis includes work by the author that has been published or accepted for publication as described in the text. Except where reference is made in the text of the thesis, this thesis contains no other material published elsewhere or extracted in whole or in part from a thesis accepted for the award of any other degree or diploma. No other person's work has been used without due acknowledgment in the main text of the thesis. This thesis has not been submitted for the award of any degree or diploma in any other tertiary institution.

_____

Saba Rabab

22 July 2021

Acknowledgements

I would like to gratefully acknowledge the following people who helped me throughout my PhD.

My supervisor, Prof Hans Daetwyler, I cannot express in words my respect and admiration for you as a supportive and understanding supervisor. Your kind nature and hardworking personality have always pushed me to work even harder throughout this journey. I will always cherish that I was fortunate enough to work under your supervision.

My supervisors, Prof Phoebe Chen, and Dr Noel Cogan, thank you for sharing your in-depth knowledge and for being there in every milestone to support and encourage me.

Computational biology group members, thank you for your help and support throughout my PhD journey. Dr Fan Shi and Dr Ed Breen, thank you for your corporation and guidance and providing me the data for analysis whenever I required. I would like to especially acknowledge Dr Youngjun Li for his continuous support and guidance. It would have been difficult without your corporation and thorough knowledge on quantitative genetic to finalize the statistical analysis on time.

Staff of the Molecular Plant Breeding team at DJPR Hamilton, Dr Pieter Badenhorst, for providing the images of ryegrass and sharing the knowledge of pasture breeding.

I am grateful to be blessed with best parents and siblings. The emotional support from my family kept me going. Finally, my life partner and son, your love and support have always uplifted my mood whenever I was stressed in my PhD Journey, and I will be forever grateful for having you in my life and I am certain that without my family I could not have make it happen.

Chapter 1

Introduction

Saba Rabab[1,2]

[1]School of Applied Systems Biology, La Trobe University, Bundoora, Australia

[2]Agriculture Victoria, AgriBio, Centre for AgriBioscience, Bundoora, Australia.

1.1. Background and motivations

Genetic improvement of crops is based on the selection of plants with superior traits (yield, quality attributes, disease resistance and better tolerance to biotic and abiotic stress). The selection criteria have been and still are dependent generally on measuring phenotypic performance. Conventional methods for the assessment of complete phenotypic profiles, specifically for perennial crops, require a lot of time and labour and are less precise, and destructive (e.g. forage biomass and quality). The world population is increasing continuously, and it is expected to increase by 50% by 2050, consequently increasing food demand by 70%. Therefore, there is a need to find ways to optimize the food production [1]. To maintain sustainable agriculture, conventional breeding programmes have significantly evolved in the last decade resulting in increased producibility and profitability in crop plants [2-5].

To overcome the challenges associated with the conventional methods, automation in agriculture is a necessity for smart farming to increase the overall genetic gain [6]. There are two main steps of automated phenotyping: image acquisition and image analysis. In order to

improve plant breeding programmes, accurately measured phenotypic data and genetic technology needs to be considered [7-8]. One such technology involves the selection of organisms' favourable genes to improve qualities that increase crop yield and nutrient value while using less land and in a shorter amount of time [9-12]. Moreover, a lack of large datasets for genomic analysis of complex phenotypic traits have slowed genetic progress. These problems can be rectified to some extent by the accurate and precise phenotyping using phenomics of germplasm resources.

1.2. Research problems

Genomic selection has benefited applied plant breeding in a number of ways, such as improved and rapid selection of individuals of higher breeding values, shortening of breeding cycles, improved genetic gain per year on agronomic traits as compared to conventional breeding and overall, it is cost effective [13]. Further, to improve plant breeding programmes, accurately measured phenotypic data and genomics needs to be considered. There is a wealth of knowledge regarding the genomics of plants that has accumulated in the last decade. However, there is still a significant gap between this knowledge and its utilization due to the limited phenotypic descriptions of these genomes, especially at the single plant level. Novel technologies such as multi-spectral imaging of field trials can address this gap. With digital imaging, the process of extracting phenomics is automated and accuracy is much better [14]. The accurate phenomics then assist in increasing the genetic gain in classical breeding approaches. The research problems identified in this thesis are:

1. Detection of crop field plots and rows: the accurate detection of crop plot and row in field trials along with extraction of associated data is a crucial step for phenotyping and then genomic selection. After detecting the rows, the extracted plant data from

rows can be used for downstream analysis. For example, plant physical characteristics or phenotypes can be associated with genetic markers in genome-wide association studies and genomic selection. However, the accurate detection of crop rows is a difficult task with the presence of certain limitations such as variable outdoor environment conditions, confusion of crops with weeds, irregular shape of crops and curved and irregular paths.

2. Extraction of accurate individual plant phenotypes: automated phenotyping technologies using digital imaging have helped to overcome the shortcomings of traditional manual phenotyping methods of plants. However, when plants overlap, it is difficult to extract accurate individual plant phenotypes such as normalized difference vegetation index and plant area from digital images.

3. Genomic selection and competition effects among individual plants: after the development of novel forage phenomics pipelines for ryegrass, which reduces the genotype-phenotype gap, the next problem is genomic prediction of the overall plant performance using quantitative genetic techniques. Further, by including the competition effects in the genomic prediction model for predicting genomic breeding values, the goal is to understand how much phenotypic variation is explained by competition among individual plants.

1.3. Research contributions and thesis outline

The main contributions of this thesis to address the above-mentioned research problems are:

Chapter 2: This chapter presents a brief literature background and review of the research problems discussed.

Chapter 3: This chapter presents a new crop row detection algorithm in high resolution field trial images that does not require any pre-known information such as crop row spacing, number of crop rows in the digital images to detect accurate crop rows. The proposed algorithm is also effective in complex conditions such as presence of noise, weeds, irregular crop shapes, poor light, shadows and variable illumination.

Chapter 4: This chapter proposes a new method for extracting individual plants' phenomics such as plant area and normalized difference vegetation index from digital field trial images. The method focuses on both the extraction of these regions from a multispectral image taken by an un-crewed aerial vehicle and the linking of these regions with individual plant biomass. The utility of the approach is evaluated by correlating individual plant phenomic bio-characteristics and plant biomass as estimated by fresh weight at harvest.

Chapter 5: This chapter presents the genomic prediction and competition (indirect genetic) effects among individual ryegrass plants. The phenomics of area extracted through circular regions are first validated by examining the best linear unbiased prediction and Bayesian genomic prediction models. The competition effects are then analysed using genomic best linear unbiased prediction models with and without covariance between direct and indirect genetic effects.

Chapter 6: This chapter discusses the research contributions and presents the future directions of this thesis.

1.4. Acknowledgments

1.5.   References

[1]   D. C-Godoy and J. Dewbre, "Economic Importance of Agriculture for Poverty Reduction", OECD Food, Agriculture and Fisheries Working Papers, Expert Systems with Applications, No. 23, OECD Publishing, 2010.

[2]   T. B. Brown, R. Cheng, X. R. R. Sirault, T. Rungrat, K. D. Murray, M. Trtilek, R. T. Furbank, M. Badger, B. J. Pogson and J. O. Borevitz, "TraitCapture: genomic and environment modelling of plant phenomic data", Current Opinion in Plant Biology, vol. 18, pp. 73-79, Apr. 2014.

[3]   J. Kumar, A. Pratap and S. Kumar, "Plant Phenomics: An Overview", Phenomics in Crop Plants: Trends, Options and Limitations, pp. 1-10, Springer India, 2015.

[4]   M. B. Sticklen, "Feedstock Crop Genetic Engineering for Alcohol Fuels", Crop Science, vol. 47, no. 6, pp. 2238-2248, Nov. 2007.

[5]   M. Tester and P. Langridge, "Breeding technologies to increase crop production in a changing world", Science, vol. 327, no. 5967, pp. 818-839, Feb. 2010.

[6]   S. S. Katariya, S. S. Gundal, M. T. Kanawade and K. Mazhar, "Automation in agriculture", International journal of recent scientific research, vol. 6, no. 6, pp. 4453-4456, 2015.

[7]   R. C. O'Malley and J. R. Ecker, "Linking genotype to phenotype using the Arabidopsis unimutant collection", The Plant Journal, vol. 61, no. 6, pp. 928-967, Mar. 2010.

[8]   D. Weigel and M. Richard, "The 1001 Genomes Project for Arabidopsis thaliana", Genome Biology, vol. 10, pp. 1-5, May. 2009.

[9]   S. B. Cannon, G. D. May and S. A. jackson, "Three Sequenced Legume Genomes and Many Crop Species: Rich Opportunities for Translational Genomics", Plant Physiology, vol. 151, pp. 970-977, Nov. 2009.

[10]   J. P. Vogel et al., International Brachypodium Initiative, "Genome sequencing and analysis of the model grass Brachypodium distachyon", Nature, vol. 463, no. 7282, pp. 763-770, Feb. 2011.

[11]   S. Atwell et al., "Genome-wide association study of 107 phenotypes in Arabidopsis thaliana inbred lines", Nature, vol. 465, no. 7298, pp. 627-657, Jun. 2010.

[12]   M. Wang, N. Jiang, T. Jia, L. Leach, J. Cockram, J. Comadran, P. Shaw, R. Waugh and Z. Luo, "Genome-wide association mapping of agronomic and morphologic traits in highly structured populations of barley cultivars", Theoretical and Applied Genetics, vol. 124, no. 2, pp. 233-246, Feb. 2012.

[13]   T. H. Meuwissen, B. J. Hayes and M. E. Goddard, "Prediction of total genetic value using genome-wide dense marker maps", Genetics, vol. 157, no. 4, pp. 1819–1847, 2001.

[14]   M. M. Rahaman, D. Chen, Z. Gillani, C. Klukas and M. Chen, "Advanced phenotyping and phenotype data analysis for the study of plant growth and development", Frontiers in Plant Science, vol. 6, pp. 1–15, 2015.

Chapter 2

Literature Review

Saba Rabab[1,2]

[1]School of Applied Systems Biology, La Trobe University, Bundoora, Australia

[2]Agriculture Victoria, AgriBio, Centre for AgriBioscience, Bundoora, Australia.

Genomic selection is a procedure that estimates genomic breeding values using genome wide marker information [1]. Genomic selection needs accurate and large-scale phenotyping of organisms to increase genetic gain. Therefore, phenotyping plays a key role in the success of standard phenotypic selection as well as genomic selection models. With high throughput phenomics techniques, the phenomic-genomic gap can be reduced to increase the overall productivity in terms of yield/biomass in forage crops, thereby increasing the profitability for farmers and the breeding companies.

In the first section of this chapter, we present the brief overview of digital images and some of the basic operations associated with them. For a detailed reading on this subject, refer to [2]. Further, we will present a short review on crop row detection and extraction of phenomics from digital images. In the second section, we will present a brief review on the genomic selection and competition effects in various organisms.

2.1. Phenotyping of organisms

Phenotyping of organisms can be defined as a set of algorithms or methods used to quantify the physical traits such as growth, architecture and composition with a certain precision and accuracy. For individual plants, phenotyping is based on biochemical, physiological,

morphological, and molecular structures. The current manual phenotyping techniques are time consuming, slow, expensive, and prone to human error. These shortcomings can be overcome by employing automated phenotyping methods such as extraction from digital images which consists of two mains parts: image analysis and image acquisition.

2.1.1.   Image acquisition

Image acquisition is the attainment of digital images from various electronic devices. Digital images may vary in sensor size, megapixel rating and bit rate. Each pixel captures light and translates it into a digital number. The size of the sensor influences the quality/accuracy of the digital number captured and the bit rate describes the number of tones available for a given colour e.g. an 8-bit image can describe a colour as 256 tonal values where a 16-bit image could describe the same colour as 65,536 tonal values. To standardise this variation in quality between different digital cameras, we can down-sample the data. The higher the resolution of an image, the more information it contains, and the more computational overhead is required to process it.

2.1.2.   What is a digital image?

A digital image is a representation of a real image as a set of number elements that can be stored and processed by a digital computer. These number elements are called pixels organized in a rectangular grid. In a grey image, the numerical value of a pixel represents the light intensity at the pixel location; the higher the value of a pixel the brighter that location is and vice-versa. Usually, the pixel value of a grey image is between [0, 255]. The pixel value of 255 represents the pure white pixel, the pixel value of 0 represents the pure black pixel and in between there are grey pixels. The width of a digital image is defined by the number of columns of pixels and the height of a digital image is defined by the number of rows of pixels.

Fig. 2.1. represents a grey image with 20 columns and 22 rows. Each pixel denoted as a square shaped represents the light intensity. The brighter pixels have the numerical values towards 255 and darker pixels have the numerical values towards 0.

2.1.3.   Colour image

A colour image is usually a collection of three grey images stitched together, with each grey image representing the intensity of a primary colour (either red, green or blue). Fig. 2.2(a) shows a colour Lena image [3]. Each colour pixel is a combination of three grey pixels with values between [0, 255]. Fig. 2.2(b) shows the red frame of Fig. 2.2(a). Each pixel in Fig. 2.2(b) represents the intensity of red colour in Fig. 2.2(a). The higher the value of a pixel the redder that location in Fig. 2.2(a) is and vice-versa. Similarly, Fig. 2.2(c) and Fig. 2.2(d) represent the green and blue grey frames, respectively. To emphasize this point, Fig. 2.3(a) shows a colour image and Fig. 2.3(b)-(d) show the red, green and blue frames of Fig. 2.3(a), respectively. It can be visualized that the red frame (Fig. 2.3(b)) has bright pixels demonstrating the maximum contribution of red colour in Fig. 2.3(a). On the other hand, the green (Fig. 2.3(c)) and blue (Fig. 2.3(d)) frames has dark pixels demonstrating the minimum contribution of green and blue colours respectively in Fig. 2.3(a). A similar kind of pattern can be found in Fig. 2.4(a)-(d) and Fig. 2.5(a)-(d) for green and blue colour images respectively.

2.1.4.   Colour to grey image

A colour image can be converted into grey image reducing the size of the image, while retaining most of the visual information. In most of the applications, a grey image is enough to do many tasks so there is no need to use more complicated and harder-to-process colour images. There are many ways we can convert a colour image into grey depending upon the needs and requirements of the application. One way is to get individual frame (red, green or
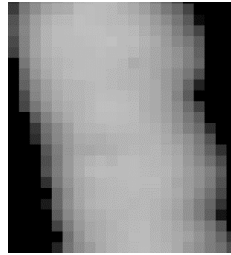
Fig. 2.1. A grey image with 20 columns and 22 rows. Each pixel denoted as a square shaped represents the light intensity. The brighter pixels have the numerical values towards 255 and darker pixels have the numerical values towards 0.

| (a) | (b) | (c) | (d) |
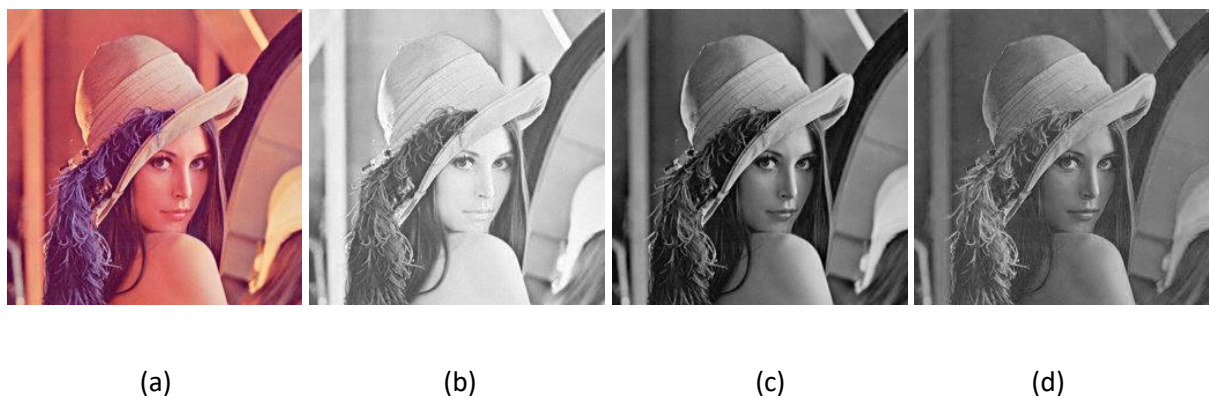
Fig. 2.2. Lena colour image [2] with (a) red, (b) green and (c) blue frames. Each frame represents the intensity of the respective colour; white pixels show greater intensity of that colour and vice-versa.

| (a) | (b) | (c) | (d) |

Fig. 2.3. (a) Red colour image with (b) red, (c) green and (d) blue frames. The red frame (b) has bright pixels demonstrating the maximum contribution of red colour in Fig. 2.3(a). On the other hand, the green (c) and blue (d) frames has dark pixels demonstrating the minimum contribution of green and blue colours respectively in Fig. 2.3(a).

(a)   (b)   (c)   (d)
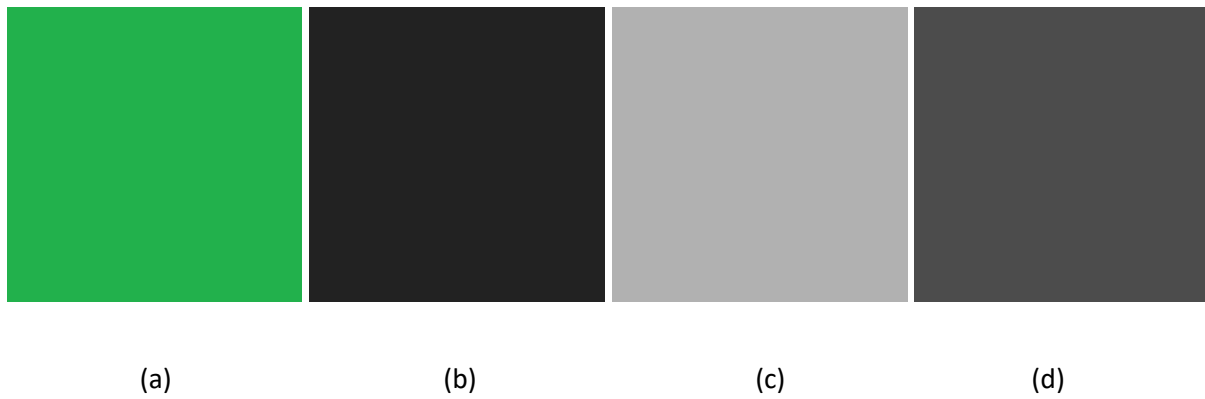
Fig. 2.4. (a) Green colour image with (b) red, (c) green and (d) blue frames. The green frame (c) has bright pixels demonstrating the maximum contribution of green colour in Fig. 2.4(a). On the other hand, the red (b) and blue (d) frames has dark pixels demonstrating the minimum contribution of red and blue colours respectively in Fig. 2.4(a).

(a)   (b)   (c)   (d)
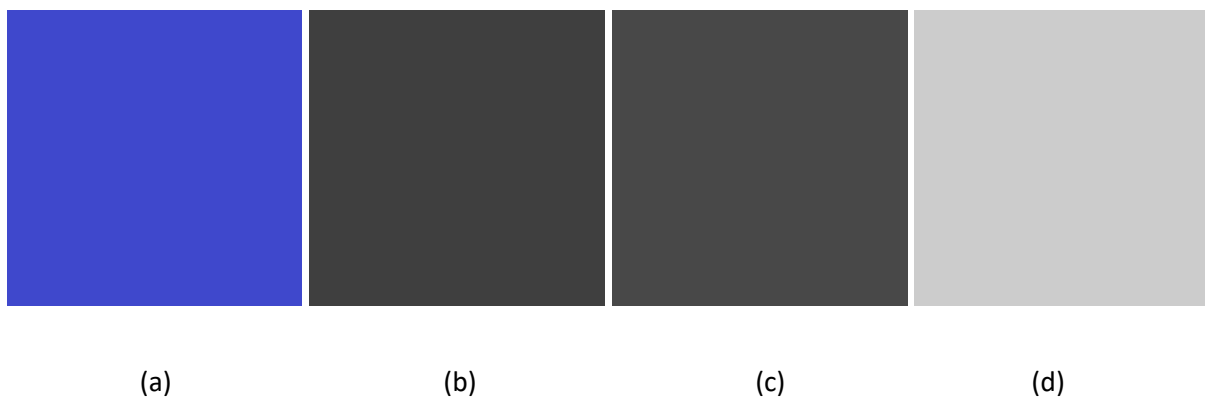
Fig. 2.5. (a) Blue colour image with (b) red, (c) green and (d) blue frames. The blue frame (d) has bright pixels demonstrating the maximum contribution of blue colour in Fig. 2.5(a). On the other hand, the red (b) and green (c) frames has dark pixels demonstrating the minimum contribution of red and green colours respectively in Fig. 2.5(a).

blue) as grey image. The other method is to get the average of three frames. However, this method is not effective as human eyes are differently sensitive to the primary colours. The eyes are most sensitive to green light, less sensitive to red light, and least sensitive to blue light. The more effective method is to get the weighted average of these colours given as:

$$Grey = \ 0.299R \ + \ 0.587G \ + \ 0.114B. \tag{2.1}$$

In plant phenomics applications, we are often interested in extracting the greenness of plants. One way is to get the green frame as it is, however, the green frame itself can give false band for the vegetation. A more suitable way to extract greenness is to use the Normalised Difference Vegetation Index (NDVI) [4]. NDVI is based on the red and near infrared bands. The NDVI value is always between -1 and 1. The NDVI value between -1 and 0 shows the plant is dead, whereas value towards 1 shows the healthy plant. Besides NDVI, there are other methods to extract the greenness, one such method is given by Burgos-Artizzu [5]:

$$Greenness = \ 1.262G - 0.884R - 0.311B. \tag{2.2}$$

2.1.5. Grey to binary image

Converting grey to binary image is often required for many purposes; one such example is to extract the region of interest. Moreover, converting into binary significantly reduces the size and overhead of computation. The grey image can be converted into binary image with only two binary values $\in [0,1]$; white (binary value: 1), which represented the region of interest and black (binary value: 0), which represented the background. A grey image is converted into binary by thresholding the grey pixels to a certain threshold, given as:

$$Binary = \begin{cases} 1 & if \ grey > threshold, \\ 0 & otherwise. \end{cases} \tag{2.3}$$

The threshold value can be chosen based on the grey image to effectively extract the region of interest. Instead of manual thresholding, the Otsu binary thresholding [6] can be employed to automatically perform clustering-based image thresholding on a grey image returning a threshold value. This threshold can then be used to convert the grey image into binary.

2.1.6.   Review of crop row detection

In this section, the different methodologies for the crop row classification will be reviewed. A summary of the reviewed works is also given in Table 2.1. There are four columns; the first one represents the capability level to detect straight crop rows, with three possible values of poor, moderate and good. The second column shows whether the method can detect the curved crop rows or not. The ability to perform in complex conditions such as presence of weed and noise with three possible levels of poor, moderate and good is shown in column 3. Finally, whether the method needs initial information such as the number of crop rows and spacing between the crop rows before the detection of crop rows is represented in column 4.

Hough transform methods

To detect lines, circles and parametric curves, the Hough transform [7] was developed in 1962. Later, it was applied to identify straight lines in digital images. A simple straight crop row detection algorithm for wheat crop fields was developed and presented in [8]. Basic image processing operations such as binarization and segmentation were used followed by Hough transform. The algorithm [8] showed good results on digital images where wheat growth was in early stages. However, the algorithm does not illustrate good performance in complex conditions. Further, the algorithm [8] required information about the crop field before its deployment making its application limited. To increase the computational efficiency of Hough transform, a modified version, the random Hough transform [9] was presented for the detection of crop field rows. The simulation scenarios presented were too simple containing digital images of a single crop row. Although, the computational speed is much faster than the original Hough transform, but the algorithm did not have the ability to perform in complex conditions. To get better results of crop row detection in the presence of weed,

Table 2.1. A summary of the reviewed works.

Method	Straight crop rows detection level	Curved crop rows detection	Effective in complex conditions	Pre-known variables (crop numbers, crop spacing etc)
Hough transform and vanishing point [8]	Moderate	No	Poor	Yes
Random Hough transformation [9]	Poor	No	Poor	Yes
Gabor filtering + Hough transform [10]	Good	Yes	Moderate	No
Hough transform [11]	Moderate	No	Poor	No
Horizontal strips [12]	Moderate	No	Poor	Yes
Horizontal bands [13]	Good	No	Moderate	Yes
Linear regression [14]	Good	No	Moderate	Yes

Least squares linear regression [15]	Good	No	Good	Yes
Heuristic algorithms [16]	Good	No	Moderate	Yes
Stereovision-based [17]	Good	No	Moderate	No
K-Means clustering [20]	Good	No	Moderate	Yes
Linear regression + multi-ROIs [21]	Good	No	Good	Yes
Linear regression + multi-ROIs + Hough transform [22]	Good	Yes	Good	Yes
Hough transform + filtering [23]	Good	No	Poor	No
Convolutional neural network [24]	Good	No	Good	No

Global energy minimization [25]	Good	Yes	Good	No

an algorithm [10] based on Hough transform and Gabor filtering was presented. An extension of Hough transform was developed which showed good performance in complex conditions without the need of any pre-information. Also, the extended version of Hough transform outperformed Gabor filtering. To detect weed between the crop rows, a machine-vision based system is developed employing Hough transform [11]. The spacing between the crop rows was first determined followed by the weed detection. The detected weed can then be destroyed automatically with the help of control spray saving a lot of time and labour.

Exploration of horizontal strips

A computer vision-based method for crop row detection algorithm reduced the computational burden by removing the image segmentation step [12]. The digital images were captured continuously from a colour camera installed on the computer vision-based system and forwarded for processing to the computer. The removal of image segmentation helped in real-time processing of the captured images by lowering the computational complexity of the overall algorithm. The algorithm for crop row detection was based on the lateral position and estimation of the orientation of centre lines of crop rows via weighted linear regression. To determine the accuracy, the position of a reference string was used to compare it with the calculated crop row centre line. To detect crop rows and weed automatically, another method [13] used the grey digital images obtained by the transformation from colour images. The crop row spacing was known before the deployment

of the algorithm, which divided the grey scale images into eight equal horizontal bands. The results achieved from the automated system correlated well with the manual assessment.

Linear regression

Linear regression can be used for the predictive analysis. A vision guidance system was developed based on linear regression to detect crop rows [14]. The digital images are divided into three segments, and, in each segment, a cost function and linear regression was used to identify crop rows. There was pre-known information in form of number of crop rows and spacing between crop rows. Further, the performance of the algorithm reduces in the presence of visual noise from weeds. Another method [15] also employed linear regression to detect crop rows in maize fields in the presence of high weed. The algorithm consisted of three main steps: image segmentation, thresholding, and crop row detection. Vegetation index was used for image segmentation, the crops and weeds were separated using thresholding and crop row detection used least squares linear regression to identify crop rows. A pre-generated template was used to identify crop rows which consisted of information such as number of crop rows to be detected, the location of crop rows and the area to be explored in digital images.

Blob analysis and Stereo-based

Blob (Binary Large OBject) analysis based on the analysis of consistent image regions is a fundamental technique of machine vision [16]. In digital images, blob analyses determine the regions of interest that have different properties as compared to the background. Based on blob analyses, a method for crop row detection was presented in [16]. Binarization was used to transform the digital image into binary followed by the image segmentation. The binary objects with less than 200 image pixels were discarded as they can represent noise and

background. Therefore, the objects with more than 200 pixels are merged together to make a potential crop row. The angles of the principal axes and locations for centre of gravity of all blob objects were then calculated to determine whether these blob objects belong to a crop row or not. The algorithm [16] demonstrated good results on laboratory images but performed poorly on real crop field images. Furthermore, the discontinuity within the crop rows impacted the accuracy of the algorithm. For straight and curved crop rows detection, an effective stereovision-based algorithm was presented [17]. The algorithm consisted of functions for elevation map creation, stereo-image processing, and navigation point discrimination. A three-dimensional crop elevation map was reconstructed first followed by the search for optimal search points. This method was deployed in a soya bean field for the testing of crop row detection [17] with promising results. The extensions of this work by the same authors are presented in [18, 19] for three-dimensional crop row structure mapping and guidance.

Other methods

A method based on K-Means clustering was used to aggregate similar image objects to detect straight crop rows [20]. A confusion matrix was used to test the performance with accuracy of over 90%. A crop row detection algorithm was presented based on multiple regions of interest [21]. Basic image processing operations such as colour to grey, binarization and segmentation were employed with the assumption that the spacing between crop rows was consistent. Accumulation of green image pixels was used to identify straight as well as curved crop rows in maize fields [22]. There were three main steps: image segmentation, identification of starting point for crop rows and detection of crop rows. The image segmentation consisted of extraction of regions of interest, identification of greenness,

binarization and morphological operations. The starting points for crop rows were identified using Hough transform. The image segmentation and acquisition were the same as applying Hough transform with the exception that the vertical projection was applied before Hough transform. Finally, the crop rows were detected using least squares regression analyses. Further, curved crop rows were identified with the help of polynomial equations. The algorithm [22] showed better results as compared to Hough transform when simulated on maize field images. An embedded guiding system for unmanned aerial vehicles (UAVs) was proposed along with the crop row detection algorithm and an algorithm for generating the necessary parameters to control the UAV [23]. The algorithm for crop row detection can be divided into two main steps: image segmentation and crop row detection. Image segmentation consisted of transformation from colour to grey images, binarization, edge detection and calculation of average edges. The crop row detection was done using Hough transform followed by line filtering and line follower. The accuracy claimed was 100% on the presented image dataset, however, the image dataset was simple to process and free of any noise. Using an UAV, another method [24] was proposed for machine-vision crop row detection system. The crop rows were identified using a deep learning approach, Convolutional Neural Networks (CNN). The algorithm [24] illustrated better accuracy results as compared to the other works, however, the computational complexity of CNN is very high making them unsuitable for real-time processing for crop row detection. Using global energy minimization, a crop row detection algorithm for straight and curved rows was developed [25]. Dynamic programming and perspective projection of crop rows were used to detect crop rows. The algorithm [25] was simulated on their own image dataset which consisted of various scenarios and showed excellent results. Further, the performance of the proposed algorithm

[25] outperformed other methods. The only downside was the usage of pre-generated template, which make it unsuitable for many use cases.

In the above-mentioned proposals, one of the common drawbacks is the need for vital information such as number, spacing and location of crop rows before the deployment of crop row detection algorithms. Also, in some proposals, there is need for the pre-generated template for their implementation. These limitations imply that these proposals cannot be applied in wide range of field trials. In this thesis, a robust crop row detection algorithm was proposed that showed good results without the need of any template and any pre-information except for weed intensity and therefore can be applied to a wider range of crop fields demonstrating the novelty of the work. The proposed work was robust in challenging conditions such as poor illumination, variable light, sudden shadows, presence of weeds and noise and irregular crop shape. Various tests and analyses were performed to examine the strength of the proposed work and the Receiver Operating Characteristic graph has been applied for the first time in crop row detection algorithm testing to the best of authors' knowledge. Lastly, the superiority of the proposed work was showed by comparing it with the several state-of-art methods.

2.1.7.   Review of single plant phenomics

The application of machine vision for the extraction of plants phenomics such as NDVI started almost 30 years ago [26]. There has been huge advancement in monitoring large crop fields using sensor technologies. However, the extraction of phenomics for single plants was done primarily in controlled environments. For instance, in the previous proposals [27-33], the individual plants were captured in a very simplistic setting; either there were few plants in a digital image, or the individual plants were not merged into each other.

Most breeding programs concentrate on whole crop row or whole plot phenotypes, which is often enough. However, the phenotypes of individual plants are of importance to examine family or population uniformity in both in- and outbred species. Uniformity is important because growers desire high forage biomass with even growth throughout a paddock and it is also a characteristic for determining plant breeder's rights. Moreover, as each plant is genetically unique, it may be of importance to observe the competition effects between the individual plants [34], that is the effect of individual plants on the neighbour plants. The uniformity and the overall biomass yield can be inferior in the paddock if the individual plants are overly competitive in a forage cultivar. The manual calculation of phenomics of individual plants can be time consuming, and therefore, the automated phenomic solutions are required.

The objective of this thesis is to automatically extract accurate individual plants' phenomics such as area and NDVI values from the TIFF file images of field trials. There are initial estimates of the individual plants' regions in form of bounding boxes that assist in the extraction of the mentioned phenomics. However, there are certain problems with the rectangular shaped bounding boxes leading to identify circular bounding boxes for extraction of accurate area of individual plants.

Circular Hough Transform (CHT) [35-36] is a popular approach to detect circles in digital images. It is very effective in detecting multiple circles with different radii in a digital image and even with somewhat irregular circular shapes. However, CHT does not perform good where the circles are overlapping and merged to each other, just as in case of our research problems.

The above-mentioned existing proposals are not effective for our research problems; therefore, a new and robust algorithm is developed for the extraction of individual plants' phenomics from digital images. Further, most of the existing proposals work in a very controlled environment and for single plants per image. The proposed algorithm was implemented on a field trial image dataset taken from the top view. Each field trial image consisted of thousands of plants, and despite of overlapping of adjacent plants, the proposed work showed sufficient accuracy demonstrating the novelty and originality as compared to the previous works.

2.2. Genomic selection

Genomic selection (GS) is breeding using DNA information [1]. It increases the accuracy of selection and chooses the best candidates from each family including good performing individuals from families that perform poorly on average. In addition to increased precision when selecting breeding candidates, GS can potentially also reduce inbreeding as we can use individuals from many families, thereby increasing the genetic gain with GS. Though, in many breeding applications high selection intensity and rapid turn-over of generations often outweighs these reductions inbreeding per generation. In this section, we will briefly introduce the strategies leading to GS.

2.2.1. Ryegrass selection strategies

Several selection strategies have been applied in ryegrass breeding. One of the earliest methods used in conventional breeding is phenotypic selection. In this method, crop varieties are selected based on the experience of the breeder and observed phenotypes to achieve genetic gain of the target trait. However, this scheme requires a lot of time and labour for a

complete phenotypic profile. It requires that each line or population is phenotyped before selection decisions can be made.

Furthermore, with the early advancements in the field of computer science, best linear unbiased prediction (BLUP) model was presented by Henderson in 1975 [37] and it became the most popular and standard method for genetic evaluation as it has good predictive accuracy for most traits and training populations. However, ryegrass is an outbreed pasture grass and its varieties are made up of multiple parents. Therefore, each parent contribution is unknown and thus it is difficult to capture accurate pedigree for the breeding values. Hence, incomplete pedigree limits the application of BLUP in many forage breeding programs.

2.2.2. Marker assisted selection

Marker assisted selection (MAS) uses genetic markers related to the specific trait of interest for early selection in animals and plants. Moreover, the DNA-based marker information can be exploited to improve the accuracy of estimated breeding values for traits whose phenotypes are hard to measure otherwise. The success of MAS is subject to adequate linkage disequilibrium between a marker and the phenotypic quantitative trait locus (QTL) and the QTL explaining the considerable proportion of the variation for the trait. However, often the relationship among marker and QTL is not substantial, and hence rejected [38]. Existing MAS methods can be validated only for a few major effect genes as compared to many genes with small effects [39]. Since, forage agronomic traits have complex genetic architecture, where trait performance is determined by many genes with small effects. Thus, MAS technique may lack the ability to fully capture the genetic variance in such scenarios, hence this limits its application in forages.

2.2.3.   Genomic selection and competition effects

GS is estimating the genetic worth of the individual based on the whole genome rather than few markers, thus capturing all the diversity from that genome [40]. GS develops a prediction model that contain the phenotypic and genotypic data of training population, sufficient to estimate the genomic estimated breeding values (GEBVs) for all the individuals of the breeding population without the knowledge of specific gene location [41].

GS together with high throughput phenotyping can help in selecting for ryegrass agronomic traits (dry matter yield, persistency), which are otherwise hard to measure or time consuming [40]. The accuracy of GS is highly dependent on reference population size, heritability values of the desired trait and the genetic diversity of breeding populations [42]. However, one of the technical challenges in implementing the GS in crop plants is to accurately measure the phenotypic data. The precise phenotypic data is crucial because it is used to train the GS model to exactly predict GEBVs of breeding population. Numerous papers have evaluated the possible utilization of GS in simulations and experimental investigations in some of the major crops [43-47]. The application of GS in perennial forage crops is appealing as it can significantly reduce the length of the breeding cycle [48]. The scenarios for GS in perennial forage crops such as grasses and legumes have been evaluated in [49-50]. In [49], the challenge of limited extent of linkage disequilibrium is addressed by presenting two schemes for the implementation of GS; the first one is slight modification of existing schemes that helped in the reduction of overall cost. The second scheme allows two rounds of selection within a time-period required previously for one round of selection resulting in potentially double the genetic gain. In [50], the benefits of GS such as reduce cycle time, increase

selection accuracy and reduce operational costs are presented by evaluating different methods.

It is universally known that there is competitive interaction among most animals and plants within or across species [51-52]. Global diversity of ryegrass synthetic lines or populations is high and there is the potential for competition between individual plants or a population. Competition can affect the heritable components, consequently affecting the phenotype and their response to multilevel selection. The interaction among individuals can be social (performance, accommodation, behaviour) with higher organisms, or physical such as in plants due to limited basic survival resources (water, sunlight, space, nutrients). Reduction of such competitive interactions is crucial for improving overall animal wellbeing and increased productivity in plants. Therefore, it is vital to understand how competition effects selection and how to reduce negative competition interaction in artificial breeding programmes for overall increased genetic gain.

In this thesis, I investigated the interaction among individual ryegrass plants by extracting individual plant phenomics together with Indirect genetic effect (IGE) models. The indirect genetic effect is defined as the interaction in which the genotype of an individual can influence the phenotypic trait value of its neighbours. The IGEs have already been studied for the trees in which the definition of accurate phenotype is comparatively easy as compared to ryegrass because individual trees are physically distant from each other. In case of ryegrass, individual plants often overlap hence the extraction of individual plant phenomics is not a straightforward task. In this thesis, I defined single plant phenotypes from images taken by an un-crewed aerial vehicle in row planted perennial ryegrass. I then used the single plant phenotypes to investigate genomic prediction accuracy and competition effects using IGE

models. This thesis provides the first application of IGE models in pasture grasses which is the novelty of this work.

This thesis investigated the presence of IGE for individual ryegrass plants. It has been shown that individual ryegrass plant performance correlates poorly with the performance of multiple plants grown in swards or plots. In this thesis, the field trial for ryegrass plants were designed with a significant gap of 60cm between the rows. Therefore, for the interactive behaviour study there were two neighbours in the row (top and bottom) per focal plant at distance allowing for overlap and competition of plants. The results of this first study of IGEs in ryegrass will provide information on their importance in ryegrass breeding.

2.3. Acknowledgments

2.4. References

[1]   T. H. Meuwissen and M. E. Goddard, "Prediction of identity by descent probabilities from marker-haplotypes", Genetics Selection Evolution, vol. 33, no. 6, pp. 605-634, 2001.

[2]   R. C. Gonzalez and R. E. Woods, "Digital Image Processing", Pearson/Prentice Hall, 4th Edition, 2018.

[3]   http://ndevilla.free.fr/lena/

[4]   J. Xue and B. Su, "Significant Remote Sensing Vegetation Indices: A Review of Developments and Applications", Journal of Sensors, vol. 2017, pp. 1-17, 2017.

[5]   X. P. B-Artizzu, A. Ribeiro, M. Guijarro and G. Pajares, "Real-time image processing for crop/weed discrimination in maize fields", Computers and Electronics in Agriculture, vol. 75, no. 2, pp. 337-346, 2011.

[6]   N. Otsu, "A Threshold Selection Method from Gray-Level Histograms", IEEE Transactions on Systems, Man, and Cybernetics, vol. 9, no. 1, pp. 62-66, 1979.

[7]   P. V. C. Hough, "A method and means for recognizing complex patterns", US Patent Office No. 3069654.

[8]   G. Jiang, X. Wang, Z. Wang and H. Liu, "Wheat rows detection at the early growth stage based on Hough transform and vanishing point", Computers and Electronics in Agriculture, vol. 123, pp. 211-223, 2016.

[9]   R. Ji and L. Qi, "Crop-row detection algorithm based on Random Hough Transformation", Mathematical and Computer Modelling, vol. 54, no. 3-4, pp. 1016-1020, 2011.

[10]   G. Jones, C. Gée and F. Truchetet, "Modelling agronomic images for weed detection and comparison of crop/weed discrimination algorithm performance", Precision Agriculture, vol. 10, no. 1, pp. 1-15, 2009.

[11]   M. Asif, S. Amir, A. Israr and M. Faraz, "A Vision System for Autonomous Weed Detection Robot", International Journal of Computer and Electrical Engineering, vol. 2, no. 3, pp. 486-491, 2010.

[12]   H. T. Sogaard and H. J. Olsen, "Determination of crop rows by image analysis without segmentation", Computers and Electronics in Agriculture, vol. 38, pp. 141-158, 2003.

[13]   T. Hague, N. D. Tillett and H. Wheeler, "Automated crop and weed monitoring in widely spaced cereals", Precision Agriculture, vol. 7, no. 1, pp. 21-32, 2006.

[14]   J. Billingsley and M. Schoenfisch, "The successful development of a vision guidance system for agriculture", Computers and Electronics in Agriculture, vol. 16, no. 2, pp. 147-163, 1997.

[15]   M. Montalvo, G. Pajares, J. M. Guerrero, J. Romeo, M. Guijarro, A. Ribeiro, J. J. Ruz and J. M. Cruza, "Automatic detection of crop rows in maize fields with high weeds pressure", Expert Systems with Applications, vol. 39, no. 15, pp. 11889-11897, 2012.

[16]   V. Fontaine and T. G. Crowe, "Development of line-detection algorithms for local positioning in densely seeded crops", Canadian Biosystems Engineering, vol. 48, no. 7, pp. 19-29, 2006.

[17]   M. Kise, Q. Zhang and F. R. Más, "A Stereovision-based Crop Row Detection Method for Tractor-automated Guidance", Biosystems Engineering, vol. 90, no. 4, pp. 357-367, 2005.

[18]   M. Kise and Q. Zhang, "Development of a stereovision sensing system for 3D crop row structure mapping and tractor guidance", Biosystems Engineering, vol. 101, no. 2, pp. 191-198, 2008.

[19]   F. R-Más, Q. Zhang and J. F. Reid, "Stereo vision three-dimensional terrain maps for precision agriculture", Computers and Electronics in Agriculture, vol. 60, no. 2, pp. 133-143, 2008.

[20]   K. N. Ramesh, N. Chandrika, S. N. Omkar, M. B. Meenavathi and V. Rekha, "Detection of Rows in Agricultural Crop Images Acquired by Remote Sensing from a UAV", International Journal of Image, Graphics and Signal Processing, vol. 8, no. 11, pp. 25-31, 2016.

[21]   G. Jiang, Z. Wang and H. Liu, "Automatic detection of crop rows based on multi-ROIs", Expert Systems with Applications, vol. 42, no. 5, pp. 2429-2441, 2015.

[22]   I. G-Santillán, J. M. Guerrero, M. Montalvo and G. Pajares, "Curved and straight crop row detection by accumulation of green pixels from images in maize fields", Precision Agriculture, vol. 19, no. 1, pp. 18-41, 2018.

[23]   M. Basso and E. P. de Freitas, "A UAV Guidance System Using Crop Row Detection and Line Follower Algorithms", Journal of Intelligent & Robotic Systems, vol. 97, pp. 605-621, 2020.

[24]   M. D. Bah, A. Hafiane and R. Canals, "CRowNet: Deep Network for Crop Row Detection in UAV Images", CRowNet: Deep Network for Crop Row Detection in UAV Images, vol. 8, pp. 5189-5200, 2019.

[25]   I. Vidović, R. Cupec and Ž. Hocenski, "Crop row detection by global energy minimization", Pattern Recognition, vol. 55, pp. 68-86, 2016.

[26]   C. J. Tucker, "Red and photographic infrared linear combinations for monitoring vegetation", Remote Sensing of Environment, vol. 8, no. 2, pp. 127-150, May. 1979.

[27]   K. Neumann et al., "Dissecting spatiotemporal biomass accumulation in barley under different water regimes using high-throughput image analysis", Plant, Cell & Environment, vol. 38, no. 10, pp. 1980-1996, Oct. 2015.

[28]   O. Tackenberg, "A New Method for Non-destructive Measurement of Biomass, Growth Rates, Vertical Biomass Distribution and Dry Matter Content Based on Digital Image Analysis", Annals of Botany, vol. 99, no. 4, pp. 777-783, Apr. 2007.

[29]   D. Chen et al., "Dissecting the phenotypic components of crop plant growth and drought responses based on high-throughput image analysis", Plant Cell, vol. 26, no. 12, pp. 4636-4655, Dec. 2014.

[30]   A. Hartmann, T. Czauderna, R. Hoffmann, N. Stein and F. Schreiber, "HTPheno: an image analysis pipeline for high-throughput plant phenotyping", BMC Bioinformatics, vol. 12, no. 148, pp. 1-9, May. 2011.

[31]   R. Subramanian, E. P. Spalding and N. J. Ferrier, "A high throughput robot system for machine vision-based plant phenotype studies", Machine Vision and Applications, vol. 24, no. 3, pp. 619-636, Apr. 2013.

[32]   N. D. Miller, B. M. Parks and E. P. Spalding, "Computer-vision analysis of seedling responses to light and gravity", The Plant Journal, vol. 52, no. 2, pp. 374-381, Aug. 2007.

[33]   R. T. Clark et al., "Three-Dimensional Root Phenotyping with a Novel Imaging and Software Platform", Plant Physiology, vol. 156, pp. 455-465, Jun. 2011.

[34]   J. C. e Silva and R. J. Kerr, "Accounting for competition in genetic analysis, with particular emphasis on forest genetic trials", Tree Genetics & Genomes, vol. 9, pp. 1-17, 2012.

[35]   T. J. Atherton and D. J. Kerbyson, "Size invariant circle detection", Image and Vision Computing, vol. 17, no. 11, pp. 795-803, Sep. 1999.

[36]   H. K. Yuen, J. Princen, J. Illingworth and J. Kittler, "Comparative study of Hough Transform methods for circle finding", Image and Vision Computing, vol. 8, no. 1, pp. 71-77, Feb. 1990.

[37]   C. R. Henderson, "Best linear unbiased estimation and prediction under a selection model", Biometrics, vol. 31, no. 2, pp. 423-447, 1975.

[38]   N. F. Grinberg et al., "Implementation of Genomic Prediction in Lolium perenne (L.) Breeding Populations", Frontiers in Plant Science, vol. 7, pp. 1-10, 2016.

[39]   Y. Xu and J. H. Crouch, "Marker-Assisted Selection in Plant Breeding: From Publications to Practice", Crop Science, vol. 48, no. 2, pp. 391-407, 2008.

[40]   Z. Lin et al., "Genetic Gain and Inbreeding from Genomic Selection in a Simulated Commercial Breeding Program for Perennial Ryegrass", Plant Genome, vol. 9, no. 1, pp. 1–12, 2016.

[41]   T. H. Meuwissen, B. J. Hayes and M. E. Goddard, "Prediction of total genetic value using genome-wide dense marker maps", Genetics, vol. 157, no. 4, pp. 1819–1847, 2001.

[42]   H. D. Daetwyler, B. Villanueva and J. A. Woolliams, "Accuracy of Predicting the Genetic Risk of Disease Using a Genome-Wide Approach", PLOS One, vol. 3, no. 10, pp. 1–8, 2008.

[43]   R. Bernardo and J. Yu, "Prospects for Genomewide Selection for Quantitative Traits in Maize", Genetics, vol. 47, no. 3, pp. 1082-1090, 2007.

[44]   X. Wang, Y. Xu, Z. Hu and C. Xu, "Genomic selection methods for crop improvement: Current status and prospects", The Crop Journal, vol. 6, no. 4, pp. 330-340, 2018.

[45]   J-L. Jannink, A. J. Lorenz and H. Iwata, "Briefings in Functional Genomics", The Crop Journal, vol. 9, no. 2, pp. 166–177, 2010.

[46]   A. R. Bentley et al., "Applying association mapping and genomic selection to the dissection of key traits in elite European wheat", Theoretical and Applied Genetics, vol. 127, no. 12, pp. 2619-2651, 2014.

[47]   Y. Wang et al., "The accuracy of prediction of genomic selection in elite hybrid rye populations surpasses the accuracy of marker-assisted selection and is equally augmented by multiple field evaluation locations and test years", BMC Genomics, vol. 15, pp. 1-12, 2014.

[48]   D. Grattapaglia and M. D. V. Resende, "Genomic selection in forest tree breeding", Tree Genetics & Genomes, vol. 7, pp. 241–255, 2011.

[49]   B. J. Hayes et al., "Prospects for genomic selection in forage plant species", Plant Breeding, vol. 132, pp. 133-143, 2013.

[50]   R. M. S. Resende, M. D. Casler and M. D. V. de Resende, "Genomic Selection in Forage Breeding: Accuracy and Methods", Crop Breeding & Genetics, vol. 54, no. 1, pp. 143-156, 2014.

[51]   P. Bijma, W. M. Muir and J. A. M. Van Arendonk, "Multilevel Selection 1: Quantitative Genetics of Inheritance and Response to Selection", Genetics, vol. 175, no. 1, pp. 277-288, 2007.

[52]   P. Bijma, W. M. Muir, E. D. Ellen, J. B. Wolf and J. A. M. Van Arendonk, "Multilevel

        Selection 2: Estimating the Genetic Parameters Determining Inheritance and Response

        to Selection", Genetics, vol. 175, no. 1, pp. 289–299, 2007.

Chapter 3

A template-free machine vision-based crop row detection algorithm

Saba Rabab[1,2,] *Pieter Badenhorst[3], Yi-Ping Phoebe Chen[4] and Hans D. Daetwyler[1,2]

[1]School of Applied Systems Biology, La Trobe University, Bundoora, Australia

[2]Agriculture Victoria, AgriBio, Centre for AgriBioscience, Bundoora, Australia.

[3]Agriculture Victoria, Hamilton Centre, Hamilton, Australia.

[4]Department of Computer Science and Information Technology, La Trobe University, Bundoora, Australia.

*Corresponding Author

Author Contributions: SR and HD developed the experimental design; SR developed algorithms and carried out the majority analyses; YC and HD advised on analyses; SR and PB collected or processed initial data; HD and YC supervised the study; SR and HD wrote the paper; all authors have read and approved the paper.

3.1. Abstract

Due to the increase in the use of precision agriculture, field trials have increased in size to allow for genomic selection tool development by linking quantitative phenotypic traits to sequence variations in the DNA of various crops. Crop row detection is an important step to enable the development of an efficient downstream analysis pipeline for genomic selection. In this paper, an efficient crop row detection algorithm was proposed that detected crop rows in colour images without the use of templates and most other pre-information such as number of rows and spacing between rows. The method only requires input on field weed intensity. The algorithm was robust in challenging field trial conditions such as variable light, sudden shadows, poor illumination, presence of weeds and noise and irregular crop shape. The algorithm can be applied to crop images taken from the top and side views. The algorithm was tested on a public dataset with side view images of crop rows and on Genomic Sub-Selection dataset in which images were taken from the top view. Different analyses were performed to check the robustness of the algorithm and to the best of authors' knowledge, the Receiver Operating Characteristic graph has been applied for the first time in crop row detection algorithm testing. Lastly, comparing this algorithm with several state-of-the-art methods, it exhibited superior performance.

Keywords: Crop row detection, perspective projection, triangular matrix, accuracy, complexity.

3.2. Introduction

Agriculture is the primary industry sector ensuring food security and underpinning economic growth. Agriculture contributes heavily to different aspects of the personal and collective

lives. It is the major source of income in developing countries with almost 70% of the population relying on agriculture [1]. Agriculture is the underpinning industry to feed a growing world population and the last billion-dollar industry to be digitized. The advent of newer technologies has led to the next "green" revolution in agriculture allowing for the use of digital technologies to enable genomic selection in outbreeding species, where large-scale phenotyping was a limiting factor. The large data volumes generated by these technologies pose new data analysis challenges. Data extraction requires the identification of crops from background in images, which then enables the application of data in downstream analysis. These processes also need to be implemented in an automated manner so that data processing is fast, accurate and user friendly. The use of automation in agriculture has gained huge attention and has become very beneficial in the last three decades [2-3]. A more specific case of automation in agriculture is precision agriculture [4-5].

Precision agriculture is a management strategy that analyses and processes temporal, spatial and individual data aiming to improve productivity and profitability, while sustaining the quality of the surrounding environment. Machine vision can enhance precision agriculture through digital phenotyping, grading and sorting, machine guidance and livestock identification. The application of machine vision systems in agriculture is increasing over time. A few of the examples of its applications are real-time imaging of crops, management maps, automatic guidance and quality control. High resolution cameras fitted on satellites and drones can assist in detecting the in-field heterogeneous mix of crops, weeds and soil with high precision. They can also be used in weed infested areas of the field to apply herbicides in a targeted manner. Out of the numerous applications of precision agriculture, crop plot and row detection in field trials and extraction of associated data is an important research focus for phenotyping and then genomic selection as it is a crucial step in data extraction. It

has attracted numerous studies [6-13], which worked on different aspects of crop row and weed detection. After detecting the rows, the extracted plant data from rows can be used for downstream analysis. For example, plant physical characteristics or phenotypes can be associated with genetic markers in genome-wide association studies and genomic selection [14-15]. In turn, these analyses can be used to identify plants with an increased genetic potential for productivity and resource use efficiency. While there are several advantages to automatic crop row detection using machine vision, there are also certain challenges, including:

- outdoor environment conditions: factors like variable light conditions, shadows, complex backgrounds, poor illumination can affect the image quality.

- confusion of crops with weeds: regular plants and crops can be confused with high density weeds that have similar visual patterns.

- irregular shape of crops: growth variation of plants and crops resulting in different plant shapes and volumes can lead to false detection.

- curved and irregular paths: the crop rows can be curved or irregular in shape. Also, the movements of the vehicle in irregular terrain can affect the resulting captured images.

The high-level description of a general crop row detection process is illustrated in Fig. 3.1. The third step is crop row classification. In the literature, the classification of crop rows often requires known input parameters such as number of rows, spacing between rows and intensity of weeds in a crop image. Furthermore, in some proposals, a template is generated first which is used in the main algorithm. This limits the level of automation and applicability to field trials where the input parameters are varied or unknown and fails when the number
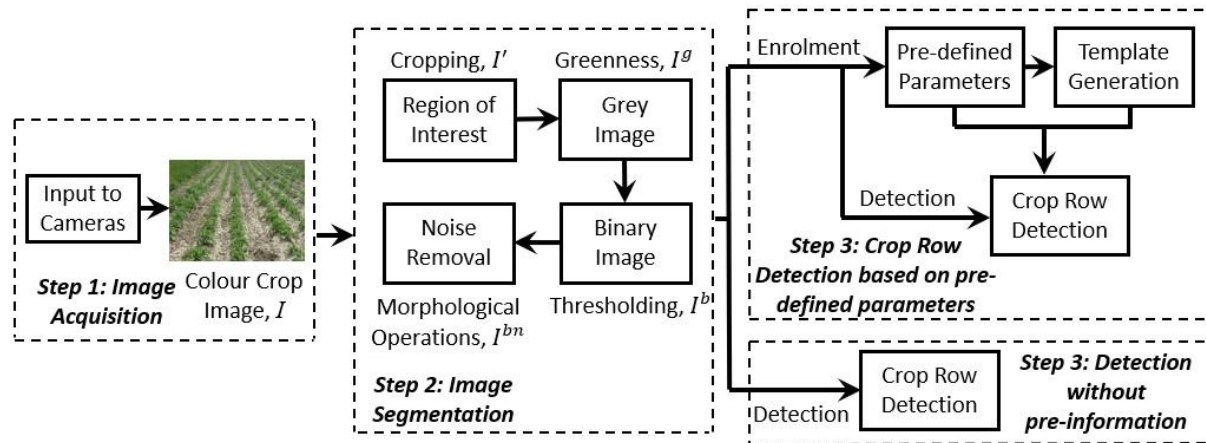
Fig. 3.1. The high-level description of a general crop row detection process is illustrated. There are three major steps involved in crop row detection: image acquisition, image segmentation and crop row detection.

of rows, spacing between rows or another parameter varied. Therefore, a robust crop row detection system is required that can be applied to a wide variety of field trials in an automated manner without the need for known input parameters enabling a crop row detection algorithm that caters for the described challenges mentioned above.

The contributions and aims of this study were:

1. A crop row detection algorithm that detects crop rows in colour images without the use of known input parameters relating to the images with an accuracy of over 90% in the Genomic Sub-Selection dataset. The proposed algorithm can thus be applied to a wide range of field trials.

2. The algorithm is effective in challenging conditions such as variable light, shadows, poor illumination, presence of weed and noise and irregular shape of crops with an accuracy of 84% when applied to a challenging public dataset [16].

3. The algorithm can be applied to crop images which are taken from the top and side views.

4. A novel method of applying Receiver Operating Characteristic (ROC) curve for the first time (to the best of authors' knowledge) in the testing of a crop row detection algorithm. ROC graphical plot demonstrates the diagnostic ability of a binary classifier system by plotting True Positive Rate versus False Positive Rate.

3.3. Background

In this section, the major steps of crop row detection will be described as shown in Fig. 3.1.

3.3.1. Crop row classification

The last and final step is the classification of crop rows. Given the binary image with low noise intensity, it is easy to draw lines on the remaining white pixels detecting the crop rows. However, the images are complex making this step not straightforward. In this section, the different methodologies for the crop row classification will be reviewed.

Hough transform methods

The Hough transform [17] was introduced in 1962 for detecting lines, parametric curves and circles. A decade later, it was used in digital images for detecting straight lines. A wheat crop row detecting algorithm applied the Hough transform to obtain straight lines from binary images after image acquisition and segmentation [12]. Vanishing points were used to finally extract the real wheat rows. A high detection rate of up to 90% was demonstrated for the early wheat growth stages. The algorithm [12] cannot detect crop rows in complex conditions, such as large amounts of weeds, sky, and end of crop rows. A modified version of Hough transform, the random Hough transform, was proposed to reduce computational complexity [7]. This algorithm was tested on three types of plant densities: sparse, general and intensive. The simulation results confirmed that the random Hough transform was adaptive to the

different length and volume of the plants as compared to simple Hough transform. However, the algorithm does not have the capacity to work in complex scenarios such as the presence of weeds. A comparative study on weed discrimination measured and compared the effectiveness of the developed algorithms [18]. It was concluded that the results obtained by the Hough transform were better as compared to Gabor filtering [18]. Furthermore, an extension of the Hough transform [18] was proposed based on the previous results applied on images with top view. The Hough transform has also been adapted for autonomous weed detection [19]. This method [19] was used to calculate the current pose and orientation between the crops. The simulations were conducted with greater than 50% success rate. All Hough Transform methods are limited to straight crop rows and perform poorly in curved rows.

Exploration of horizontal strips

A crop row detection algorithm which removed the image segmentation step significantly reduced the image processing computational burden [9]. Prior to the estimation of the row positions, several points indicating row centres were determined. These points were obtained by dividing the greyscale image resulting from colour combination into a number of horizontal strips and subsequently it estimated where the rows intersect each individual strip. The simulation results confirmed an accuracy within the range of ±6mm to ±12mm depending upon the plant development in the field. However, the algorithm [9] exhibited poor results if there was only one row per image. Moreover, the presence of weeds significantly decreased the accuracy of the algorithm [9]. Another method [20] of automated crop and weed monitoring in widely spaced cereal crops transforms the digital images from the camera from RGB to grey. The original image was transformed to grey scale and then divided into eight

horizontal bands. The row spacing in image pixels can be calculated for each of the horizontal bands using a pinhole model of the camera optics. The results of the automated mapping appear to be consistent with manual assessment.

Linear regression

Linear regression is used for the predictive analysis. A study using linear regression has been used successfully for the development of a vision guidance system in agriculture [21] to detect crop rows. A major drawback of this system was that its insensitivity to additional visual noise from weeds. The crops are divided into three crop row segments and in each segment, they used linear regression and a cost function to outline the rows. In [6], linear regression was also applied for the automatic detection of crop rows in maize fields with high weed pressure. After image acquisition and segmentation using an excess green index, the third step was to apply linear regression to obtain the straight-line equations corresponding to the crop rows. However, some prior knowledge was required for crop row detection; the expected location of each row, the number of crop rows and area covered by the digital image. Crop row detection using linear regression without image segmentation can be done via image analysis.

Blob analysis and Stereo-based

Blob (Binary Large OBject) analysis based on the analysis of consistent image regions is a fundamental technique of machine vision [22]. Blob analysis identifies the regions of a digital image that have different properties such as colour or brightness compared to their surroundings. A method based on blob analysis for the development of line-detection algorithms for local positioning in densely seeded crops was presented by [22]. The digital images were first segmented and transformed into binary form. The blob objects with less than 200 pixels were ignored because they can represent noise in the crop rows and therefore

the objects with more than 200 pixels are gathered together to form a possible crop row. After the identification of all blobs, their locations for centre of gravity and angles of the principal axes were calculated. Stereo vision generally refers to the perception of depth and three-dimensional structure. The method [22] showed poor results when applied to real crop fields as compared to laboratory images due to less information in crop filed images then laboratory images. Furthermore, the discontinuity between the crop rows impacted the value of accuracy of the algorithm [22]. An effective and robust stereovision-based crop row detection method for tractor-automated guidance [23] encompasses stereo-image processing functions for elevation map creation and navigational point determination. From the digital image taken from a stereovision camera, a three-dimensional crop elevation map was generated first and then optimal navigation points from the map are generated. This method was deployed in a soya bean field for the testing of crop row detection [23] with promising results. The extensions of this work by the same authors are presented by [24-25] for three-dimensional crop row structure mapping and guidance.

Other methods

K-Means clustering for spectra (which was further improved by spatial methods) was used for the detection of crop rows [10]. A combination of clustering and linear regression methods [8] was used for the automatic detection of crop rows based on multiple regions of interest. Crop row detection has also been done with the help of accumulation of green image pixels [8]. Other than straight line rows, the proposed algorithm [8] can determine curved crop rows as well as irregular inter-row spaces. The simulations showed good results in terms of accuracy and computational complexity. Vertical projection in combination with Hough transform has been employed [8] for a machine vision-based crop rows detection. In this

algorithm, the first two steps of image acquisition and image segmentation were the same as performing a Hough transformation except for a vertical projection being applied before the use of the Hough transform for crop row detection. The algorithm [8] is only compared with the standard Hough transform and therefore it is difficult to comment on the superiority and effectiveness of the algorithm. An unmanned aerial vehicles guidance system using crop row detection and line follower algorithms was developed [26]. The algorithm has two parts; one for crop row detection, which is responsible for the correct identification of the crop rows and a second for Line Filter that is responsible for generating the driving parameters sent to the flight controller. It is claimed that that the crop row detection algorithm has an accuracy of 100%. However, the image data considered is simple to process and is essentially free of weeds. Another method for crop row detection in unmanned aerial vehicles images is developed [27]. The images are taken from the top view instead of side view. Convolution neural networks are employed to increase the accuracy rate of crop row detection. However, with these networks, the computation time is very high making them less suitable for real-time applications. Crop row detection by global energy minimization is proposed [16]. Dynamic programming is employed to detect both straight and curved crop rows. Their experiments demonstrated that the proposed method [16] outperforms the other considered methods in straight crop row detection. However, a template is generated based on the pre-information prior to the detection stage making it not suitable for all the crop fields.

One of the common drawbacks in the above-mentioned methods is the need of important information such as number and spacing of rows prior to the implementation of crop row detection algorithms. Also, in some proposals a template is generated first to be used in crop row detection. This implies that there is no single algorithm that can be applied to each crop field. In this paper, a crop row detection algorithm is proposed that does not require the pre-

information such as number and spacing of rows and therefore can be applied to a wider variety of crop fields.

3.4. Methods

The proposed algorithm was applied on a public data set [16]. The complete evaluation image set contained 281 images and is available from their web page [28]. The images contained a varied number of crop rows, varied spacing and varied weed intensity. The images were originally captured at resolution 2560 × 1920 pixels and then resized to 320 × 240 pixels. This subsampling reduced the required computation time without significant loss of information for the purposes of crop row detection. A small sample of six down-sized images of this dataset is shown in Fig. 3.2. In the next subsections, all the steps in the proposed crop row detection algorithm will be explained and the resulting images will be showed to aid the reader's understanding of the process.

3.4.1.   Identification of greenness

Let the original colour image be denoted as I^o with X number of image pixel rows, Y number of pixel columns and Z number of frames. Let $I^o(x, y, z) \in [0, 255]$ be a grey value of an image pixel of image I^o at x^{th} row, y^{th} column and z^{th} frame. There are three frames in a colour image; red, green and blue. Let R_f, G_f and B_f represents red, green and blue frames of I^o, respectively. Furthermore, $R_f(x, y)$, $G_f(x, y)$ and $B_f(x, y)$ represent the grey values of these individual frames respectively at the xth row and y^{th} column. The greenness in I^o was identified using the following equation [29]:

$$I^g(x, y) = 1.262 * G_f(x, y) - 0.884 * R_f(x, y) - 0.311 * B_f(x, y),$$

$$\forall x \in \chi, \chi = [1, X], \forall y \in y, y = [1, Y], \qquad (3.1)$$

<center>(a)   (b)   (c)</center>

<center>(d)   (e)   (f)</center>
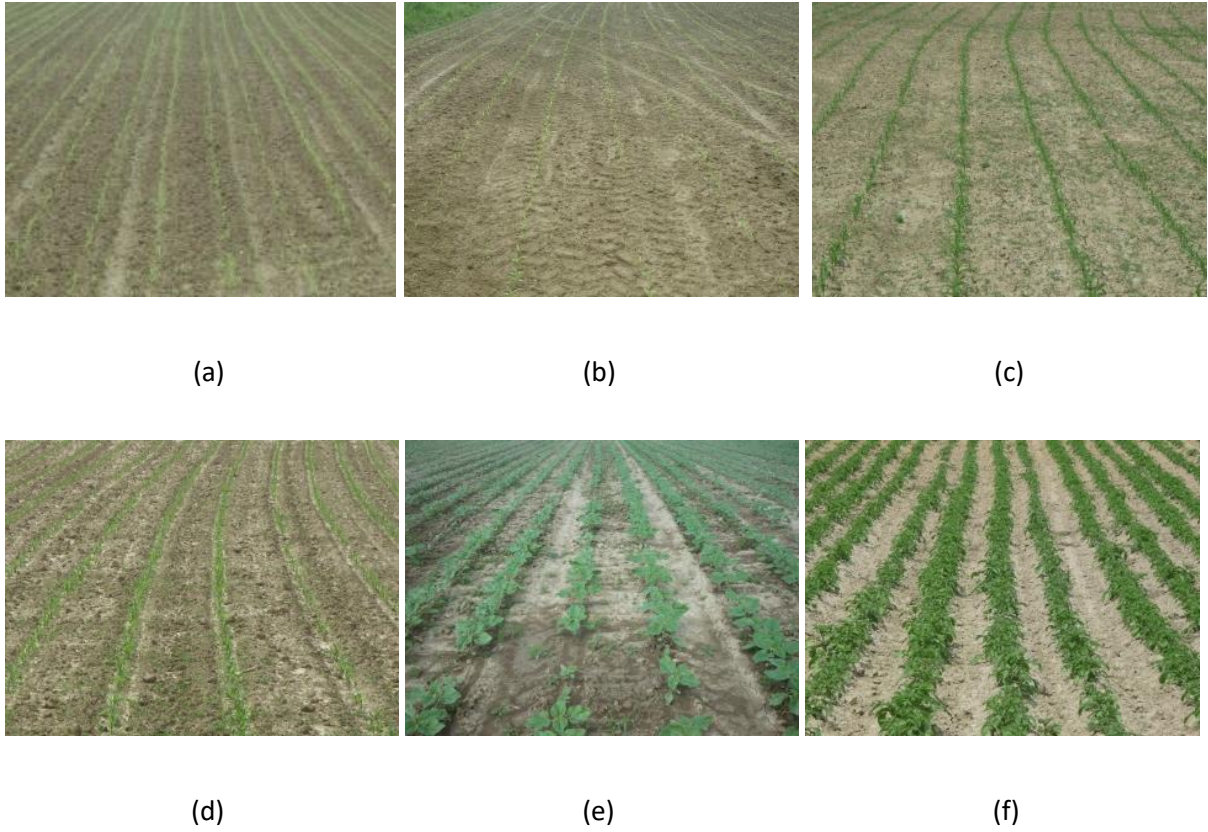
Fig. 3.2. (a-f) A small sample of six images of the public dataset available at [16]. These images have a varied number of crop rows, varied spacing and varied weed intensities. The original resolution of images are 2560 × 1920 pixels and then resized to 320 × 240 pixels.

where, I^g is a grey image whose pixels with greater intensity represents the green pixels of I^o. Fig. 3.3(a-f) illustrates the greenness of Fig. 3.2(a-f) when Eq. (3.1) is applied.

3.4.2. Grey to binary

The grey image whose values $\in [0,255]$ highlighted the greenness can be converted into binary image with only two grey values $\in [0,1]$; white (binary value: 1), which represented the greenness and black (binary value: 0), which represented the background. The Otsu binary thresholding [30] was employed, which was used to automatically perform clustering-based image thresholding returning a value of threshold, th_{Otsu}. The binary image I^b was obtained using the following:

<center>(a)   (b)   (c)</center>

<center>(d)   (e)   (f)</center>
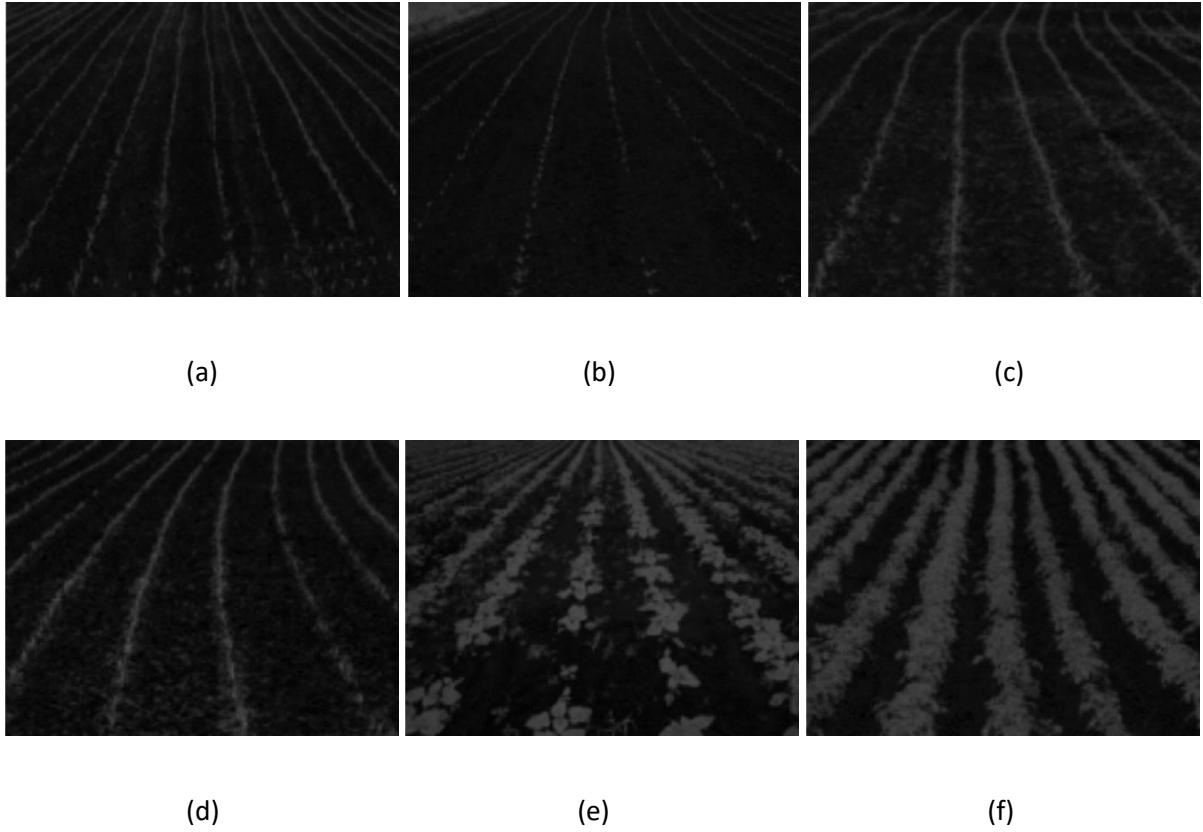
Fig. 3.3. (a-f) Identification of greenness using Eq. (3.1) applied on images shown in Fig. 3.2 (a-f). Degree of pixel whiteness indicates the level of greenness and black pixels represent the background.

$$I^b(x,y) = \begin{cases} 1 & if \ I^g(x,y) > th_{Otsu}, \\ 0 & otherwise, \end{cases} \quad \forall x \in \chi, \chi = [1,X], \forall y \in y, y = [1,Y]. \quad (3.2)$$

The Otsu binary image thresholding was applied on Fig. 3.3(a-d) and results are shown in Fig. 3.4(a-f).

3.4.3. Removing smaller objects

While the binary images successfully identified crop rows, weeds were also identified because of their green colour. Weeds should not be classified as crops and must be removed from the image before identifying rows. To do so, an algorithm was developed based on arithmetic operations. It was assumed that weeds are usually smaller binary objects compared to connected crop row binary objects. A binary object is shown in Fig. 3.5.

<table>
<tr><td>(a)</td><td>(b)</td><td>(c)</td></tr>
<tr><td>(d)</td><td>(e)</td><td>(f)</td></tr>
</table>
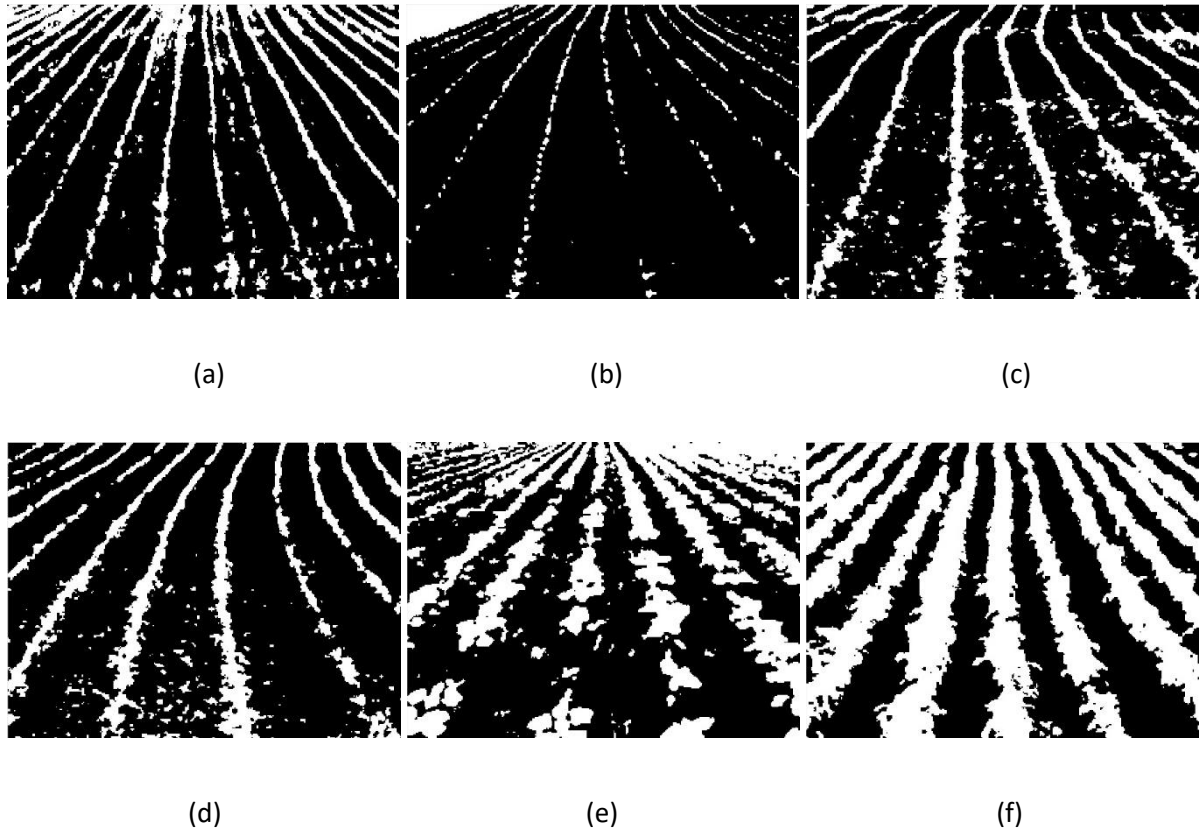
Fig. 3.4. (a-f) Binary images resulting Otsu binary thresholding on images shown in Fig. 3.3(a-f) respectively. The white pixels represent the greenness and black pixels represent the background.
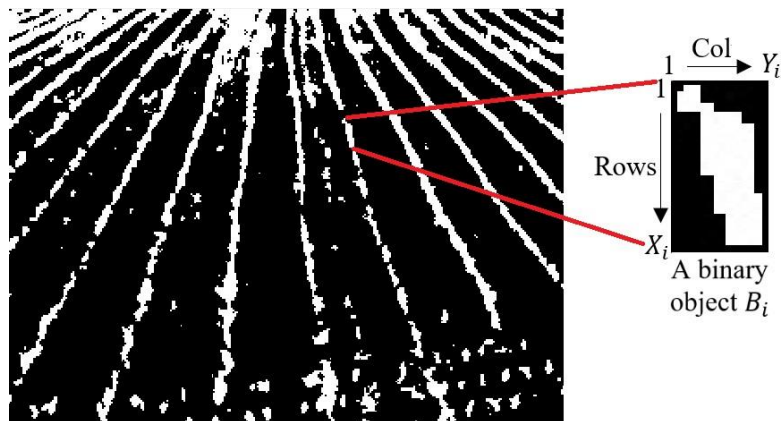
Fig. 3.5. A binary object which is a collection of white pixels connected with each other. The number of rows in B_i is denoted as X_i and number of columns is denoted as Y_i.

Let a binary object be denoted as $B_i, \forall i \in \grave{N}, \grave{N} = [1, 2, \dots, N]$, where, N was the total number of binary objects in an image. The number of rows in B_i was denoted as X_i and number of columns was denoted as Y_i.

First, the mean of each binary object was calculated using following:

$$A_i = \sum_{x}^{X_i} \sum_{y}^{Y_i} I^b(x, y), \qquad \forall i \in \grave{N}, \tag{3.3}$$

where, A_i was the area of binary object B_i. Then the mean size of all objects' areas, M was calculated as:

$$M = \frac{\sum_i^N A_i}{N}. \tag{3.4}$$

The smaller binary objects can be eliminated if the area of the individual binary object was less than the half of the mean area across all objects, that is:

$$I^b(x, y) = 0, \qquad if \ A_i < M/2,$$

$$\forall x \in \chi_i, \chi_i = [1, X_i], \forall y \in \ y_i, y_i = [1, Y_i], \forall i \in \grave{N}, \grave{N} = [1, N]. \tag{3.5}$$

The threshold of half of the mean was set based on the authors' own testing on the observed database. It can be adjusted based on the intensity of weeds in a crop field. This is the only parameter that should be known prior to the implementation of the developed algorithm. The elimination of smaller binary objects is shown in Algorithm 3.1 and the resulting images of applying this process on images in Fig. 3.4 (a-f) are shown in Fig. 3.6 (a-f). Most of the smaller objects, which represent weeds (noise), have been eliminated and the larger binary objects remained primarily identified the crop rows.

Algorithm 3.1. The process of eliminating smaller binary objects from the binary image.

Inputs: Binary image, I^b, binary objects, $B_i, \forall i \in \grave{N}, X_i, Y_i$.

Outputs: Binary image with reduced smaller binary objects, I^b.

1:    $for\ i\ =\ 1:N$

2:        $A(i)\ =\ Area(I_i^b)$

3:    $M\ =\ mean(A)$

4:    $for\ i\ =\ 1:N$

5:        $if\ A(i) < M/2$

6:            $for\ x\ =\ 1:X_i$

7:                $for\ y\ =\ 1:Y_i$

8:                    $I^b(x,y) = 0$
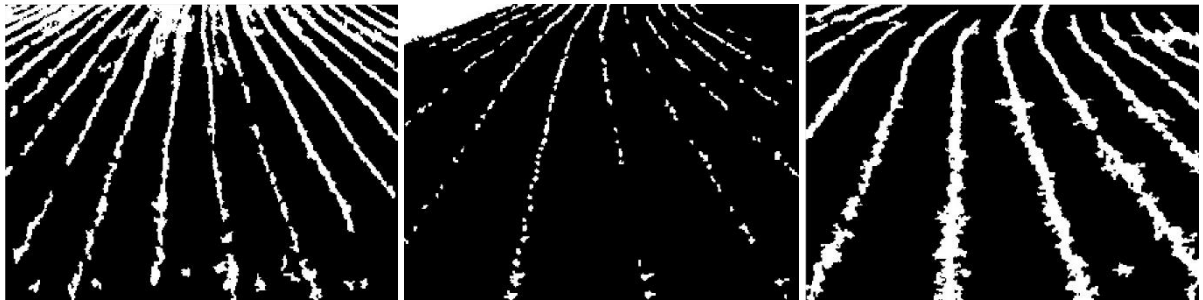
(a)   (b)   (c)

(d)   (e)   (f)

Fig. 3.6. (a-f) Binary images with smaller binary objects removed using Algorithm 3.1.

3.4.4. Joining row objects

Once smaller binary objects have been removed, the remaining binary objects belonging to the same crop row must be joined. To perform this step, it was important to understand the perspective projection of crop rows [12] shown in Fig. 3.7. The projection was from the side view of the crop field. The crop rows were straighter in the middle of the crop image and started tilting while moving towards the other side of the crop image. In other words, the angle of crop rows with respect to the centre of the crop image increased as moving away from the centre of the crop image. Furthermore, the spacing between the crop rows is at the maximum at the bottom of the crop image and decreased while moving upward. The following subsections will explain the systematic joining of binary crop row objects.

Bounding box and columns point of row objects

The first step was to identify the bounding box of each binary object (Fig. 3.8) with respect to original crop image dimensions and to identify its column and row points. In Fig. 3.8, c_1 and c_2 represent the starting and ending column points of binary object, respectively and r_1 and r_2 represent the starting and ending row points of binary object, respectively. In the same
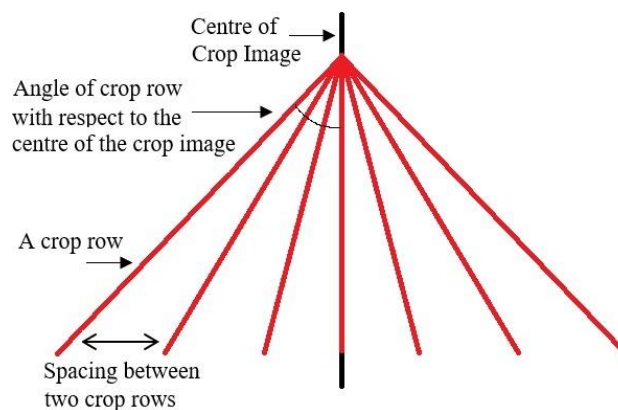
Fig. 3.7. The perspective projection of crop rows. The projection is from the side view of the crop field.

50
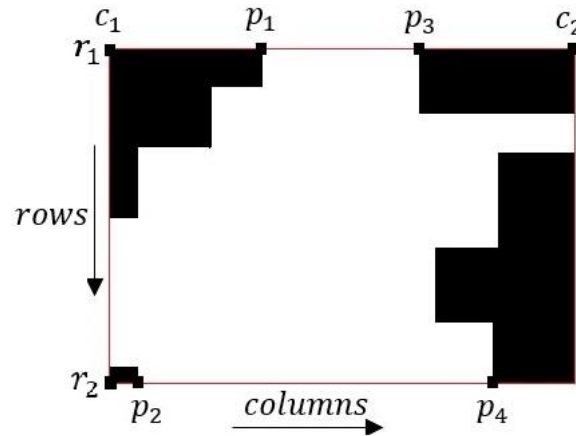
Fig. 3.8. The bounding box of a binary object.

figure, p_1 and p_2 represent the starting column points of first and last row of the object respectively and p_3 and p_4 represent the ending column points of first and last row of the object, respectively. These points will assist in determining the location of the binary object with respect to the column position of the original crop image.

Determining the side of the object

Regarding the perspective projection of crop rows, the next step was to find the side of the binary object with respect to the centre column of the crop row image, that is, whether the object was left or right of centre in the crop row image. If the object did not overlap with the centre (i.e. it is full on one side), its location was clear (Fig. 3.9a+b). However, if the object overlapped the centre column then its location will be determined based on points p_1, p_2, p_3 and p_4. If the binary object was tilted towards the right side of the crop image, or if the differences of both p_1 and p_2 and p_3 and p_4 were positive, then the object was declared to be on the left side as shown in Fig. 3.9(c) and vice versa for objects tilted towards the left of the centre (Fig. 3.9d). Furthermore, if the difference of p_1 and p_2 was positive and the difference of p_3 and p_4 was negative or vice-versa, then its location was based on the absolute value of the difference. If the absolute value of the difference between p_1 and p_2 was greater

than the absolute value of the difference between p_3 and p_4, then the location of the object was defined as left, otherwise right as shown in Fig. 3.9(e) and 3.9(f), respectively. Absolute values were taken to determine the width of image pixels. If the width of image pixels between the points p_1 and p_2 was greater than the width of image pixels between the points p_3 and p_4 then the location of the object was defined as left, otherwise right. The process in form of an equation is given below:

(a)   (b)   (c)

(d)   (e)   (f)
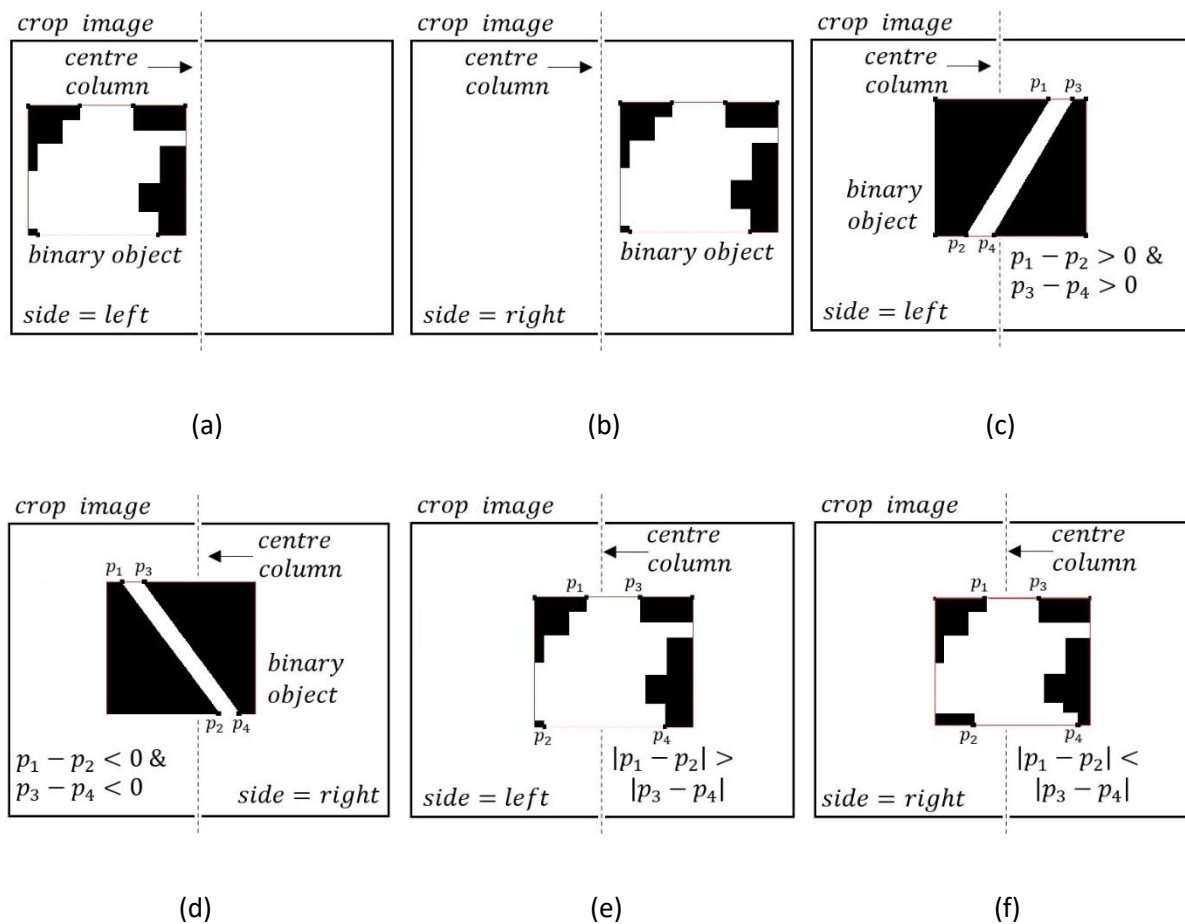
Fig. 3.9. Determination of the location of binary object with respect to the centre column of the crop image. **(a)-(b)** The objects are completely on one of either side. **(c)-(f)** The decision is based on points p_1, p_2, p_3 and p_4. Based on the differences of p_1 and p_2 and p_3 and p_4, the side will be determined.

$$Side = \begin{cases} Left & if\ (c_1 < centre\ \&\ c_2 < centre), \\ Right & if\ (c_1 > centre\ \&\ c_2 > centre), \\ \quad \begin{cases} Left & if\ (p_1 - p_2 > 0\ \&\ p_3 - p_4 > 0), \\ Right & if\ (p_1 - p_2 < 0\ \&\ p_3 - p_4 < 0), \\ \quad \begin{cases} Left & if\ (|p_1 - p_2| > |p_3 - p_4|), \\ Right & if\ (|p_1 - p_2| \leq |p_3 - p_4|), \end{cases} \end{cases} \end{cases}$$ (3.6)

where, $centre$ was the centre column of the crop image and & represented the logical AND operator.

Creating a triangle matrix

The objective was to connect binary objects that belonged to the same row. To achieve that, after determining the side, the next step was to create a triangular matrix of 1s. A triangular matrix was created based on respective location and size. The size was defined as a square matrix using the row position of the binary object (r_1). The size of the triangular matrix was greatest for an object located at the bottom of the crop image and decreased as the object's position moved towards the top of the crop image. Specifically, the size, sz of the triangular matrix was determined as:

$$sz = \left\lceil s_{min} + \left(\frac{s_{max} - s_{min}}{X - 1} \right) (r_1 - 1) \right\rceil,$$ (3.7)

where, s_{min} and s_{max} were the minimum and maximum sizes of the triangular matrix with $s_{min} = 2$ and $s_{max} \approx 0.5 * X$, r_1 represented the starting row point of binary object and $\lceil . \rceil$ was a ceiling function. Eq. (3.7) mapped the row range $\in [1, X]$ to triangular matrix sizes $\in [s_{min}, s_{max}]$. The left matrix, mat_L was created as:

$$mat_L(a, b) = \begin{cases} 0 & if\ a + b - 1 > sz, \\ 1 & otherwise, \end{cases}$$

$$\forall a, b \in S, S = [1, sz].$$ (3.8)

Similarly, the right matrix, mat_R was created as:

$$mat_R(a,b) = \begin{cases} 1 & for\ a \leq b, \\ 0 & for\ a > b, \end{cases}$$

$$\forall a, b \in S, S = [1, sz]. \tag{3.9}$$

Joining objects

The triangular matrix and binary object information was used to connect row binary objects. The principle is that if two binary objects (B_i and B_j) were close enough to potentially lie on the same crop row then these two binary objects should be joined. To see whether B_i and B_j should be connected, first, the triangular matrix was placed on top of the binary object, B_i. For an object located at the left side of the crop image, the triangular matrix was placed at $I^b(r_1, p_3)$ and for an object located at the right side of the crop image, the triangular matrix was placed at $I^b(r_1, p_1)$. As the binary object consisted of collection of 1s and so does the triangular matrix, this will temporarily create one big binary object. This big binary object for the left triangular matrix is given as:

$$I^b(x', y') = I^b(x, y) \mid mat_L(a, b),$$

$$x' \in X_i', X_i' = [r_1 - sz + 1, r_2],$$

$$y' \in Y_i', Y_i' = [c_1, p_3 + sz - 1], \tag{3.10}$$

where, | represented the logical OR operator. Similarly, the big binary object for the right triangular matrix is given as:

$$I^b(x', y') = I^b(x, y) \mid mat_R(a, b),$$

$$x' \in X_i', X_i' = [r_1 - sz + 1, r_2],$$

$$y' \in Y_i', Y_i' = [p_1 - sz + 1, c_2]. \tag{3.11}$$

If this big binary object, $I^b(x', y')$, overlapped with any other binary object, let say B_j then

Fig. 3.10. Two examples of joining two binary objects with each other. **(a)** A binary object, B_i placed at the left side of the centre of the column. A left triangular matrix of size 6 is placed at $I^b(r_1, p_3)$ which overlaps with the other binary object, B_j results in joining B_i and B_j. **(b)** A binary object, B_i placed at the right side of the centre of the column. A right triangular matrix of size 6 is placed at $I^b(r_1, p_1)$ which overlaps with the other binary object, B_j results in joining B_i and B_j.

the triangular matrix was removed and B_i and B_j were connected. Two examples of joining two binary objects with each other is shown in Fig. 3.10(a)-(b). The pseudo-code for joining row objects is shown in Algorithm 3.2.

Images in Fig. 3.11 (a)-(f) demonstrated the joined objects. The images, however, were cropped from the top side as the crop rows were almost merged into each other and therefore it was unnecessary to detect crop rows at the top side. Moreover, once the crop rows were identified in the middle of the image, they can be extended towards the top and bottom of the image. Furthermore, for this step, the images were also cropped at the bottom to reduce the computational complexity and to increase the accuracy of the proposed

(a)   (b)   (c)

(d)   (e)   (f)
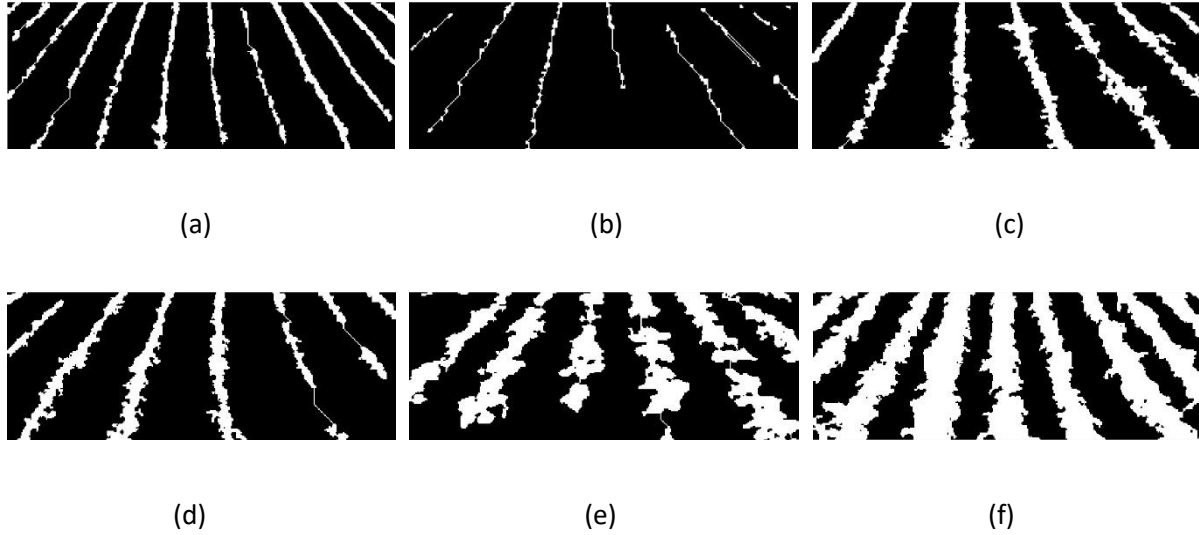
Fig. 3.11(a)-(f) The results of joining binary objects applied on the crop images illustrated in Fig. 3.6(a)-

(f). The images, however, are cropped from the top side and the bottom side to improve the efficiency

and effectivity of the proposed algorithm. The effects of joining objects can be visualised in **(a), (b),**

(d) and **(e)**. The crop rows in **(c)** and **(f)** are already connected and therefore the impact of this step is

not highlighted.

Algorithm 3.2. The whole process of joining row objects in form of a pseudocode.

Inputs: Binary image, I^b, binary objects with bounding boxes, $B_i, p_1, p_2, p_3,$
$p_4, r_1, r_2, c_1, c_2 \ \forall i \in N, X_i, Y_i, s_{min}, s_{max}.$

Outputs: Binary image with connected binary objects, I^b.

1: $for \ i \ = \ 1 : N$

2:        $side = side\_det(p_1, p_2, p_3, p_4, r_1, r_2, c_1, c_2)$

3:        $size = \ size\_det(r_1, r_2, s_{min}, s_{max})$

4:        $matrix = triangular\_matrix(side, size)$

5:        $I^b = joining \ objects(I^b, matrix, B_i, B_j)$

---

algorithm. It is to be noted that the crop rows will always be straight at the bottom of the

crop image irrespective of the fact that the crop rows are curved at the top. Therefore,

cropping images from the bottom will not introduce any error or false information. Binary

objects were not joined if the distance between them was more than sz, irrespective of the

fact that both binary objects belonged to the same row. This situation could be seen in the

sixth and seventh crop rows of Fig. 3.11(b), where binary objects of the same row cannot be

joined as the distance between them was greater than sz.

3.4.5.   Extending longer objects

The next step was to extend those objects whose vertical length (number of pixel rows) was

more than 70% of X, if objects beyond this threshold would all be crop rows. This step was

applied to all binary objects except those that were full crop rows. A binary object was

classified as a full crop row based on the following:

$Object_{row}$

$$= \begin{cases} complete & if\ ((r_1 = 1\ \&\ r_2 = X)|r_1 = 1\ \&\ c_1 = 1|(r_1 = 1\ \&\ c_2 = Y)), \\ not\ complete, & otherwise. \end{cases} \qquad (3.12)$$

The incomplete rows were extended by considering the bounding box of the binary object,

where p_1 represented the column of the first image pixel (white) of the first row and p_3

represented the column position of the last image pixel (white) of the first row. Applying this

to the other rows, let l_2^i represent the column position of the first image pixel (white) of the

second row of ith binary object and q_2^i represent the column position of the last image pixel

(white) of the second row of ith binary object. For simplicity and clarity, write p_1 as l_1^i and p_3

as q_1^i. Continuing this, consider a vector L^i, which consists of all the l_t^i values of all the rows

of ith binary object and consider a vector Q^i, which consists of all the q_t^i values of all the rows

of the ith binary object, where, $t = [1,\ r_2 - r_1 + 1]$, such that, $L^i = [l_1^i, l_2^i, ..., l_{r_2-r_1+1}^i]$, $Q^i =$

$[q_1^i, q_2^i, \dots, q_{r_2-r_1+1}^i]$. The mean or the values of the middle columns of these vectors were

placed in a vector, $U = [\mu_1, \mu_1, \dots, \mu_{r_2-r_1+1}]$ whose values were calculated as:

$$\mu_t = \left[\frac{l_t^i + q_1^i}{2}\right], \forall t = [1, r_2 - r_1 + 1]. \tag{3.13}$$

Also, add r_1, r_2 into vector, $\gamma = [r_1, r_2]_{1 \times r_2-r_1+1}$. Fitting a polynomial of curve to the vector in

a straight line with degree one;

$$\beta = polyfit(U, \gamma), \tag{3.14}$$

where, $polyfit(.)$ is a function requiring vectors U and y and return the slope, sl and y-

intercept, int of a straight line. Using β, those objects can be extended whose length is more

than 70% of X as follows:

$$\begin{cases} c_i^* = sl * r_i^* + int, & \forall r_i^* = [1, r_1], & if \ r_1 \neq 1, & 3.15(a) \\ c_i^* = sl * r_i^* + int, & \forall r_i^* = [r_2, X], & if \ r_2 \neq X. & 3.15(b) \end{cases}$$

$$\begin{cases} I^b(r_i^*, c_i^*) = 1, & \forall r_i^* = [1, r_1], & 3.16(a) \\ I^b(r_i^*, c_i^* - 1) = 1, & \forall r_i^* = [1, r_1], & 3.16(b) \\ I^b(r_i^*, c_i^* + 1) = 1, & \forall r_i^* = [1, r_1]. & 3.16(c) \end{cases}$$

$$\begin{cases} I^b(r_i^*, c_i^*) = 1, & \forall r_i^* = [r_2, X], & 3.17(a) \\ I^b(r_i^*, c_i^* - 1) = 1, & \forall r_i^* = [r_2, X], & 3.17(b) \\ I^b(r_i^*, c_i^* + 1) = 1, & \forall r_i^* = [r_2, X]. & 3.17(c) \end{cases}$$

3.4.6. Extending other row objects

The last step was to extend the remaining objects if they belong to a crop row. The decision

that these remaining objects belong to a row or not was based on the minimum distance of

the columns between the objects considered as the full crop rows. A binary object as a full

crop row is given in Eq. (3.12). Let say there were N^* number of full rows in I^b. For each full

row, first, the vectors, L^i and Q^i were determined. Let put L^i and Q^i, $\forall i \in [1, N^*]$ of all the

full rows in a single matrix, L and Q. L and Q were two matrices whose columns correspond

to the individual values of L^i and Q^i for each of the full row respectively. These matrices are given as:

$$
L = \begin{bmatrix} l_1^1 & l_1^2 & \cdots & l_1^{N^*} \\ l_2^1 & l_2^2 & \cdots & l_2^{N^*} \\ \vdots & \vdots & \ddots & \vdots \\ l_X^1 & l_X^2 & \cdots & l_X^{N^*} \end{bmatrix}_{X \times N^*} , \tag{3.18}
$$

$$
Q = \begin{bmatrix} q_1^1 & q_1^2 & \cdots & q_1^{N^*} \\ q_2^1 & q_2^2 & \cdots & q_2^{N^*} \\ \vdots & \vdots & \ddots & \vdots \\ q_X^1 & q_X^2 & \cdots & q_X^{N^*} \end{bmatrix}_{X \times N^*} , \tag{3.19}
$$

where, X was the length of each of the column of L and Q even though the individual length of these columns depended on the values of r_1 and r_2 of the individual binary objects. However, the actual values remained the same and the length was still $r_2 - r_1 + 1$ for the individual binary objects. The rest of the elements were assigned with the zero values.

The next step was to determine the distance in terms of columns between two consecutive full crop rows for the whole image. This is illustrated in Fig. 3.12, in which there are $N^* = 3$ full crop rows and 6 image rows (this is a small example to explain the process, the public dataset [28] considered here has 240 image rows in each crop image). The distance between two consecutive crop rows for all the full crop rows was determined and placed in a matrix, D and given as:

$$
D = \begin{bmatrix} l_1^2 - q_1^1 & l_1^3 - q_1^2 & \cdots & l_1^{N^*} - q_1^{N^*-1} \\ l_2^2 - q_2^1 & l_2^3 - q_2^2 & \cdots & l_2^{N^*} - q_2^{N^*-1} \\ \vdots & \vdots & \ddots & \vdots \\ l_X^2 - q_X^1 & l_X^3 - q_X^2 & \cdots & l_X^{N^*} - q_X^{N^*-1} \end{bmatrix}_{X \times N^*-1} . \tag{3.20}
$$

The next step was to find the minimum of distance of each row of D, as below:

$$
D_{min} = \left[\min \left(l_t^2 - q_t^1, l_t^3 - q_t^2, \ldots, l_t^{N^*} - q_t^{N^*-1} \right) \right]_{1 \times X}, \qquad \forall t = [1, X]. \tag{3.21}
$$
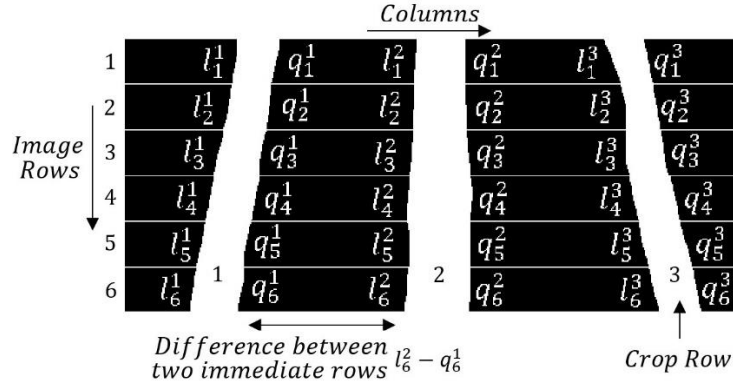
Fig. 3.12. Distance in terms of columns between two consecutive full crop rows for all the full crop rows. In the image, there are $N^* = 3$ full crop rows and 6 image rows.

D_{min} was a vector whose individual values, $d_{min}^t, t \in [1, X]$, were for all the image rows and corresponded to the minimum and *standard* distance between two consecutive crop rows.

This D_{min} was used in determining the other binary objects as the crop rows. This process was repeated for each binary object for the decision. If the difference between the distance and D_{min} was small enough, then the binary object was considered as the part of a potential crop row otherwise that binary object was deleted.

Let say a binary object, B_j has $L^j = [l_1^j, l_2^j, \dots, l_{r_2 - r_1 + 1}^j]$ and let compare its distance with the next immediate full crop row which has $Q^i = [q_1^i, q_2^i, \dots, q_{r_2 - r_1 + 1}^i]$. The comparison will be between each element of L^j and each element of Q^i. A temporary variable was taken and initialized to zero, i.e. $count = 0$. The comparison is given as:

$$count = count + 1, \quad if \; |l_t^j - q_t^i| < th_{dis} * d_{min}^t,$$

$$\forall \, t \in [1, r_2 - r_1 + 1], \tag{3.22}$$

where, th_{dis} was the distance threshold or a percentage tolerance level. The accuracy or number of truly detected crop rows can be increased with the increase in th_{dis}, but this would

also increase the falsely detected crop rows. Finally, the object was determined as a crop row based on the following check:

$$object = part\ of\ crop\ row,\quad if\ count > th_{count} * (r_2 - r_1 + 1), \qquad (3.23)$$

where, th_{count} was the count threshold or a percentage tolerance level. If the $count$ was greater than a user defined fraction of the length of the binary object, then the binary object was considered as a potential part of a crop row otherwise this binary object would be deleted. The accuracy or number of truly detected crop rows can be increased with the decrease in th_{count}, however, at the same time, this would also increase the falsely detected crop rows.

(a)   (b)   (c)

(d)   (e)   (f)
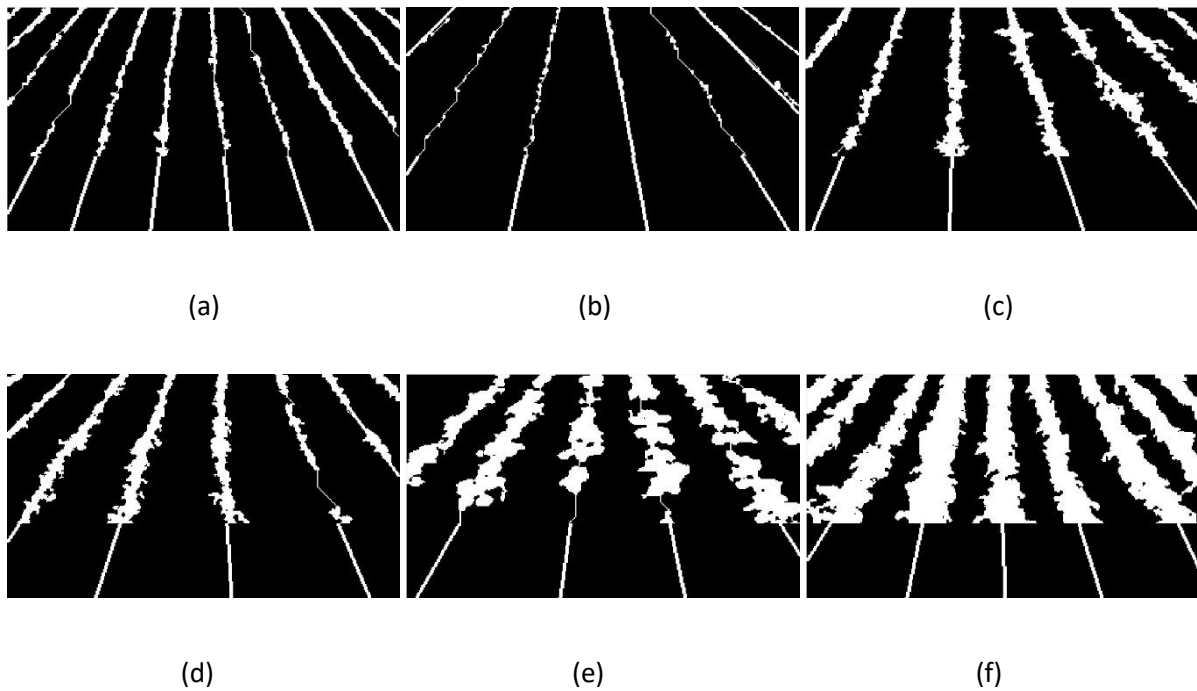
Fig. 3.13. (a)-(f) The results of extending binary objects applied on the crop images illustrated in Fig. 3.11(a)-(f). The binary objects shown in these images only represent the completely detected crop rows.

Table 3.1. Values of the input parameters used for the experiments.

Parameter	Value	Parameter	Value
s_{min}	2	th_{dis}	0.30
s_{max}	20	th_{count}	0.50

The results of this step applied on the images illustrated in Fig. 3.11(a)-(f) are shown in Fig. 3.13(a)-(f). Also, these images were extended to the bottom of the crop images to negate the effect of cropping done earlier.

3.5. Results

The proposed algorithm was applied on a public data set [16], which consisted of 281 images and can be downloaded from their web page [28]. The parameters used in these results are mentioned in Table 3.1. The values of th_{dis} and th_{count} are fixed and should remain same for testing on other image databases as well. However, to test the robustness of the developed algorithm, the values of these two thresholds can be tuned to see the values of False Positive Rates and True Positive Rates as explained later. Similarly, as mentioned earlier, $s_{min} = 2$ and $s_{max} \approx 0.5 * X$. The value of s_{max} considered for the observed image database is 20 and should be changed for other image databases depending upon the size of images. As an example, some of the results of the proposed algorithm on the images are shown in Fig. 3.14 (a)-(o), in which crop rows are labelled as red.

As is apparent from the figures, the proposed algorithm is robust and can detect any number of crop rows with any spacing between them. The rare limitation of the proposed algorithm is that it requires the spacing between the crop rows to be reasonably consistent. The effects of this limitation can be seen in Fig. 3.14(e), in which one row cannot be detected and in

(a)   (b)   (c)

(d)   (e)   (f)

(g)   (h)   (i)

(j)   (k)   (l)

(m)   (n)   (o)
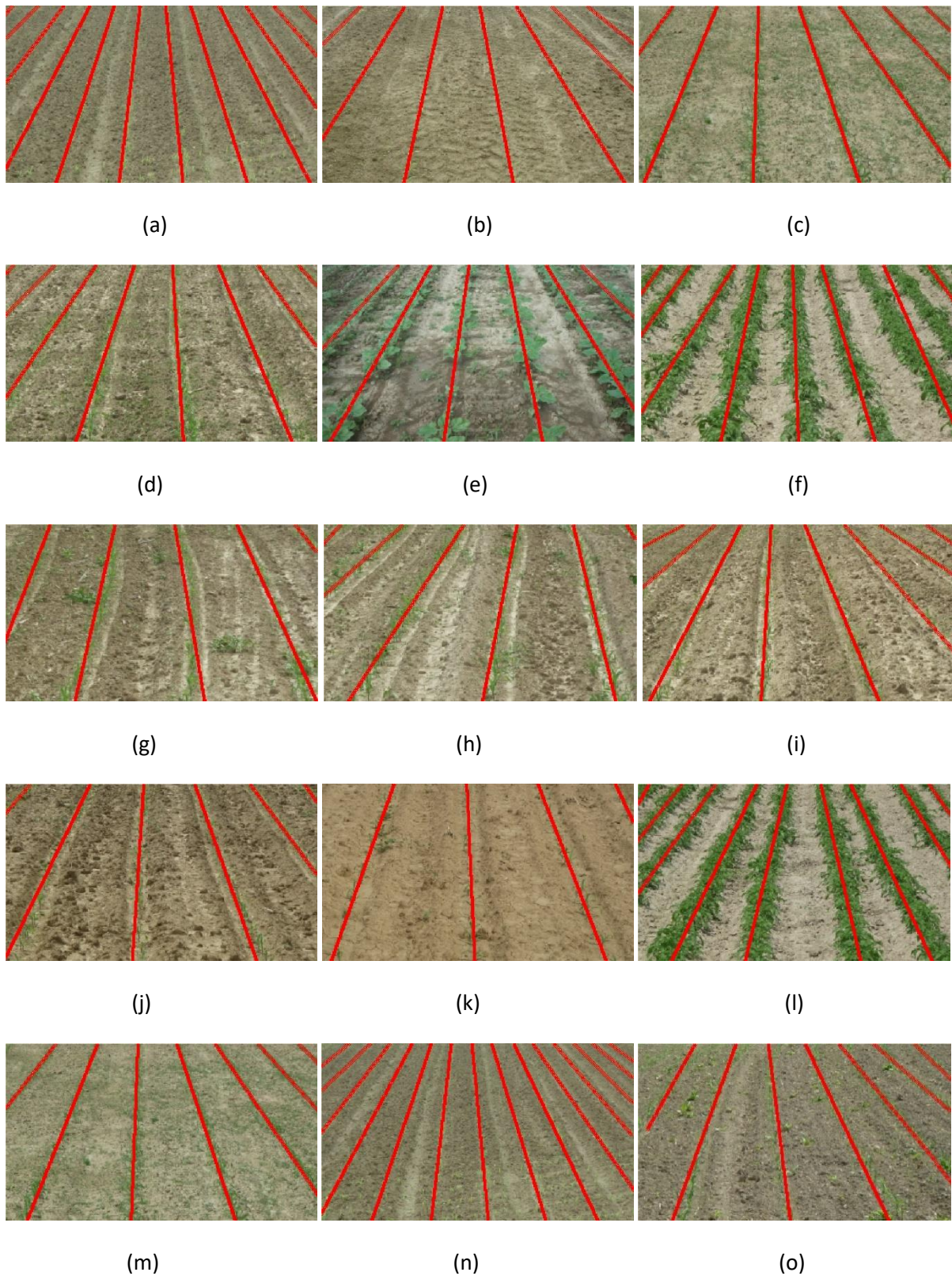
Fig. 3.14. (a)-(o) Few of the results of the proposed algorithm applied on the images of the dataset

[16]. The images in Fig. 3.14(a)-(f) are the same considered in Fig. 3.13(a)-(f).

Fig. 3.14(f) where one false crop row is detected.

3.5.1. Genomic Sub-Selection (GSS) dataset

Beside the image dataset taken from the perspective projection, the algorithm was tested in the Genomic Sub-Selection (GSS) image dataset in which images were taken from the top view. The GSS trial contains 50 perennial ryegrass cultivars with an aim to enable genomic selection [14] analyses grown in replicated rows of 32 plants each. The aims of these field trials were the development of phenomic processing pipelines to define novel traits, the estimation and prediction of hybrid vigour and inclusion of single plant competition effects in genomic selection. An example colour image of the GSS field trial is shown in Fig. 3.15(a) and a grey frame of a GSS image is shown in Fig. 3.15(b). Images were taken with a GoPro Hero 4 (GoPro, San Mateo, CA, USA) deployed on a 3DR Solo quadcopter (3D Robotics, Berkeley, CA, USA).

(a)   (b)
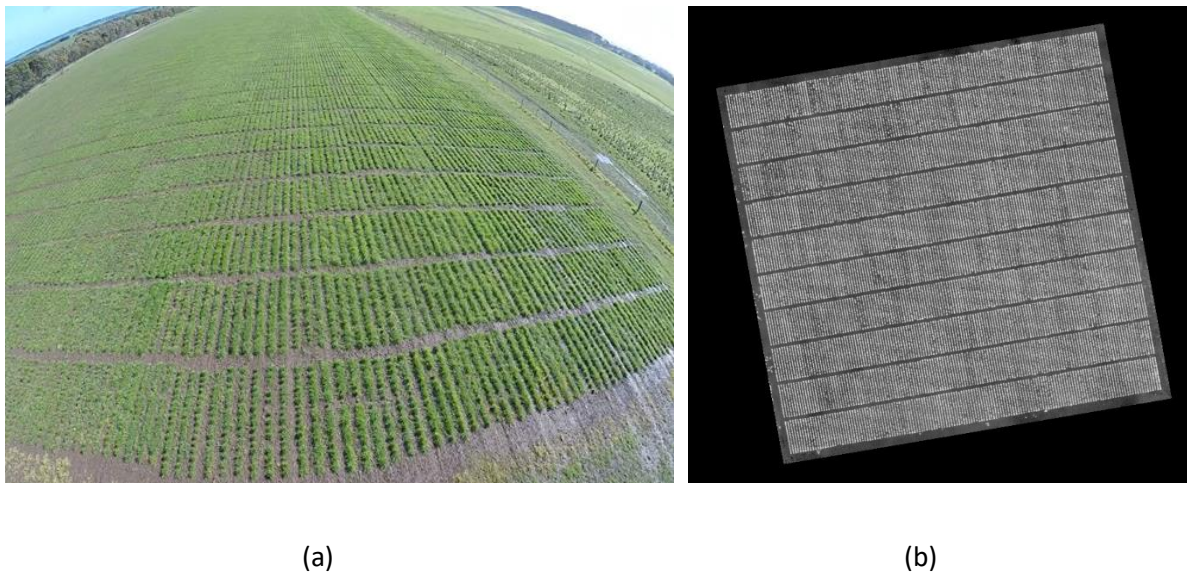
Fig. 3.15. An example of GSS field trial in colour form is shown in **(a)** and a grey frame of a GSS image is shown in **(b)**. The white pixels in **(b)** represent greenness in GSS image and black pixels represent background. In **(b)**, there are 10 major crop rows and in each major crop row, there are 150 minor crop rows for a total of 1500 crop rows.

The proposed algorithm for crop row detection was modified to be applied on the GSS images. A geo-rectified ortho-mosaic image (Fig. 3.15(b)) was created with Pix4D (Pix4D SA, Prilly, Switzerland) software. The image was geo-rectified with the aid of 12 ground control points distributed across the GSS field trial. The ortho-mosaic was cropped and rotated. For illustration purposes, only a subsection of the whole trial is shown in Fig. 3.16, but the algorithm was applied on the entire picture.

The grey image was converted into binary using the same Otsu binary thresholding [30] mentioned earlier (Fig. 3.16(b)). The weeds or noise in these images was minimal and, therefore, the step of removing smaller objects could be ignored. However, some crop rows were overlapping as can be seen in the first major crop row of Fig. 3.16(b). To shrink or thin these overlapped crop rows, the binary image erosion was used [31]. Binary image erosion removes image pixels from the boundaries of the binary image with the help of a pre-defined structuring element. Let take I^b as a binary image shown in Fig. 3.16(b). The image erosion applied on I^b with the help of a structuring element st is given as [31]:

$$I^b \ominus st = \left\{ z | (st)_z \cap I^{b^c} \neq \emptyset \right\}, \tag{3.24}$$

where, $\ominus$ was a binary image erosion of st on I^b, z was a translation vector (z_1, z_2), $(st)_z$ was translation of st by point $z = (z_1, z_2)$, $\cap$ was an intersection or logical AND operator, $(.)^c$ was a compliment or logical NOT operator and $\emptyset$ was an empty set. The Eq. (3.24) can also be stated as:

$$I^b \ominus st = \bigcap_{z \in st} I^b{}_{-z}, \tag{3.25}$$

where, $I^b{}_{-z}$ represented the translation of I^b by $-z$. The structuring element st used in this work is a square of 1s of size 4.

The result of binary erosion applied on Fig. 3.16(b) by st is shown in Fig. 3.16(c) and the binary objects have been shrunk.

Once the objects are eroded, the next step was to extend them using the process mentioned above. However, due to the image being taken in top view, the extension of the binary objects was best done by placing a rectangular shape object over the top of the binary objects. Furthermore, the crop rows are disconnected due to the major crop row sections. Thus, there are intended gaps between the major crop rows and must be classified before the crop row detection. The gaps were labelled as black rows identified with the help of following:

$$row_i = black \quad if \sum_{j=1}^{Y} I^b(i,j) < th_{row\_gap} * Y, \quad \forall i \in [1, X] \quad\quad (3.26)$$

where, th_{row_gap} was a threshold for the row gaps. The accuracy or number of truly detected crop rows can be increased with the increase in th_{row_gap}. However, this will also increase the number of falsely detected rows. The gaps between the minor crop rows can be identified as black columns with the help of the following:

$$column_j = black \quad if \sum_{i=1}^{X} I^b(i,j) < th_{col\_gap} * X, \quad \forall j \in [1, Y] \quad\quad (3.27)$$

where, th_{col_gap} was a threshold for the column gaps. The accuracy or number of truly detected crop rows can be increased with the increase in th_{col_gap}. However, at the same time, this will also increase the falsely detected crop rows. Once the black rows and columns were classified, the rest of the spaces belonged to the crop rows. These crop rows were labelled with the red marker depicting the detected crop rows as shown in Fig. 3.16(d). The values of both th_{row_gap} and th_{col_gap} in the experiments were set to 0.1. The accuracy achieved for GSS dataset is over 90%.

(a)   (b)

(c)   (d)
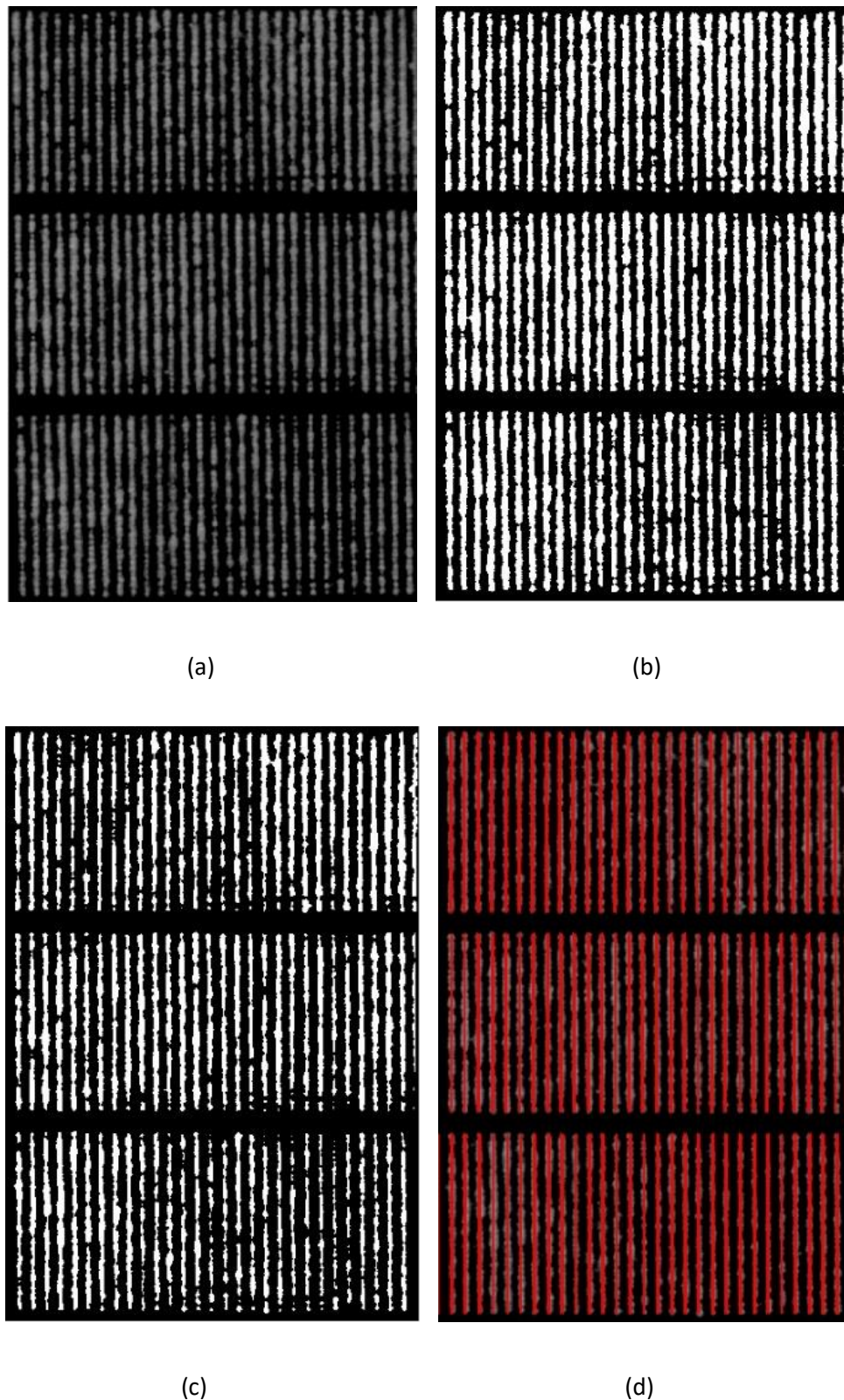
Fig. 3.16. (a) A sub-part of Fig. 3.15(b) which is cropped and rotated into a rectangular form. **(b)** The result of Otsu binary thresholding applied on (a). **(c)** The result of binary erosion applied on (b) by st in which the binary objects have been shrunk. **(d)** Detected crop rows marked in red.

67

3.5.2.   **Performance evaluation**

To evaluate the performance of the proposed algorithm, several parameters have been considered. To the best of the authors' knowledge, one of them, the Receiver Operating Characteristic, was used for the very first time in assessing the performance of any crop row detection algorithm. These parameters are explained in accordance with the proposed algorithm as follows:

Accuracy

In crop row detection, accuracy is the measure of percentage of detected rows in a crop row field. To declare a detected crop row as an actual row, the detected crop row was compared with the crop row of the ground truth image. A ground truth image was created with the help of an expert who defines the actual crop rows in an image. The ground truth images can be created with the help of a software [16]; in that case, the expert defines two or more points lying on a crop row in a test image and the developed software automatically generates a smooth curve passing through these points. The same procedure was undertaken for the adjacent crop row in the image. According to these two curves representing midlines of two adjacent crop rows, the curves for the remaining crop rows in the image are reconstructed. Or, the ground truth images can be manually generated by the expert specifying all the crop rows.

To check whether a detected row was the actual row or not, different parameters can be used for the validation of a crop row such as distance/deviation or the length of the detected row. In terms of distance, the difference between the position of the detected crop row and the actual crop row of the ground truth image should be less than the specified threshold to be accepted as an actual crop row. Furthermore, the detected row can be declared as the actual

row if the length of the detected row was close to the length of the actual crop row of the ground truth image.

The proposed algorithm was applied with the input parameters mentioned in Table 3.1. As stated earlier, accuracy gives the percentage of detected crop rows in an image. For instance, in Fig. 3.17(a) which represented a crop image having eight crop rows, the algorithm detected seven crop rows and, therefore, the accuracy in this case was 7/8*100%=87.5%. For the public dataset [16], the accuracy of the proposed algorithm was nearly 84%.

Drawback with accuracy

Accuracy alone is not enough to test the robustness of the algorithm. For instance, in the same crop image shown in Fig. 3.17(a), if the algorithm has detected seven actual crop rows and one false row as shown in Fig. 3.17(b), the accuracy is still 87.5%. Therefore, other parameters need to be considered to comment on the robustness of the crop row detection algorithm.

                    (a)   (b)

Fig. 3.17. (a) A crop image having eight crop rows **(b)** A crop row image with one false detected row (non-crop row).

Receiver Operating Characteristic (ROC) graph

The problem with the accuracy mentioned before can be resolved with the ROC analysis. It has been applied in various applications, from medicine to computer science, in applications like face recognition, image hashing and many others. However, in crop row detection, to the best of the authors' knowledge, ROC analysis has been applied here for the very first time. ROC has four parameters:

True positive rate

True positive rate (TPR) is the number of correctly detected rows. It is equivalent to the accuracy mentioned earlier. In the example shown in Fig. 3.17(a), seven out of eight crop rows are detected and therefore, in this case, $TPR = 7/8$.

False negative rate

False negative rate (FNR) is the number of not correctly detected rows. In the same example shown in Fig. 3.17(a), one out of eight crop rows are not detected and therefore, in this case, $FNR = 1/8$. Also, $FNR = 1 - TPR$.

True negative rate

True negative rate (TNR) is the number of correctly detected non-crop rows. Let say, there are ten positions in a crop image where there is no crop row and if the algorithm detects eight positions as non-rows position, then $TNR = 8/10$.

False positive rate

False positive rate (FPR) is the number of not correctly detected non-crop rows. Let say, in the same example given in TNR case, if the algorithm cannot detect two positions as non-rows position, then $FPR = 2/10$. Also, $FPR = 1 - TNR$. TPR and FPR have been

considered to comment on the robustness of the crop row detection algorithm; the remaining two parameters are their reciprocal. For the public dataset [16], using the same input parameters mentioned in Table 3.1, the TPR is about 84% and the FPR is 6%. However, these values are just for the individual values of the input parameters. The interest is in observing the inclusive performance of the algorithm when certain input parameters, such as th_{dis} and th_{count} are varied from minimum to maximum values. Based on the overall performance of the algorithm one can set the appropriate input parameters which suit the real-time application.

Sensitivity

Sensitivity is the measure of the proportion of actual positives that were correctly identified. This is equivalent to the TPR observed over a range of a certain input parameter. Fig. 3.18(a) shows the graph of sensitivity against the input parameter of th_{gap} for the range between 10% (0.10) and 100% (1.00) keeping the other input parameters constant as mentioned in Table 3.1. The minimum accuracy is 80% at $th_{gap} = 0.10$ and starts to increase as th_{gap} increases. Finally, the accuracy is at its maximum when $th_{gap} = 1.00$. Similarly, Fig. 3.18(b) shows the graph of sensitivity against the input parameter of th_{count} for the range between 10% (0.10) and 100% (1.00) keeping the other input parameters constant as mentioned in Table 3.1. The minimum accuracy is 80.8% at $th_{count} = 0.10$ and starts to increase as th_{count} increases. Finally, the accuracy is maximum at $th_{count} = 1.00$. By looking at these graphs, one can say that the values of th_{gap} and th_{count} should be set to 1.00 to achieve the maximum accuracy. However, at these values, the FPR is also maximum, as explained in the next section.

Specificity

Specificity is the measure of the proportion of actual negatives that are correctly identified.

This is equivalent to the TNR or $1 - FPR$ observed over a range of a certain input parameter.

The graphs of specificity can be shown to illustrate the actual negatives that are correctly

(a)   (b)
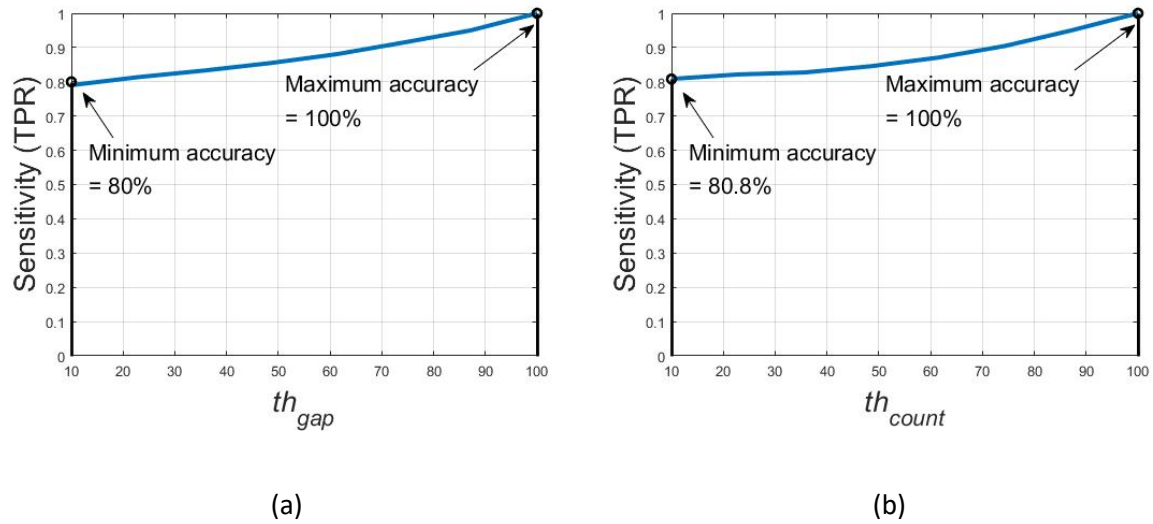
Fig. 3.18. The graph of sensitivity against the input parameter of th_{gap} for the range between 10%

(0.10) and 100% (1.00) keeping the other input parameters constant mentioned in Table 3.1.

(a)   (b)
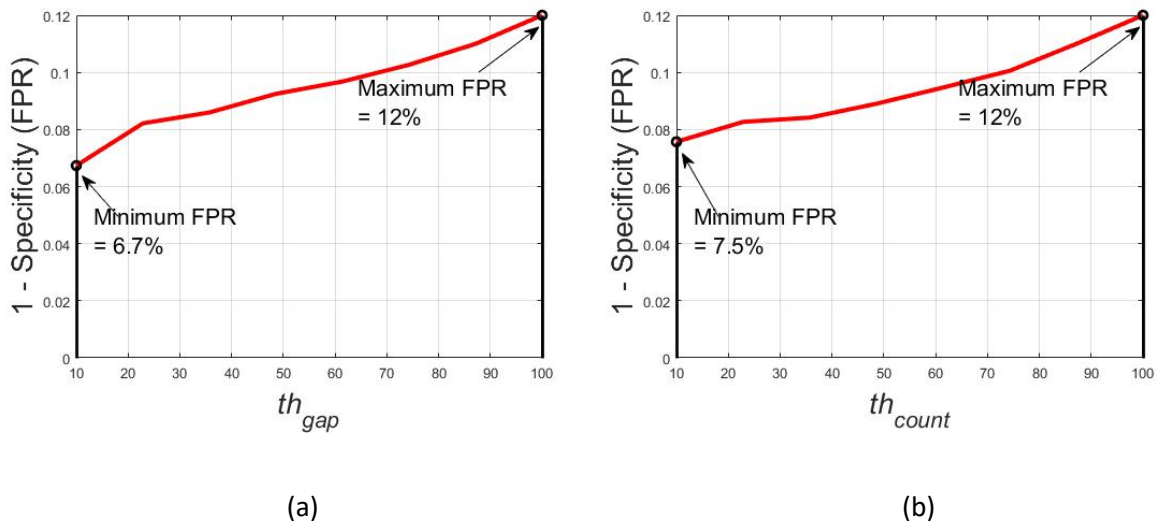
Fig. 3.19. The graph of FPR against the input parameter of th_{gap} for the range between 10% (0.10)

and 100% (1.00) keeping the other input parameters constant mentioned in Table 3.1.

identified or the actual negatives which are not correctly identified. Fig. 3.19(a) shows the graph of 1-specificity (FPR) against the input parameter of th_{gap} for the range between 10% (0.10) and 100% (1.00) keeping the other input parameters constant as mentioned in Table 3.1. The minimum value of 1-specificity (FPR) is 6.7% at $th_{gap} = 0.10$ and increases as th_{gap} increases. Finally, the value of 1-specificity (FPR) is at its maximum (12%) when $th_{gap} = 1.00$. Similarly, Fig. 3.19(b) shows the graph of 1-specificity (FPR) against the input parameter of th_{count} for the range between 10% (0.10) and 100% (1.00) keeping the other input parameters constant as mentioned in Table 3.1. The minimum value of 1-specificity (FPR) is 7.5% at $th_{count} = 0.10$ and starts to increase as th_{count} increases. Finally, the value of 1-specificity (FPR) is maximum (12%) at $th_{count} = 1.00$. By looking at these graphs, one can say that the values of th_{gap} and th_{count} should be set to 0.10 to achieve the minimum FPR, however, at these values, the TPR or accuracy is also minimum. There is a trade-off between TPR and FPR. Therefore, one must set the appropriate values of these thresholds according to the requirement of the real time applications. To adopt the appropriate values of these thresholds, a comparison of *TPR* and *FPR* is given, in terms of a ROC graph, as explained in the next section.

ROC graph

A ROC graph can be used to see the relation between TPR and FPR, to choose an appropriate value of the input threshold and to observe the robustness of the algorithm. Fig. 3.20 (a) shows a ROC graph considering th_{gap}. When FPR is minimum (0-6.7%), the TPR is 80% and then increases to a maximum (100%) when FPR is 12%. In some applications, this can be an interesting point because the accuracy is at its maximum and FPR is very low. However, in applications where t minimum FPR is the priority, this point with a specific value of th_{gap}

(a)   (b)
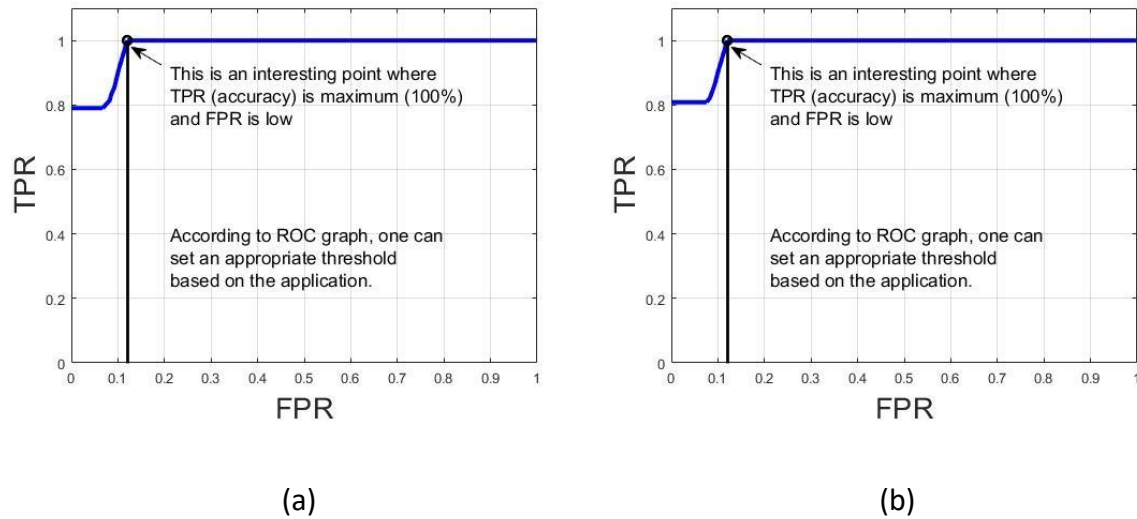
Fig. 3.20. (a) ROC graph considering th_{gap}. The FPR is plotted on the x-axis and TPR is plotted on the y-axis. **(b)** ROC graph considering th_{count}.

cannot be used. According to the need of the application, one can set an appropriate value of th_{gap}. To check the performance of the algorithm, the area under curve (AUC) of the ROC graph is calculated. In an ideal scenario, the AUC is 1 and the algorithm is considered as robust if AUC is close to 1. For Fig. 3.20(a), the value of AUC is 0.98125 demonstrating the robustness of the proposed algorithm. Similarly, Fig. 3.20 (b) shows a ROC graph considering th_{count}. When FPR is minimum (0-7.5%), the TPR is 80%. The TPR starts to increase after that point and becomes a maximum (100%) when FPR is 12%. The AUC of 0.98128 shows the robustness of the proposed algorithm.

3.5.3. Comparison with other algorithms

To compare the proposed algorithm, the parameter accuracy was sub-optimal, because it differs from study to study. Furthermore, the standards, environment and assumptions deployed in other studies differ from the current study. For instance, in other studies, the number and spacing of crop rows in an image were known, contrary to this investigation. Therefore, the accuracy of the results was compared with other studies considering the same

image database [28]. The other methods are Hough Transform [11], Hough transform with

Template [11], Linear Regression [6] and Template Matching followed by Global Energy

Minimization [16]. There were 34 images taken with straight crop rows as Hough Transform

and Linear Regression can only detect straight rows. The results of accuracy of the proposed

algorithm with comparisons to the other methods are shown in Table 3.2 depicting the

superiority of the proposed work. Also, the computational time of algorithms was compared.

As crop row detection may be applied in real time, computational time is very important. For

example, the vision system deployed on a moving vehicle must process the captured images

(or frames of video), show the resulting images and perform pre-defined tasks on them before

capturing the next images. It was required that the computational time is less than or equal

to the time spent between the acquisition of two (or set of) images to synchronize with the

hardware platform. Fig. 3.21 shows the comparative results of computational time of the

proposed algorithm and that of other studies. Metrics were normalized based on the system

specifications and size of the images used in each study. It was shown that the proposed

algorithm has faster performance than the other algorithms.
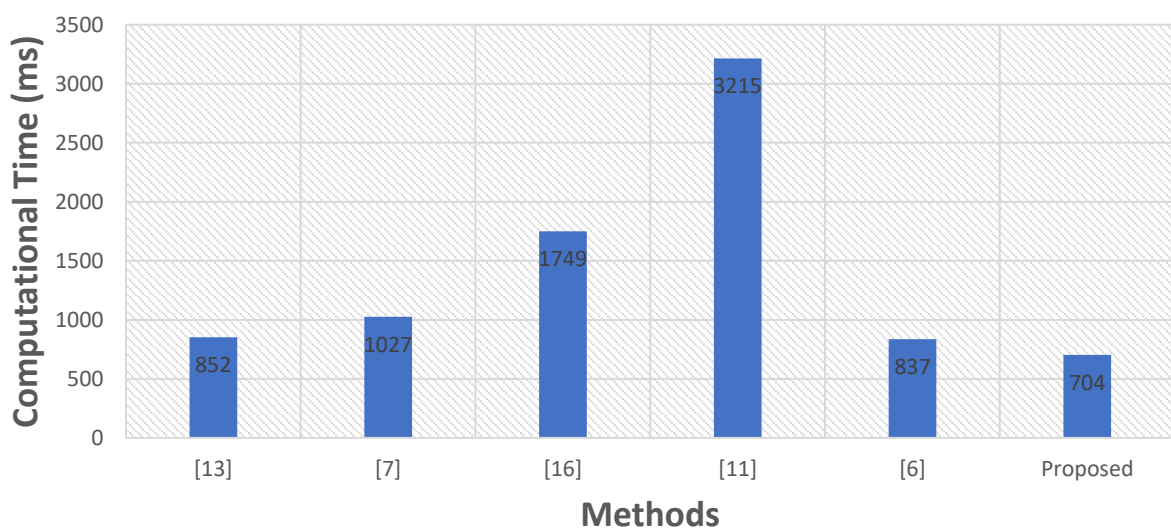
Fig. 3.21. Computational time of algorithms.

Table 3.2. Comparative results of accuracy of the proposed algorithm with other published studies. Accuracy of other methods were directly taken from their respective publications.

Methods	Accuracy (%)
Linear Regression [6]	57.2
Hough Transform [11]	62.2
Hough Transform with Template [11]	67.9
Template Matching followed by Global Energy Minimization [16]	73.7
Proposed	84.0

3.6. Conclusion

This paper proposed a new crop row detection algorithm that does not require pre-information such as number of crop rows and spacing between crop rows. The only information the algorithm needs is the approximate intensity of weeds. Furthermore, there is no need for template to be used in the detection stage. Therefore, the proposed algorithm can be applied to a wide variety of crop fields. The crop row detection phenotype data can be used for downstream analysis such as genomic selection or for the development of phenomic processing pipelines to define novel traits.

The proposed algorithm of detecting crop rows involved various image processing operations, such as identification of greenness, binarization and binary image erosion. Besides these basic operations, the proposed algorithm utilized the perspective projection of crop rows to identify the row objects. These objects of a same row are then connected with each other and extended using the triangular matrices. The proposed algorithm can also be applied to

the images taken from the top view with some modifications. Like all new proposals, it is strongly encouraged to do the analysis of the algorithm before its immediate deployment. The algorithm could potentially be extended to identify weeds in crop fields.

3.7. Acknowledgments

3.8. References

[1]   D. C-Godoy and J. Dewbre, "Economic Importance of Agriculture for Poverty Reduction", OECD Food, Agriculture and Fisheries Working Papers, Expert Systems with Applications, No. 23, OECD Publishing, 2010.

[2]   S. S. Katariya, S. S. Gundal, M. T. Kanawade and K. Mazhar, "Automation in agriculture", International journal of recent scientific research, vol. 6, no. 6, pp. 4453-4456, 2015.

[3]   D. Caldwell, "Robotics and Automation in the Food Industry", Current and Future Technologies, 1st Edition, eBook ISBN: 9780857095763, pp. 1-528, 2012.

[4]   R. Bongiovanni and J. L-Deboer, "Precision Agriculture and Sustainability", Precision Agriculture, vol. 5, no. 4, pp. 359-387, 2004.

[5]   S. Banu, "Precision Agriculture: Tomorrows Technology for Todays Farmer", Journal of Food Processing & Technology, pp. 468-473, 2015.

[6]   M. Montalvo, G. Pajares, J. M. Guerrero, J. Romeo, M. Guijarro, A. Ribeiro, J. J. Ruz and J. M. Cruza, "Automatic detection of crop rows in maize fields with high weeds pressure", Expert Systems with Applications, vol. 39, no. 15, pp. 11889-11897, 2012.

[7]   R, Ji and L. Qi, "Crop-row detection algorithm based on Random Hough Transformation", Mathematical and Computer Modelling, vol. 54, no. 3-4, pp. 1016-1020, 2011.

[8]   G. Jiang, X. Wang, Z. Wang and H. Liu, "Wheat rows detection at the early growth stage based on Hough transform and vanishing point", Computers and Electronics in Agriculture, vol. 123, pp. 211-223, 2016.

[9]   H. T. Sogaard and H. J. Olsen, "Determination of crop rows by image analysis without segmentation", Computers and Electronics in Agriculture, vol. 38, pp. 141-158, 2003.

[10] K. N. Ramesh, N. Chandrika, S. N. Omkar, M. B. Meenavathi and V. Rekha, "Detection of Rows in Agricultural Crop Images Acquired by Remote Sensing from a UAV", International Journal of Image, Graphics and Signal Processing, vol. 8, no. 11, pp. 25-31, 2016.

[11] T. Bakker, H. Wouters, K. V. Asselt, J. Bontsema, L. Tang, J. Müller and G. V. Straten, "A vision-based row detection system for sugar beet", Computers and Electronics in Agriculture, vol. 60, no. 1, pp. 87-95, 2008.

[12] G. Jiang, Z. Wang and H. Liu, "Automatic detection of crop rows based on multi-ROIs", Expert Systems with Applications, vol. 42, no. 5, pp. 2429-2441, 2015.

[13] I. G-Santillán, J. M. Guerrero, M. Montalvo and G. Pajares, "Curved and straight crop row detection by accumulation of green pixels from images in maize fields", Precision Agriculture, vol. 19, no. 1, pp. 18-41, 2018.

[14] T. H. Meuwissen, B. J. Hayes and M. E. Goddard, "Prediction of total genetic value using genome-wide dense marker maps", Genetics, vol. 157, no. 4, pp. 1819-1847, 2001.

[15] P. M. Visscher, N. R. Wray, Q. Zhang, P. Sklar, M. I. McCarthy, M. A. Brown and J. Yang, "10 Years of GWAS Discovery: Biology, Function, and Translation", The American Journal of Human Genetics, vol. 101 no. 1, pp. 5-22, 2017.

[16] I. Vidović, R. Cupec and Ž. Hocenski, "Crop row detection by global energy minimization", Pattern Recognition, vol. 55, pp. 68-86, 2016.

[17] P. V. C. Hough, "A method and means for recognizing complex patterns", US Patent Office No. 3069654.

[18] G. Jones, C. Gée and F. Truchetet, "Modelling agronomic images for weed detection and comparison of crop/weed discrimination algorithm performance", Precision Agriculture, vol. 10, no. 1, pp. 1-15, 2009.

[19] M. Asif, S. Amir, A. Israr and M. Faraz, "A Vision System for Autonomous Weed Detection Robot", International Journal of Computer and Electrical Engineering, vol. 2, no. 3, pp. 486-491, 2010.

[20] T. Hague, N. D. Tillett and H. Wheeler, "Automated crop and weed monitoring in widely spaced cereals", Precision Agriculture, vol. 7, no. 1, pp. 21-32, 2006.

[21] J. Billingsley and M. Schoenfisch, "The successful development of a vision guidance system for agriculture", Computers and Electronics in Agriculture, vol. 16, no. 2, pp. 147-163, 1997.

[22] V. Fontaine and T. G. Crowe, "Development of line-detection algorithms for local positioning in densely seeded crops", Canadian Biosystems Engineering, vol. 48, no. 7, pp. 19-29, 2006.

[23] M. Kise, Q. Zhang and F. R. Más, "A Stereovision-based Crop Row Detection Method for Tractor-automated Guidance", Biosystems Engineering, vol. 90, no. 4, pp. 357-367, 2005.

[24] M. Kise and Q. Zhang, "Development of a stereovision sensing system for 3D crop row structure mapping and tractor guidance", Biosystems Engineering, vol. 101, no. 2, pp. 191-198, 2008.

[25] F. R-Más, Q. Zhang and J. F. Reid, "Stereo vision three-dimensional terrain maps for precision agriculture", Computers and Electronics in Agriculture, vol. 60, no. 2, pp. 133-143, 2008.

[26] M. Basso and E. P. de. Freitas, "A UAV Guidance System Using Crop Row Detection and Line Follower Algorithms", Journal of Intelligent & Robotic Systems, vol. 97, pp. 605-621, 2019.

[27] M. D. Bah, A. Hafiane and R. Canals, "CRowNet: Deep Network for Crop Row Detection in UAV Images", IEEE Access, vol. 8, pp. 5189-5200, 2019.

[28] http://www.etfos.unios.hr/r3dvgroup/index.php?id=crd_dataset/

[29] X. P. B-Artizzu, A. Ribeiro, M. Guijarro and G. Pajares, "Real-time image processing for crop/weed discrimination in maize fields", Computers and Electronics in Agriculture, vol. 75, no. 2, pp. 337-346, 2011.

[30] N. Otsu, "A Threshold Selection Method from Gray-Level Histograms", IEEE Transactions on Systems, Man, and Cybernetics, vol. 9, no. 1, pp. 62-66, 1979.

[31] R. E. Woods and R. C. Gonzalez, "Digital Image Processing", Global Edition.

Chapter 4

A new method for extracting individual plant bio-characteristics from high-resolution digital images

Saba Rabab[1,2, *], Edmond Breen[2], Alem Gebremedhin[3], Fan Shi[2], Pieter Badenhorst[4], Yi-Ping Phoebe Chen[5] and Hans D. Daetwyler[1,2]

[1]School of Applied Systems Biology, La Trobe University, Bundoora, Australia

[2]Agriculture Victoria, AgriBio, Centre for AgriBioscience, Bundoora, Australia.

[3]Agriculture Victoria, Victoria, Grain Innovation Park, Horsham, Australia.

[4]Agriculture Victoria, Hamilton Centre, Hamilton, Australia.

[5]Department of Computer Science and Information Technology, La Trobe University, Bundoora, Australia.

[*]Corresponding Author

Author Contributions: SR, YC, and HD developed the experimental design; SR developed algorithms and carried out the majority of analyses; ED, FS, PB, and HD advised on analyses; ED, AG, FS and PB collected or processed initial data or phenotypes; HD and YC supervised the study; SR and HD wrote the paper; all authors have read and approved the paper.

4.1. Abstract

The extraction of automated plant phenomics from digital images has advanced in recent years. However, the accuracy of extracted phenomics, especially for individual plants in a field environment, requires improvement. In this paper, a new and efficient method of extracting individual plant areas and their mean normalized difference vegetation index from high-resolution digital images is proposed. The algorithm was applied on perennial ryegrass row field data multispectral images taken from the top view. First, the centre points of individual plants from digital images are located to exclude plant positions without plants. Second, the accurate area of each plant is extracted using its centre point and radius. Third, the accurate mean normalized difference vegetation index of each plant is extracted and adjusted for overlapping plants. The correlation between the extracted individual plant phenomics and fresh weight ranged between 0.63 and 0.75 across 4 time points. The methods proposed are applicable to other crops, where individual plant phenotypes are of interest.

Keywords: Plant phenomics, image processing, area, centre points, and normalized difference vegetation index.

4.2. Introduction

Due to the exponentially increasing consumption of food, fuel, and feed by the burgeoning world population, global agricultural demand is growing. Global cereal grain production must increase by 70% by 2050 to meet food demand [1-2]. Forages are also an important feed source for animals that produce dairy, meat, and fibre products, and they play a crucial role in maintaining a good natural environment. In parallel, growing climate unpredictability is

shifting crop production onto marginal lands, intensification of existing agricultural practices, and displacement of natural ecosystems [3]. Conventional methods for plant breeding such as phenotypic and pedigree selection have significantly increased crop yields worldwide [4]. Nevertheless, these methods alone will not be enough to meet the projected global food demands [5, 6]. Moreover, these traditional methods are costly, require intensive labour resources, are lower throughput and time consuming. Genomic breeding approaches (e.g., genomic selection) will assist in increasing crop and pasture production [7, 8] and a wealth of plant genomic knowledge has been accumulated over the last decade [9-12]. However, genomic selection requires large training sets of lines that are well characterized with both genomics and phenotypes. Traditional phenotyping methods are often too laborious and costly for large plant collections leading to a significant gap between genomic knowledge and its connection to phenotypes. These problems can be rectified to some extent by the accurate and precise phenotyping of germplasm with novel technologies.

Phenotyping of organisms [13-16] can be defined as a set of protocols or methodologies applied to measure the physical characteristics such as architecture, growth and composition with a certain accuracy and precision. For plants, phenotyping is based on morphological, physiological, biochemical, and molecular structures. Current phenotyping methods of plants is considered slow, expensive, sometimes destructive and can cause variations between observations due to human operator variability. This has led to a growth in automated phenotyping technologies that overcome these shortcomings. One such automated method relies on digital imaging, which contains two main steps: image acquisition and image analysis. Image acquisition is a process where a digital representation (image) of the crop field is obtained using an imaging sensor. Image acquisition can generally be classified into seven

groups with respect to plant phenotyping [16]: mono-RGB vision, multi- and hyperspectral cameras, stereo vision, LIDAR technology, fluorescence imaging, tomography imaging and thermography, and time of flight cameras. Image analysis on the other hand deals with the extraction of the useful information regarding plants from the digital images involving pre-processing, segmentation, and feature extraction [17]. The pre-processing step can include operations such as image cropping, image rotation, contrast improvement, colour mapping, image, smoothing, and edge detection [18]. The applications of these methods for phenotyping depend upon the output requirements and several factors. Image segmentation's main goal is to differentiate between the irrelevant or background objects and objects (segments) of interest using colour, texture and statistical measures. For example, Otsu binary thresholding [19] is a segmentation algorithm used to automatically perform clustering-based image segmentation returning a value of threshold. The threshold can then be used to discriminate between the background and foreground of a digital image using methods such as Watershed transformation [20]. Feature extraction is also an important factor in automated phenotyping using digital images. The measurements extracted from the image segments, such as area, normalized difference vegetation index (NDVI) is placed into feature vectors which summarize the physical characteristics of each plant or plant region identified. The digital information extracted from the images in the form of NDVI, surface area, width, height, and circular shape can be linked to the degree of greenness, fresh weight, and biomass of the plant. Phenomic bio-characteristics such as NDVI or plant area can be correlated or predictive of plant biomass yield, which is the main production phenotype in forage species and is a characteristic contributing to grain yield in other crops [21, 22]. Bio-characteristics, if sufficiently correlated, can then be used as proxy phenotypes for biomass in genomic se-lection to select the best populations and generate genetic gain over

generations. Furthermore, as image derived bio-characteristics are non-destructive, they can be collected at multiple time-points during the growth cycle of crops, giving rise to novel phenotypes for genomic selection and breeding purposes (e.g., change in biomass over time, growth, or senescence rate).

Most plant breeding applications focus on plot or row phenotypes consisting of multiple plants, which is often sufficient. However, individual plant phenotypes are of interest to investigate family or population uniformity in both in- and outbred species. Uniformity is important because growers desire high forage biomass with even growth throughout a paddock and it is also a characteristic for determining plant breeder's rights. Furthermore, in outbred species, it may be of interest to understand the effect of individual plants on plants in close proximity, so called competition effects [23], as each plant is genetically unique. If plants in a forage cultivar are overly competitive, overall biomass yield and uniformity is expected be suboptimal in the paddock. The manual collection of individual plant characteristics is especially laborious and automated phenomic solutions are required.

We propose a new method for extracting the area of individual plants from digital field trial images. The method focuses on both the extraction of these regions from a multispectral image taken by an uncrewed aerial vehicle and the linking of these regions with individual plant biomass. The utility of the approach is evaluated by correlating individual plant phenomic bio-characteristics and plant biomass as estimated by fresh weight at harvest. The study is organized as follows: Section 2 provides the work problem statements, Section 3 describes the proposed algorithm in detail, Section 4 explains the experimental results and comparative analysis on perennial ryegrass field data, and Section 5 outlines conclusions.

4.3. Problem Statements

The proposed algorithm was applied to perennial ryegrass row field data for which images were taken from the top view. The field trial contained 50 perennial ryegrass cultivars grown in replicated rows of 32 plants per row. Perennial ryegrass is a diploid outbred species where each individual plant is genetically unique and each cultivar would have at least four parental cultivars, making them genetically diverse. Each replication was considered as a plot and contained three rows of 32 spaced plants each (i.e., 96 plants/plot). The experimental unit was, therefore, a plot of 8 × 1.8 m. The expected spacing between plants was 25 cm and between rows was 60 cm. The field trial contained a total of 48,000 individual plants in 10 blocks. The total area of the field experiment was 8,100 m^2. In part, the aims of these field trials were the development of phenomics processing pipelines to define novel traits for the estimation and prediction of plant performance (e.g., biomass yield, flowering time). Images were taken with a Parrot Sequoia (Parrot Drones S.A.S., Paris, France) multispectral camera deployed on a 3DR Solo quadcopter. The camera capture images simultaneously at four bands including green (530–570 nm), red (640–680 nm), red edge (730–740nm), and near-infrared (770–810 nm). It also has GPS and sensor and incident light sensors. The flight mission was planned by Tower Beta software. Aerial images were collected using the unmanned aerial system (UAS) on a weekly basis over the GS trial site, and data from four flight dates in 2017 was used for this analysis. Imaging dates were synchronized with each harvest. Flight operations were conducted under bright, sunny weather conditions to minimize noise from environmental variation. The UAS flight altitude was set at 20 m above ground level, and the flight speed was 6 m/s with 75% side and forward overlap of images. At this flight altitude and

(a)   (b)
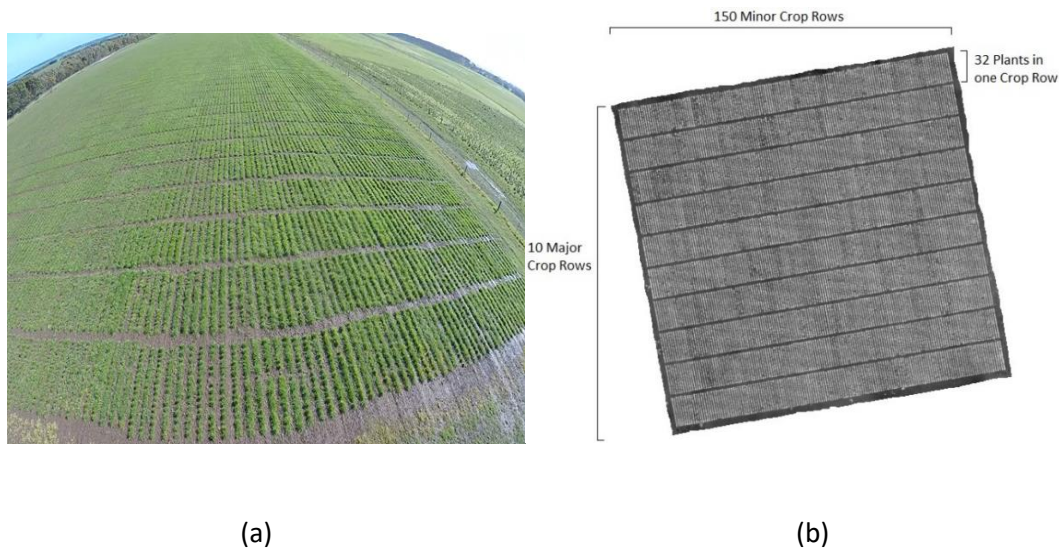
Fig. 4.1. (a) An example of field trial in RGB form and **(b)** a grey scale image of the perennial ryegrass field trial stitched together from aerial images.

speed, the spatial resolution of the images was 2 cm/pixel. The same flight path was followed on each date. Image reflectance was corrected using Airinov calibration plates with known reflectance values (MicaSense Inc., Seattle, WA, USA). An example colour image of the field trial is shown in Fig. 4.1(a) and a grey scale image of the field trial area is shown in Fig. 4.1(b). The white pixels (NDVI TIFF image) in Fig. 4.1(b) mostly represent greenness in the trial image and black pixels represent background. In Fig. 4.1(b), there are 10 blocks, and in each block, there are 150 plant-rows for a total of 1500 crop rows. Furthermore, in each plant-row, there are 32 plants resulting in 48,000 plants in each field-trial image.

The goal is to automatically extract phenomic traits such as area and NDVI value of each plant from each field trial's TIFF file image. In principle, other vegetation indexes such as Green Normalized Difference Vegetation Index, RedEdge Normalized Difference Vegetation Index, Soil Adjusted Vegetation Index and Enhanced Vegetation Index could also be used. The extraction of these traits makes use of the experimental field trial design specifying the layout

of plant-rows and the plants within each row to help define the boundary or bounding boxes for plant-rows and initial estimates of the individual plant regions. The row polygons of row-plants are identified using projection methods, as outlined in [22], followed by the identification of centre-points of individual plants. These centre-points then assist in identifying the individual plant polygons. Fig. 4.2(a) shows the layout of bounding boxes for several row polygons and Fig. 4.2(b) shows the bounding boxes for individual plant polygons. These bounding boxes assist in extracting phenomics traits of interest. For instance, the bounding box region can be cropped, and the area can be calculated by multiplying the number of non-zero pixels with the area of one pixel in cm^2. Further, the mean NDVI value is calculated by taking the mean of NDVI values of all non-zero pixels within that region.

In images where there is moderate plant growth (Fig. 4.2), the extraction of phenomics is relatively simple. The plants are almost entirely confined in their individual bounding boxes

(a)   (b)

Fig. 4.2. Bounding Boxes of **(a)** 3 plant-row boxes and **(b)** their individual plant boxes.

A bounding box where no plant is grown.
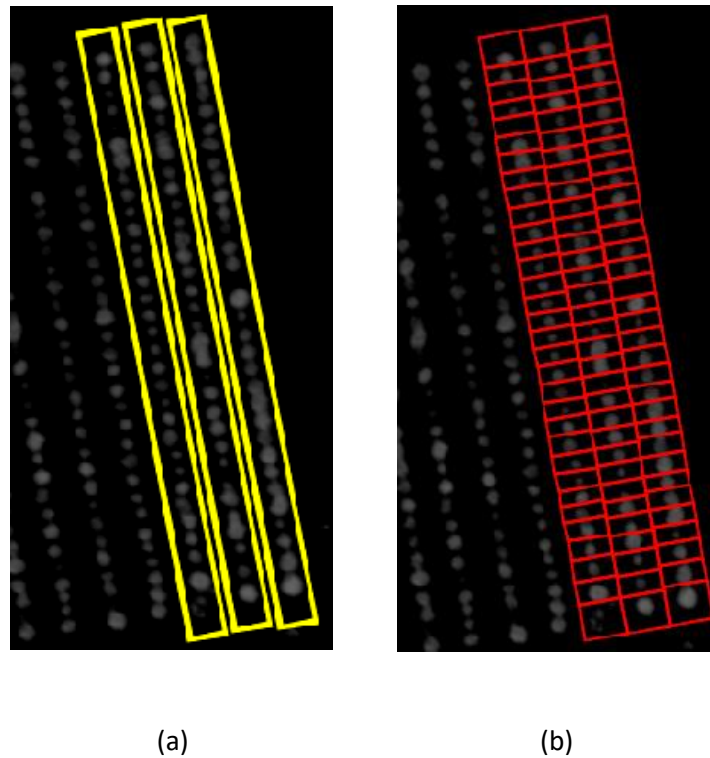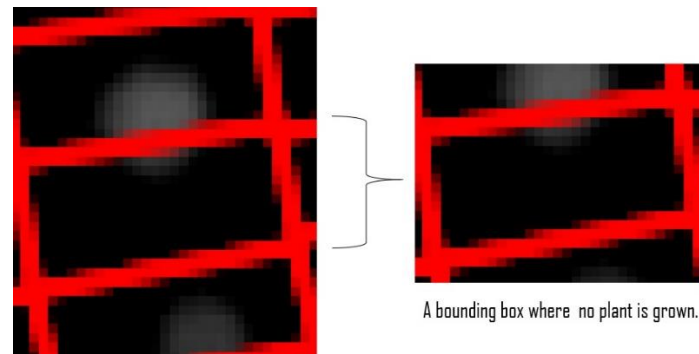
Fig. 4.3. A bounding box without a plant, but due to the overlapping of the top plant, the bounding box have some image pixels that are erroneously classified as plant.

referred to as plant boxes, and therefore the area and mean NDVI value can be calculated easily. However, there are bounding boxes where plants have not grown at all, but due to encroachment of adjacent plants, their bounding boxes have some image pixels that show NDVI signals as shown in Fig. 4.3. These NDVI values can be mistaken for the plant in the box, which has died or not grown at all when it was in fact the neighboring plant. Also, the plants can overgrow and overlap into adjacent plants (Fig 4.4(a)). In such case calculating the area by counting the number of non-zero pixels in that bounding box (Fig. 4.4(b)) will not be accurate. Therefore, a possibly more accurate area is hypothesized in Fig. 4.4(c) of the same plant by highlighting a circular plant region. In summary, these problems are the main objectives of our work to identify the accurate area of individual plants, and includes the following sub-objectives:

1. To identify bounding boxes with no plants.

2. To calculate accurate individual plant areas despite overlapping of adjacent plants.

3. To calculate accurate individual plant NDVI values despite overlapping of adjacent plants.
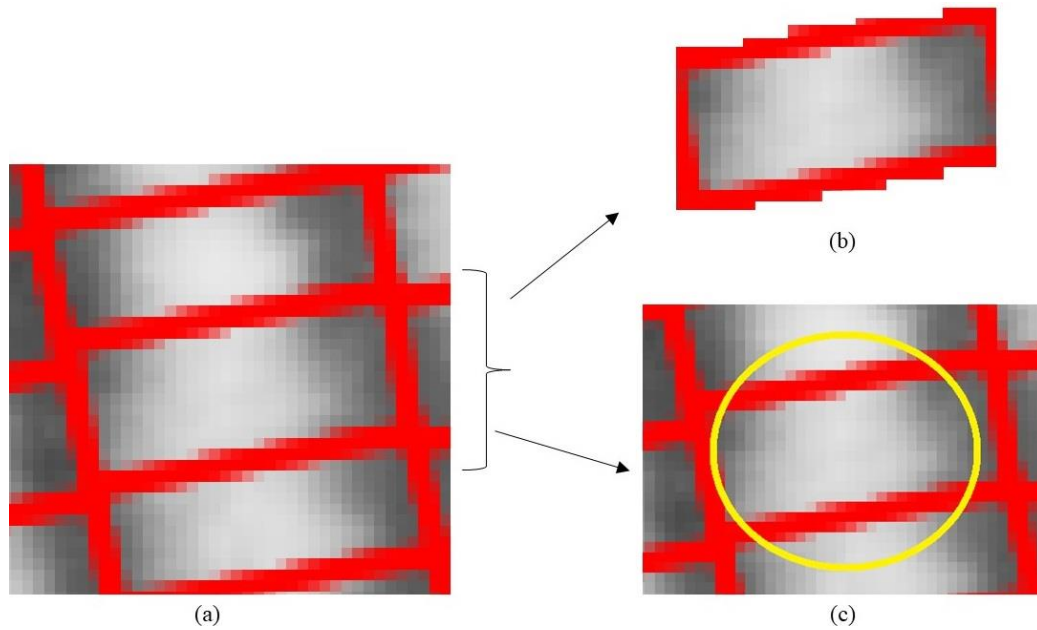
Fig 4.4. (a) Plants overgrow from their bounding boxes and overlapping to adjacent plants. **(b)** Rectangular bounding box of a plant; the area equal to the bounding box is not accurate as plant is overgrown form the bounding box. **(c)** A potentially more accurate representation of area is illustrated with a circular plant region.

4.4. Methods

The use of machine vision in phenotyping started almost three decades ago for the extraction of NDVI values [24]. Since then, there has been huge progress in monitoring large fields using sensor technologies. However, the applications involved simple digital data, which is usually extracted in controlled environments. In the previous proposals [25-31], the examined plants were captured in very controlled and simplistic environment; either there was only one plant per digital image, or the plants were not overlapping.

To detect circles in images, Circular Hough Transform (CHT) [32] and its variants [33] have become common methods in numerous image processing applications. CHT is very effective in detecting circles in digital images, even with somewhat irregular circular shapes. However,

Pixel Size: 4.2849 cm2	**Pixel Size:** 3.6864 cm2	**Pixel Size:** 3.7636 cm2	**Pixel Size:** 4.6656 cm2
(a)	(b)	(c)	(d)
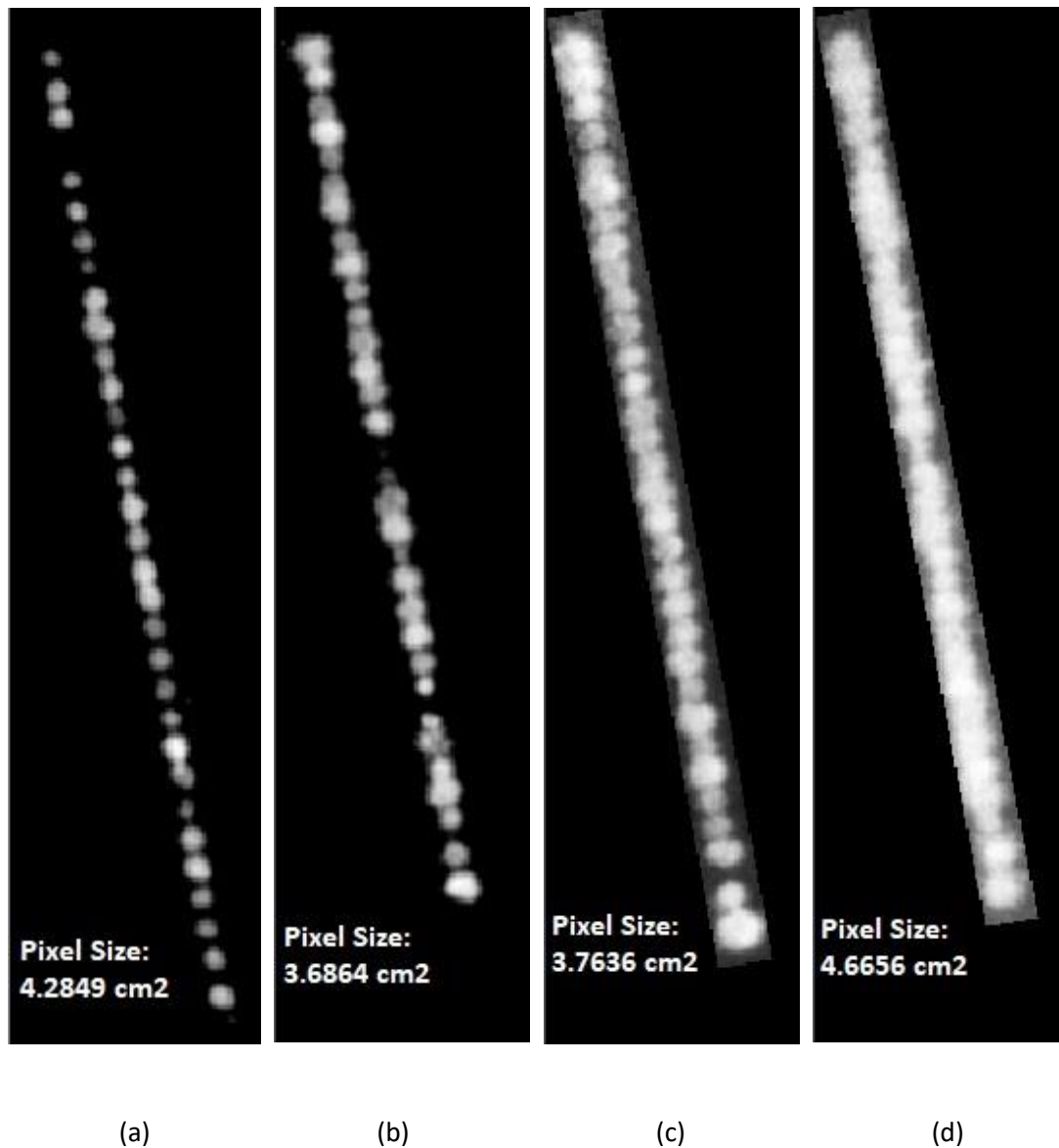
Fig. 4.5. (a)-(d) A small set of different crop rows extracted from four field trial images taken on **(a)** 9th May 2017, **(b)** 5th July 2017, **(c)** 11th September 2017 and **(d)** 20th November 2017. Note that the rows at different time points are not exactly the same length as pixel size varied slightly from expected 2cm. Values were converted to metric to standardize between capture dates.

it performs poorly when circles are merged and overlapping to each other, just as in case of our research problems.

These existing works do not provide solutions relevant to our mentioned problems; therefore, we have developed a new and effective image-based phenotyping method. The proposed

algorithm was developed and implemented on field trial image dataset in which images were taken from the top view. A sample of a single crop row image from the field trial, taken at four time points, is shown in Fig. 4.5 (a)-(d). We have employed MATLAB version R2019a for the simulations and analyses of our work. In the next subsections, the proposed algorithm is explained, and images are shown to aid the reader's understanding.

4.4.1.   Background correction

Let I be the two-dimensional matrix for a single plant box image with size r, c, where r is the total number of image rows and c is the total number of image columns. It is to be noted that the plants are at specific angle, but we did not rotate them for the analysis. As the plant's geometry is somewhat circular, the rotation will not affect the extraction of centre point and radius as explained below. I is considered for one individual plant and there are 32 such plants in one crop row as shown, Fig. 4.5(a).Moreover, let $I(i,j)$ represents the NDVI value of image pixel at i^{th} row and j^{th} column of I, and $I(i,j) \in [-1, 1]$. The first step was to remove any background values, which does not contain plant pixels. To remove the unnecessary background, Otsu binary thresholding [19] was employed, to automatically perform clustering-based image thresholding returning a value of threshold, th_{Otsu}. The background corrected image of a single plant, I^b is obtained using the following:

$$I^b(i,j) = \begin{cases} I(i,j) & if \quad I(i,j) > th_{Otsu}, \\ 0 & otherwise. \end{cases} \qquad (4.1)$$

The Otsu image thresholding for background correction was applied on Fig. 4.5(a)-(d) and results are shown in Fig. 4.6(a)-(d).

(a)   (b)   (c)   (d)
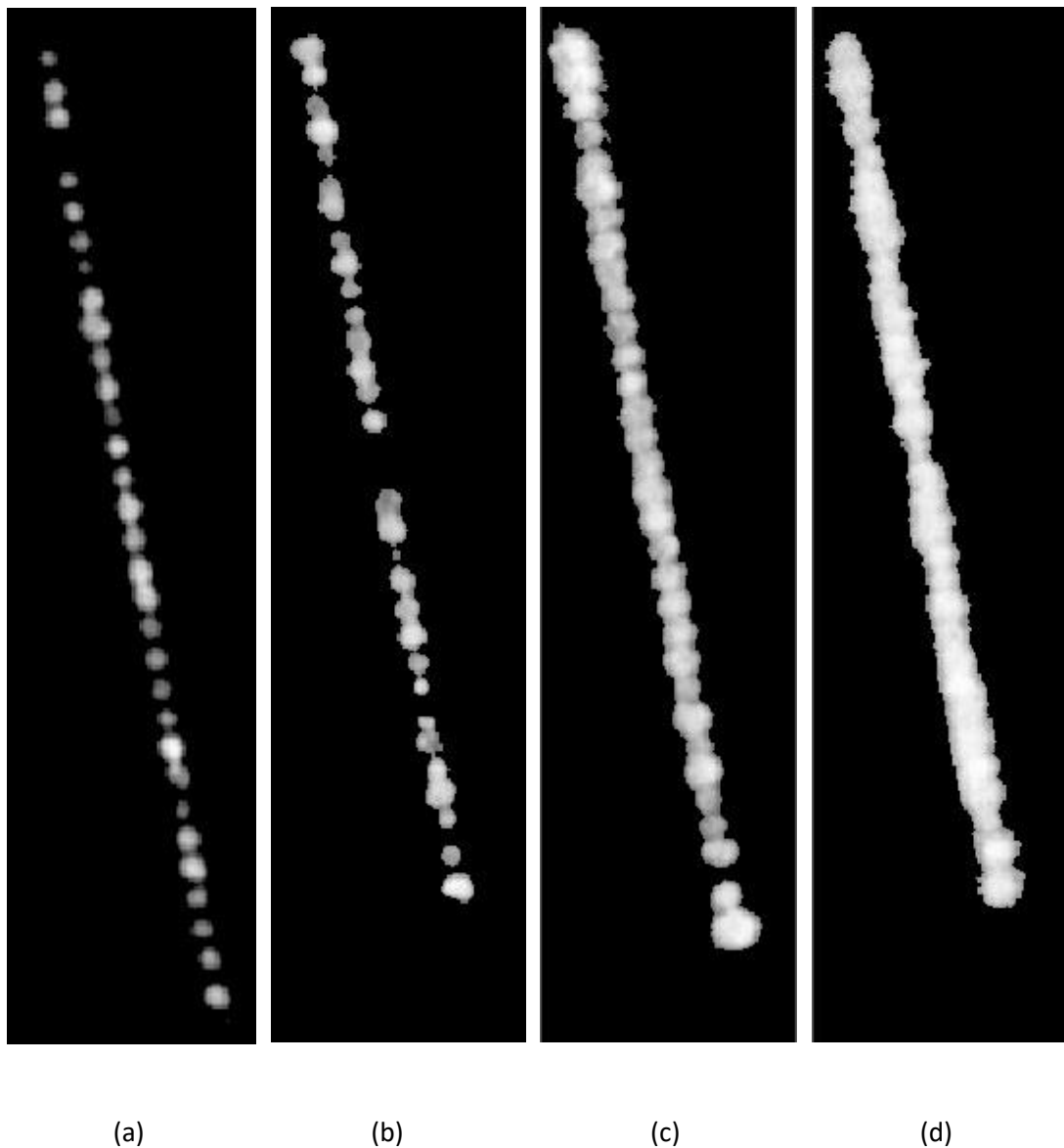
Fig. 4.6. (a)-(d) Background corrected images obtained from applying Otsu thresholding on images shown in Fig. 4.5(a)-(d) respectively. Grey pixels represent NDVI intensity and black pixels represent the background.

4.4.2. Centre Point Calculation

Whether a rectangular plant bounding box contained a plant was determined by identifying the centre point of a plant. If there is a centre point in a bounding box, then it contains a plant and vice-versa. As mentioned in the problem statement, bounding boxes where defined

based on row layouts and expected plant number and spacing per row following [22]. The

distribution of greenness or NDVI values in an individual plant assists in finding the plant

centres (Fig. 4.7). The greenness is likely to be at a maximum in the centre of plant and

gradually decreases towards the plant's edges. Therefore, the centre point should correspond

to or near a location of an image pixel with the maximum NDVI value. However, there can be

more than one pixel whose values correspond to the maximum NDVI and they can be in

different places. Another solution could consider the middle point of the bounding box as the

plant centres. However, the assumption is not always justified as plant locations could deviate

from bounding box centres. Our approach combines these two methods. This allows for the

correction of NDVI maxima that are at bounding box edges but have false values due to

encroaching neighbouring plants. The centred positions of a plant image are determined as

follows:

$$\{(i,j) \mid I^b(i,j) \geq 0.6 * I_{max}; \forall i \, \epsilon \, [0.2r, 0.8r]; \forall j \, \epsilon \, [1, c]\} \tag{4.2}$$

Where, I_{max} is the maximum value of I^b. Without loss of generality, the above equation

specifies a set of image positions within a given plant-box, as shown in Fig. 4.4(b), with its

origin specified at (1,1) and with r rows and c columns that have intensity values that satisfy

$I^b(i,j) \geq 0.6 * I_{max}$. The optimization value of 0.6 is based on trial and error and was

chosen based on visual inspection. Increasing the value beyond 0.6 will result in more centred

image pixels and vice-versa. We recommend to investigate this threshold when applying the

algorithm to new datasets. This set will be empty if there is no centre point, otherwise the

average i, Θ_r and average j, Θ_c, location (Θ_r, Θ_c) is used to define a plant's centre point

within its corresponding plant-box. The goal is to locate a centre point of the plant which

cannot be at top or
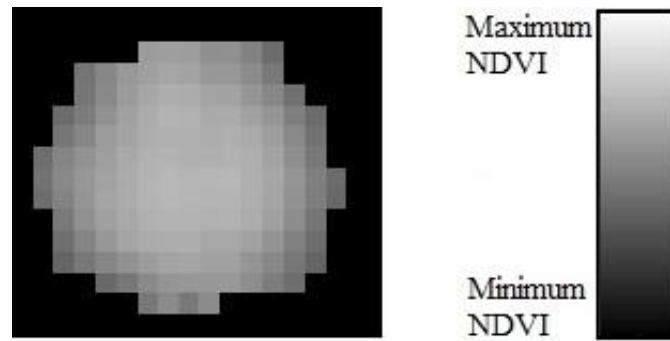
Fig. 4.7. Distribution of image pixels in terms of greenness or NDVI values in an individual plant.

bottom of the image, therefore the search row domain in each plant-box is constrained to not include the top and bottom 20% of the rows. In our study, plants were generally planted at equal distances justifying this assumption. In field data where this is not the case, further development of the algorithm may be needed. This process was then applied to all plant-boxes within each field image.

The results of this step applied to images shown in Fig. 4.6(a)-(d) are shown in Fig. 4.8(a-d). The centre points are represented by a red plus symbol. The algorithm correctly identified the number of plants in a crop row. For instance, Fig. 4.8(a) has only 31 plants with centre points labelled and Fig. 4.8 (b) has only 30 plants. The identification of centre points has solved the first research problem, that is, the bounding boxes with no plants have been identified.

4.4.3.   Extraction of Plant Areas

The next goal is to extract the individual plant areas. The distribution of plant pixels is somewhat circular and symmetric (Fig. 4.7). To define the circular plant region associated with each plant-box containing a plant, requires only a centre point and a corresponding radius. The centre points have been calculated in the previous step and the radius is calculated by measuring the distance in terms of number of non-zero image pixels from the centre point to

<div align="center">(a)   (b)   (c)   (d)</div>
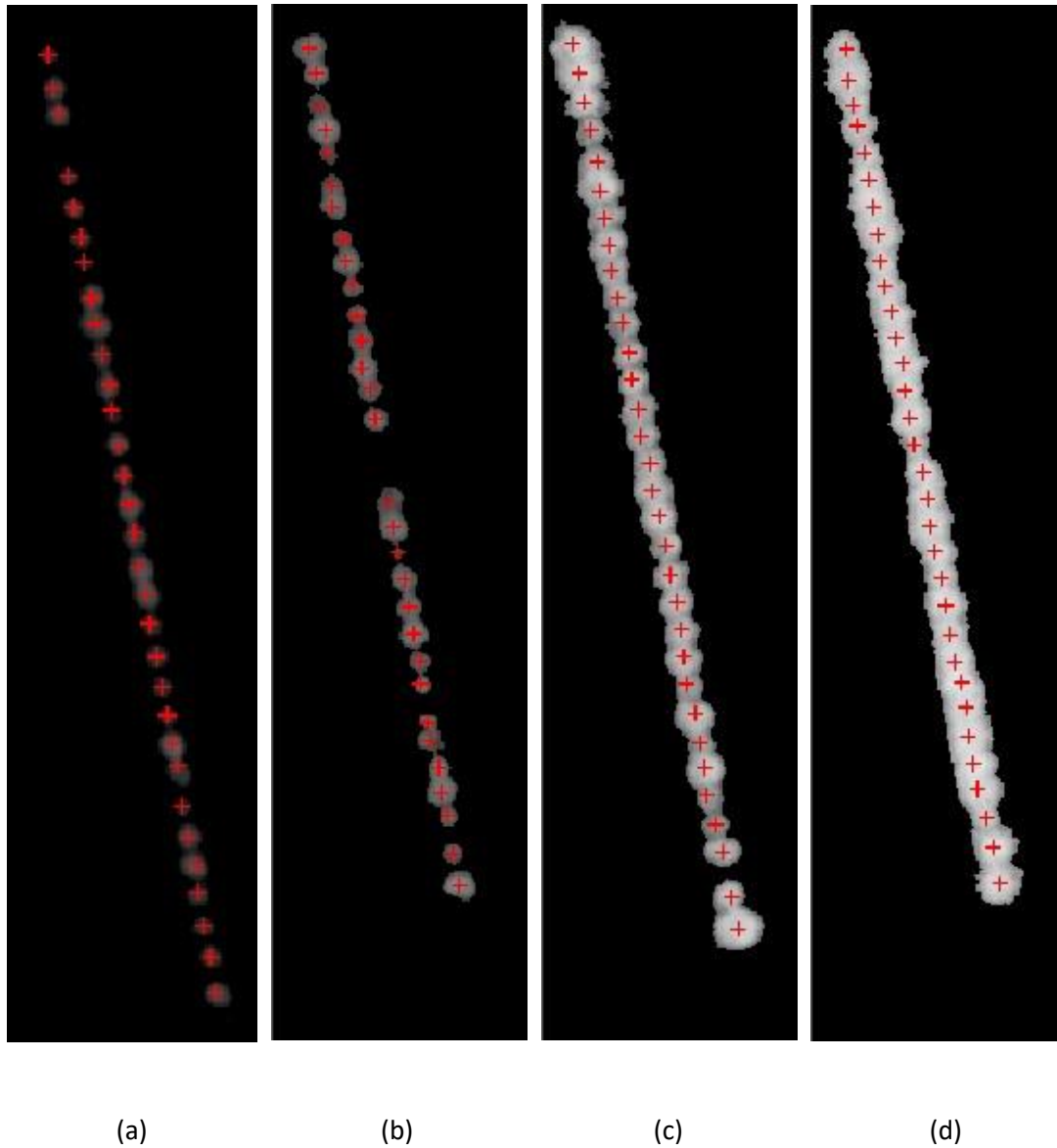
Fig. 4.8. (a)-(d) Identification of centre points using Algorithm 1.
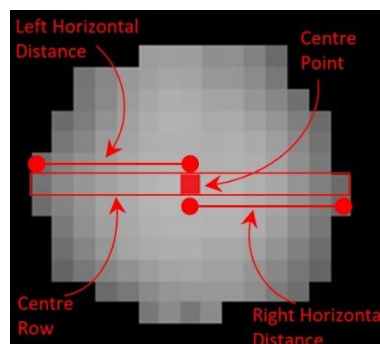
Fig. 4.9. Distribution of image pixels with labelling of centre point, centre row and horizontal distances

from centre point to the horizontal extremes.

the horizontal extreme. Fig. 4.9 shows the same plant illustrated in Fig. 4.7 with labelling of centre point, centre row and horizontal distances from centre point to the horizontal extremes. These horizontal distances give the possible radius of the plant. The vertical distances are not taken for consideration as the adjacent plants may overlap at vertical (at both top and bottom; except the 1st and 32nd plant of the row) positions. For each centre pixel defined above (Θ_r, Θ_c), let its corresponding radius be defined by:

$$radius = \max\{\text{abs}(\Theta_c - j)|\; I^b(\Theta_r, j) \geq 0.6 * I_{max}\} \qquad (4.3)$$

Using the radii and centre points, the circular plant regions of each plant are extracted (Fig. 4.10a-d). The extraction of radii and the circular plant regions has solved the second research problem, that is, the accurate area of the individual plants is calculated despite the overlapping of adjacent plants. Furthermore, the area is calculated by taking the product of number of non-zero pixels with the area of one pixel in cm^2 within that region.

4.4.4. Extraction of NDVI values

As mentioned earlier, due to the overlapping of the adjacent plants, the NDVI values can be inflated at top and bottom positions as depicted in Fig. 4.10(c)-(d). Therefore, the overlapping pixels rows at top and bottom positions must be identified and adjusted.

Finding the Overlapping Pixel Rows

Considering a single crop row (32 plants), the overlapping pixels rows for each plant can be extracted using the centre points and radii calculated earlier. Let $P_x, x \in [1, 2, ..., 32]$ be a plant whose overlapping rows are to be extracted. The centre point and radius for P_x are calculated earlier and let be denoted as (Θ_r^x, Θ_c^x) and R_x, respectively. The number of overlapping rows at the bottom position, ρ_{bottom}^x of plant P_x is extracted as:

$$\rho_{bottom}^{x} = (\Theta_r^x + R_x) - (\Theta_r^{x+1} - R_{x+1}) - 1. \qquad (4.4)$$

Similarly, the number of overlapping rows at the top position, ρ_{top}^{x} of plant P_x is extracted as:

$$\rho_{top}^{x} = (\Theta_r^{x-1} + R_{x-1}) - (\Theta_r^x - R_x) - 1. \qquad (4.5)$$

(a) (b) (c) (d)
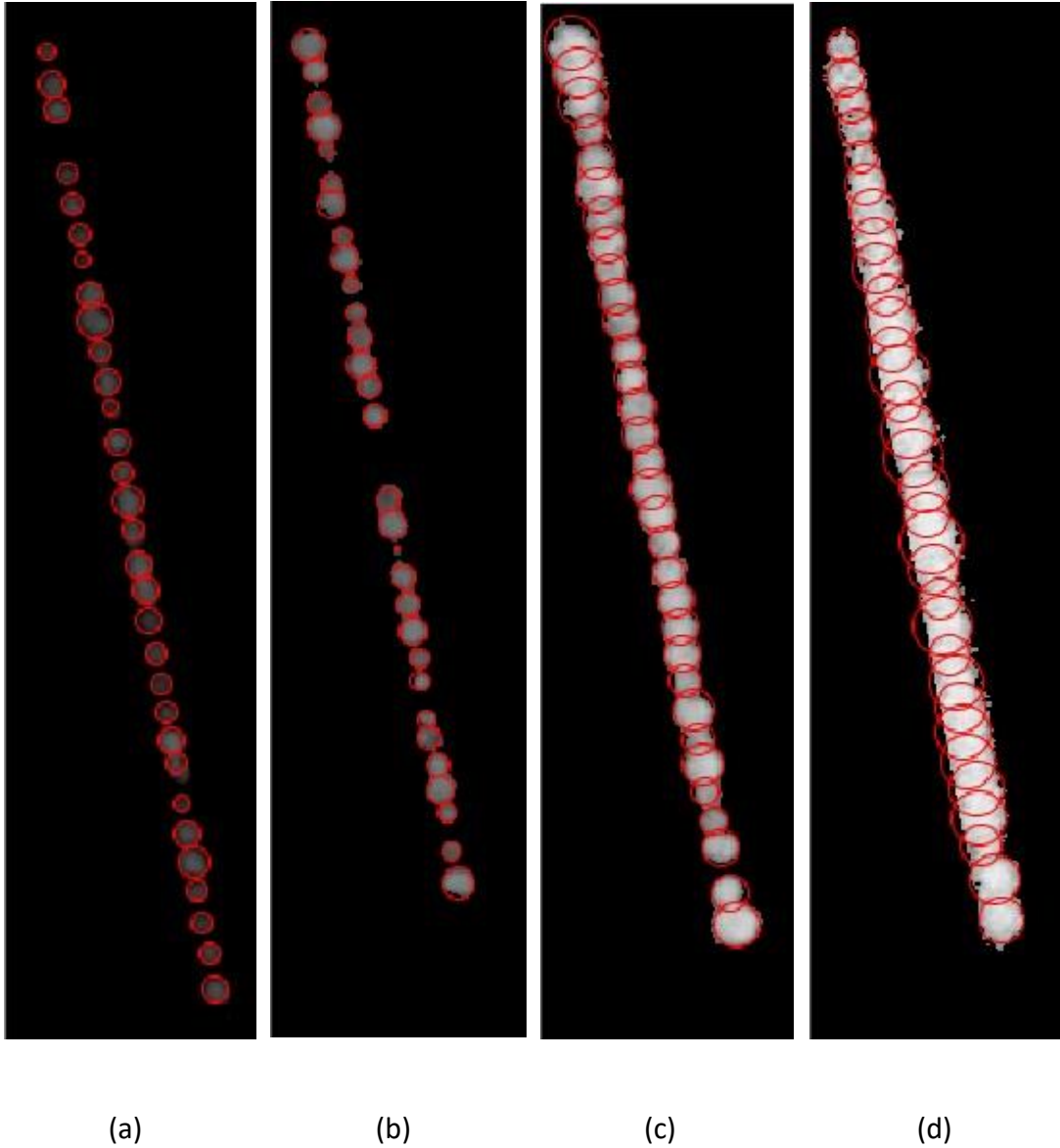
Fig. 4.10. (a)-(d) Extraction of circular plant regions and accurate area of individual plants from Fig. 4.8 using Algorithm 4.2.

It is to be noted that ρ^x_{bottom} for P_x at bottom position is same as ρ^x_{top} for P_{x+1} at top position. This is illustrated in Fig. 11 with three plants and their centre points and radii. Moreover, the first plant is overlapping to the second plant at the bottom position and the reverse is true for the second plant. Similarly, the second plant overlaps the third plant at the bottom position and vice-versa. Using equations (4.4)-(4.5), it can be calculated that $\rho^1_{bottom} = \rho^2_{top} = 2$ and $\rho^2_{bottom} = \rho^3_{top} = 3$. These are the number of pixels rows where the NDVI values are likely inflated and should be adjusted before consideration. Note that $\rho^x > 0$, if there is overlap, otherwise there is no overlap and therefore no adjustment needed.

Adjusting NDVI values at Overlapping Pixel Rows

The symmetrical distribution of plant NDVI values with centre maxima and a gradual decrease towards the boundary of plant informs the adjustment procedure for overlapping pixel rows (Fig. 4.7).
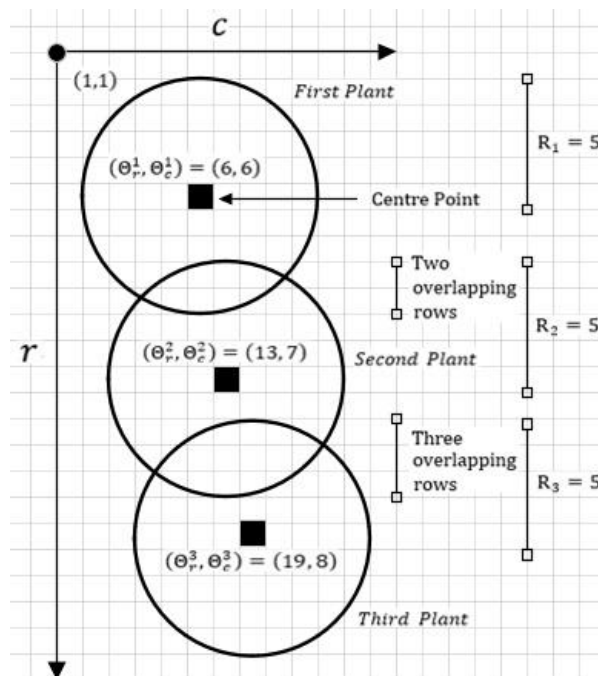
Fig. 4.11. Three plants in a crop row overlapping at top and bottom positions. The centre points and radii are also mentioned which assist in extracting those overlapping rows.

Care must be taken to exclude overlapping areas from the determination of maximum and minimum NDVI values. The use of the centre row avoids overlapping areas and increases the accuracy of maxima and minima. There are three steps described as follows:

1. The maximum and minimum NDVI values of the plant are first calculated, labelled as I_{max}^b and I_{min}^b respectively.

2. The whole centre row is updated and will be used as a reference for the adjustment of plant pixels at overlapping rows. The step size, which is the difference of NDVI values between two adjacent pixels, is calculated as:

$$I_{step} = \frac{I_{max}^b - I_{min}^b}{R - 1}. \tag{4.6}$$

The centre row is then updated with the following values:

$$I^b(\Theta_r, :)$$

$$= \left[I_{min}^b, I_{min}^b + I_{step}, I_{min}^b + 2 * I_{step}, \dots \dots, I_{max}^b, \dots \dots, I_{min}^b + 2 * I_{step}, I_{min}^b \right.$$

$$\left. + I_{step}, I_{min}^b \right]_{1 \times (2R-1)}. \tag{4.7}$$

3. Let's take a symmetric reference vector, $\mathbf{V_{sym}}$, such that $\mathbf{V_{sym}} = [1, 2, 3, \dots, R - 2, R - 1, R, R - 2, R - 1, \dots, 3, 2, 1]$. The NDVI values are adjusted as following:

$$I^b(i,j)$$

$$= \begin{cases} I^b(\Theta_r, i+j-R) & if \; \left[\left(V_{sym}(i) + V_{sym}(j) \right) > R+1 \right] \& [i \text{ is an overlapping row}], \\ I^b(\Theta_r, 1) & if \; \left[\left(V_{sym}(i) + V_{sym}(j) \right) \le R+1 \right] \& [i \text{ is an overlapping row}], \\ I^b(i,j) & otherwise, \qquad\qquad\qquad \forall \, i \in [1,r], \forall \, j \in [1,c]. \end{cases} \tag{4.8}$$

As an example, after adjustment, the plant matrix I^b will look like the following 2-dimensional matrix if each pixel of I^b is adjusted, considering the plant has seven rows and seven columns.

$$I^b$$

$$= \begin{bmatrix} I^b_{min} & I^b_{min} & I^b_{min} & I^b_{min} & I^b_{min} & I^b_{min} & I^b_{min} \\ I^b_{min} & I^b_{min} & I^b_{min} & I^b_{min} + I_{step} & I^b_{min} & I^b_{min} & I^b_{min} \\ I^b_{min} & I^b_{min} & I^b_{min} + I_{step} & I^b_{min} + 2*I_{step} & I^b_{min} + I_{step} & I^b_{min} & I^b_{min} \\ I^b_{min} & I^b_{min} + I_{step} & I^b_{min} + 2*I_{step} & I^b_{max} & I^b_{min} + 2*I_{step} & I^b_{min} + I_{step} & I^b_{min} \\ I^b_{min} & I^b_{min} & I^b_{min} + I_{step} & I^b_{min} + 2*I_{step} & I^b_{min} + I_{step} & I^b_{min} & I^b_{min} \\ I^b_{min} & I^b_{min} & I^b_{min} & I^b_{min} + I_{step} & I^b_{min} & I^b_{min} & I^b_{min} \\ I^b_{min} & I^b_{min} & I^b_{min} & I^b_{min} & I^b_{min} & I^b_{min} & I^b_{min} \end{bmatrix}_{7\times 7}$$

To validate the results obtained from the digital adjusted plants, the phenomics of these plants are correlated with the manually harvested fresh weights. The higher value of correlation confirms the accuracy of extracted phenomics of adjusted plants. The results are obtained by considering two phenomics; 1) area and 2) mean NDVI values of adjusted plants.

After the adjustment of NDVI values and the extraction of circular plant regions, the next aim is to extract the area and mean NDVI value of each plant for each field trial image. Individual plant area was calculated as the product of number of non-zero pixels with the area of one pixel in cm^2 within the circular plant region. Mean NDVI was tabulated by calculating the mean NDVI values of non-zero pixel with the bounding box. The area provides information about the size of the plant and the mean NDVI value indicates how dense the plant canopy is. Note that area and mean NDVI value may not be correlated, e.g., a plant with small area can have a similar mean NDVI value as a plant occupying a large area.

4.4.5.   Testing of Algorithm

Fresh biomass weights were collected for a subset of 480 perennial ryegrass plants to measure their individual biomass yield. The field trial was located and operated by Agriculture Victoria Research, Hamilton, Victoria, Australia (37.8464°S, 142.0737°E). The Hamilton region is in the Victorian high rainfall zone with generally >600mm per year of rain. Fresh weights were available for four harvesting dates (9th May 2017, 5th July 2017, 11th September 2017 and 20th November 2017) in different seasons of the year 2017 [34]. Harvest dates were determined by the growth stage of the individual plants, in which the 2–3 leaf stage was considered as a standard simulated grazing stage. The above-ground biomass was harvested manually at 5 cm height.

The following phenomics metrics were compared via Pearson correlations (ř) [35]: mean NDVI of rectangular bounding boxes, area of rectangular bounding boxes, unadjusted mean NDVI of circular plant regions, adjusted mean NDVI of circular plant regions and area of circular plant regions.

4.5. Results and Discussions

The robustness of the proposed algorithm was tested by correlating extracted phenomics metrics with harvest fresh weights. Metrics included area calculated from rectangular bounding boxes and their mean unadjusted and adjusted NDVI. The fresh biomass weight value per individually harvested plant (82.48–127.18 g) varied across seasons in 2017. Moreover, measured seasonal fresh biomass weight in 2017 indicated a wide variability of biomass values (~1.41–428 g) for each measurement season for the individual plants [34].

This suggests that biomass yield had enough variation to use to correlate the NDVI and plant phenomics.

Pearson correlation coefficients (ř) between the area of circular plant regions and fresh weights for four field trial images from four timepoints are shown in Table 4.1 and Figs. 4.12 (a-d). The values of ř for these four images demonstrate a good relationship between

(a)   (b)

(c)   (d)
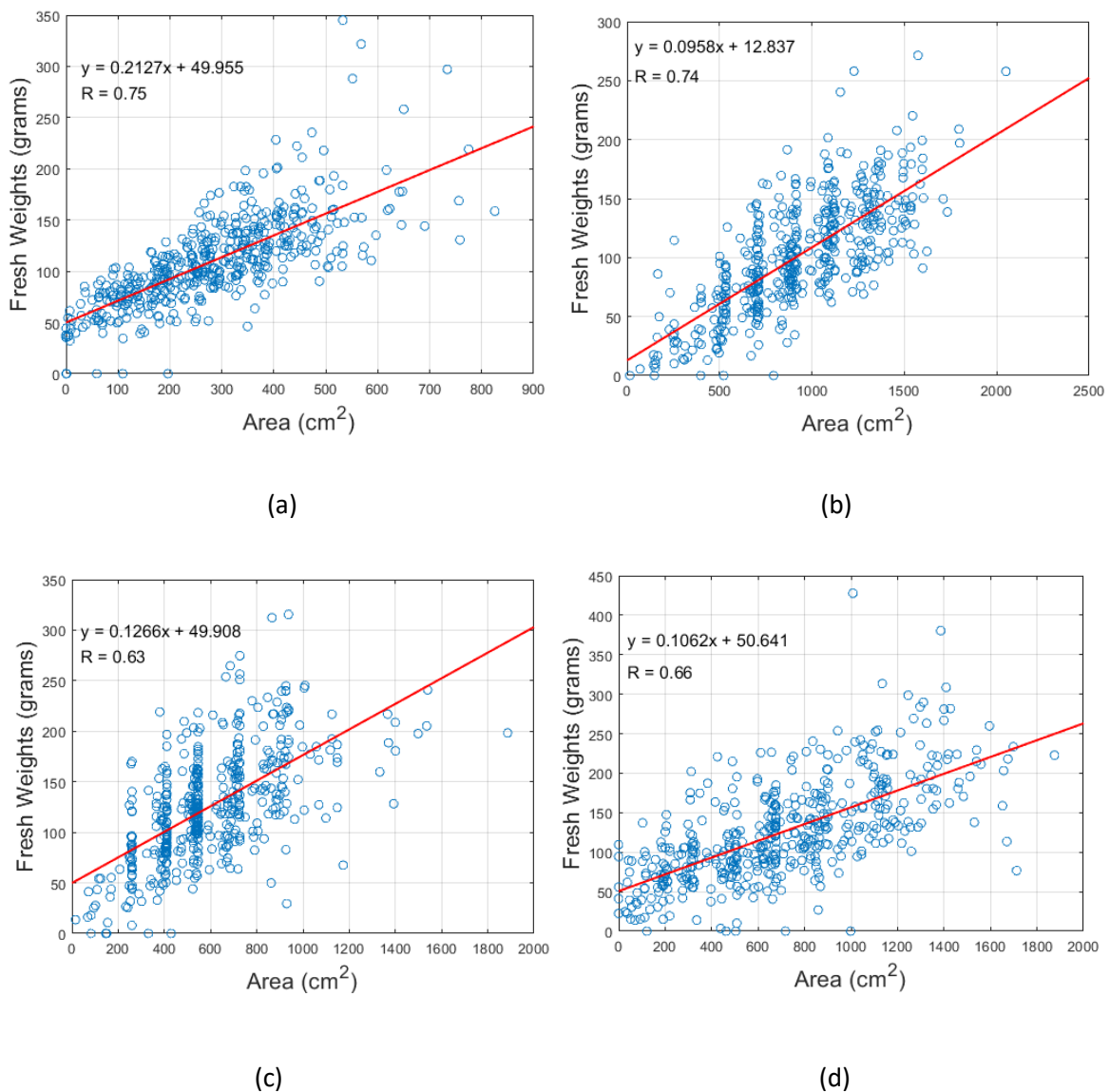
Fig. 4.12. Correlation coefficients between fresh weight of subset of 480 perennial ryegrass plants and circular area for field trial images taken on **(a)** 9th May 2017, **(b)** 5th July 2017, **(c)** 11th September 2017 and **(d)** 20th November 2017.

Table 4.1. Values of řcalculated for the area extracted from rectangular and circular plant regions

with the fresh weights of subset of 480 perennial ryegrass plants.

Image Time Point	Correlation	
	Area of Rectangular Bounding Boxes	**Area of Circular plant regions**
9th May 2017	0.74	0.75
5th July 2017	0.30	0.74
11th September 2017	0.28	0.63
20th November 2017	0.30	0.66

Table 4.2. Correlations of mean NDVI and fresh weights of subset of 480 perennial ryegrass plants for

rectangular boxes and proposed circular plant regions: with unadjusted and adjusted NDVI values.

Image Time Point	Correlation		
	Unadjusted NDVI from Rectangular Boxes	**Unadjusted NDVI from Circular plant regions**	**Adjusted NDVI from Circular plant regions**
9th May 2017	0.56	0.56	0.57
5th July 2017	0.55	0.58	0.59
11th September 2017	0.52	0.54	0.55
20th November 2017	0.51	0.53	0.56

fresh weight and circular area (0.63 – 0.75). The correlation could likely be further improved by including height measures [36]. Areas extracted from circular plant regions were more correlated with fresh weights than those from rectangular boxes (Table 4.1). The advantage of the circular areas was less pronounced at the May 2017 time point, which also had the lowest number of plants overlapping across boxes. However, for the other timepoints with a higher degree of plant overlap, the correlation for circular plant regions were substantially higher than the rectangular boxes. There are two main reasons for that: 1) most plants in those three field trial images had overgrown across bounding boxes and merged with adjacent plants, thus rectangular bounding boxes will not provide an accurate measure of area, and 2) rectangular boxes may show area that is entirely due to neighbouring plants overlapping, leading to area or NDVI being attributed to missing plants. These factors erode the accuracy of rectangular bounding boxes, especially when there is substantial biomass.

To see the trends of individual plants' values of fresh weight and extracted phenomics, the ranges of fresh weight and area were normalized to a single range of [0, 100] and plotted as

Fig. 4.13. Comparisons between the individual plant values of normalized values of fresh weights and areas for first 100 plants in a same range of [0, 100] for the field trial image taken on 5th July 2017.

a comparison in Fig. 4.13, which shows that plant fresh weight and area follow a very similar pattern on 9th May 2017. This pattern is consistent with the other time points (Suppl Fig. 4.1-4.3).

We further compared the mean adjusted and unadjusted plant NDVI of circular plant regions and unadjusted NDVI of rectangular boxes to fresh weights (Table 4.2). The correlations were moderate for rectangular boxes and ranged between 0.51 and 0.56. Circular plant regions slightly improved correlations to 0.53 and 0.58. The relatively low improvement is due to NDVI values being similar for both types of bounding boxes despite large difference in area. Further small correlation improvements (range 0.55 – 0.59) were achieved by adjusting NDVI values for circular plant regions by accounting for plant overlap. While the improvement observed from adjusting NDVI here was minor, the adjustment methods applied could be useful for other trials, crops or even data types (e.g., point clouds).

The multi-spectral images used in this study had a pixel size of approximately 2cm. This was sufficient to distinguish single perennial ryegrass plants. The succesfull application of our algorithm to other image datasets depends on their relative pixel and plant size. Further, we set numercial threshold for NDVI intensity and the search space within the bounding box to detect plant centres. In part, these values are expected to be dataset specific and could depend on achieving relative uniform plant spacing, and, therefore, should be revisited during application. Finally, further improvements may be needed to the determination of radii, especially when plants are large and overlap substantially (Table 4.1, timepoints 3 and 4), which adds noise and causes some overestimation.

The correlation of our phenomic bio-characteristics (plant areas and adjusted NDVI) found in our study is at a level useful to provide proxy phenotypes of individual biomass in field. Plant

breeding, with or without genomics, requires the phenotypic screening of many breeding lines to select the best for commercialization or as parents for the next breeding cycle. Further, methods such as genomic selection require a large training population of phenotype lines with genome-wide DNA markers [37]. The advantage of sensor-based methods is that they are non-destructive and consume less time, which makes them suitable to be taken at multiple time points during the growing season. In pasture grasses, growth rate and recovery after harvest are key properties that only non-destructive sensor-based methods can investigate at sufficient scale to be useful for plant breeding. Further as pasture grasses are outbreeding (i.e. they cannot self-pollinate making each plant genetically unique), it can be of importance to measure single plants for research and selection purposes. Of particular interest is the genetic predisposition of individual plants to compete with plants in close proximity in the field because highly competitive plants will lead to non-uniform growth patterns in the paddock, which is undesirable. The bio-characteristics defined in our study will provide crucial information at the individual plant level to better understand the phenome-to-genome relationships of biomass production and other important traits.

4.6. Conclusions

An efficient and effective solution presented in the paper is to develop a machine-vision mathematical model that can extract plant phenomic bio-characteristics with sufficient accuracy despite of overlapping of adjacent plants. The estimation of plant areas when plants are very large and overlap substantially could potentially be improved in future studies. The mathematical model consisted of three parts: locating of centre points, extracting the area by means of radius and centre point, and extracting of mean NDVI via adjustment of overlapping plant regions. Overall, correlations of phenomic metrics with fresh weights were

moderate, with plant area derived from circular plant regions were more strongly correlated than NDVI derived measures. The proposed NDVI adjustment for overlapping plant portions increased correlations with fresh weights slightly. Like all new proposals, we strongly encourage the evaluation of the algorithm performance before deployment. The algorithms presented in this study can be applied to a wide variety of crops and to other field trial designs.

4.7. Acknowledgments

Supplementary Materials
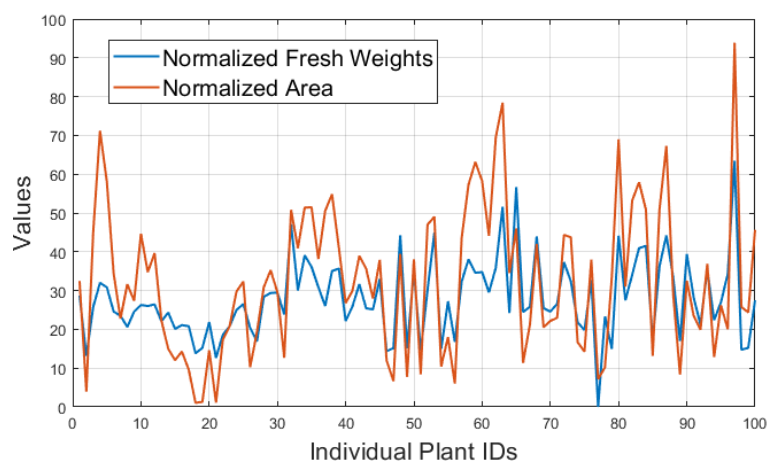
Supp. Fig. 4.1. Comparisons between the individual plant values of normalized values of fresh weights and areas for first 100 plants in a same range of [0, 100] for the field trial image taken on 9th May 2017.
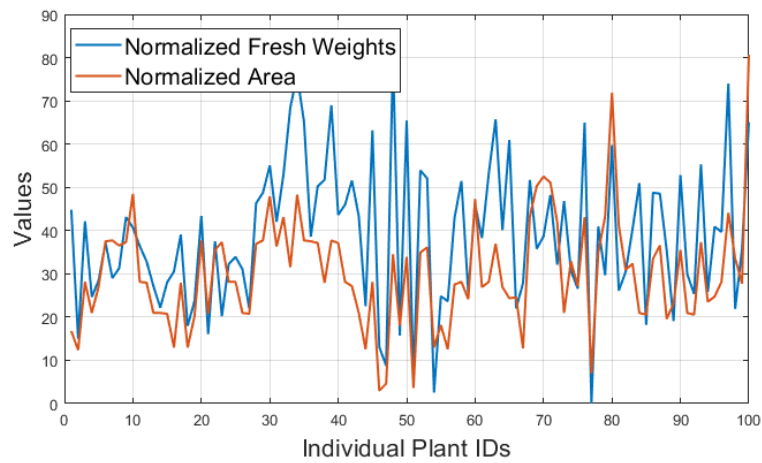
Supp. Fig. 4.2. Comparisons between the individual plant values of normalized values of fresh weights and areas for first 100 plants in a same range of [0, 100] for the field trial image taken on 11th September 2017.
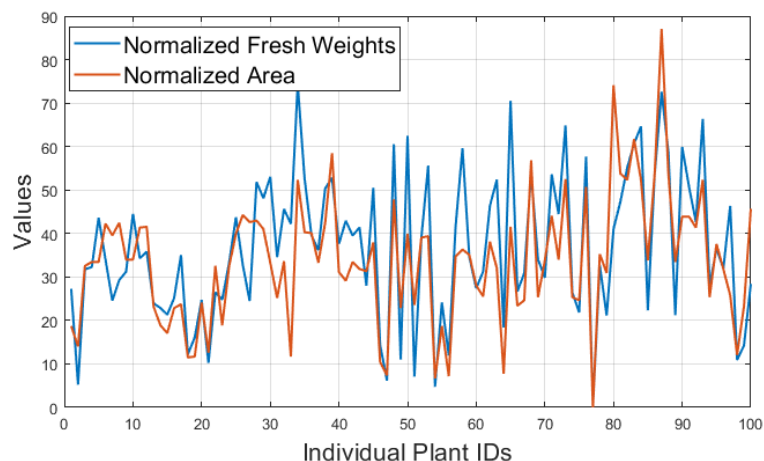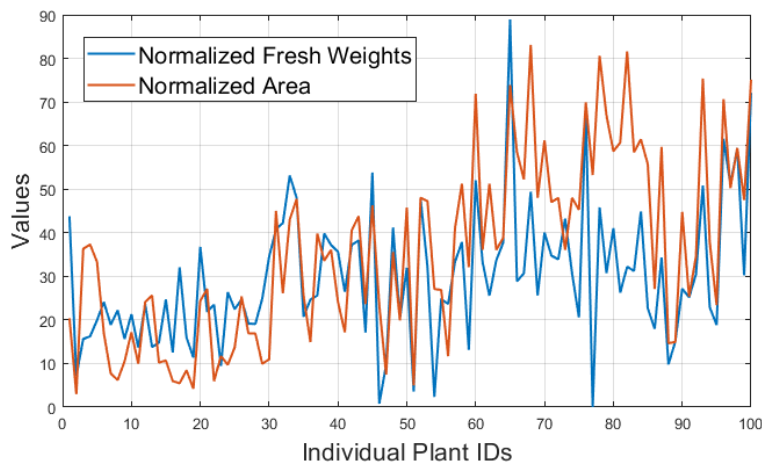

Supp. Fig. 4.3. Comparisons between the individual plant values of normalized values of fresh weights and areas for first 100 plants in a same range of [0, 100] for the field trial image taken on 20th November 2017.

4.8. References

[1]   M. Tester and P. Langridge, "Breeding technologies to increase crop production in a changing world", *Science*, vol. 327, no. 5967, pp. 818-840, Feb. 2010.

[2]   S. P. Long, A. M-Colon and X-G. Zhu, "Meeting the Global Food Demand of the Future by Engineering Crop Photosynthesis and Yield Potential", *Cell*, vol. 161, no. 1, pp. 56-66, Mar. 2015.

[3]   T. B. Brown, R. Cheng, X. R. R. Sirault, T. Rungrat, K. D. Murray, M. Trtilek, R. T. Furbank, M. Badger, B. J. Pogson and J. O. Borevitz, "TraitCapture: genomic and environment modelling of plant phenomic data", *Current Opinion in Plant Biology*, vol. 18, pp. 73-79, Apr. 2014.

[4]   J. Kumar, A. Pratap and S. Kumar, "Plant Phenomics: An Overview", *Phenomics in Crop Plants: Trends, Options and Limitations*, pp. 1-10, Springer India, 2015.

[5]   M. B. Sticklen, "Feedstock Crop Genetic Engineering for Alcohol Fuels", *Crop Science*, vol. 47, no. 6, pp. 2238-2248, Nov. 2007.

[6]   M. Tester and P. Langridge, "Breeding technologies to increase crop production in a changing world", *Science*, vol. 327, no. 5967, pp. 818-839, Feb. 2010.

[7]   R. C. O'Malley and J. R. Ecker, "Linking genotype to phenotype using the Arabidopsis unimutant collection", *The Plant Journal*, vol. 61, no. 6, pp. 928-967, Mar. 2010.

[8]   D. Weigel and M. Richard, "The 1001 Genomes Project for Arabidopsis thaliana", *Genome Biology*, vol. 10, pp. 1-5, May. 2009.

[9]   S. B. Cannon, G. D. May and S. A. jackson, "Three Sequenced Legume Genomes and Many Crop Species: Rich Opportunities for Translational Genomics", *Plant Physiology*, vol. 151, pp. 970-977, Nov. 2009.

[10]   J. P. Vogel *et al.*, International Brachypodium Initiative, "Genome sequencing and analysis of the model grass Brachypodium distachyon", *Nature*, vol. 463, no. 7282, pp. 763-770, Feb. 2011.

[11]   S. Atwell *et al.*, "Genome-wide association study of 107 phenotypes in Arabidopsis thaliana inbred lines", *Nature*, vol. 465, no. 7298, pp. 627-657, Jun. 2010.

[12]   M. Wang, N. Jiang, T. Jia, L. Leach, J. Cockram, J. Comadran, P. Shaw, R. Waugh and Z. Luo, "Genome-wide association mapping of agronomic and morphologic traits in highly structured populations of barley cultivars", *Theoretical and Applied Genetics*, vol. 124, no. 2, pp. 233-246, Feb. 2012.

[13]   J. M. Lucocq, "Efficient quantitative morphological phenotyping of genetically altered organisms using stereology", *Transgenic Research*, vol. 16, pp. 133-145, 2007.

[14]   K. Chung, M. M. Crane and H. Lu, "Automated on-chip rapid microscopy, phenotyping and sorting of C. elegans", *Nature Methods*, vol. 5, pp. 637–643, June. 2008.

[15]   R. Sozzani and P. N. Benfey, "High-throughput phenotyping of multicellular organisms: finding the link between genotype and phenotype", *Genome Biology*, vol. 12, pp. 1-7, 2011

[16]   N. de Souza, "High-throughput phenotyping", *Nature Methods*, vol. 7, pp. 1-1, 2010.

[17]   F. P-Sanz, P. J. Navarro and M. E-Cortines, "Plant phenomics: an overview of image acquisition technologies and image data analysis algorithms", *Gigascience*, vol. 6, no. 11, pp. 1-18, Nov. 2017.

[18]   V. Badrinarayanan, A. Kendall and R. Cipolla, "SegNet: A Deep Convolutional Encoder-Decoder Architecture for Image Segmentation", *IEEE Transactions on Pattern Analysis and Machine Intelligence*, vol. 39, no. 12, pp. 2481-2495, Jan. 2017.

[19]   N. Otsu, "A Threshold Selection Method from Gray-Level Histograms", *IEEE Transactions on Systems, Man, and Cybernetics*, vol. 9, no. 1, pp. 62-66, 1979.

[20]   L. Vincent and P. Soille, "Watersheds in digital spaces: an efficient algorithm based on immersion simulations", *IEEE Transactions on Systems, Man, and Cybernetics*, vol. 13, no. 6, pp. 583-598, Jun. 1991.

[21]   B. P. Banerjee, G. Spangenberg and S. Kant, "Fusion of Spectral and Structural Information from Aerial Images for Improved Biomass Estimation", *Remote Sensing*, vol. 12, no. 19, pp. 1-22, Sep. 2020.

[22]   A. Gebremedhin *et al.*, "Development and Validation of a Phenotyping Computational Workflow to Predict the Biomass Yield of a Large Perennial Ryegrass Breeding Field Trial", *Frontiers in plant science*, vol. 11, May. 2020.

[23]   J. C. e Silva and R. J. Kerr, "Accounting for competition in genetic analysis, with particular emphasis on forest genetic trials", *Tree Genetics & Genomes*, vol. 9, pp. 1-17, 2012.

[24]   C. J. Tucker, "Red and photographic infrared linear combinations for monitoring vegetation", *Remote Sensing of Environment*, vol. 8, no. 2, pp. 127-150, May. 1979.

[25]   K. Neumann *et al.*, "Dissecting spatiotemporal biomass accumulation in barley under different water regimes using high-throughput image analysis", *Plant, Cell & Environment*, vol. 38, no. 10, pp. 1980-1996, Oct. 2015.

[26]   O. Tackenberg, "A New Method for Non-destructive Measurement of Biomass, Growth Rates, Vertical Biomass Distribution and Dry Matter Content Based on Digital Image Analysis", *Annals of Botany*, vol. 99, no. 4, pp. 777-783, Apr. 2007.

[27]   D. Chen *et al.*, "Dissecting the phenotypic components of crop plant growth and drought responses based on high-throughput image analysis", *Plant Cell*, vol. 26, no. 12, pp. 4636-4655, Dec. 2014.

[28] A. Hartmann, T. Czauderna, R. Hoffmann, N. Stein and F. Schreiber, "HTPheno: an image analysis pipeline for high-throughput plant phenotyping", *BMC Bioinformatics*, vol. 12, no. 148, pp. 1-9, May. 2011.

[29] R. Subramanian, E. P. Spalding and N. J. Ferrier, "A high throughput robot system for machine vision-based plant phenotype studies", *Machine Vision and Applications*, vol. 24, no. 3, pp. 619-636, Apr. 2013.

[30] N. D. Miller, B. M. Parks and E. P. Spalding, "Computer-vision analysis of seedling responses to light and gravity", *The Plant Journal*, vol. 52, no. 2, pp. 374-381, Aug. 2007.

[31] R. T. Clark *et al.*, "Three-Dimensional Root Phenotyping with a Novel Imaging and Software Platform", *Plant Physiology*, vol. 156, pp. 455-465, Jun. 2011.

[32] T. J. Atherton and D. J. Kerbyson, "Size invariant circle detection", *Image and Vision Computing*, vol. 17, no. 11, pp. 795-803, Sep. 1999.

[33] H. K. Yuen, J. Princen, J. Illingworth and J. Kittler, "Comparative study of Hough Transform methods for circle finding", *Image and Vision Computing*, vol. 8, no. 1, pp. 71-77, Feb. 1990.

[34] A. Gebremedhin *et al.*, "Development and Validation of a Model to Combine NDVI and Plant Height for High-Throughput Phenotyping of Herbage Yield in a Perennial Ryegrass Breeding Program", *Remote Sensing*, vol. 11, no. 21, pp. 1-19, Oct. 2019.

[35] J. L. Rodgers and W. A. Nicewander, "Thirteen Ways to Look at the Correlation Coefficient", *The American Statistician*, vol. 42, no. 1, pp. 59-66, Feb. 1988.

[36] A. Gebremedhin *et al.*, "Development and Validation of a Phenotyping Computational Workflow to Predict the Biomass Yield of a Large Perennial Ryegrass Breeding Field Trial", *Frontiers in Plant Science*, https://doi.org/10.3389/fpls.2020.00689, May. 2020.

[37] H. D. Daetwyler, B. Villanueva and J. A. Woolliams, "Accuracy of Predicting the Genetic

Risk of Disease Using a Genome-Wide Approach", *Plos One*, vol. 3, no. 10, pp. 1-8, Oct.

2008.

Chapter 5

Genomic Prediction of Plant Area and Competition Effects of Individual Ryegrass Plants

Saba Rabab[1,2], Yongjun Li[2], Luke W Pembleton[2], Junping Wang[3], Michelle C Drayton[2], Fan Shi[2], Preeti Thakur[2], Carly M Elliot[3], Pieter Badenhorst[3], Yi-Ping Phoebe Chen[4] and Hans D. Daetwyler[1,2]

[1]School of Applied Systems Biology, La Trobe University, Bundoora, Australia

[2]Agriculture Victoria, AgriBio, Centre for AgriBioscience, Bundoora, Australia.

[3]Agriculture Victoria, Hamilton Centre, Hamilton, Australia.

[4]Department of Computer Science and Information Technology, La Trobe University, Bundoora, Australia.

Author Contributions: SR, YL, and HD developed the experimental design; SR, HD, and YL developed methodology; SR carried out the majority of analyses; LP, MD, and PT generated genotype data; FS, JW, CE and PB collected or processed phenotypes; HD and YC supervised the study; SR, YL and HD wrote the paper; all authors have read and approved the chapter.

5.1. Abstract

The genetic component of the impact of an individual on its neighbours, known as indirect genetic effects (IGEs), have been studied in animals and trees, but the impact of indirect genetic effects on pasture plants has to date not been examined. Ryegrass biomass yield is poorly correlated between plants grown separately or in swards or plots, which is a finding often attributed to competition effects. We defined individual plant phenomic predictors of biomass yield in perennial ryegrass from multi-spectral images across nine timepoints and investigated the presence of IGEs using genomic mixed linear models to understand a) whether IGEs were present in the species, and b) if present, whether they indicated cooperative or competitive action. Genomic heritabilities and genomic prediction accuracy for the extracted phenotypes in four cultivars were moderate (~0.3) and comparable to literature biomass values, indicating that our novel phenotype was suitable for further analysis. Genomic best linear unbiased prediction models of with and without IGEs in the cultivars revealed that a moderate level of IGEs existed in all cultivars and that direct and indirect genetic effects had a consistently negative covariance. The inclusion of IGEs always improved model fit as judged from LogLikelihoods. However, the estimate of negative covariance was only significant for one cultivar. Our results indicate that negative impact of ryegrass plants on its surrounding plants is moderate at best and that routine fitting of IGE models in breeding is not required.

Keywords: Phenomics, competition, indirect genetic effect, ryegrass, pasture grass, genomic prediction

5.2. Introduction

Perennial ryegrass (*Lolium perenne* L.) is one of the most widely grown pasture grasses native to Europe, temperate regions (New Zealand, Australia) and USA. It is an important forage grass for feeding livestock due to its nutritional qualities, high palatability, and digestibility. Since it is highly digestible, it aids in maintaining high dry matter intake levels of the grazing animal leading to outstanding animal performance. Perennial ryegrass is often a preferred choice for long term pastures as it is easy to establish and can remain in well-managed favourable environments for at least 4 years. It can be grown on a wide range of soils with other forage crops and recovers rapidly from heavy grazing [1]. Due of its rapid establishment, perennial ryegrass is also widely used for worn turf-area restoration. Therefore, 33,000 tons of perennial ryegrass seed is sold annually in Europe for turf usage [2]. In Australia, at least 6 million hectares of perennial ryegrass-based pastures are used for the dairy, sheep and meat industries [3]. Moreover, ryegrass holds the largest share of the forage seed market (>9000 t yr^{-1}) in Australia as compared with other forage species (e.g., tall fescue [*Festuca arundinacea* Schreb.], white clover [*Trifolium repens* L.], <1000 t yr^{-1}) [4].

Genetic improvement programmes have always been vital for the pastoral industry. However, genetic progress has been slow (0.7% yield gain per year) [5] and conventional phenotypic ryegrass selection schemes incur long breeding cycles (12-14 years) as phenotypes need to be measured across multiple stages and seasons. Further, pasture grasses are outbred, and varieties are made up of multiple parents, making accurate pedigree capture difficult for the breeding values as each parents' contribution is unknown. Thus, pedigrees are often incomplete and limit the application of best linear unbiased prediction (BLUP) [6]. Genomic prediction is a method that applies genome-wide markers to capture the relationship

between populations to estimate genomic breeding values [7]. The method is being applied in forage breeding and simulations have shown that it would increase genetic gain substantially [8-11]. Hence, it is important to know how genetic improvement of perennial ryegrass is directly linked to increase the productivity by choosing the most appropriate cultivars through improved breeding programmes.

Ryegrass synthetic lines or populations are diverse and there is the potential for competition effects between individual plants or a population that could affect its overall performance. It has also been shown that individual plant performance does not correlate well with plot performance in ryegrass [12-13]. Therefore, for genetic improvement of breeding populations, interaction among individuals may need to be considered. The interaction among individuals can be cooperative or competitive depending on the target trait. The interaction in which the genotype of an individual can influence the phenotypic trait value of its neighbours is known as indirect genetic effect (IGE). IGEs can have profound effects on total heritable variance in a population and consequently impact the response to selection. IGEs are a common natural phenomenon in animals, plants, and laboratory organisms. There are several examples of IGEs: the influence of the genetic effect of a mother on the trait value of her offspring [14-15], social interaction and behaviours in laboratory microorganisms [16], and competition effect among trees on growth rate in trunk diameter [17]. The competitive interaction in trees can reduce yield and growth due to competition for basic resources such as light, water and nutrients for survival. Such competitive interaction in livestock can not only reduce the overall growth and productivity, but in some cases can cause injury or death [18].

IGEs can be classified into two frameworks; direct consequence IGEs of individual trait values known as trait-based framework, and a variance-component framework in which phenotypic variance is decomposed into a direct and an indirect additive genetic component. To estimate the breeding values and variance components, the incorporation of IGEs in the ordinary linear mixed models in organism breeding has significantly improved experimental research [19]. For instance, the incorporation of IGEs in animal breeding within the ordinary quantitative genetic framework has greatly facilitated the understanding and the possible role in response to the selection [20]. Further, the trait based IGE models have initiated both experimental and theoretical work in the field of evolutionary biology [21-22].

The interactions can be either cooperative or competitive among individuals. Numerically, the cooperative and competitive interactions are defined by positive and negative covariance values. The covariance is an important factor that determines the influence of IGEs on the possible response to selection and heritable variation; a positive covariance value suggests increase in both possible response to selection and total heritable variation and a negative covariance value decreases both [23].

To numerically determine the interactions between individual plants, it is necessary to accurately extract the phenotypes of individuals. In case of trees, the definition of accurate phenotypes is relatively easy as compared to ryegrass as individual trees are physically apart from each other. In case of ryegrass, individual plants often overlap making it a difficult task to accurately extract phenomics such as area and normalized difference vegetation index from digital images. In our previous work [24], we have extracted individual plant phenomics from digital perennial ryegrass field data images. In this paper, these extracted phenotypes

are associated with genetic markers to estimate variance components for direct and indirect genetic effects and genomic prediction.

5.3. Methods

5.3.1. Phenotyping

The individual plant phenomics (plant area and normalized difference vegetation index; NDVI) of perennial ryegrass row field data were extracted using digital images taken from the top view [24]. A Parrot Sequoia (Parrot Drones S.A.S., Paris, France) multispectral camera was deployed on a 3DR Solo quadcopter to capture the digital images of field trials. The camera has incident light sensors and GPS. Tower Beta software was used to plan the flight mission. Images were captured simultaneously at four bands including green (530–570 nm), red (640–680 nm), red edge (730–740nm), and near-infrared (770–810 nm). The un-crewed aerial system (UAS) captured images of the trial site on a weekly basis. There were nine flight dates (four in 2017, two in 2018 and three in 2019) used for this study. The noise from environmental variation was minimized by conducting flight operations under sunny, bright weather conditions. The flight speed of UAS was set to 6 m/s, the flight altitude was set at 20 m above ground level with 75% side and forward overlap of images. The spatial resolution of the digital images was 2 cm/pixel at this flight speed and altitude. For each date, the same flight path was followed. Airinov calibration plates were used to correct image reflectance with known reflectance values (MicaSense Inc., Seattle, WA, USA).

The field trial was located in Hamilton, Victoria and contained a total of 48,000 individual plants in 10 blocks (referred as major crop rows) grown in replicated rows of 32 plants per row (referred as minor crop rows). Further, there were 50 perennial ryegrass cultivars replicated in the field trial, where each replication was considered as a plot and contained

three rows of 32 spaced plants each (i.e., 96 plants/plot). Each individual plant was genetically unique (perennial ryegrass is outbred) and there were at least four parental cultivars for each cultivar making them genetically diverse. The vertical spacing between the individual plants was 25 cm and the horizontal spacing between individual rows was 60 cm. The experimental unit of a single plot was 8 × 1.8 m making the total area of the field experiment to be 8,100 m^2. In part, the objective of the field trial was to estimate and predict the plant performance such as biomass yield and flowering time using phenomics processing pipelines.

The phenomic data of individual plants from this field trial were extracted from digital images as described in Rabab et al [24]. As the individual plants overlapped and merged into each other, the proposed algorithm [24] aimed to accurately extract the area covered by the individual plants and then their individual NDVI values. The algorithm assumed that the structure of individual plants was somewhat circular and was based on the calculation of centre points and radii of individual plants. These bio-characteristics of area and NDVI are then used in genomic prediction to select the best metrics. For the genomic prediction we considered the phenomics from four GSS images taken on four harvesting dates (9th May 2017, 5th July 2017, 11th September 2017 and 20th November 2017) in different seasons of the year 2017. Further, for phenomics, we considered area and mean NDVI values of individual plants extracted from rectangular bounding boxes [25] and circular bounding boxes [24]. The correlation values of genomic prediction for different phenomics assist in determining the best phenomics measures for genetic gain. For genomic mixed linear models to investigate IGEs, there were nine GSS trial images (9th May 2017, 5th July 2017, 11th September 2017, 20th November 2017, 19th June 2018, 22nd August 2018, 12th August 2019, 30th September 2019 and 10th November 2019) considered in different seasons of the years 2017, 2018 and 2019. Data was available for four *Lolium perenne* (LP) cultivars (LP423, LP714, LP730 and LP955).

5.3.2.   Genotyping

Leaf tissue of single plants was harvested at the trial site and mRNA was extracted using the mRNA Dynabead kit (Life Technologies, Carlsbad, CA) following manufacturer's instructions. A transcriptome genotyping-by-sequencing (GBSt) approach was then applied as in Malmberg et al [26]. Sequencing was carried out on Illumina HiSeq 3000 and for each individual circa 6M paired end reads were generated and aligned with *BWA-mem* [27] to the Shinozuka et al. [28] ryegrass transcriptome reference assembly. Variant calling was performed with *bcftools mpileup* and *bcftools call* using a predefined SNP list filtering on a minimum read depth of four. Loci with more than 25% missing data in samples which had less than 50% missing data were removed. Subsequently, samples with more than 90% missing data were removed. This resulted in 2274 individuals with 100,530 single nucleotide polymorphisms (SNP). The genotypes have been coded as the number of copies of the second allele at the marker. For instance, if the alleles at the marker were A and B, and a plant had the genotype AA, the plant would have a 0 coded genotype. If the genotype were AB or BA, the coded genotype would be 1, and BB would be 2. Missing SNP genotypes were imputed with LinkImpute [29].

5.3.3.   Statistical analysis

Genomic prediction

Three genomic prediction models were implemented in R. The method ridge regression BLUP (rrBLUP, a method similar to GBLUP) was run using "mixed.solve" function in the "rrBLUP" R package and the genomic prediction with Bayes A and Bayes B [7] were done using the "BGLR" R package with 50,000 iterations and 25,000 burn-in [32]. These three methods were chosen because the genetic architecture of our novel traits had not been investigated before. The Bayesian methods can better accommodate markers with larger effects, while rrBLUP treats markers similarly.

Genomic prediction was evaluated within timepoint across four cultivars in a cross-validation, where a random 20% of phenotypes were masked and predicted from the remaining phenotypes. Best linear unbiased esitmations (BLUEs) per individual plant were calculated by individual as a fixed effect in a mixed linear model. The accuracy of genomic prediction was estimated as the Pearson correlation of Genomic Estimated Breeding Values (GEBVs) and overall BLUEs across the four cultivars.

Direct and indirect effects

Phenomics data were analysed using mixed linear models with a general form below, implemented in ASREML [30]:

$$\mathbf{y} = \mathbf{Xb} + \mathbf{Za} + \mathbf{e}, \tag{5.1}$$

where, $\mathbf{y}$ is a vector of phenomics, $\mathbf{b}$ is the vector of fixed effects including the overall mean, $\mathbf{X}$ is a design matrix relating phenomics to fixed effects, $\mathbf{Z}$ is a design matrix relating phenomics to the additive genetic effects, $\mathbf{a}$ is a vector of random additive genetic effects (GEBVs) and $\mathbf{e}$ is a vector of random residuals normally distributed, i.e., $\sim N(0, I\sigma_e^2)$, σ_e^2 is the residual variance and I is the identity matrix.

Two GBLUP (genomic best linear unbiased prediction) models were examined in this paper, GBLUP models with or without competition effects. In the GBLUP model without the competition effects, $\mathbf{a}$ is normally distributed as $\sim N(0, \mathbf{G}\sigma_a^2)$, where σ_a^2 is the additive genetic variance and $\mathbf{G}$ is the genomic relationship matrix based on SNP data [31]. The mean and marker effects are predicted as:

$$\begin{bmatrix} \hat{\mathbf{b}} \\ \hat{\mathbf{a}} \end{bmatrix} = \begin{bmatrix} \mathbf{X'X} & \mathbf{X'Z} \\ \mathbf{Z'X} & \mathbf{Z'Z} + \mathbf{G}^{-1}(\sigma_e^2/\sigma_a^2) \end{bmatrix}^{-1} \begin{bmatrix} \mathbf{X'y} \\ \mathbf{Z'y} \end{bmatrix}. \tag{5.2}$$

GBLUP with indirect genetic effects

For competition among the individual plants, the focal plant had two neighbouring plants in the row, one above and one below, which were initially planted 25 cm apart from the focal plant. The plants in the adjacent rows of the focal plant were 60 cm apart and therefore were not considered as neighbour plants. Plants were matched to genotypes based on their row, column, and plot position. While genotypes of 2274 individual plants had phenotypes and genotypes available, not all plants with phenotype data were genotyped.

In the GBLUP model with competition effects, the vector of additive genetic effects $\mathbf{a}$ contains two sub vectors with a notation of $\mathbf{a}' = (\mathbf{a}'_d, \mathbf{a}'_i)$ with a design matrix defined as $\mathbf{Z} = (\mathbf{Z}_d, \mathbf{Z}_i)$, where $\mathbf{a}'_d$ is a vector of the direct additive genetic effects, $\mathbf{a}'_i$ is a vector of the indirect additive genetic effects, $\mathbf{Z}_d$ relates the phenomics of the focal individual to its own direct additive genetic effects, and $\mathbf{Z}_i$ relates the phenomics of a focal individual to its indirect additive genetic effects on its nearest neighbours.

The variance-covariance submatrix for the random terms in $\mathbf{a}$ was defined as:

$$Var \begin{bmatrix} \mathbf{a}'_d \\ \mathbf{a}'_i \end{bmatrix} = \begin{bmatrix} \sigma^2_{a_d} & \sigma_{a_{di}} \\ \sigma_{a_{di}} & \sigma^2_{a_i} \end{bmatrix} \otimes \mathbf{G}, \tag{5.3}$$

where, $\sigma^2_{a_d}$ is the direct additive genetic variance, $\sigma^2_{a_i}$ is the indirect additive genetic variance, $\sigma_{a_{di}}$ is the genetic covariance between direct and indirect additive effects, and $\otimes$ is the Kronecker product. We were interested in finding $\sigma^2_{a_d}$, $\sigma^2_{a_i}$ and $\sigma_{a_{di}}$ which explained the magnitude of direct and indirect genetic effects on phenomic trait values.

All nine timepoints of data were combined within each of the cultivar and a fixed effect for timepoint was fitted in each of the following GBLUP models in ASReml [30]:

    i.   Model 1: standard GBLUP model without indirect genetic effects among neighbouring individual plants.

ii.   Model 2: GBLUP model with both direct and indirect genetic effects, but without covariance between direct and indirect effects.

iii.   Model 3 (full model): GBLUP model with both direct and indirect genetic effects, and covariance between direct and indirect effects.

To test the significance of variance and covariance parameter estimates, Log likelihood-ratio (LogL) tests were performed. LogL_1 is the LogL-ratio value for Model 1 LogL_2 for Model 2 and LogL_3 for Model 3. A higher LogL indicates that a model is a better fit to the data. The significance of the difference between models was measured using a Chi square test [33] with one degree of freedom (df).   For further comparison of the three models, the Akaike information criterion (AIC) were computed for each model, where smaller AIC values reflect a better model fit.

Heritability

The narrow sense heritability, h^2, was calculated as:

$$h^2 = \frac{\sigma_{a_d}^2}{\sigma_{a_d}^2 + \sigma_{a_i}^2 + \sigma_e^2}, \tag{5.4}$$

where, σ_e^2 is the residual variance, $\sigma_{a_d}^2$ is the additive direct variance and $\sigma_{a_i}^2$ is the additive indirect variance. h^2 is calculated for each cultivar combining the phenomics of all GSS images. The proportion of genetic variance explained by the indirect effect, P_{ai}^2 was calculated as:

$$P_{ai}^2 = \frac{\sigma_{a_i}^2}{\sigma_{a_d}^2 + \sigma_{a_i}^2}. \tag{5.5}$$

These ratios were calculated per cultivar for each model, where applicable.

5.4. Results

5.4.1.   Genomic prediction

Best linear unbiased estimations (BLUEs) were calculated employing GBLUP model without

competition using combined data of nine timepoints per cultivar (LP423, LP714, LP730 and LP955). The summary statistics, such as mean, standard deviation, minimum and maximum BLUEs, were similar across the four cultivars 5.1.

We used the rrBLUP and Bayesian genomic prediction models to determine the best phenomics for genetic analysis by analysing the correlation values of these models. We extracted area and NDVI phenomics for rectangular and circular regions [24]. Genomic prediction accuracy ranged from 0.20 to 0.45 (Table 5.2). There were only minor differences between rrBLUP, Bayes A and Bayes B. across the four timepoints (9th May 2017, 5th July 2017, 11th September 2017 and 20th November 2017) investigated for the novel phenomics traits rectangular NDVI, circular area and circular NDVI. This indicated that the traits were polygenic in nature with few larger effect loci. Higher accuracy was observed for circular area phenomics measures than rectangular metrics. Further, the circular area measure was more consistent in genomic prediction accuracy than circular NDVI and, therefore, circular area was used for further analysis of genomic prediction and competition effects.

Table 5.1. Stats of BLUEs across four cultivars.

Cultivars	Mean	Standard Deviation	Minimum	Maximum
LP423	149	42	19	347
LP714	149	51	-32	332
LP730	197	36	57	340
LP955	160	35	43	342

Table 5.2. Genomics prediction results for rrBLUP, Bayes A and Bayes B at four time points across four cultivars.

Time Points	rrBLUP			Bayes A			Bayes B		
	Rect. NDVI	Circ. NDVI	Circ. Area	Rect. NDVI	Circ. NDVI	Circ. Area	Rect. NDVI	Circ. NDVI	Circ. Area
20170509	0.29	0.32	0.38	0.31	0.33	0.38	0.32	0.35	0.38
20170705	0.27	0.28	0.39	0.26	0.22	0.41	0.27	0.23	0.41
20170911	0.20	0.35	0.33	0.20	0.36	0.34	0.36	0.36	0.34
20171120	0.45	0.43	0.37	0.43	0.40	0.36	0.43	0.42	0.37
Mean	0.30	0.35	0.37	0.30	0.33	0.37	0.35	0.34	0.38

5.4.2.   Direct and indirect effects

Variance components and IGEs were estimated with GBLUP models using combined data of nine timepoints per cultivar (LP423, LP714, LP730 and LP955). We use the sequential modelling approach starting with the GBLUP model without any competition followed by the competition model without covariance and lastly the competition model with covariance. Table 5.3 shows the variances and covariances values for the GBLUP models for all four cultivars. The GBLUP competition models with and without covariance for LP423 did not converge and therefore (co)variances estimates were not conclusive. The magnitude additive direct genetic variance, $\sigma^2_{a_d}$ illustrates the impact of genetics on phenomics phenotypes. The additive indirect genetic variance, $\sigma^2_{a_i}$ demonstrates the scale of competition effects among the individual plants. Of the three cultivars, LP714 had the highest $\sigma^2_{a_i}$, at 457 and 962 for competition effects models with and without covariance, respectively, followed by LP730 and LP955, which had small $\sigma^2_{a_i}$, indicating no or little competition among plants. Evidence for competition can also be observed from the covariance values, though these were relatively small. The decreasing trend again followed the same order LP714, LP730, and LP955.

Table 5.3. Variance components for three GBLUP models.

	Models	Additive Variance, $\sigma^2_{a_d}$	Additive Indirect Variance, $\sigma^2_{a_i}$	Co-variance, $\sigma_{a_{di}}$	Residual Variance, σ^2_e
LP423	Model 1	**1587**	---	**---**	5614
	Model 2				
	Model 3		Did not converge.		
LP714	Model 1	**3105**	---	**---**	5257
	Model 2	**3325**	457	**---**	4929
	Model 3	**2951**	962	**-103**	4893
LP730	Model 1	**2310**	---	**---**	6360
	Model 2	**5509**	324	**---**	6795
	Model 3	**2688**	22	**-77**	6817
LP955	Model 1	**3143**	---	**---**	4248
	Model 2	**3129**	68	**---**	4193
	Model 3	**3136**	6	**-36**	4239

Model 1: GBLUP with no competition; Model 2: GBLUP with competition without covariance; and Model 3: GBLUP with competition with covariance.

5.4.3.   Heritability

Narrow sense heritability, h^2, was moderate for all cultivars and models ranging from 0.22 to 0.43. Further, demonstrating that the circular plant areas were a phenomic phenotype that was able to capture a genetic component (Table 5.4). To demonstrate the effect of competition, the proportion of genetic variance, P^2_{ai} , was also calculated (Table 5.4). The P^2_{ai} values for LP714 were 24% and 12% for GBLUP competition models with and without covariance, respectively, displaying some competition. However, the P^2_{ai} values for LP730 and LP955 were less than 5% indicating very little competition among individual plants for these cultivars.

Table 5.4. Heritability and proportion of genetic variance values for GBLUP models.

	Models	Heritability, $h^2 =$ $\sigma^2_{a_d}/(\sigma^2_{a_d} + \sigma^2_{a_i} + \sigma^2_e)$	Proportion of genetic variance, P^2_{ai} $= \sigma^2_{a_i}/(\sigma^2_{a_i} + \sigma^2_{a_d})$
LP423	Model 1	0.22	---
	Model 1	0.37	---
	Model 2	0.38	0.121
LP714	Model 3	0.33	0.245
	Model 1	0.27	---
	Model 2	0.43	0.055
LP730	Model 3	0.28	0.008
	Model 1	0.43	---
	Model 2	0.42	0.021
LP955	Model 3	0.42	0.002

5.4.4.   Model comparisons

Model significance is presented in Table 5.5. The LogL values for Model 2 were always greater than Model 1 across all the cultivars showing that the Model 2 is better a better fit to the data than Model 1. However, the LogL values do not have a constant pattern when compared between Model 2 and Model 3 making it difficult to comment whether fitting a covariance between direct and indirect effects is of value. The values for test statistic were greater than 3.84 for all the cultivars demonstrating the significance of the indirect additive genetic effect and the covariance between direct and indirect additive genetic effect. Specifically, for LP714, the test statistic between Model 2 and Model 1 was significantly higher (88.12) as compared to the other cultivars. However, for LP730 and LP955, the LogL was actually lower for Model 3, indicating its fit deteriorated by estimating a covariance.

Table 5.5. LogL and Chi square test values for GBLUP models.

	Models	LogL*	Test Against	Test Statistic	AIC
LP714	Model 1	71			39860 (2 Parameters)
	Model 2	115	Model 1	88.12 (df=1)	39774 (3 Parameters)
	Model 3	120	Model 2	9.436 (df=1)	39766 (4 Parameters)
LP730	Model 1	-6891			53787 (2 Parameters)
	Model 2	-6886	Model 1	10.26 (df=1)	53779 (3 Parameters)
	Model 3	-6895	Model 2	18.34 (df=1)	53799 (4 Parameters)
LP955	Model 1	-1224			62453 (2 Parameters)
	Model 2	-1212	Model 1	24.94 (df=1)	62430 (3 Parameters)
	Model 3	-1222	Model 2	19.98 (df=1)	62452 (4 Parameters)

*LogL values for LP714 are reported relative to a base of -20000.000. LogL values for LP730 are reported relative to a base of -20000.000. LogL values for LP955 are reported relative to a base of -30000.000.

5.5. Discussion

We demonstrated the interactive behaviour among individual ryegrass plants with IGE models. The extraction of individual plant phenomics is essential to numerically determine the interactions between individual plants. This the first application of IGE models in pasture grasses. The difficulty in extraction of individual plant phenomics in ryegrass arises due to ryegrass plants often overlapping, making it a difficult task to accurately extract phenomics

such as area and normalized difference vegetation index from a digital image. We extracted individual plant phenomics from digital perennial ryegrass field data images [24] and linked these extracted phenotypes with genetic markers to estimate variance components for direct and indirect genetic effects and genomic prediction.

Increased biomass is the main goal in perennial ryegrass breeding programs which requires accurately extracted phenotypes. The validation of extracted phenotypes is crucial for genomic prediction and investigating interaction among spaced ryegrass plants. The correlation values of genomic prediction for different phenomics assist in determining the best phenomics to achieve genetic gain. Therefore, we used genomic prediction to predict novel phenotypes and compared results between different genomic prediction models. The circular area measure was found to be more consistent and higher in genomic prediction accuracy. Moreover, the moderate heritability of the direct effect and genomic prediction accuracy were comparable to normal biomass yield hence circular plant areas were considered an appropriate phenotype to be used in further analysis of genomic prediction and competition effects [4, 34].

For the statistical analysis, GBLUP models 1) without competition, 2) with competition but without covariance and 3) full model with competition and covariance were used. We estimated the variances and covariances for three cultivars (LP423, LP714, LP730 and LP955). The additive direct genetic variance, $\sigma_{a_d}^2$ values specify that the phenomic variance can be partially explained by genomics. The competition effect among individual plants can be identified by the additive indirect genetic variance, the $\sigma_{a_i}^2$ component. The cultivars LP730 and LP955 had small $\sigma_{a_i}^2$, signifying no or little competition among individual ryegrass plants. Moreover, for LP714 the additive indirect variance component increased from model 2 to

model 3. The results revealed that all cultivars exhibited negative covariance but in LP714 we can identify significant negative covariance, as indicated by the LogL test and AIC. Therefore, LP714 provided the most conclusive evidence for competition effects among the three ryegrass cultivars. The significance of variance and covariance parameter estimates was tested by performing loglikelihood ratio tests. To determine the difference between the three models, comparison between these models are done. We found that Model 2 was always more likely than Model 1. The estimation of a covariance between direct and indirect covariances only improved model fit for one cultivar. This may be demonstration of the limited power of our experiment to estimate multiple variance components.

For the IGE model, we only considered neighbours above and below the focal plant in the row, ignoring plants in adjacent rows at a distance of 60cm. This trial design would allow plants to partly avoid competition through use of resources between rows. This may have affected our estimates of competition between plants. Therefore, it is possible that the impact of IGEs in plots would be higher when plants are grown closer together instead of our rows design.

The overall low to moderate level of competition estimated in our study is in contrast to results comparing performance of spaced plants to sward or plot performance, which tend not to be correlated [13]. As discussed, this could be due to the power of our experiment or due to the field trial design. Increasing the number of plants tested per cultivar would increase power, but that was beyond the scope of the current study. We did attempt to fit all cultivars together in one overall mixed model, which did not converge. Aside from study specific reasons, it is also possible that selection has favoured ryegrass cultivars in which plants are not overly competitive when grown in close proximity. Breeders are encouraged

to select cultivars that perform well and are also unform to be able to register the variety for plant variety rights. Further, limited competition of plants in plots need not be genetically incompatible with plants making use of additional resources when grown separately.

While our study has provided initial information on indirect genetic effects in ryegrass, the results need further confirmation. Further, collecting individual plant phenotypes under competition is not feasible routinely in a commercial setting. The relatively low level of competition also does not support the application of IGE models in breeding programs. Nevertheless, uniformity in plots may be a simple measure to select high yielding non-competitive cultivars. This could also be accomplished with novel phenomics, such as variance of NDVI or, more broadly, variance in predicted biomass per plot.

5.6. Acknowledgements

5.7. References

[1]   https://www.dairyaustralia.com.au/feed-and-nutrition/growing-feed-for-the-herd/growing-pastures/perennial-ryegrass#.YIYQ8_kzY2w

[2]   J. P. Sampoux et al., "Breeding perennial ryegrass (Lolium perenne L.) for turf usage: an assessment of genetic improvements in cultivars released in Europe, 1974–2004", Grass and Forage Science, vol. 68, pp. 33-48, May. 2012.

[3]   https://pasture.io/ryegrass/about-perennial-ryegrass

[4]   B. J. Hayes et al., "Prospects for genomic selection in forage plant species", Plant Breeding, vol. 132, pp. 133-143, 2013.

[5]   P. W. Wilkins and M. O. Humphreys, "Progress in breeding perennial forage grasses for temperate agriculture", The Journal of Agricultural Science, vol. 140, no. 2, pp. 129–150, 2003.

[6]   M. O. Humphreys, "Genetic improvement of forage crops - past, present and future", Journal of Agricultural Science, vol. 143, pp. 441-448, 2005.

[7]   T. H. Meuwissen, B. J. Hayes and M. E. Goddard, "Prediction of total genetic value using genome-wide dense marker maps", Genetics, vol. 157, no. 4, pp. 1819–1847, 2001.

[8]   Z. Lin et al., "Genetic Gain and Inbreeding from Genomic Selection in a Simulated Commercial Breeding Program for Perennial Ryegrass", Plant Genome, vol. 9, no. 1, pp. 1–12, 2016.

[9]   L. W. Pembleton et al., "Exploitation of data from breeding programs supports rapid implementation of genomic selection for key agronomic traits in perennial ryegrass", Theoretical and Applied Genetics, vol. 131, no. 9, pp. 1891–1902, 2018.

[10]   X. Guo et al., "Genomic Prediction in Tetraploid Ryegrass Using Allele Frequencies Based on Genotyping by Sequencing", Frontiers in Plant Science, vol. 9, pp. 1–14, 2018.

[11] M. J. Faville et al., "Divergent Genomic Selection for Herbage Accumulation and Days-To-Heading in Perennial Ryegrass", Agronomy, vol. 10, no. 3, pp. 1–14, 2020.

[12] L. W. Pembleton et al., "Exploitation of data from breeding programs supports rapid implementation of genomic selection for key agronomic traits in perennial ryegrass", Theoretical and Applied Genetics, vol. 131, pp. 1891–1902, 2018.

[13] G. C. Heineck et al., "Relationships and influence of yield components on spaced-plant and sward seed yield in perennial ryegrass", Grass and Forage Science, vol. 75, no. 4, pp. 424-437, 2020.

[14] G. E. Dickerson, "Composition of hog carcasses as influenced by heritable differences in rate and economy of gain", Iowa Agriculture and Home Economics Experiment Station Research Bulletin, vol. 354, pp. 492–524, 1947.

[15] R. L. Willham, "The covariance between relatives for characters composed of components contributed by related individuals", Biometrics, vol. 19, pp. 18–27, 1963.

[16] B. J. Crespi, "The evolution of social behaviour in microorganisms", Trends in Ecology & Evolution, vol. 16, pp. 178–183, 2001.

[17] S. Brotherstone, "Competition effects in a young sitka spruce (Picea sitchensis, Bong. Carr) Clonal Trial", Silvae Genetica, vol. 60, pp. 149–155, 2011.

[18] W. M. Muir, "Incorporation of Competitive Effects in Forest Tree or Animal Breeding Programs", Genetics, vol. 170, no. 3, pp. 1247–1259, 2005.

[19] W. M. Muir and A. P. Schinckel, "Incorporation of competitive effects in breeding programs to improve productivity and animal well-being", Proceedings of the World Congress on Genetics Applied to Livestock Production, vol. 2002, no. 14, pp. 1–4, 2002.

[20] P. Bijma, W. M. Muir and J. A. M. V. Arendonk, "Multilevel Selection 1: Quantitative Genetics of Inheritance and Response to Selection", Genetics, vol. 175, no. 1, pp. 277–288, 2007.

[21] J. W. McGlothlin, "How to measure indirect genetic effects: the congruence of trait-based and variance-partitioning approaches", Evolution, vol. 63, no. 7, pp. 1785-1795, 2009.

[22] A. J. Moore, E. D. Brodie III and J. B. Wolf, "Interacting phenotypes and the evolutionary process: I. direct and indirect genetic effects of social interactions", Evolution, vol. 51, pp. 1352–1362, 2007.

[23] P. Bijma, "A general definition of the heritable variation that determines the potential of a population to respond to selection", Genetics, vol. 189, no. 4, pp. 1347-1359, 2011.

[24] S. Rabab, E. Breen, A. Gebremedhin, F. Shi, P. Badenhorst, Y-P. P. Chen and H. D. Daetwyler, "A New Method for Extracting Individual Plant Bio-Characteristics from High-Resolution Digital Images", Remote Sensing, vol. 13, no. 6, pp. 1–18, 2021.

[25] A. Gebremedhin et al., "Development and Validation of a Phenotyping Computational Workflow to Predict the Biomass Yield of a Large Perennial Ryegrass Breeding Field Trial", Frontiers in Plant Science, vol. 11, pp. 1-16, 2020.

[26] M. M. Malmberg et al., "Genotyping-by-sequencing through transcriptomics: implementation in a range of crop species with varying reproductive habits and ploidy levels", Plant Biotechnology Journal, vol. 16, no. 4, pp. 877-889, 2018.

[27] H. Li, R. Durbin, "Fast and accurate short read alignment with Burrows–Wheeler transform", Bioinformatics, vol. 25, no. 14, pp. 1754–1760, 2009.

[28] H. Shinozuka, N. O. I. Cogan, G. C. Spangenberg and J. W .Forster, "Quantitative Trait Locus (QTL) meta-analysis and comparative genomics for candidate gene prediction in perennial ryegrass (Lolium perenne L.)", BMC Genetics, vol. 13, pp. 1-12, 2012.

[29] D. Money, K. Gardner, Z. Migicovsky, H. Schwaninger, G-Y. Zhong and S. Myles, "LinkImpute: Fast and Accurate Genotype Imputation for Nonmodel Organisms", G3: Genes, Genomes, Genetics, vol. 5, no. 11, pp. 2383-2390, 2015.

[30] A. R. Gilmour et al., "ASReml User Guide", NSW Department of Industry and Investment, Release 3.0, 2009

[31] P. M. VanRaden, "Efficient Methods to Compute Genomic Predictions", Journal of Dairy Science, vol. 91, no. 11, pp. 483-495, Oct. 2014.

[32] P. Pérez and G. d. l. Campos, "Genome-Wide Regression and Prediction with the BGLR Statistical Package", Genetics, vol. 198, no. 2, pp. 4414-4423, Nov. 2008.

[33] A. J. F. Griffiths et al., "An Introduction to Genetic Analysis", The American Statistician, 7th edition, New York: W. H. Freeman; 2000.

[34] L. W. Pembleton et al., "Exploitation of data from breeding programs supports rapid implementation of genomic selection for key agronomic traits in perennial ryegrass", Theoretical and Applied Genetics, vol. 131, no. 9, pp. 1891-1902, 2018.

Chapter 6

General Discussion

Saba Rabab[1,2]

[1]School of Applied Systems Biology, La Trobe University, Bundoora, Australia

[2]Agriculture Victoria, AgriBio, Centre for AgriBioscience, Bundoora, Australia.

This PhD thesis was primarily focused on developing methods to accurately extract in-field phenomics measures for perennial ryegrass and analyse their competition effects for improved genetic gain by incorporating genomic selection (GS). The genomic sub-selection (GSS) field trial data set was used, which contained 50 perennial ryegrass cultivars with replicated rows of 32 plants each. Few images of the GSS trial were available at the beginning of the thesis and processing and the extraction of data from images needed development, which became an important research focus. The images were sufficient to apply precision agriculture strategies for digital phenotyping. The outcomes of this thesis provide insights to automation in ryegrass field trials for digital phenotyping, genomic selection and competition effects among individual plants and its effect on practical ryegrass breeding programmes.

The thesis chapters have evolved from exploiting machine vision strategies for automatic crop row detection to phenomics data extraction that can be applied in commercial ryegrass field trials. First, a novel template free crop row detection algorithm was developed that did not require any pre-known crop information such as crop spacing and number of rows. The proposed algorithm was also robust in varied conditions such as poor illumination, small weed quantity and irregular crop rows (chapter 3). The thesis then further investigated the

extraction of the individual plant phenomics. Therefore, a novel method for extracting

individual plant bio characteristics (plant area and adjusted NDVI) from high quality field trial

images was proposed (chapter 4). The method not only focused on accurate extraction of

regions at the individual plant level, but also effectively linked these regions with individual

plant biomass. The accuracy of the proposed work was verified by correlating harvest plant

biomass with individual plant phenomics (Area, NDVI). The accurate extraction of individual

plant phenomics was essential for genomic prediction of the overall plant performance using

quantitative genetic techniques. Thus, the thesis then further investigated whether there is

competition among individual plants in ryegrass (chapter 5). Furthermore, it was explored

how competition affects the genomic prediction model for predicting genomic breeding

values. The goal was to understand whether there is competition among individual plants and

what role phenotypic variation plays in competition effects.

This general discussion concentrates on four main areas which summarizes each chapter and

discuss both theoretical and practical aspect of the thesis. 1) Machine vision crop row

detection. 2) Extraction of individual plant phenomics. 3) Incorporation of GS models and

competition effects. 4) Further research required to bridge the pheno-geno gap and

competition effects.

6.1. Processing of images for machine vision crop row detection

There has been impressive progress over the time in the development of several genomic

resources that have been practically implemented in crop science for overall improved

genetic gain. However, phenotypic technologies have failed to follow the pace hence we

observe the pheno-geno gap. Therefore, the development of sophisticated techniques for

attainment of quantitative traits is an important research area to explore. In plant breeding,

the generation of high-quality quantitative data needs automation. Automation for high through-put phenotyping is often based on various imaging techniques (discussed in chapter 2 and 3). In this thesis, the software Pix4Dmapper Pro (version 4.3.31 Pix4D, Lausanne, Switzerland, https://pix4d.com) was used for processing of the raw images into ortho-mosaics for applying image analysis techniques. For the attainment of accurate and efficient phenotypic data, the first and foremost step for digital phenotyping was crop row detection in the GSS field trial.

For crop row detection, after the pre-processing of images (image rotation, cropping, noise removal, contrast improvement etc), the fundamental step was the classification of the crop rows. There are several techniques available in literature for crop row classification which are mostly based on template generation and worked under specific circumstances (discussed in literature review). For a binary image with low noise intensity, crop row detection is essentially just connecting the white pixels in the image. However, most of the field trial images are complex and required a novel algorithm that can be applied to these images for crop row detection. Moreover, the motivation was to develop a crop row detection algorithm that is template free and did not require any pre-information (number of crop rows, crop row spacing, etc). The proposed algorithm [1] detected all the crop rows effectively in GSS field trial in which the images were taken from the top view. It also worked effectively when applied to a public data set [2] of 281 images with varied crop conditions (number of rows, spacing, varied weed intensity). To assess the performance of the algorithm, several parameters have been considered one being the accuracy. The accuracy of the proposed algorithm for GSS data set was 87.5% and for public data set of 281 images it was 84%. Another metric, receiver operating characteristic (ROC) graph was also used for the first time (according to my knowledge) in crop row detection. The area under curve (AUC) of 0.98128

of the ROC graphs showed the robustness of the proposed algorithm. The algorithm was also compared with other methods available in literature (chapter3) and proved superior. Computational time is of paramount importance for real time crop row detection system, therefore, the computational time of the proposed algorithm with existing algorithms was compared (Table 3.2) and it outperformed other approaches.

Recently, the development of crop models to capture the quantitative information of crop growth and development have received extensive attention. Crop models have progressively entered the practical application stage. The incorporation of crop functional structure models with machine vision strategies, global positioning system (GPS) technologies, and the Internet of Things would aid in further development of digital agriculture and assist in technical support for modern agriculture [3].

The algorithm proposed in Chapter 3 had a limitation that it needs the approximate intensity of weeds as the only pre-information for accurately detecting crop rows. Also, the performance of the algorithm decreases significantly in case of high weed intensity as it fails to differentiate crop rows from weeds. This problem can be catered for by applying some sort of weed detection algorithm [4-5] first followed by the crop row detection algorithm. However, it proved effective for the GSS field trial by accurately detecting all the crop rows, which was necessary for the next step of individual plant detection.

6.2. Extraction of individual plant phenomics from GSS trial images

The extraction of individual plant phenomics are of importance for automated phenotyping as they aid in investigating family or population uniformity in plant species (inbred and outbred). Finkel [6] proposed that for plant scientists phenomic imaging could shift plant breeding towards hands-free work. This would require an increased number of imaging

based, non-destructive and automatic high-throughput phenotypic data that is accurately acquired and analysed. In image based phenomics research, crop phenotypic data collection is just the first step followed by the extraction of valuable agronomic and physiological traits from image features. Classical image processing pipelines, under controlled conditions, can often provide adequate phenotypic results such as NDVI [7], biomass [8], chlorophyll responses [8] and compactness [9].

The best way to increase crop productivity is genetic improvement by breeding. With the increased and rapid progression in the field of functional genomics and sequencing, an increased number of crop genomes can be sequenced. Consequently, dozens of genes influencing the key agronomic traits have been identified. However, the present genome sequence information has not been fully exploited due to the lack of crop phenotypic data for understanding the complex characteristics of multiple genes [10-11]. Hence, for crop improvement, extraction of automatic, efficient, and accurate phenotypic data that can be linked to genotypic data (at all growth stages) is equally important as crop genomic information [12]. Therefore, in this thesis, I worked on extraction of individual plant phenomics to bridge this pheno- geno gap.

For the extraction of individual plant phenomics, image segmentation was considered. Image segmentation is crucial for distinguishing background from regions of interest, individual plants in my case. There are several image segmentation algorithms available in the literature as discussed in chapter 4. The digital image information extracted can be linked to the plant bio characteristics such as area and NDVI, which can be used to estimate plant biomass yield. Therefore, a new method was proposed [13] that automatically extracted the phenomics traits (NDVI and area) for each plant of the GSS trial. The method was based on the calculation

of centre points and radii of individual plants with the assumption that the structure of individual plants was somewhat circular.

The ryegrass field trial was located in Hamilton, Victoria, Australia (37.8464_S, 142.0737_E) and operated by Agriculture Victoria Research. For the extraction of phenomics traits, an experimental field trial design was used, specifying the layouts for individual rows and individual plants. To measure individual biomass yield, fresh weights for 480 perennial ryegrass plants were collected. Fresh biomass was available for four harvesting dates in different seasons of 2017. Harvest dates were based on the individual plant growth, the two to three leaf stage was taken into consideration as the preferred simulated grazing stage.

There are several methods available in literature for capturing individual plant phenomics as cited in chapter 4. However, none of them were found suitable for my research problem. The phenomics extraction was simple in images with less growth. Nevertheless, identifying the accurate area was not a straightforward task with increased plant growth as plants started merging. Therefore, the proposed algorithm catered to the problems associated with the overgrowth of the plants for accurate NDVI and area estimation. The effectiveness of the proposed algorithm was tested by correlating harvest fresh weights with the extracted phenomics. Pearson correlations (*r*) was used to compare the phenomics metrics. The correlation ranged between 0.63 to 0.75 for the four field trial images for four time points.

In this thesis, the multi-spectral GSS images used had a pixel size of almost 2cm. This was enough to distinguish single perennial ryegrass plants. For the successful deployment of the proposed work to other image data sets, careful consideration of their relative pixel and plant size is required. Furthermore, to detect plant centres, I considered the search space within the bounding box of individual plant and set a numerical threshold for NDVI intensity. This

numerical threshold and other parameters are specific for the image dataset considered in this work and thus should be revisited during application on other image datasets. Another important factor to consider in practical applications is the accurate determination of radii when plants overlap substantially, adding noise and causing some overestimation. The estimation of accurate individual plant (large and overlapped) area and further improvement in correlation could potentially be achieved in future studies by incorporating plant height measures. The height data together with volume and leaf features could provide better and accurate estimation of the individual plant phenotypes. In this thesis, the extracted individual plant bio-characteristics (area and NDVI) provided crucial information at individual plant level to better link phenomics with individual plant genomics.

6.3. Incorporation of GS models and competition effect

Pasture grasses are usually outbreeding which makes each plant genetically unique. Therefore, the phenotypic evaluation at individual plant level may be necessary to understand competition effects and to fully explore the potential of genomic selection (GS) programmes. It is known that yield in spaced plants versus plots is lowly correlated and it is assumed that this is due to plant response when competing for resources [14]. However, it is unknown whether ryegrass plants are competitive or cooperative and highly competitive plants with negative impacts on neighbouring plants would lead to non-uniform growth patterns in the paddock, which is undesirable. Using plant bio characteristics, the thesis then investigated the presence of competition effects in ryegrass plants.

To numerically determine the interactions between individual plants, it was essential to precisely extract the phenotypes of individual plants. In ryegrass each individual plant was genetically unique (perennial ryegrass is outbred) and there were at least four parental

cultivars for each cultivar making them genetically diverse. I have extracted individual plant phenomics from digital perennial ryegrass field data images as discussed in Chapter 4 and the next step was to link these extracted phenotypes with genetic markers to estimate variance components for genomic prediction and direct and indirect genetic effects. There were 2274 individual plants whose 100,530 single nucleotide polymorphisms (SNPs) were available. These plants originated from four cultivars: LP423, LP714, LP730 and LP955.

Genomic Prediction (GP) was used to predict novel phenotypes and a comparison was done between different GP models. For the genomic prediction using best linear unbiased prediction (GBLUP) and Bayesian methods BayesA and BayesB [15], the phenomics of four GSS images taken on four harvesting dates (9th May 2017, 5th July 2017, 11th September 2017 and 20th November 2017) in different seasons of the year 2017 were considered. Further, for phenomics, area and mean NDVI values of individual plants were considered that were extracted from rectangular bounding boxes and circular bounding boxes. The correlation values of genomic prediction for different phenomics assist in determining the best phenomics for genetic gain. The correlation values of circular bounding boxes were better and hence were considered for further analysis to investigate the competition effects in individual ryegrass plants.

For the statistical analysis of competition effects (i.e. indirect genetic effects), the phenomics data were analysed in ASREML using mixed linear models. Moreover, three GBLUP models were examined: 1) GBLUP model without competition effects, 2) GBLUP model with competition effects, but without covariance and 3) GBLUP model with competition effects and covariance. Models 2 and 3 defined the neighbouring plants above and below in the row (25cm distance) in the indirect effects model but did not consider neighbours in separate rows due to them being further away (60cm).

The results demonstrated that all cultivars exhibited negative covariance, but in LP714 significant negative covariance was identified. Therefore, LP714 seemed to exhibit biggest competition effects among all the cultivars. Additionally, to check how much phenotypic variance was explained by genetic effects, heritability was calculated for all the four cultivars. The heritability values for all the cultivars were generally greater than 0.3, demonstrating the direct effects of genetics on phenomics and providing a validation for the phenomics metrics developed. Furthermore, to test the significance of variance and covariance parameter estimates, loglikelihood ratio tests were performed. The difference in models with and without indirect genetic effects (without covariance) were significant for all cultivars demonstrating the significance of the indirect additive genetic effect. Precisely, for LP714, the test statistic between Model 2 and Model 1 was significantly higher (88.12) as compared to the other cultivars.

In this thesis, heritability of the direct effect and genomic prediction accuracy were comparable to normal biomass yield [16]. All three cultivars exhibited competition (negative covariance) but the model with covariance was only significant for LP714 when compared to the competition effects model without covariance. The field trials were designed with a gap of 60cm between rows, therefore, for the interactive behaviour study of individual ryegrass plants only two neighbours (top and bottom) were available. It was possible for plants to avoid each other and still grow large by utilizing resources between rows. Another research direction could be to analyse the plants interactive behaviour in plots when they are grown close together instead of in rows. This would require definition of plot variability phenomics measures.

6.4. Limitations and further research directions to bridge the Pheno-Geno gap

This thesis focused on developing methods for phenomics extraction from high resolution images of perennial ryegrass and analysed competition effects by incorporating genomic selection models. The results were validated with different performance metrics. While the solutions presented according to the research problems are encouraging, there are limitations which could be addressed going forward one being an increased reference population.

Improved genetic gain is the goal of selective breeding in plant populations. The size of the population and population diversity is important to fully exploit the potential of genomic selection. Increased higher reference population size improves the accuracy of Genomic Estimated Breeding Values (GEBVs) for selection candidates and, consequently, individuals can be selected as early as possible. Therefore, larger training populations, and higher marker density are generally required for better accuracy of GEBVs in both self and open pollinated plants. In this thesis, an increased reference population could possibly result in lower standard error therebyimproving correlation between GEBVs and BLUEs and provide a better genomic prediction estimation. Further, ensuring that a higher proportion of plants was genotyped would likely have improved the power of my analyses.

Another limitation was related to the requirement of the bounding boxes for individual plant identification. In this thesis, the bounding boxes for individual plants were necessary especially in timepoints where plants started merging. With the assumption that the individual plant shapes are circular, there are methods available in the literature such as Circular Hough transform and its variants [17-18] that are widely used in many image processing applications for detecting circles. These methods can even detect the irregular

circular shapes. However, they fail to perform effectively when circles started overlapping just like the research problem we addressed. Therefore, a similar method for overlapping plants could be developed. Such methods could potentially provide the boundary of the circles in plant overlapping scenarios, eliminating the need of bounding boxes for individual plants, and making the individual phenomics extraction process for pasture plants more universal.

Further, as the plants age, some die in the middle making it difficult to deploy the proposed algorithm [13] on these sorts of images because the centre point in the proposed algorithm [13] is calculated based on the maximum greenness point. However, this problem can be tackled by applying the reverse methodology for the detection of centre point. Greenness is likely to be at a minimum in the centre of plant and gradually increases towards the plant's edges. Therefore, the centre point should correspond to or near a location of an image pixel with the minimum NDVI value.

Beside these challenges, there are some opportunities to advance plant phenotyping by digital phenotyping. High throughput phenotyping is paramount for improved genetic gain in plant science. However, the implementation of automated phenotyping is still in its infancy [19]. In plant phenotyping, there has been considerable progress in data management. Nevertheless, the routine availability of complex phenotyping data often remain unavailable as there is a lack of standardized format for data handling and storage. Therefore, a major goal in plant sciences is the incorporation of data into searchable and organized data base using the FAIR data (findable, available, identifiable, reusable) principle [20]. The entire data acquisition pipeline including the meta data with clear measurement protocols, sensor calibrations, measurement explanation of the obtained images needs to be standardized to create public data sets that could potentially aid in developing improved phenomics techniques. In the plant science community, MIAPPE (Minimal Information about Plant

Phenotyping Experiments, www.miappe.org) took initiative to standardized data [21-23].

However, it lacked an explicit data model, which left some users struggling in representing

their experiment. Therefore, automation in plant breeding coupled with lack of comparable

standards across phenotyping trials could be addressed for bridging the phenomics-genomics

gap to accelerate genetic gain. It is important to implement standards for generating and

describing the data with adequate meta data to make them available publicly for

implementing novel machine learning techniques for advanced phenotyping [24].

In plant phenotyping, many types of sensors are vital to address varied needs with respect to

targets, ease of operation and accuracy. In the past decade, advancement in the innovative

sensor technologies and phenotyping methods have been proposed [25-26]. Different

sensors are utilized to measure different biochemical traits for phenotyping applications. This

gave rise to two major challenges: cost and data storage problems. Therefore, the fusion into

one smart cost-effective multispectral sensor invention could solve these issues by allowing

real-time and simultaneously retrieval of structural and biochemical traits. There are many

computational challenges in image processing such as the handling of incomplete, noisy,

imprecise, vague, and overloading information [27-28]. However, some computational

techniques, for instance neural networks [29], fuzzy logic [30] and evolutionary methods [31],

have shown promising potential to solve such image processing problems. Also, the systems

capturing real time data are highly sensitive to time factors, so computational delay could

cause significant loss of information that should be addressed. Moreover, for future field

phenotyping, imaging and sensor technologies must be designed to integrate minimal

metadata from the experiment. The process of linking the meta data to sensor data and

transforming it into traits in an automatic way should be investigated for advanced

phenotyping. The developed methods should be inexpensive, user-friendly, robust and applicable to real-world problems which could be a hurdle in automation.

In this research work, the GSS trial was designed in such a way that genotyped varieties are scattered though out the field trial. Moreover, plants in such a setting could potentially had competitive interactions which was investigated in this thesis. However, the field trial was designed with significant gap between individual rows so the competitive interactions (if any) could be only from neighbouring plants (top and bottom). Another research direction could be to analyse the plants interactive behaviour in plots when plants are close together instead of in rows. Further, instead of just using the mean NDVI of individual plants other statistics such as standard deviation and variance across a plot could be used. Moreover, in this thesis only NDVI was used to estimate biomass, other spectral vegetative indices such as the Simple Ratio, Triangular Vegetation Index, Green Normalized Difference Vegetation Index or LiDAR could be used to investigate and compare the results for better estimation of biomass means and variability [32-33]. Another important research area in which initial efforts seems promising [34] but needs significant attention in future field-based phenotyping could be the real time data processing with error free and automated plot detection. The automatic plot detection together with automatic circular plant detection (merged plants) model could potentially be a milestone in field-based plant phenotyping.

Not all plants per cultivar were genotyped, which lead to neighbours of focal plants with missing information in the GBLUP model. However, we know the mean relationships between plants in a cultivar from the off-diagonals of the genomic relationship matrix. It may be possible to assume mean relationships for non-genotyped plants. This would add phenotypes

to the analysis and may increase power. However, it is possible that the genomic relationship matrix may not invert properly as many plants would have the same values for off-diagonals. The main contributions of this thesis were the development of template free crop row detection algorithm to aid in automation in agriculture for smart farming. Another highlight of this thesis was the extraction of individual plant phenomics especially in cases where plants overgrow and start merging. Moreover, the genetic impact of a plant on its neighbour in pasture plants (not known before) was investigated. Individual plant phenomics and genetic markers were used to determine whether these impacts were positive (beneficial) or negative (competitive) through the estimation of indirect genetic effects. The investigation of four ryegrass populations across 9 time points showed that there exist indirect genetic effects and they were negatively correlated with direct effects, showing that ryegrass plants do exhibit competitive behaviour.

6.5. Acknowledgments

6.6. References

[53] S. Rabab, P. Badenhorst, Y-P. P. Chen and H. D. Daetwyler, "A template-free machine vision-based crop row detection algorithm", Precision Agriculture, vol. 22, pp. 124–153, 2021.

[54] I. Vidović, R. Cupec and Ž. Hocenski, "Crop row detection by global energy minimization", Pattern Recognition, vol. 55, pp. 68-86, 2016.

[55] P. Song et al., "High-throughput phenotyping: Breaking through the bottleneck in future crop breeding", The Crop Journal, vol. 9, no. 3, pp. 633-645, 2021.

[56] A. S. M. M. Hasan, F. Sohel, D. Diepeveen, H. Laga, M. G. K. Jones, "A survey of deep learning techniques for weed detection from images", Computers and Electronics in Agriculture, vol. 184, 106067, 2021.

[57] B. Liu and R. Bruch, "Weed Detection for Selective Spraying: a Review", Current Robotics Reports, vol. 1, pp. 19–26, 2020.

[58] E. Finkel, "With 'Phenomics,' Plant Scientists Hope to Shift Breeding Into Overdrive", Science, vol. 325, no. 5939, pp. 380-381, 2009.

[59] D. Leister, "Large-scale evaluation of plant growth in Arabidopsis thaliana by non-invasive image analysis", Plant Physiology and Biochemistry, vol. 37, no. 9, pp. 671-678, 2009.

[60] A. Walter, F. Liebisch and A. Hund, "Plant phenotyping: from bean weighing to image analysis", Plant Methods, vol. 11, no. 14, pp. 1–11, 2015.

[61] J. D. Vylder et al., "Rosette Tracker: An Open Source Image Analysis Tool for Automatic Quantification of Genotype Effects", Plant Physiology, vol. 160, no. 3, pp. 1149–1159, 2012.

[62] C. Shi et al., "Gene regulatory network and abundant genetic variation play critical roles in heading stage of polyploidy wheat", BMC Plant Biology, vol. 19, no. 6, pp. 1–16, 2019.

[63] W. Yao, G. Li, Y. Yu and Y. Ouyang, "funRiceGenes dataset for comprehensive understanding and application of rice functional genes", GigaScience, vol. 7, no. 1, pp. 1–9, 2018.

[64] H. Feng et al., "An integrated hyperspectral imaging and genome-wide association analysis platform provides spectral and genetic insights into the natural variation in rice", Scientific Reports, vol. 7, no. 1, pp. 1–10, 2017.

[65] S. Rabab, E. Breen, A. Gebremedhin, F. Shi, P. Badenhorst, Y-P. P. Chen and H. D. Daetwyler, "A New Method for Extracting Individual Plant Bio-Characteristics from High-Resolution Digital Images", Remote Sensing, vol. 13, no. 6, pp. 1–18, 2021.

[66] G. C. Heineck et al., "Relationships and influence of yield components on spaced-plant and sward seed yield in perennial ryegrass", Grass and Forage Science, vol. 75, no. 4, pp. 424-437, 2020.

[67] T. H. Meuwissen, B. J. Hayes and M. E. Goddard, "Prediction of total genetic value using genome-wide dense marker maps", Genetics, vol. 157, no. 4, pp. 1819–1847, 2001.

[68] L. W. Pembleton et al., "Exploitation of data from breeding programs supports rapid implementation of genomic selection for key agronomic traits in perennial ryegrass", Theoretical and Applied Genetics, vol. 131, no. 9, pp. 1891-1902, 2018.

[69] T. J. Atherton and D. J. Kerbyson, "Size invariant circle detection", Image and Vision Computing, vol. 17, no. 11, pp. 795-803, Sep. 1999.

[70] H. K. Yuen, J. Princen, J. Illingworth and J. Kittler, "Comparative study of Hough Transform methods for circle finding", Image and Vision Computing, vol. 8, no. 1, pp. 71-77, Feb. 1990.

[71] J. Walter et al., "The application of precision phenotyping technologies to a wheat breeding program", GRDC Update Papers, 2007.

[72] M. D. Wilkinson et al., "The FAIR Guiding Principles for scientific data management and stewardship", Scientific Data, vol. 3, pp. 1-9, Feb. 2016.

[73] E. A. Papoutsoglou et al., "Enabling reusability of plant phenomic datasets with MIAPPE 1.1", Scientific Data, vol. 227, no. 1, pp. 260-273, Mar. 2020.

[74] L A-Hernández et al., "Knowledge representation and data sharing to unlock crop variation for nutritional food security", Crop Science, vol. 60, no. 2, pp. 516-529, Mar. 2020.

[75] C. Pommier et al., "Editorial: Phenotyping; From Plant, to Data, to Impact and Highlights of the International Plant Phenotyping Symposium - IPPS 2018", Frontiers in Plant Science, pp. 1-3, Dec. 2020.

[76] S. Tsaftaris, M. Minervini and H. Scharr, "Machine Learning for Plant Phenotyping Needs Image Processing", Trends in Plant Science, vol. 21, no. 12, pp. 989-991, Dec. 2016.

[77] F. Tardieu et al., "Plant Phenomics, From Sensors to Knowledge", Current Biology, vol. 27, no. 15, pp. R770-R783, Aug. 2017.

[78] F. Coppens et al., "Unlocking the potential of plant phenotyping data through integration and data-driven approaches", Current Opinion in Systems Biology, vol. 4, pp. 58-63, Aug. 2017.

[79] K-H. Yap, L. Guan and S. W. Perry, "Adaptive Image Processing: A Computational Intelligence Perspective", CRC Press, Second Edition, 2010.

[80] L. Xing, J. Siebers and P. Keall, "Computational Challenges for Image-Guided Radiation Therapy: Framework and Current Research", Seminars in Radiation Oncology, vol. 17, no. 4, pp. 245-257, Oct. 2007.

[81] H. Azarmdel, A. Jahanbakhshi, S. S. Mohtasebi and A. R. Muñoz, "Evaluation of image processing technique as an expert system in mulberry fruit grading based on ripeness level using artificial neural networks (ANNs) and support vector machine (SVM)", Current Biology, vol. 166, pp. 1-12, Aug. 2020.

[82] A. Soltani, T. Battikh, I. Jabri and N. Lakhou, "A new expert system based on fuzzy logic and image processing algorithms for early glaucoma diagnosis", Biomedical Signal Processing and Control, vol. 40, pp. 366-377, Feb. 2018.

[83] L. Rundo et al., "MedGA: A novel evolutionary method for image enhancement in medical imaging systems", Expert Systems with Applications, vol. 119, no. 15, pp. 387-399, Apr. 2019.

[84] B. P. Banerjee, G. Spangenberg and S. Kant, "Fusion of Spectral and Structural Information from Aerial Images for Improved Biomass Estimation", Remote Sensing, vol. 12, no. 19, pp. 1-22, Sep. 2020.

[85] P. Nguyen et al., "Design of an Unmanned Ground Vehicle and LiDAR Pipeline for the High-Throughput Phenotyping of Biomass in Perennial Ryegrass", Remote Sensing, vol. 13, no. 1, pp. 1-20, Dec. 2020.

[86] B. A. Barrett et al., "Developing new tools for pasture plant breeding", Journal of New Zealand Grasslands, vol. 80, pp. 1-8, Aug. 2018.

Check for updates

A template-free machine vision-based crop row detection algorithm

Saba Rabab[1,2] · Pieter Badenhorst[3] · Yi-Ping Phoebe Chen[4] · Hans D. Daetwyler[1,2]

Abstract

Due to the increase in the use of precision agriculture, field trials have increased in size to allow for genomic selection tool development by linking quantitative phenotypic traits to sequence variations in the DNA of various crops. Crop row detection is an important step to enable the development of an efficient downstream analysis pipeline for genomic selection. In this paper, an efficient crop row detection algorithm was proposed that detected crop rows in colour images without the use of templates and most other pre-information such as number of rows and spacing between rows. The method only requires input on field weed intensity. The algorithm was robust in challenging field trial conditions such as variable light, sudden shadows, poor illumination, presence of weeds and noise and irregular crop shape. The algorithm can be applied to crop images taken from the top and side views. The algorithm was tested on a public dataset with side view images of crop rows and on Genomic Sub-Selection dataset in which images were taken from the top view. Different analyses were performed to check the robustness of the algorithm and to the best of authors' knowledge, the Receiver Operating Characteristic graph has been applied for the first time in crop row detection algorithm testing. Lastly, comparing this algorithm with several state-of-the-art methods, it exhibited superior performance.

Keywords Crop row detection · Perspective projection · Triangular matrix · Accuracy · Complexity

✉ Saba Rabab
  saba.rabab@agriculture.vic.gov.au

1   School of Applied Systems Biology, La Trobe University, Bundoora, Australia

2   Agriculture Victoria, AgriBio, Centre for AgriBioscience, Bundoora, Australia

3   Agriculture Victoria, Hamilton Centre, Hamilton, Australia

4   Department of Computer Science and Information Technology, La Trobe University, Bundoora, Australia

Springer

Introduction

Agriculture is the primary industry sector ensuring food security and underpinning economic growth. Agriculture contributes heavily to different aspects of the personal and collective lives. It is the major source of income in developing countries with almost 70% of the population relying on agriculture (Cervantes-Godoy and Dewbre 2010). Agriculture is the underpinning industry to feed a growing world population and the last billion-dollar industry to be digitized. The advent of newer technologies has led to the next "green" revolution in agriculture allowing for the use of digital technologies to enable genomic selection in outbreeding species, where large-scale phenotyping was a limiting factor. The large data volumes generated by these technologies pose new data analysis challenges. Data extraction requires the identification of crops from background in images, which then enables the application of data in downstream analysis. These processes also need to be implemented in an automated manner so that data processing is fast, accurate and user friendly. The use of automation in agriculture has gained huge attention and has become very beneficial in the last three decades (Katariya et al. 2015; Caldwell 2012).

According to the International Society of Precision Agriculture (https://www.ispag.org), precision agriculture is a management strategy that analyses and processes temporal, spatial and individual data aiming to improve productivity and profitability, while sustaining the quality of the surrounding environment. Machine vision can enhance precision agriculture through digital phenotyping, grading and sorting, machine guidance and livestock identification. The application of machine vision systems in agriculture is increasing over time. A few of the examples of its applications are real-time imaging of crops, management maps, automatic guidance and quality control. High resolution cameras fitted on satellites and drones can assist in detecting the in-field heterogeneous mix of crops, weeds and soil with high precision. They can also be used in weed infested areas of the field to apply herbicides in a targeted manner. Out of the numerous applications of precision agriculture, crop plot and row detection in field trials and extraction of associated data is an important research focus for phenotyping and then genomic selection as it is a crucial step in data extraction. It has attracted numerous studies (Montalvo et al. 2012; Jiang et al. 2016; Ramesh et al. 2016; García-Santillán et al. 2018) working on different aspects of crop row and weed detection. After detecting the rows, the extracted plant data from rows can be used for downstream analysis. For example, plant physical characteristics or phenotypes can be associated with genetic markers in genome-wide association studies and genomic selection (Meuwissen et al. 2001; Visscher et al. 2017). In turn, these analyses can be used to identify plants with an increased genetic potential for productivity and resource use efficiency. While there are several advantages to automatic crop row detection using machine vision, there are also certain challenges, including:

- Outdoor environment conditions: factors like variable light conditions, shadows, complex backgrounds, poor illumination can affect the image quality;
- Confusion of crops with weeds: regular plants and crops can be confused with high density weeds that have similar visual patterns.
- Irregular shape of crops: growth variation of plants and crops resulting in different plant shapes and volumes can lead to false detection.
- Curved and irregular paths: the crop rows can be curved or irregular in shape. Also, the movements of the vehicle in irregular terrain can affect the resulting captured images.

The high-level description of a general crop row detection process is illustrated in Fig. 1. The third step is crop row classification. In the literature, the classification of crop rows often requires known input parameters such as number of rows, spacing between rows and intensity of weeds in a crop image. Furthermore, in some proposals, a template is generated first which is used in the main algorithm. This limits the level of automation and applicability to field trials where the input parameters are varied or unknown and fails when the number of rows, spacing between rows or another parameter varied. Therefore, a robust crop row detection system is required that can be applied to a wide variety of field trials in an automated manner without the need for known input parameters enabling a crop row detection algorithm that caters for the described challenges mentioned above.

The contributions and aims of this study were:

1 Develop a crop row detection algorithm that detects crop rows in colour images without the use of known input parameters relating to the images. The proposed algorithm has been applied on a Genomic Sub-Selection dataset and achieved an accuracy of over 90%.
2 The algorithm must be effective in challenging conditions such as variable light, shadows, poor illumination, presence of weed and noise and irregular shape of crops. We have applied the proposed algorithm on a challenging public dataset (Cupec 2018) and achieved an accuracy of 84%.
3 The algorithm can be applied to crop images which are taken from the top and side views.

A novel method of applying Receiver Operating Characteristic (ROC) curve for the first time (to the best of authors' knowledge) in the testing of a crop row detection algorithm. ROC graphical plot demonstrates the diagnostic ability of a binary classifier system by plotting true positive rate versus false positive rate.

Background

In this section, the major steps of crop row detection will be described as illustrated in Fig. 1.
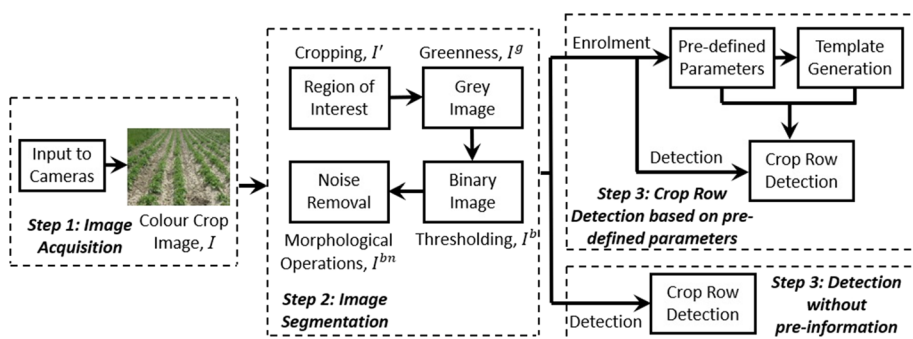

Fig. 1 The high-level description of a general crop row detection process is illustrated. There are three major steps involved in crop row detection; image acquisition, image segmentation and crop row detection

Crop row classification

The most important step is the classification of crop rows. Given the binary image with low noise intensity, it is easy to draw lines on the remaining white pixels detecting the crop rows. However, the images are complex making this step not straightforward. In this section, the different methodologies for the crop row classification will be reviewed.

Hough transform methods

The Hough transform (Hough 1960) was introduced in 1962 for detecting lines, parametric curves and circles. A decade later, it was used in digital images for detecting straight lines. A wheat crop row detecting algorithm has applied the Hough transform to obtain straight lines from binary images after image acquisition and segmentation (Jiang et al. 2016). Vanishing points were used to finally extract the real wheat rows. A high detection rate of up to 90% was demonstrated for the early wheat growth stages. The algorithm cannot detect crop rows in complex conditions, such as large amounts of weeds, sky and end of crop rows. A modified version of the Hough transform, the random Hough transform, was proposed to reduce computational complexity (Ji and Qi 2011). This algorithm was tested on three types of plant density; sparse, general and intensive. The simulation results confirmed that the random Hough transform was adaptive to the different length and volume of the plants as compared to the simple Hough transform. However, the algorithm did not have the capacity to work in complex scenarios such as in the presence of weeds. A comparative study on weed discrimination measured and compared the effectiveness of the developed algorithms (Jones et al. 2009). It was concluded that the results obtained by the Hough transform were better as compared to Gabor filtering. Furthermore, an extension of the Hough transform (Jones et al. 2009) was proposed based on the previous results applied on images from a top view. The Hough transform has also been adapted for autonomous weed detection (Asif et al. 2010). This method was used to calculate the current pose and orientation between the crops. The simulations were conducted with greater than 50% success rate. All Hough Transform methods are limited to straight crop rows and perform poorly in curved rows.

Exploration of horizontal strips

A crop row detection algorithm which removed the image segmentation step significantly reduced the image processing computational burden (Sogaard and Olsen 2003). Prior to the estimation of the row positions, several points indicating row centres were determined. These points were obtained by dividing the greyscale image resulting from colour combination into a number of horizontal strips and subsequently it estimated where the rows intersect each individual strip. The simulation results confirmed an accuracy within the range of ± 6 mm to ± 12 mm depending upon the plant development in the field. However, the algorithm exhibited poor results if there was only one row per image. Moreover, the presence of weeds significantly decreased the accuracy of the algorithm. Another method (Hague et al. 2006) of automated crop and weed monitoring in widely spaced cereal crops transformed the digital images from the camera from RGB to grey. The original image was transformed to grey scale and then divided

into eight horizontal bands. The row spacing in image pixels can be calculated for each of the horizontal bands using a pinhole model of the camera optics. The results of the automated mapping appear to be consistent with manual assessment.

Linear regression

Linear regression can be used for the predictive analysis. A study using linear regression has been used successfully for the development of a vision guidance system in agriculture (Billingsley and Schoenfisch 1997) to detect crop rows. A major drawback of this system was its insensitivity to additional visual noise from weeds. The crops were divided into three crop row segments and in each segment, they used linear regression and a cost function to outline the rows. In Montalvo et al. (2012), linear regression was also applied for the automatic detection of crop rows in maize fields with high weed pressure. After image acquisition and segmentation using an excess green index, the third step was to apply linear regression to obtain the straight-line equations corresponding to the crop rows. However, some prior knowledge was required for crop row detection; the expected location of each row, the number of crop rows and area covered by the digital image. Crop row detection using linear regression without image segmentation can also be done via image analysis.

Blob analysis and stereo-based

Blob (Binary Large OBject) analysis based on the analysis of consistent image regions is a fundamental technique of machine vision (Fontaine and Crowe 2006). Blob analysis identifies the regions of a digital image that have different properties such as colour or brightness compared to their surroundings. A method based on blob analysis for the development of line-detection algorithms for local positioning in densely seeded crops was presented by Fontaine and Crowe (2006). The digital images were first segmented and transformed into binary form. The blob objects with less than 200 pixels were ignored because they can represent noise in the crop rows and therefore the objects with more than 200 pixels are gathered together to form a possible crop row. After the identification of all blobs, their locations for centre of gravity and angles of the principal axes were calculated. Stereo vision generally refers to the perception of depth and three-dimensional structure. The method (Fontaine and Crowe 2006) showed poor results when applied to real crop fields as compared to laboratory images due to less information in crop field images than laboratory images. Furthermore, the discontinuity between the crop rows impacted the value of accuracy of the algorithm. An effective and robust stereovision-based crop row detection method for tractor-automated guidance (Kise et al. 2005) encompasses stereo-image processing functions for elevation map creation and navigational point determination. From the digital image taken from a stereovision camera, a three-dimensional crop elevation map was generated first and then optimal navigation points from the map were generated. This method was deployed in a soya bean field for the testing of crop row detection (Kise and Zhang 2008) with promising results. The extensions of this work by the same authors are presented by Kise and Zhang (2008) and Rovira-Más et al. (2008) for three-dimensional crop row structure mapping and guidance.

Other methods

K-Means clustering for spectra (which was further improved by spatial methods) was used for the detection of crop rows by Ramesh et al. (2016). A combination of clustering and linear regression methods (Jiang et al. 2015) was used for the automatic detection of crop rows based on multiple regions of interest. Crop row detection has also been done with the help of accumulation of green image pixels (Jiang et al. 2015). Other than straight line rows, the proposed algorithm can determine curved crop rows as well as irregular inter-row spaces. The simulations showed good results in terms of accuracy and computational complexity. Vertical projection in combination with a Hough transform has been employed (Jiang et al. 2015) for a machine vision-based crop rows detection. In this algorithm, the first two steps of image acquisition and image segmentation were the same as performing a Hough transformation except for a vertical projection being applied before the use of the Hough transform for crop row detection. The algorithm was only compared with the standard Hough transform and therefore it is difficult to comment on the superiority and effectiveness of the algorithm. An unmanned aerial vehicles guidance system using crop row detection and line follower algorithms was developed by Basso and Freitas (2019). The algorithm has two parts; one for crop row detection, which was responsible for the correct identification of the crop rows and a second for Line Filter that was responsible for generating the driving parameters sent to the flight controller. It was claimed that the crop row detection algorithm had an accuracy of 100%. However, the image data considered was simple to process and essentially free of weeds. Another method for crop row detection in unmanned aerial vehicles images was developed by Bah et al. (2019). The images were taken from the top view instead of side view. Convolution neural networks were employed to increase the accuracy rate of crop row detection. However, with these networks, the computation time was very high making them less suitable for real-time applications. Crop row detection by global energy minimization was proposed by Vidović et al. (2016). Dynamic programming was employed to detect both straight and curved crop rows. Their experiments demonstrated that the proposed method outperformed the other methods considered for straight crop row detection. However, a template was generated based on the pre-information prior to the detection stage making it not suitable for all crop fields.

One of the common drawbacks in the above-mentioned methods is the need for important information such as number and spacing of rows prior to the implementation of crop row detection algorithms. Also, in some proposals, a template was generated first to be used in crop row detection. This implies that there is no single algorithm that can be applied to each crop field. In this paper, a crop row detection algorithm was proposed that does not require pre-information such as number and spacing of rows and therefore can be applied to a wider variety of crop fields.

Methods

The proposed algorithm was applied to a public data set (Vidović et al. 2016). The complete evaluation image set contained 281 images and is available from their web page (Cupec 2018). The images contained a varied number of crop rows, varied spacing and
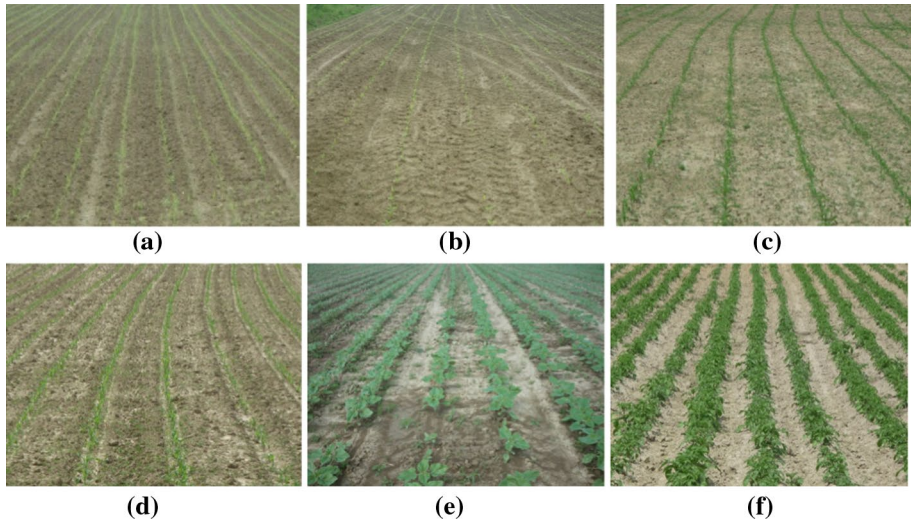
Fig. 2 a–f A small sample of six images of the public dataset available at Vidović et al. (2016). These images have a varied number of crop rows, varied spacing and varied weed intensities. The original resolution of images were 2560×1920 pixels and then resized to 320×240 pixels

varied weed intensity. The images were originally captured at resolution 2560×1920 pixels and then resized to 320×240 pixels. This subsampling reduced the required computation time without significant loss of information for the purposes of crop row detection. A small sample of six down-sized images of this dataset is shown in Fig. 2. In the next subsections, all the steps in the proposed crop row detection algorithm will be explained and the resulting images will be showed to aid the reader's understanding of the process.

Identification of greenness

Let the original colour image be denoted as I^o with X number of image pixel rows, Y number of pixel columns and Z number of frames. Let $I^o(x, y, z) \in [0, 255]$ be a grey value of an image pixel of image I^o at xth row, yth column and zth frame. There are three frames in a colour image; red, green and blue. Let R_f, G_f and B_f represents red, green and blue frames of I^o, respectively. Furthermore, $R_f(x, y)$, $G_f(x, y)$ and $B_f(x, y)$ represent the grey values of these individual frames respectively at the xth row and yth column. The greenness in I^o was identified using the following equation (Burgos-Artizzu et al. 2011):

$$I^g(x, y) = 1.262 * G_f(x, y) - 0.884 * R_f(x, y) - 0.311 * B_f(x, y),$$

$$\forall x \in \chi, \chi = [1, X], \forall y \in \mathcal{y}, \mathcal{y} = [1, Y], \tag{1}$$

where, I^g is a grey image whose pixels with greater intensity represents the green pixels of I^o. Figure 3a–f illustrates the greenness of Fig. 2a–f when Eq. (1) is applied.
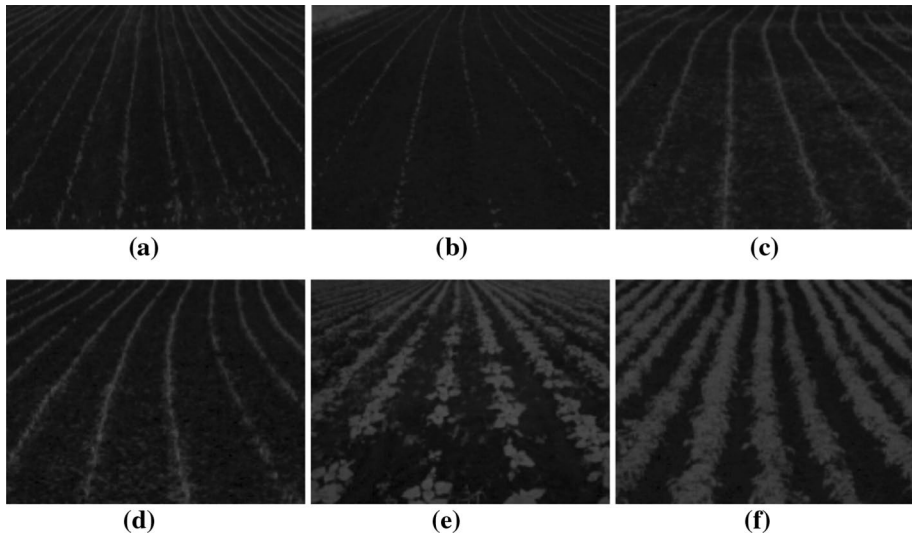
Fig. 3 a–f Identification of greenness using Eq. (1) applied on images shown in Fig. 2a–f. Degree of pixel whiteness indicates the level of greenness and black pixels represent the background
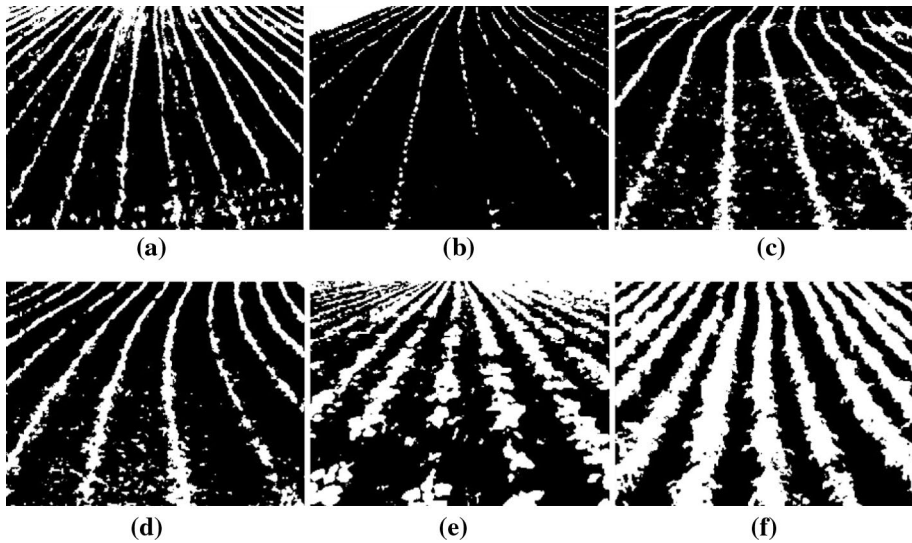

Fig. 4 a–f Binary images resulting from Otsu binary thresholding on images shown in Fig. 3a–f respectively. The white pixels represent the greenness and black pixels represent the background

Grey to binary

The grey image whose values $\in [0,255]$ highlighted the greenness can be converted into binary image with only two grey values $\in [0,1]$; white (binary value: 1), which represented the greenness and black (binary value: 0), which represented the background. The Otsu binary thresholding (Otsu 1979) was employed to automatically perform clustering-based image thresholding returning a value of threshold, th_{Otsu}. The binary image I^b was obtained using the following:

$$I^b(x,y) = \begin{cases} 1 & if \;\; I^g(x,y) > th_{Otsu}, \\ 0 & otherwise, \end{cases} \quad \forall x \in \chi, \chi = [1,X], \forall y \in \acute{y}, \acute{y} = [1,Y].$$

(2)

The Otsu binary image thresholding was applied on Fig. 3a–d and results are shown in Fig. 4a–f.

Removing smaller objects

While the binary images successfully identified crop rows, weeds were also identified because of their green colour. Weeds should not be classified as crops and must be removed from the image before identifying rows. To do so, an algorithm was developed based on arithmetic operations. It was assumed that weeds are usually smaller binary objects compared to connected crop row binary objects. A binary object is shown in Fig. 5.

Let a binary object be denoted as $B_i, \forall i \in$, Ń, Ń = [1, 2, ... , N], where, N was the total number of binary objects in an image. The number of rows in B_i was denoted as X_i and number of columns was denoted as Y_i.

First, the mean of each binary object was calculated using the following:

$$A_i = \sum_x^{X_i} \sum_y^{Y_i} I^b(x,y), \qquad \forall i \in \grave{N},$$

(3)

Fig. 5 A binary object which is a collection of white pixels connected with each other. The number of rows in B_i is denoted as X_i and number of columns is denoted as Y_i
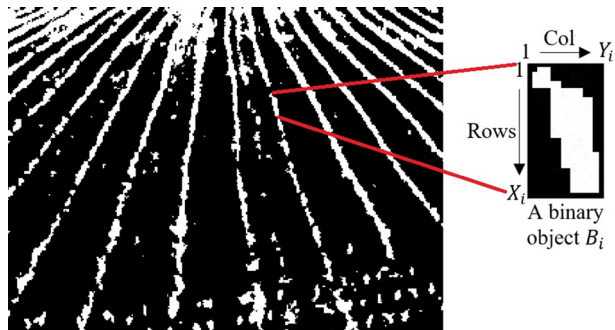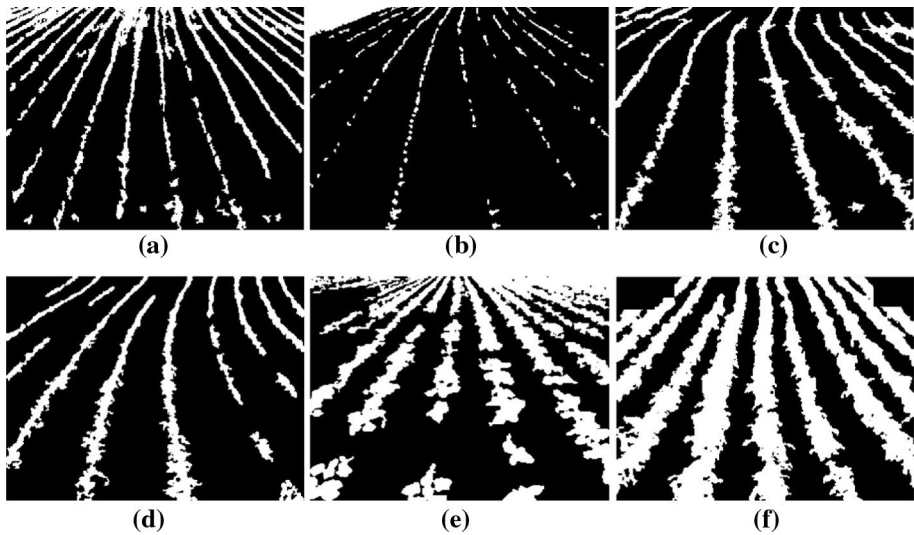
Fig. 6 a–f Binary images with smaller binary objects (assumed to be weeds) removed using Algorithm 1

where, A_i was the area of binary object B_i. Then the mean size of all objects' areas, M was calculated as:

$$M = \frac{\sum_i^N A_i}{N}. \tag{4}$$

The smaller binary objects can be eliminated if the area of the individual binary object was less than the half of the mean area across all objects, that is:
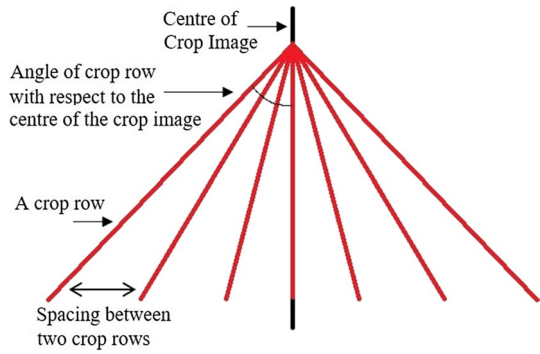
$$I^b(x, y) = 0, if A_i < M/2,$$

$$I^b(x, y) = 0, \qquad if\ A_i < M/2, \tag{5}$$

$$\forall x \in \chi_i, \chi_i = [1, X_i], \forall y \in y_i, y_i = [1, Y_i], \forall i \in \grave{N}, \grave{N} = [1, N].$$

The threshold of half of the mean was set based on the authors' own testing on the observed database. It can be adjusted based on the intensity of weeds in a crop field. This is the only parameter that should be known prior to the implementation of the developed algorithm. The elimination of smaller binary objects is shown in Algorithm 1 and the resulting images of applying this process on images in Fig. 4a–f are shown in Fig. 6a–f. Most of the smaller objects, which represent weeds (noise), have been eliminated and the larger binary objects remaining primarily identified the crop rows.

Fig. 7 The perspective projection of crop rows. The projection is from the side view of the crop field

Centre of Crop Image

Angle of crop row with respect to the centre of the crop image

A crop row

Spacing between two crop rows

Algorithm 1. The process of eliminating smaller binary objects from the binary image.

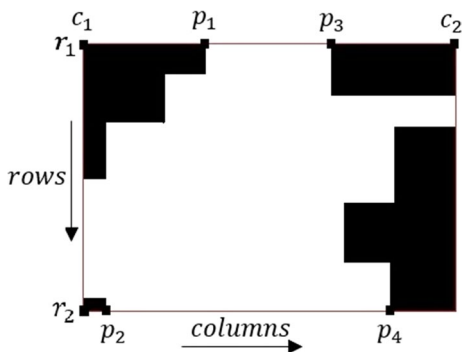**Inputs:** Binary image, I^b, binary objects, B_i, $\forall i \in \hat{N}, X_i, Y_i$.

Outputs: Binary image with reduced smaller binary objects, I^b.

1:     $for\ i\ =\ 1{:}\,N$

2:         $A(i)\ =\ Area(I_i^b)$

3:     $M\ =\ mean(A)$

4:     $for\ i\ =\ 1{:}\,N$

5:         $if\ A(i) < M/2$

6:             $for\ x\ =\ 1{:}\,X_i$

7:                $for\ y\ =\ 1{:}\,Y_i$

8:                    $I^b(x,y) = 0$

Fig. 8 The bounding box of a binary object

c_1 p_1 p_3 c_2

r_1

$rows$

r_2

p_2 $columns$ p_4

Joining row objects

Once smaller binary objects have been removed, the remaining binary objects belonging to the same crop row must be joined. To perform this step, it was important to understand the perspective projection of crop rows (Vidović et al. 2016; Pajares et al. 2016; Romeo et al. 2012) shown in Fig. 7. The projection was from the side view of the crop field. The crop rows were straighter in the middle of the crop image and started tilting while moving towards the other side of the crop image. In other words, the angle of crop rows with respect to the centre of the crop image increased moving away from the centre of the crop image. Furthermore, the spacing between the crop rows was at the maximum at the bottom of the crop image and decreased while moving upward. The following subsections will explain the systematic joining of binary crop row objects.

Bounding box and columns point of row objects

The first step was to identify the bounding box of each binary object (Fig. 8) with respect to original crop image dimensions and to identify its column and row points. In Fig. 8, c_1 and c_2 represent the starting and ending column points of binary object, respectively and r_1 and r_2 represent the starting and ending row points of binary object, respectively. In the same figure, p_1 and p_2 represent the starting column points of first and last row of the object respectively and p_3 and p_4 represent the ending column points of first and last row of the object, respectively. These points will assist in determining the location of the binary object with respect to the column position of the original crop image.
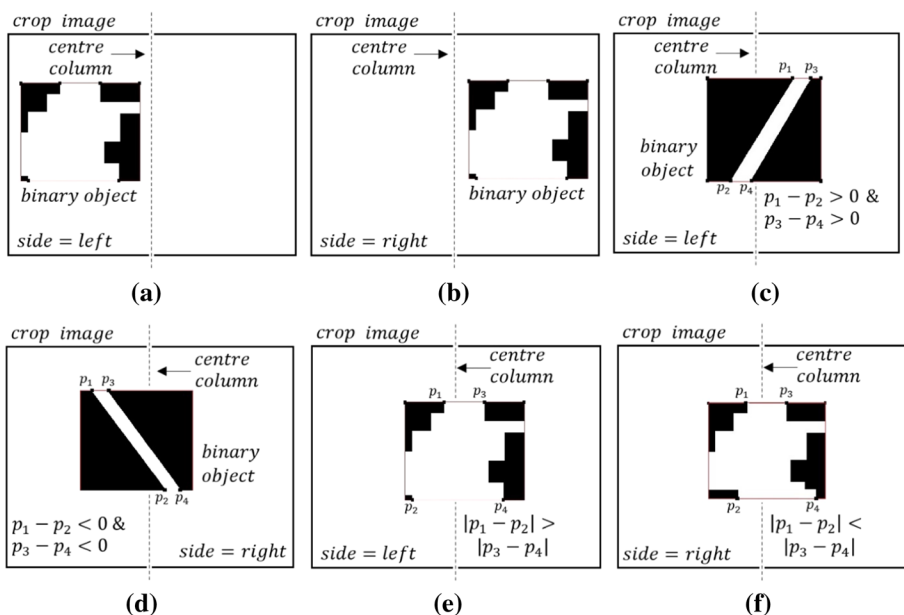

Fig. 9 Determination of the location of binary object with respect to the centre column of the crop image. **a, b** The objects are completely on one of either side. **c–f** The decision is based on points p_1, p_2, p_3 and p_4. Based on the differences of p_1 and p_2 and p_3 and p_4, the side will be determined

Determining the side of the object

Regarding the perspective projection of crop rows, the next step was to find the side of the binary object with respect to the centre column of the crop row image, that is, whether the object was left or right of centre in the crop row image. If the object did not overlap with the centre (i.e. it is full on one side), its location was clear (Fig. 9a, b). However, if the object overlapped the centre column then its location will be determined based on points p_1, p_2, p_3 and p_4. If the binary object was tilted towards the right side of the crop image, or if the differences of both p_1 and p_2 and p_3 and p_4 were positive, then the object was declared to be on the left side as shown in Fig. 9c and vice versa for objects tilted towards the left of the centre (Fig. 9d). Furthermore, if the difference of p_1 and p_2 was positive and the difference of p_3 and p_4 was negative or vice-versa, then its location was based on the absolute value of the difference. If the absolute value of the difference between p_1 and p_2 was greater than the absolute value of the difference between p_3 and p_4, then the location of the object was defined as left, otherwise right as shown in Fig. 9e and f, respectively. Absolute values were taken to determine the width of image pixels. If the width of image pixels between the points p_1 and p_2 was greater than the width of image pixels between the points p_3 and p_4 then the location of the object was defined as left, otherwise right. The process in the form of an equation is given below:

$$Side = \begin{cases} Left \ if \left(c_1 < centre \& c_2 < centre\right), \\ Right \ if \left(c_1 > centre \& c_2 > centre\right), \\ \begin{cases} Left \ if \left(p_1 - p_2 > 0 \& p_3 - p_4 > 0\right), \\ Right \ if \left(p_1 - p_2 < 0 \& p_3 - p_4 < 0\right), \\ \begin{cases} Left \ if \left(|p_1 - p_2| > |p_3 - p_4|\right), \\ Right \ if \left(|p_1 - p_2| \le |p_3 - p_4|\right), \end{cases} \end{cases} \end{cases}$$

(6)

where, *centre* was the centre column of the crop image and & represented the logical AND operator.

Creating a triangle matrix

The objective was to connect binary objects that belonged to the same row. To achieve that, after determining the side, the next step was to create a triangular matrix of ones. A triangular matrix was created based on respective location and size. The size was defined as a square matrix using the row position of the binary object (r_1). The size of the triangular matrix was greatest for an object located at the bottom of the crop image and decreased as the object's position moved towards the top of the crop image. Specifically, the size (sz) of the triangular matrix was determined as:

$$sz = \left\lceil s_{min} + \left(\frac{s_{max} - s_{min}}{X - 1}\right)(r_1 - 1) \right\rceil,$$

(7)

where, s_{min} and s_{max} were the minimum and maximum sizes of the triangular matrix with $s_{min} = 2$ and $s_{max} \approx 0.5 * X$, r_1 represented the starting row point of binary object and $\lceil \cdot \rceil$ was a ceiling function. Equation (7) mapped the row range $\in [1, X]$ to triangular matrix sizes $\in [s_{min}, s_{max}]$. The left matrix, mat_L was created as:
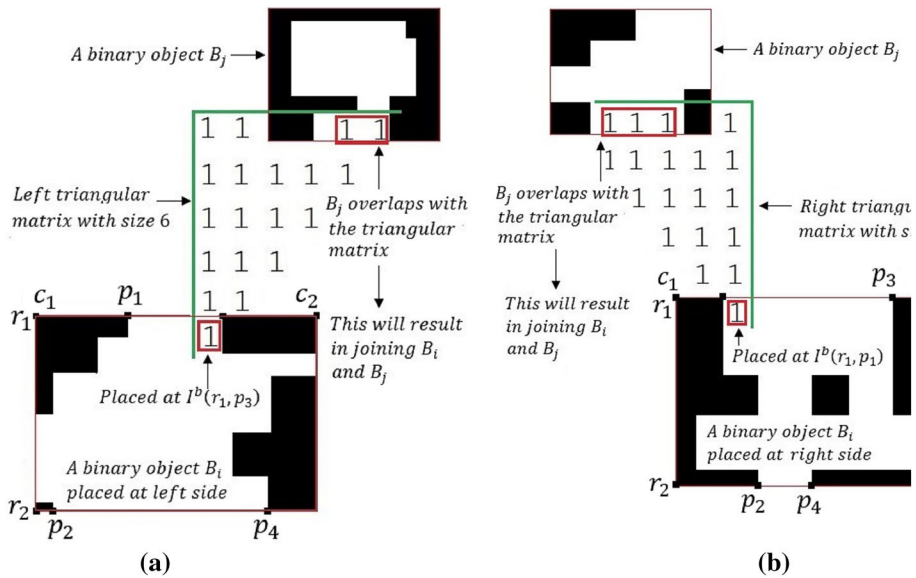
(a)   **(b)**

Fig. 10 Two examples of joining two binary objects with each other. **a** A binary object, B_i placed at the left side of the centre of the column. A left triangular matrix of size 6 is placed at $I^b(r_1, p_3)$ which overlaps with the other binary object, B_j results in joining B_i and B_j. **b** A binary object, B_i placed at the right side of the centre of the column. A right triangular matrix of size 6 is placed at $I^b(r_1, p_1)$ which overlaps with the other binary object, B_j results in joining B_i and B_j

(a)   **(b)**   **(c)**
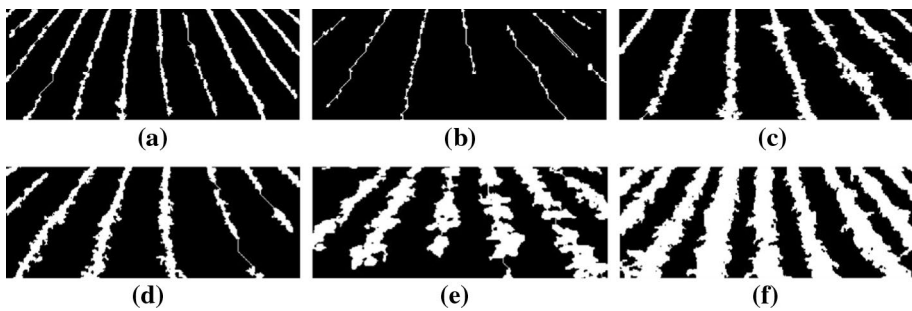
(d)   **(e)**   **(f)**

Fig. 11 **a–f** The results of joining binary objects applied on the crop images illustrated in Fig. 6a–f. The images, however, are cropped from the top side and the bottom side to improve the efficiency and effectiveness of the proposed algorithm. The effects of joining objects can be visualised in (**a**), (**b**), (**d**) and (**e**). The crop rows in (**c**) and (**f**) are already connected and therefore the impact of this step is not highlighted

$$mat_L(a,b) = \begin{cases} 0 \ if \ a+b-1 > sz, \\ 1 \ otherwise, \end{cases} \forall a,b \in S, S = [1, sz]. \tag{8}$$

Similarly, the right matrix, mat_R was created as:

$$mat_R(a,b) = \begin{cases} 1 \ for \ a \le b, \\ 0 \ for \ a > b, \end{cases} \forall a,b \in S, S = [1, sz]. \tag{9}$$

Joining objects

The triangular matrix and binary object information was used to connect row binary objects. The principle was that if two binary objects (B_i and B_j) were close enough to potentially lie on the same crop row then these two binary objects should be joined. To see whether B_i and B_j should be connected, first, the triangular matrix was placed on top of the binary object, B_i. For an object located at the left side of the crop image, the triangular matrix was placed at $I^b(r_1, p_3)$ and for an object located at the right side of the crop image, the triangular matrix was placed at $I^b(r_1, p_1)$. As the binary object consisted of a collection of ones and so does the triangular matrix, this will temporarily create one big binary object. This big binary object for the left triangular matrix is given as:

$$I^b(x', y') = I^b(x, y)|mat_L(a, b),$$
$$x' \in X_i', X_i' = [r_1 - sz + 1, r_2],$$
$$y' \in Y_i', Y_i' = [c_1, p_3 + sz - 1], \tag{10}$$

where, | represented the logical OR operator. Similarly, the big binary object for the right triangular matrix is given as:

$$I^b(x', y') = I^b(x, y)|mat_R(a, b), x' \in X_i', X_i' = [r_1 - sz + 1, r_2], y' \in Y_i', Y_i' = [p_1 - sz + 1, c_2] \tag{11}$$

If this big binary object, $I^b(x', y')$, overlapped with any other binary object, let say B_j then the triangular matrix was removed and B_i and B_j were connected. Two examples of joining two binary objects with each other is shown in Fig. 10a and b. The pseudo-code for joining row objects is shown in Algorithm 2.

Images in Fig. 11a–f demonstrated the joined objects. The images, however, were cropped from the top side as the crop rows were almost merged into each other and therefore it was unnecessary to detect crop rows at the top side. Moreover, once the crop rows were identified in the middle of the image, they can be extended towards the top and bottom of the image. Furthermore, for this step, the images were also cropped at the bottom to reduce the computational complexity and to increase the accuracy of the proposed algorithm. It is to be noted that the crop rows will always be straight at the bottom of the crop image irrespective of the fact that the crop rows are curved at the top. Therefore, cropping images from the bottom will not introduce any error or false information. Binary objects were not joined if the distance between them was more than sz, irrespective of the fact that both binary objects belonged to the same row. This situation could be seen in the sixth and seventh crop rows of Fig. 11b, where binary objects of the same row cannot be joined as the distance between them was greater than sz.

Algorithm 2. The whole process of joining row objects in form of a pseudocode.

Inputs: Binary image, I^b, binary objects with bounding boxes, $B_i, p_1, p_2, p_3, p_4, r_1, r_2, c_1, c_2 \ \forall i \in N, X_i, Y_i, s_{min}, s_{max}$.

Outputs: Binary image with connected binary objects, I^b.

1: $for \ i = 1:N$

2: $\quad side = side\_det(p_1, p_2, p_3, p_4, r_1, r_2, c_1, c_2)$

3: $\quad size = size\_det(r_1, r_2, s_{min}, s_{max})$

4: $\quad matrix = triangular\_matrix(side, size)$

5: $\quad I^b = joining \ objects(I^b, matrix, B_i, B_j)$

Extending longer objects

The next step was to extend those objects whose vertical length (number of pixel rows) was more than 70% of X, if objects beyond this threshold would all be crop rows. The 70% is based on hit and trial. This step was applied to all binary objects except those that were full crop rows. A binary object was classified as a full crop row based on the following:

$$Object_{row} = \begin{cases} complete & if\left(\left(r_1 = 1 \& r_2 = X\right)\middle|r_1 = 1 \& c_1 = 1\middle|\left(r_1 = 1 \& c_2 = Y\right)\right), \\ not\ complete & otherwise. \end{cases}$$

(12)

The incomplete rows were extended by considering the bounding box of the binary object, where p_1 represented the column of the first image pixel (white) of the first row and p_3 represented the column position of the last image pixel (white) of the first row. Applying this to the other rows, let l_2^i represent the column position of the first image pixel (white) of the second row of ith binary object and q_2^i represent the column position of the last image pixel (white) of the second row of ith binary object. For simplicity and clarity, write p_1 as l_1^i and p_3 as q_1^i. Continuing this, consider a vector L^i, which consists of all the l_t^i values of all the rows of ith binary object and consider a vector Q^i, which consists of all the q_t^i values of all the rows of the ith binary object, where, $t = [1, r_2 - r_1 + 1]$, such that, $L^i = [l_1^i, l_2^i, \ldots, l_{r_2 - r_1 + 1}^i]$, $Q^i = [q_1^i, q_2^i, \ldots, q_{r_2 - r_1 + 1}^i]$. The mean or the values of the middle columns of these vectors were placed in a vector, $U = [\mu_1, \mu_1, \ldots, \mu_{r_2 - r_1 + 1}]$ whose values were calculated as:

$$\mu_t = \left\lceil \frac{l_t^i + q_1^i}{2} \right\rceil, \forall t = [1, r_2 - r_1 + 1].$$

(13)

Also, add r_1, r_2 into vector, $\gamma = [r_1, r_2]_{1 \times r_2 - r_1 + 1}$. Fitting a polynomial of curve to the vector in a straight line with degree one;

$$\beta = polyfit(U, \gamma),$$

(14)

where, *polyfit*(.) is a function requiring vectors U and y and return the slope *sl* and y-intercept, *int* of a straight line. Using β, those objects can be extended whose length is more than 70% of X as follows:

$$\begin{cases} c_i^* = sl * r_i^* + int, \forall r_i^* = [1, r_1], \text{if} r_1 \neq 1, & (15a) \\ c_i^* = sl * r_i^* + int, \forall r_i^* = [r_2, X], \text{if} r_2 \neq X. & (15a) \end{cases}$$

$$\begin{cases} I^b\left(r_i^*, c_i^*\right) = 1, \forall r_i^* = [1, r_1], & (16a) \\ I^b\left(r_i^*, c_i^* - 1\right) = 1, \forall r_i^* = [1, r_1], & (16b) \\ I^b\left(r_i^*, c_i^* + 1\right) = 1, \forall r_i^* = [1, r_1]. & (16c) \end{cases}$$

$$\begin{cases} I^b\left(r_i^*, c_i^*\right) = 1, \forall r_i^* = [r_2, X], & (17a) \\ I^b\left(r_i^*, c_i^* - 1\right) = 1, \forall r_i^* = [r_2, X], & (17b) \\ I^b\left(r_i^*, c_i^* + 1\right) = 1, \forall r_i^* = [r_2, X]. & (17c) \end{cases}$$

Extending other row objects

The last step was to extend the remaining objects if they belonged to a crop row. The decision that these remaining objects belong to a row or not was based on the minimum distance of the columns between the objects considered as the full crop rows. A binary object as a full crop row is given in Eq. (12). Let say there were N^* number of full rows in I^b. For each full row, first, the vectors, L^i and Q^i were determined. Let put L^i and Q^i, $\forall i \in [1, N^*]$ of all the full rows in a single matrix, $\mathbf{L}$ and $\mathbf{Q}$. $\mathbf{L}$ and $\mathbf{Q}$ were two matrices whose columns correspond to the individual values of L^i and Q^i for each of the full rows respectively. These matrices are given as:

$$\mathbf{L} = \begin{bmatrix} l_1^1 & l_1^2 & \cdots & l_1^{N^*} \\ l_2^1 & l_2^2 & \cdots & l_2^{N^*} \\ \vdots & \vdots & \ddots & \vdots \\ l_X^1 & l_X^2 & \cdots & l_X^{N^*} \end{bmatrix}_{X \times N^*}, \tag{18}$$

Fig. 12 Distance in terms of columns between two consecutive full crop rows for all the full crop rows. In the image, there are $N^* = 3$ full crop rows and 6 image rows
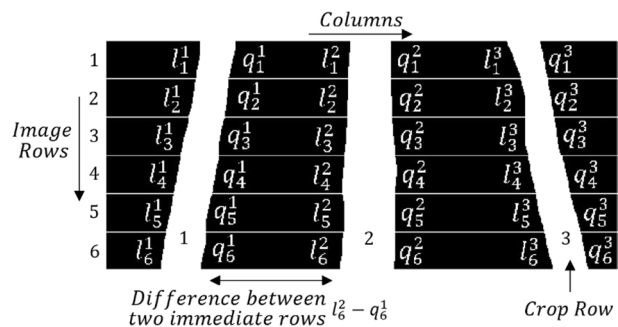
$$\mathbf{Q} = \begin{bmatrix} q_1^1 & q_1^2 & \cdots & q_1^{N^*} \\ q_2^1 & q_2^2 & \cdots & q_2^{N^*} \\ \vdots & \vdots & \ddots & \vdots \\ q_X^1 & q_X^2 & \cdots & q_X^{N^*} \end{bmatrix}_{X \times N^*}, \tag{19}$$

where, X was the length of each of the column of $\mathbf{L}$ and $\mathbf{Q}$ even though the individual length of these columns depended on the values of r_1 and r_2 of the individual binary objects. However, the actual values remained the same and the length was still $r_2 - r_1 + 1$ for the individual binary objects. The rest of the elements were assigned with the value zero.

The next step was to determine the distance in terms of columns between two consecutive full crop rows for the whole image. This is illustrated in Fig. 12, in which there are $N^* = 3$ full crop rows and 6 image rows (this is a small example to explain the process, the public dataset (Vidović et al. 2016) considered here has 240 image rows in each crop image). The distance between two consecutive crop rows for all the full crop rows was determined and placed in a matrix, $\mathbf{D}$ and given as:

$$\mathbf{D} = \begin{bmatrix} l_1^2 - q_1^1 & l_1^3 - q_1^2 & \cdots & l_1^{N^*} - q_1^{N^*-1} \\ l_2^2 - q_2^1 & l_2^3 - q_2^2 & \cdots & l_2^{N^*} - q_2^{N^*-1} \\ \vdots & \vdots & \ddots & \vdots \\ l_X^2 - q_X^1 & l_X^3 - q_X^2 & \cdots & l_X^{N^*} - q_X^{N^*-1} \end{bmatrix}_{X \times N^*-1}. \tag{20}$$

The next step was to find the minimum of distance of each row of $\mathbf{D}$, as below:

$$\mathbf{D}_{min} = \left[\min(l_t^2 - q_t^1, l_t^3 - q_t^2, \ldots, l_t^{N^*} - q_t^{N^*-1}) \right]_{1 \times X}, \forall t = [1, X]. \tag{21}$$

$\mathbf{D}_{min}$ was a vector whose individual values, $d_{min}^t, t \in [1, X]$, were for all the image rows and corresponded to the minimum and *standard* distance between two consecutive crop rows.

This $\mathbf{D}_{min}$ was used in determining the other binary objects as the crop rows. This process was repeated for each binary object for the decision. If the difference between
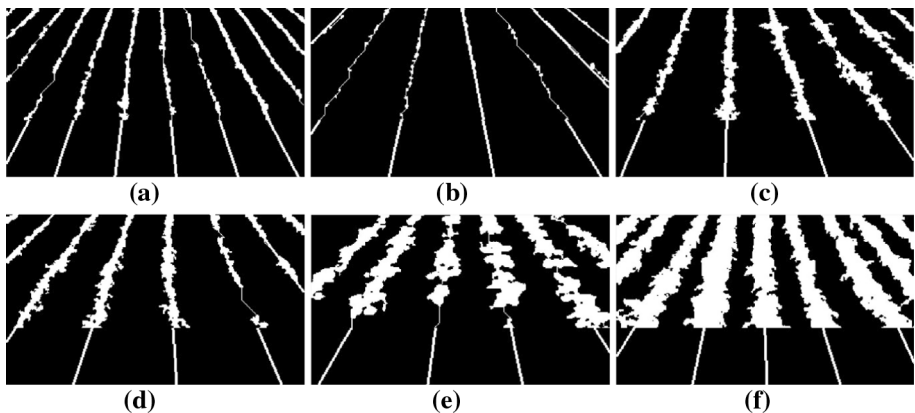

Fig. 13 a–f The results of extending binary objects applied on the crop images illustrated in Fig. 11a–f. The binary objects shown in these images only represent the completely detected crop rows

Table 1 Values of the input parameters used for the experiments

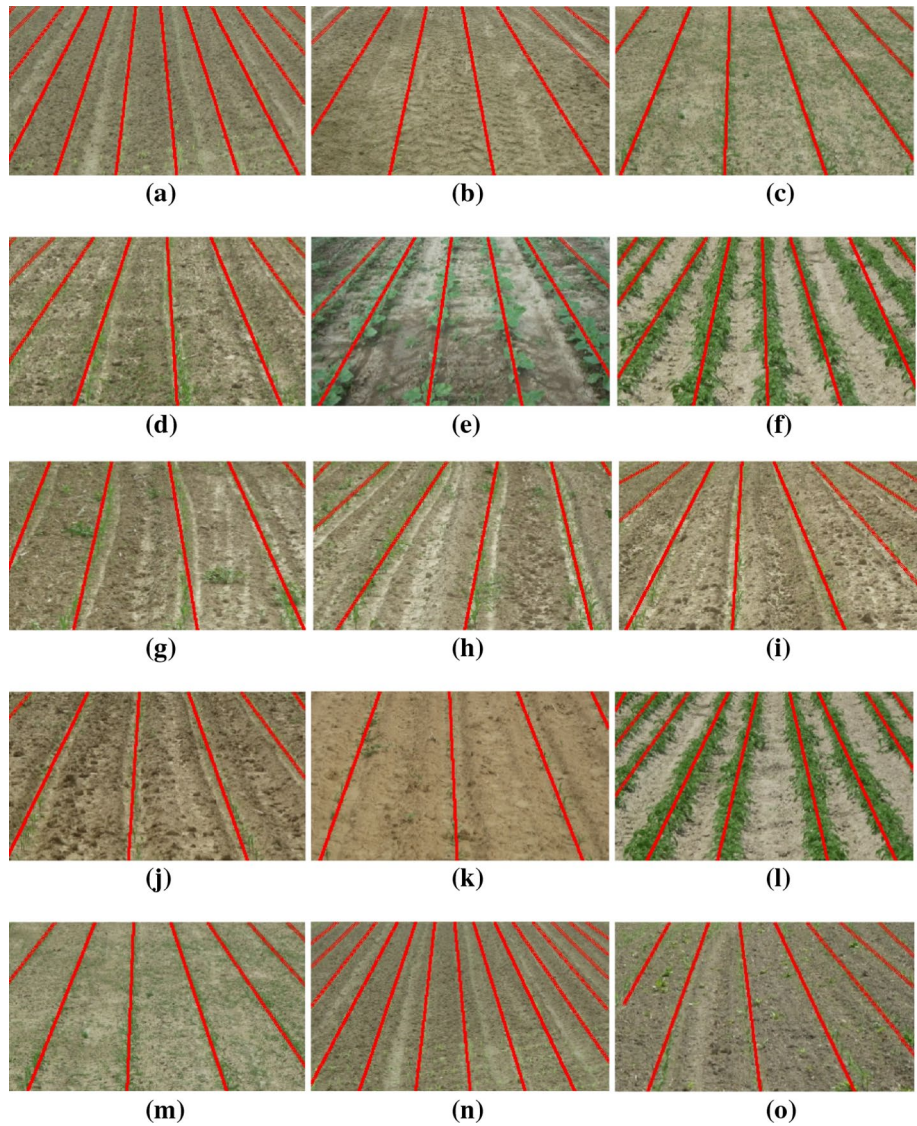| Parameter	Value	Parameter	Value
s_{min}	2	th_{dis}	0.30
s_{max}	20	th_{count}	0.50

Fig. 14 a–o A few of the results of the proposed algorithm applied to the images of the dataset (Vidović et al. 2016). The images in (a–f) are the same as considered in Fig. 13a–f

the distance and D_{min} was small enough, then the binary object was considered as the part of a potential crop row otherwise that binary object was deleted.

Let say a binary object, B_j has $L^j = [l_1^j, l_2^j, \ldots, l_{r_2-r_1+1}^j]$ and let compare its distance with the next immediate full crop row which has $Q^i = [q_1^i, q_2^i, \ldots, q_{r_2-r_1+1}^i]$. The comparison will be between each element of L^j and each element of Q^i. A temporary variable was taken and initialized to zero, i.e. $count = 0$. The comparison is given as:

$$count = count + 1, \, if \, \left| l_t^j - q_t^i \right| < th_{dis} * d_{min}^t, \quad \forall t \in [1, r_2 - r_1 + 1], \tag{22}$$

where, th_{dis} was the distance threshold or a percentage tolerance level. The accuracy or number of truly detected crop rows can be increased with the increase in th_{dis}, but this would also increase the falsely detected crop rows. Finally, the object was determined as a crop row based on the following check:

$$object = part \, of \, crop \, row, if \, count > th_{count} * (r_2 - r_1 + 1), \tag{23}$$

where, th_{count} was the count threshold or a percentage tolerance level. If the $count$ was greater than a user defined fraction of the length of the binary object, then the binary object was considered as a potential part of a crop row otherwise this binary object would be deleted. The accuracy or number of truly detected crop rows can be increased with the decrease in th_{count}, however, at the same time, this would also increase the falsely detected crop rows.

The results of this step applied on the images illustrated in Fig. 11a–f are shown in Fig. 13a–f. Also, these images were extended to the bottom of the crop images to negate the effect of cropping done earlier.

Results

The proposed algorithm was applied on a public data set (Vidović et al. 2016), which consisted of 281 images and can be downloaded from their web page (Cupec 2018). The parameters used in these results are mentioned in Table 1. The values of th_{dis} and th_{count} are fixed
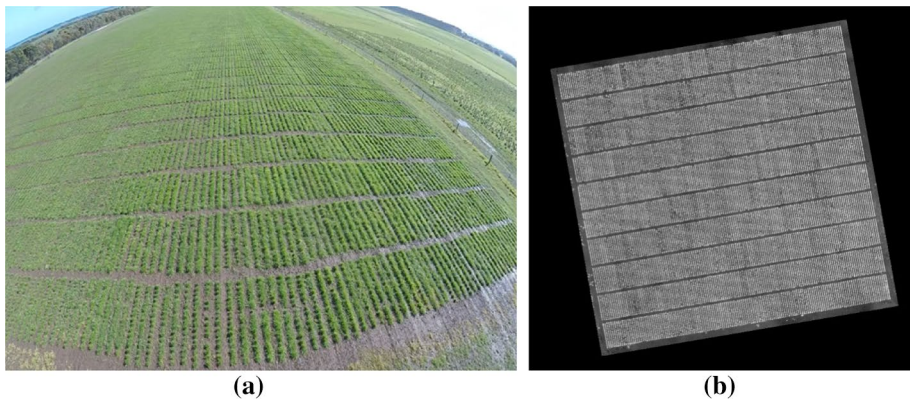

Fig. 15 An example of GSS field trial in colour form is shown in (**a**) and a grey frame of a GSS image is shown in (**b**). The white pixels in (**b**) represent greenness in GSS image and black pixels represent background. In (**b**), there are 10 major crop rows and in each major crop row, there are 150 minor crop rows for a total of 1500 crop rows (Color figure online)
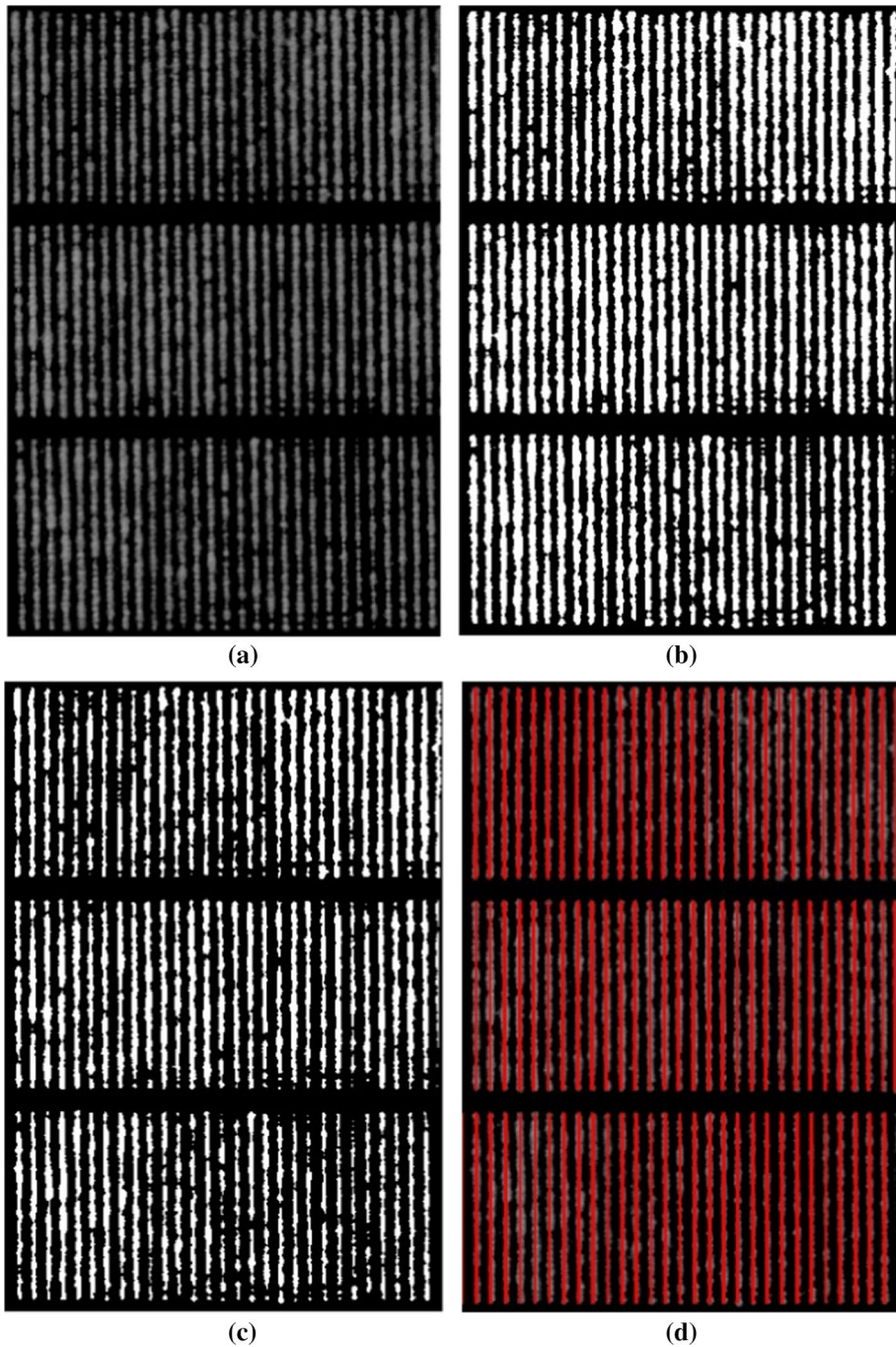
Fig. 16 **a** A sub-part of Fig. 15b which is cropped and rotated into a rectangular form. **b** The result of Otsu binary thresholding applied on (**a**). **c** The result of binary erosion applied on (**b**) by *st* in which the binary objects have been shrunk. **d** Detected crop rows marked in red (Color figure online)

and should remain the same for testing on other image databases as well. However, to test the robustness of the developed algorithm, the values of these two thresholds can be tuned to see the values of false positive rates and true positive rates as explained later. Similarly, as mentioned earlier, $s_{min} = 2$ and $s_{max} \approx 0.5 * X$. The value of s_{max} considered for the observed image database is 20 and should be changed for other image databases depending upon the size of images. As an example, some of the results of the proposed algorithm on the images are shown in Fig. 14a–o, in which crop rows are shown in red.

As is apparent from the figures, the proposed algorithm is robust and can detect any number of crop rows with any spacing between them. The rare limitation of the proposed algorithm is that it requires the spacing between the crop rows to be reasonably consistent. The effects of this limitation can be seen in Fig. 15e, in which one row cannot be detected (a small row at top left) and in Fig. 15f where one false crop row is detected.

Genomic Sub-Selection (GSS) dataset

Beside the image dataset taken from the perspective projection, the algorithm was tested in the Genomic Sub-Selection (GSS) image dataset in which images were taken from the top view. The GSS trial contains 50 perennial ryegrass cultivars with an aim to enable genomic selection (Meuwissen et al. 2001) analyses grown in replicated rows of 32 plants each. The aims of these field trials were the development of phenomic processing pipelines to define novel traits, the estimation and prediction of hybrid vigour and inclusion of single plant competition effects in genomic selection. An example colour image of the GSS field trial is shown in Fig. 15a and a grey frame of a GSS image is shown in Fig. 15b. Images were taken with a GoPro Hero 4 (GoPro, San Mateo, CA, USA) deployed on a 3DR Solo quadcopter (3D Robotics, Berkeley, CA, USA).

The proposed algorithm for crop row detection was modified to be applied on the GSS images. A geo-rectified ortho-mosaic image (Fig. 15b) was created with Pix4D (Pix4D SA, Prilly, Switzerland) software. The image was geo-rectified with the aid of 12 ground control points distributed across the GSS field trial. The ortho-mosaic was cropped and rotated. For illustration purposes, only a sub-section of the whole trial is shown in Fig. 16, but the algorithm was applied on the entire picture.

The grey image was converted into binary using the same Otsu binary thresholding (Otsu 1979) mentioned earlier (Fig. 16b). The weeds or noise in these images was minimal and, therefore, the step of removing smaller objects could be ignored. However, some crop rows were overlapping as can be seen in the first major crop row of Fig. 16b. To shrink or thin these overlapped crop rows, the binary image erosion was used (Gonzalez and Woods 2018). Binary image erosion removes image pixels from the boundaries of the binary image with the help of a pre-defined structuring element. Let take I^b as a binary image shown in Fig. 16b. The image erosion applied on I^b with the help of a structuring element st is given by (Gonzalez and Woods 2018):

$$I^b \ominus st = \left\{ z | (st)_z \cap I^{b^c} \neq \emptyset \right\}, \tag{24}$$

where, $\ominus$ was a binary image erosion of st on I^b, z was a translation vector (z_1, z_2), $(st)_z$ was translation of st by point $z = (z_1, z_2)$, $\cap$ was an intersection or logical AND operator, $(.)^c$ was a compliment or logical NOT operator and $\emptyset$ was an empty set. The Eq. (24) can also be stated as:

$$I^b \ominus st = \bigcap_{z \in st} I^b_{-z}, \tag{25}$$

where, I^b_{-z} represented the translation of I^b by $-z$. The structuring element st used in this work is a square of 1 s of size 4.

The result of binary erosion applied on Fig. 16b by st is shown in Fig. 16c and the binary objects have been shrunk.

Once the objects are eroded, the next step was to extend them using the process mentioned above. However, due to the image being taken from top view, the extension of the binary objects was best done by placing a rectangular shape object over the top of the binary objects. Furthermore, the crop rows are disconnected due to the major crop row sections. Thus, there are intended gaps between the major crop rows and must be classified before the crop row detection. The gaps were labelled as black rows identified with the help of following:

$$row_i = black \text{ if } \sum_{j=1}^{Y} I^b(i,j) < th_{row\_gap} * Y, \forall i \in [1, X] \tag{26}$$

where, th_{row_gap} was a threshold for the row gaps. The accuracy or number of truly detected crop rows can be increased with the increase in th_{row_gap}. However, this will also increase the number of falsely detected rows. The gaps between the minor crop rows can be identified as black columns with the help of the following:

$$column_j = black \text{ if } \sum_{i=1}^{X} I^b(i,j) < th_{col\_gap} * X, \forall j \in [1, Y] \tag{27}$$

where, th_{col_gap} was a threshold for the column gaps. The accuracy or number of truly detected crop rows can be increased with the increase in th_{col_gap}. However, at the same time, this will also increase the falsely detected crop rows. Once the black rows and columns were classified, the rest of the spaces belonged to the crop rows. These crop rows were labelled with the red marker depicting the detected crop rows as shown in Fig. 16d. The values of both th_{row_gap} and th_{col_gap} in the experiments were set to 0.1. The accuracy achieved for GSS dataset is over 90%.

Fig. 17 **a** A crop image having eight crop rows. **b** A crop row image with one false detected row (non-crop row)
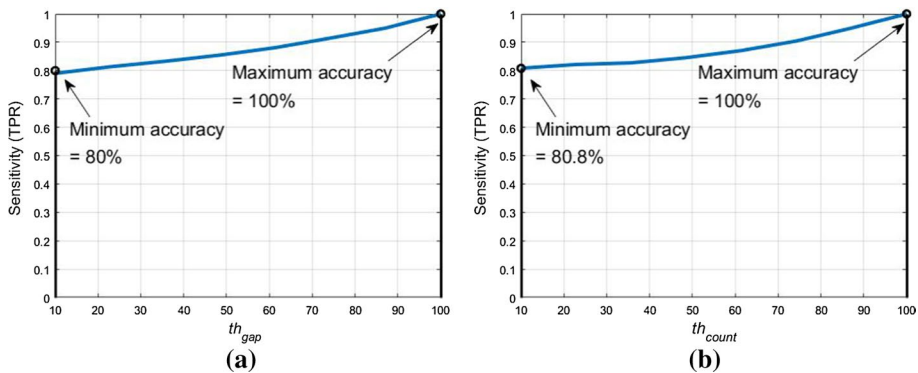
Fig. 18 **a** The graph of sensitivity against the input parameter of th_{gap} for the range between 10% (0.10) and 100% (1.00) keeping the other input parameters constant mentioned in Table 1

Performance evaluation

To evaluate the performance of the proposed algorithm, several parameters were considered. To the best of the authors' knowledge, one of them, the Receiver Operating Characteristic, was used for the very first time in assessing the performance of any crop row detection algorithm. These parameters are explained in line with the proposed algorithm as follows:

Accuracy

In crop row detection, accuracy is the measure of percentage of detected rows in a crop row field. To declare a detected crop row as an actual row, the detected crop row was compared with the crop row of the ground truth image. A ground truth image was created with the help of an expert who defines the actual crop rows in an image. The ground truth images can be created with the help of software (Vidović et al. 2016); in that case, the expert defines two or more points lying on a crop row in a test image and the developed software automatically generates a smooth curve passing through these points. The same procedure was undertaken for the adjacent crop row in the image. According to these two curves representing midlines of two adjacent crop rows, the curves for the remaining crop rows in the image are reconstructed. Or, the ground truth images can be manually generated by the expert specifying all the crop rows.

To check whether a detected row was the actual row or not, different parameters can be used for the validation of a crop row such as distance/deviation or the length of the detected row. In terms of distance, the difference between the position of the detected crop row and the actual crop row of the ground truth image should be less than the specified threshold to be accepted as an actual crop row. Furthermore, the detected row can be declared as the actual row if the length of the detected row was close to the length of the actual crop row of the ground truth image.

The proposed algorithm was applied with the input parameters mentioned in Table 1. As stated earlier, accuracy gives the percentage of detected crop rows in an image. For instance, in Fig. 17a which represented a crop image having eight crop rows, the algorithm

detected seven crop rows and, therefore, the accuracy in this case was $7/8*100\% = 87.5\%$. For the public dataset (Vidović et al. 2016), the accuracy of the proposed algorithm was nearly 84%.

Limitations of the accuracy criterion

Accuracy alone is not enough to test the robustness of the algorithm. For instance, in the same crop image shown in Fig. 17a, if the algorithm has detected seven actual crop rows and one false row as shown in Fig. 17b, the accuracy is still 87.5%. Therefore, other parameters need to be considered to comment on the robustness of the crop row detection algorithm.

Receiver operating characteristic (ROC) graph

The problem with the accuracy mentioned before can be resolved with the ROC analysis. It has been applied in various applications, from medicine to computer science, in applications like face recognition, image hashing and many others. However, in crop row detection, to the best of the authors' knowledge, ROC analysis has been applied here for the very first time. ROC has four parameters:

True positive rate

True positive rate (*TPR*) is the number of correctly detected rows. It is equivalent to the accuracy mentioned earlier. In the example shown in Fig. 17a, seven out of eight crop rows are detected and therefore, in this case, $TPR = 7/8$.
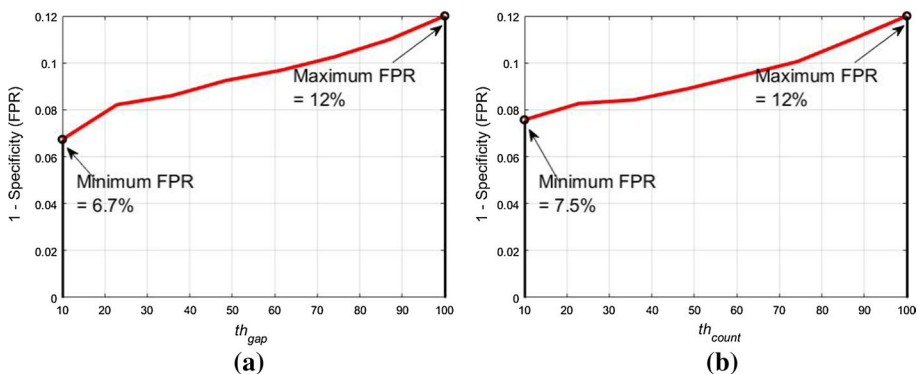

Fig. 19 a The graph of *FPR* against the input parameter of th_{gap} for the range between 10% (0.10) and 100% (1.00) keeping the other input parameters constant mentioned in Table 1

False negative rate

False negative rate (*FNR*) is the number of not correctly detected rows. In the same example shown in Fig. 17a, one out of eight crop rows are not detected and therefore, in this case, $FNR = 1/8$. Also, $FNR = 1 - TPR$.

True negative rate

True negative rate (*TNR*) is the number of correctly detected non-crop rows. Let say, there are ten positions in a crop image where there is no crop row and if the algorithm detects eight positions as non-rows position, then $TNR = 8/10$.

False positive rate

False positive rate (*FPR*) is the number of incorrectly detected non-crop rows. Let say, in the same example given in *TNR* case, if the algorithm cannot detect two positions as non-rows position, then $FPR = 2/10$. Also, $FPR = 1 - TNR$. *TPR* and *FPR* have been considered to comment on the robustness of the crop row detection algorithm; the remaining two parameters are their reciprocal. For the public dataset (Vidović et al. 2016), using the same input parameters mentioned in Table 1, the *TPR* is about 84% and the *FPR* is 6%. However, these values are just for the individual values of the input parameters. The interest is in observing the inclusive performance of the algorithm when certain input parameters, such as th_{dis} and th_{count} are varied from minimum to maximum values. Based on the overall performance of the algorithm one can set the appropriate input parameters which suit the real-time application.

Sensitivity

Sensitivity is the measure of the proportion of actual positives that were correctly identified. This is equivalent to the *TPR* observed over a range of a certain input parameter. Figure 18a shows the graph of sensitivity against the input parameter of th_{gap} for the range between 10% (0.10) and 100% (1.00) keeping the other input parameters constant as
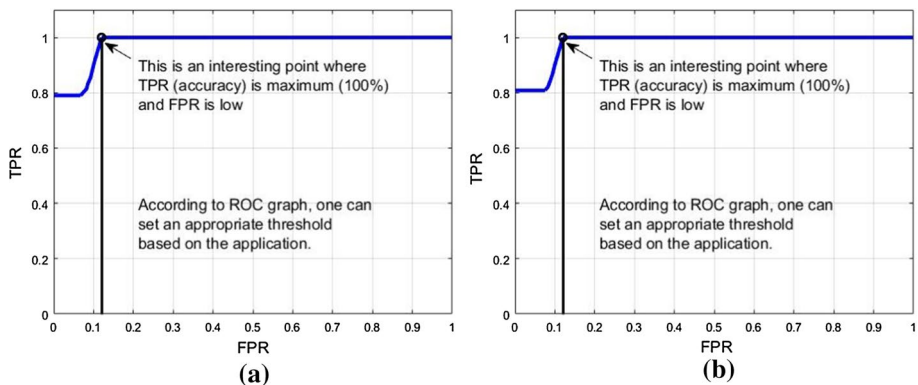

Fig. 20 **a** ROC graph considering th_{gap}. The *FPR* is plotted on the x-axis and *TPR* is plotted on the y-axis. **b** ROC graph considering th_{count}

Table 2 Comparative results of accuracy of the proposed algorithm with other published studies. Accuracy of other methods were directly taken from their respective publications

Methods	Accuracy (%)
Linear regression (Montalvo et al. 2012)	57.2
Hough transform (Bakker et al. 2008)	62.2
Hough transform with template (Bakker et al. 2008)	67.9
Template matching followed by global energy minimization (Vidović et al. 2016)	73.7
Proposed	84.0

mentioned in Table 1. The minimum accuracy is 80% at $th_{gap} = 0.10$ and starts to increase as th_{gap} increases. Finally, the accuracy is at its maximum when $th_{gap} = 1.00$. Similarly, Fig. 18b shows the graph of sensitivity against the input parameter of th_{count} for the range between 10% (0.10) and 100% (1.00) keeping the other input parameters constant as mentioned in Table 1. The minimum accuracy is 80.8% at $th_{count} = 0.10$ and starts to increase as th_{count} increases. Finally, the accuracy is maximum at $th_{count} = 1.00$. By looking at these graphs, one can say that the values of th_{gap} and th_{count} should be set to 1.00 to achieve the maximum accuracy. However, at these values, the *FPR* is also maximum, as explained in the next section.

Specificity

Specificity is the measure of the proportion of actual negatives that are correctly identified. This is equivalent to *TNR* or $1 - FPR$ observed over a range of a certain input parameter.
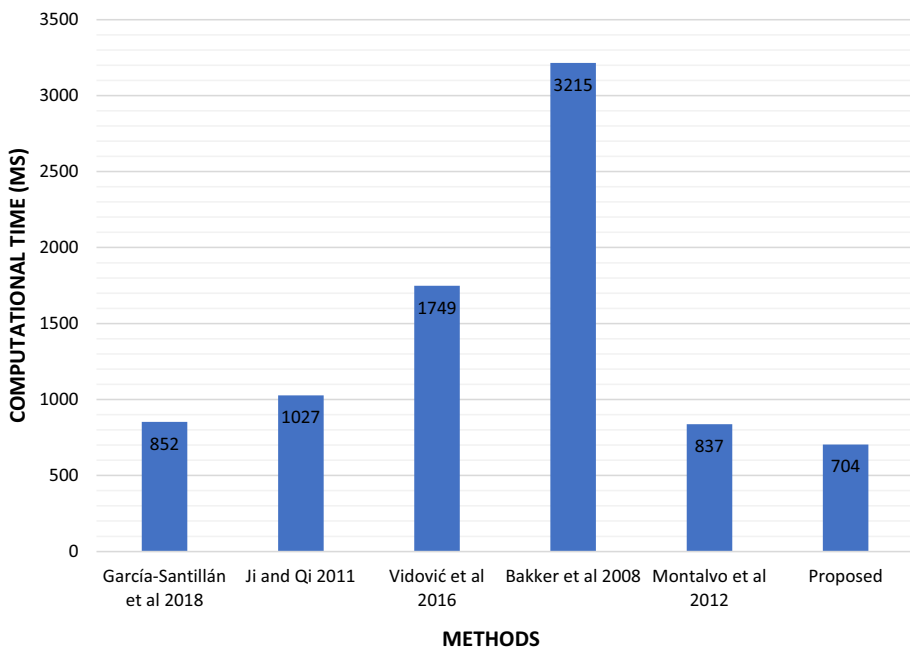

Fig. 21 Computational time for algorithms

The graphs of specificity can be shown to illustrate the actual negatives that are correctly identified or the actual negatives which are not correctly identified. Figure 19a shows the graph of 1-specificity (*FPR*) against the input parameter of th_{gap} for the range between 10% (0.10) and 100% (1.00) keeping the other input parameters constant as mentioned in Table 1. The minimum value of 1-specificity (*FPR*) is 6.7% at $th_{gap} = 0.10$ and increases as th_{gap} increases. Finally, the value of 1-specificity (*FPR*) is at its maximum (12%) when $th_{gap} = 1.00$. Similarly, Fig. 19b shows the graph of 1-specificity (*FPR*) against the input parameter of th_{count} for the range between 10% (0.10) and 100% (1.00) keeping the other input parameters constant as mentioned in Table I. The minimum value of 1-specificity (*FPR*) is 7.5% at $th_{count} = 0.10$ and starts to increase as th_{count} increases. Finally, the value of 1-specificity (*FPR*) is maximum (12%) at $th_{count} = 1.00$. By looking at these graphs, one can say that the values of th_{gap} and th_{count} should be set to 0.10 to achieve the minimum *FPR*, however, at these values, the *TPR* or accuracy is also minimum. There is a trade-off between *TPR* and *FPR*. Therefore, one must set the appropriate values of these thresholds according to the requirement of the real time applications. To adopt the appropriate values of these thresholds, a comparison of *TPR* and *FPR* is given, in terms of a ROC graph, as explained in the next section.

ROC graph

A ROC graph can be used to see the relation between *TPR* and *FPR*, to choose an appropriate value of the input threshold and to observe the robustness of the algorithm. Figure 20a shows a ROC graph considering th_{gap}. When *FPR* is minimum (0–6.7%), the *TPR* is 80% and then increases to a maximum (100%) when *FPR* is 12%. In some applications, this can be an interesting point because the accuracy is at its maximum and *FPR* is very low. However, in applications where t minimum *FPR* is the priority, this point with a specific value of th_{gap} cannot be used. According to the need of the application, one can set an appropriate value of th_{gap}. To check the performance of the algorithm, the area under curve (AUC) of the ROC graph is calculated. In an ideal scenario, the AUC is 1 and the algorithm is considered as robust if AUC is close to 1. For Fig. 20a, the value of AUC is 0.98125 demonstrating the robustness of the proposed algorithm. Similarly, Fig. 20b shows a ROC graph considering th_{count}. When *FPR* is minimum (0–7.5%), the *TPR* is 80%. The *TPR* starts to increase after that point and becomes a maximum (100%) when *FPR* is 12%. The AUC of 0.98128 shows the robustness of the proposed algorithm.

Comparison with other algorithms

To compare the proposed algorithm, the parameter accuracy was sub-optimal, because it differs from study to study. Furthermore, the standards, environment and assumptions deployed in other studies differ from the current study. For instance, in other studies, the number and spacing of crop rows in an image were known, in contrast to this investigation. Therefore, the accuracy of the results was compared with other studies considering the same image database (Cupec 2018). The other methods were Hough Transform (Bakker et al. 2008), Hough transform with Template (Bakker et al. 2008), Linear Regression (Montalvo et al. 2012) and Template Matching followed by Global Energy Minimization (Vidović et al. 2016). There were 34 images taken with straight crop rows as Hough Transform and Linear Regression can only detect straight rows. The results of accuracy of the

proposed algorithm with comparisons to the other methods are shown in Table 2 depicting the superiority of the proposed method. Also, the computational time of algorithms was compared. As crop row detection may be applied in real time, computational time is very important. For example, the vision system deployed on a moving vehicle must process the captured images (or frames of video), show the resulting images and perform pre-defined tasks on them before capturing the next images. It was required that the computational time is less than or equal to the time spent between the acquisition of two (or set of) images to synchronize with the hardware platform. Figure 21 shows the comparative results of computational time of the proposed algorithm and that of other studies. Metrics were normalized based on the system specifications and size of the images used in each study. It was shown that the proposed algorithm has faster performance than the other algorithms.

Conclusions

This paper proposed a new crop row detection algorithm that does not require pre-information such as number of crop rows and spacing between crop rows. The only information the algorithm needs is the approximate intensity of weeds. Furthermore, there is no need for a template to be used in the detection stage. Therefore, the proposed algorithm can be applied to a wide variety of crop fields. The crop row detection phenotype data can be used for downstream analysis such as genomic selection or for the development of phenomic processing pipelines to define novel traits.

The proposed algorithm for detecting crop rows involved various image processing operations, such as identification of greenness, binarization and binary image erosion. Besides these basic operations, the proposed algorithm utilized the perspective projection of crop rows to identify the row objects. These objects of a same row are then connected with each other and extended using the triangular matrices. The proposed algorithm can also be applied to the images taken from the top view with some modifications. Like all new proposals, it is strongly encouraged to do the analysis of the algorithm before its immediate deployment. The algorithm could potentially be extended to identify weeds in crop fields.

Compliance with ethical standards

Conflict of interest There is no conflict of interest to declare.

References

Asif, M., Amir, S., Israr, A., & Faraz, M. (2010). A vision system for autonomous weed detection robot. *International Journal of Computer and Electrical Engineering, 2*(3), 486–491.

Bah, M. D., Hafiane, A., & Canals, R. (2019). CRowNet: Deep network for crop row detection in UAV images. *IEEE Access, 8,* 5189–5200.

Bakker, T., Wouters, H., Asselt, K. V., Bontsema, J., Tang, L., Müller, J., et al. (2008). A vision-based row detection system for sugar beet. *Computers and Electronics in Agriculture, 60*(1), 87–95.

Basso, M., & de Freitas, E. P. (2019). A UAV guidance system using crop row detection and line follower algorithms. *Journal of Intelligent & Robotic Systems, 97,* 605–621.

Billingsley, J., & Schoenfisch, M. (1997). The successful development of a vision guidance system for agriculture. *Computers and Electronics in Agriculture, 16*(2), 147–163.

Burgos-Artizzu, X. P., Ribeiro, A., Guijarro, M., & Pajares, G. (2011). Real-time image processing for crop/weed discrimination in maize fields. *Computers and Electronics in Agriculture, 75*(2), 337–346.

Caldwell, D. (2012). *Robotics and automation in the food industry. Current and future technologies* (pp. 1–528). Cambridge, UK: Woodhead Publishing.

Cervantes-Godoy, D., & Dewbre, J. (2010). Economic importance of agriculture for poverty reduction. *OECD Food, Agriculture and Fisheries Working Papers, 23,* 1–27.

Cupec, R. (2018). *Crop row benchmark dataset.* http://www.etfos.unios.hr/r3dvgroup/index.php?id=crd_dataset/.

Fontaine, V., & Crowe, T. G. (2006). Development of line-detection algorithms for local positioning in densely seeded crops. *Canadian Biosystems Engineering, 48*(7), 19–29.

García-Santillán, I., Guerrero, J. M., Montalvo, M., & Pajares, G. (2018). Curved and straight crop row detection by accumulation of green pixels from images in maize fields. *Precision Agriculture, 19*(1), 18–41.

Gonzalez, R. C., & Woods, R. E. (2018). *Digital image processing, global edition.* New York City, USA: Pearson, ISBN-10: 9780133356724$4.

Hague, T., Tillett, N. D., & Wheeler, H. (2006). Automated crop and weed monitoring in widely spaced cereals. *Precision Agriculture, 7*(1), 21–32.

Hough, P. V. C. (1960). A method and means for recognizing complex patterns. *US Patent, Office No. 3069654.*

Ji, R., & Qi, L. (2011). Crop-row detection algorithm based on Random Hough Transformation. *Mathematical and Computer Modelling, 54*(3–4), 1016–1020.

Jiang, G., Wang, Z., & Liu, H. (2015). Automatic detection of crop rows based on multi-ROIs. *Expert Systems with Applications, 42*(5), 2429–2441.

Jiang, G., Wang, X., Wang, Z., & Liu, H. (2016). Wheat rows detection at the early growth stage based on Hough transform and vanishing point. *Computers and Electronics in Agriculture, 123,* 211–223.

Jones, G., Gée, C., & Truchetet, F. (2009). Modelling agronomic images for weed detection and comparison of crop/weed discrimination algorithm performance. *Precision Agriculture, 10*(1), 1–15.

Katariya, S. S., Gundal, S. S., Kanawade, M. T., & Mazhar, K. (2015). Automation in agriculture. *International Journal of Recent Scientific Research, 6*(6), 4453–4456.

Kise, M., Zhang, Q., & Más, F. R. (2005). A stereovision-based crop row detection method for tractor-automated guidance. *Biosystems Engineering, 90*(4), 357–367.

Kise, M., & Zhang, Q. (2008). Development of a stereovision sensing system for 3D crop row structure mapping and tractor guidance. *Biosystems Engineering, 101*(2), 191–198.

Meuwissen, T. H., Hayes, B. J., & Goddard, M. E. (2001). Prediction of total genetic value using genome-wide dense marker maps. *Genetics, 157*(4), 1819–1847.

Montalvo, M., Pajares, G., Guerrero, J. M., Romeo, J., Guijarro, M., Ribeiro, A., et al. (2012). Automatic detection of crop rows in maize fields with high weeds pressure. *Expert Systems with Applications, 39*(15), 11889–11897.

Otsu, N. (1979). A threshold selection method from gray-level histograms. *IEEE Transactions on Systems, Man, and Cybernetics, 9*(1), 62–66.

Pajares, G., Santillán, I. G., Campos, Y., Montalvo, M., Guerrero, J. M., Emmi, L., et al. (2016). Machine-vision systems selection for agricultural vehicles: A guide. *Journal of Imaging, 2*(4), 1–31.

Ramesh, K. N., Chandrika, N., Omkar, S. N., Meenavathi, M. B., & Rekha, V. (2016). Detection of rows in agricultural crop images acquired by remote sensing from a UAV. *International Journal of Image, Graphics and Signal Processing, 8*(11), 25–31.

Romeo, J., Pajares, G., Montalvo, M., Guerrero, J. M., Guijarro, M., & Ribeiro, A. (2012). Crop row detection in maize fields inspired on the human visual perception. *The Scientific World Journal, 2012,* 1–10.

Rovira-Más, F., Zhang, Q., & Reid, J. F. (2008). Stereo vision three-dimensional terrain maps for precision agriculture. *Computers and Electronics in Agriculture, 60*(2), 133–143.

Sogaard, H. T., & Olsen, H. J. (2003). Determination of crop rows by image analysis without segmentation. *Computers and Electronics in Agriculture, 38,* 141–158.

Vidović, I., Cupec, R., & Hocenski, Ž. (2016). Crop row detection by global energy minimization. *Pattern Recognition, 55,* 68–86.

Visscher, P. M., Wray, N. R., Zhang, Q., Sklar, P., McCarthy, M. I., Brown, M. A., et al. (2017). 10 years of GWAS discovery: Biology, function, and translation. *The American Journal of Human Genetics, 101*(1), 5–22.

Article

A New Method for Extracting Individual Plant Bio-Characteristics from High-Resolution Digital Images

Saba Rabab [1,2,*], **Edmond Breen** [2], **Alem Gebremedhin** [3], **Fan Shi** [2], **Pieter Badenhorst** [4], **Yi-Ping Phoebe Chen** [5] **and Hans D. Daetwyler** [1,2]

1. School of Applied Systems Biology, La Trobe University, Bundoora 3083, Australia; hans.daetwyler@agriculture.vic.gov.au
2. Agriculture Victoria, AgriBio, Centre for AgriBioscience, Bundoora 3083, Australia; ed.breen@agriculture.vic.gov.au (E.B.); fan.shi@agriculture.vic.gov.au (F.S.)
3. Agriculture Victoria, Victoria, Grain Innovation Park, Horsham 3400, Australia; alem.gebre@agriculture.vic.gov.au
4. Agriculture Victoria, Hamilton Centre, Hamilton 3300, Australia; pieter.badenhorst@agriculture.vic.gov.au
5. Department of Computer Science and Information Technology, La Trobe University, Bundoora 3083, Australia; phoebe.chen@latrobe.edu.au
*   Correspondence: saba.rabab@agriculture.vic.gov.au

Academic Editors: Lin Cao and Filiberto Pla

Abstract: The extraction of automated plant phenomics from digital images has advanced in recent years. However, the accuracy of extracted phenomics, especially for individual plants in a field environment, requires improvement. In this paper, a new and efficient method of extracting individual plant areas and their mean normalized difference vegetation index from high-resolution digital images is proposed. The algorithm was applied on perennial ryegrass row field data multispectral images taken from the top view. First, the center points of individual plants from digital images were located to exclude plant positions without plants. Second, the accurate area of each plant was extracted using its center point and radius. Third, the accurate mean normalized difference vegetation index of each plant was extracted and adjusted for overlapping plants. The correlation between the extracted individual plant phenomics and fresh weight ranged between 0.63 and 0.75 across four time points. The methods proposed are applicable to other crops where individual plant phenotypes are of interest.

Keywords: plant phenomics; image processing; plant area; plant center points; normalized difference vegetation index

1. Introduction

Due to the exponentially increasing consumption of food, fuel, and feed by the burgeoning population of the world, global agricultural demand is growing. Global cereal grain production must increase by 70% by 2050 to meet food demands [1,2]. Forages are also an important feed source for animals that produce dairy, meat, and fiber products, and they play a crucial role in maintaining a good natural environment. In parallel, growing climate unpredictability is shifting crop production onto marginal lands, leading to the intensification of existing agricultural practices, and displacement of natural ecosystems [3]. Conventional methods for plant breeding, such as phenotypic and pedigree selection, have significantly increased crop yields worldwide [4]. Nevertheless, these methods alone will not be enough to meet the projected global food demands [5,6]. Moreover, these traditional methods are costly, require intensive labor resources, have a lower throughput and are time consuming. Genomic breeding approaches (e.g., genomic selection) will assist in increasing crop and pasture production [7,8] and a wealth of plant genomic knowledge has been accumulated over the last decade [9–12]. However, genomic selection requires large training sets of lines that are well characterized with both genomics and

phenotypes. Traditional phenotyping methods are often too laborious and costly for large plant collections, leading to a significant gap between genomic knowledge and its connection to phenotypes. These problems can be rectified to some extent by the accurate and precise phenotyping of germplasm with novel technologies.

The phenotyping of organisms [13–16] can be defined as a set of protocols or methodologies applied to measure physical characteristics, such as architecture, growth and composition, with a certain accuracy and precision. For plants, phenotyping is based on morphological, physiological, biochemical, and molecular structures. Current phenotyping methods in plants are considered slow, expensive, are sometimes destructive and can cause variations between observations due to human operator variability. This has led to a growth in automated phenotyping technologies, which overcome these shortcomings. One such automated method relies on digital imaging, containing two main steps: image acquisition and image analysis. Image acquisition is a process where a digital representation (image) of the crop field is obtained using an imaging sensor. Image acquisition can generally be classified into seven groups with respect to plant phenotyping [16]: mono-red green blue (RGB) vision, multi and hyperspectral cameras, stereo vision, Light Detection and Ranging (LiDAR) technology, fluorescence imaging, tomography imaging and thermography, in addition to time of flight cameras. Image analysis, on the other hand, deals with the extraction of useful information—in regard to plants—from digital images, involving pre-processing, segmentation, and feature extraction [17]. The pre-processing step can include operations such as image cropping, image rotation, contrast improvement, color mapping, image smoothing, and edge detection [18]. The application of these methods for phenotyping depends upon the output requirements and several other factors. The main goal of image segmentation is to differentiate between the irrelevant or background objects and objects (segments) of interest by using color, texture and statistical measures. For example, Otsu binary thresholding [19] is a segmentation algorithm that is used to automatically perform clustering-based image segmentation, returning a value of threshold. The threshold can then be used to discriminate between the background and foreground of a digital image using methods such as watershed transformation [20]. Feature extraction is also an important factor in automated phenotyping using digital images. The measurements extracted from the image segments, such as area and normalized difference vegetation index (NDVI), are placed into feature vectors which summarize the physical characteristics of each identified plant or plant region. The digital information extracted from the images in the form of NDVI, surface area, width, height, and circular shape, can be linked to the degree of greenness, fresh weight, and biomass of the plant. Phenomic bio-characteristics, such as NDVI or plant area, can be correlated or used to predict plant biomass yield, which is the main production phenotype in forage species and is a characteristic that contributes to grain yield in other crops [21,22]. Bio-characteristics, if sufficiently correlated, can then be used as proxy phenotypes for biomass in genomic selection to select the best populations and generate genetic gain over generations. Furthermore, as image derived bio-characteristics are non-destructive, they can be collected at multiple time-points during the growth cycle of crops, giving rise to novel phenotypes for genomic selection and breeding purposes (e.g., change in biomass over time, growth, or senescence rate).

Most plant breeding applications focus on plot or row phenotypes consisting of multiple plants, which is often sufficient. However, individual plant phenotypes are of interest for investigating family or population uniformity in both in- and outbred species. Uniformity is important because growers desire high forage biomass with even growth throughout a paddock, while additionally, it is also a characteristic for determining plant breeder's rights. Furthermore, in outbred species, it may be of interest to understand the effect of individual plants on other plants in close proximity—so called, competition effects [23]—as each plant is genetically unique. If plants in a forage cultivar are overly competitive, the overall biomass yield and uniformity is expected be suboptimal in the paddock. The manual collection of individual plant characteristics is especially laborious and automated phenomic solutions are required.

We propose a new method for extracting the area of individual plants from digital field trial images. The method focuses on both the extraction of these regions from a multispectral image taken by an uncrewed aerial vehicle (UAV) and the linking of these regions with the biomass of individual plants. The utility of the approach is evaluated by correlating individual plant phenomic bio-characteristics and plant biomass, as estimated by fresh weight at harvest. The study is organized as follows: Section 2 provides the work problem statements, Section 3 describes the proposed algorithm in detail, Section 4 explains the experimental results and presents a comparative analysis on perennial ryegrass field data, and Section 5 outlines the conclusions.

2. Problem Statements

The proposed algorithm was applied to perennial ryegrass row field data for which images were taken from the top view. The field trial contained 50 perennial ryegrass cultivars, grown in replicated rows of 32 plants per row. Perennial ryegrass is a diploid outbred species, where each individual plant is genetically unique and each cultivar has at least four parental cultivars, making them genetically diverse. Each replication was considered as a plot and contained three rows of 32 spaced plants each (i.e., 96 plants/plot). The experimental unit was, therefore, a plot of 8×1.8 m. The expected spacing between plants was 25 cm and 60 cm between rows. The field trial contained a total of 48,000 individual plants in 10 blocks. The total area of the field experiment was 8100 m^2. In part, the aims of these field trials were to develop phenomics processing pipelines to define novel traits for the estimation and prediction of plant performance (e.g., biomass yield, flowering time). Images were taken with a Parrot Sequoia (Parrot Drones S.A.S., Paris, France) multispectral camera, deployed on a 3DR Solo quadcopter. The camera captures images simultaneously at four bands, including green (530–570 nm), red (640–680 nm), red edge (730–740 nm), and near-infrared (770–810 nm). It also has a GPS and sensor and incident light sensors. The flight mission was planned by Tower Beta software. Aerial images were collected using the UAV on a weekly basis over the GS trial site, and data from four flight dates in 2017 were used for this analysis. Imaging dates were synchronized with each harvest. Flight operations were conducted under bright, sunny weather conditions to minimize noise from environmental variation. The UAV flight altitude was set at 20 m above ground level and the flight speed was 6 m/s, with 75% side and forward overlap of images. At this flight altitude and speed, the spatial resolution of the images was 2 cm/pixel. The same flight path was followed on each date. Image reflectance was corrected using Airinov calibration plates with known reflectance values (MicaSense Inc., Seattle, WA, USA). An example color image of the field trial is shown in Figure 1a and a grey scale image of the field trial area is shown in Figure 1b. The white pixels (NDVI TIFF image) in Figure 1b mostly represent greenness in the trial image and black pixels represent the background. In Figure 1b, there are 10 blocks, and in each block, there are 150 plant rows equaling a total of 1500 crop rows. Furthermore, in each plant row, there are 32 plants, resulting in 48,000 plants in each field-trial image.

The goal was to automatically extract phenomic traits, such as area and the NDVI value of each plant, from each field trial's TIFF file image. In principle, other vegetation indexes such as the green normalized difference vegetation index, red edge normalized difference vegetation index, soil adjusted vegetation index and the enhanced vegetation index could also be used. The extraction of these traits utilizes the experimental field trial design, specifying the layout of plant-rows and the plants within each row to help define the boundary or bounding boxes for plant rows and initial estimates of the individual plant regions. The row polygons of row plants were identified using projection methods, as outlined in [22], followed by the identification of center-points of individual plants. These center-points then assisted in identifying the individual plant polygons. Figure 2a shows the layout of bounding boxes for several row polygons and Figure 2b shows the bounding boxes for individual plant polygons. These bounding boxes assist in extracting phenomics traits of interest. For instance, the bounding box region can be cropped, and the area can

be calculated by multiplying the number of non-zero pixels with the area of one pixel in cm^2. Furthermore, the mean NDVI value is calculated by taking the mean of NDVI values of all non-zero pixels within that region.
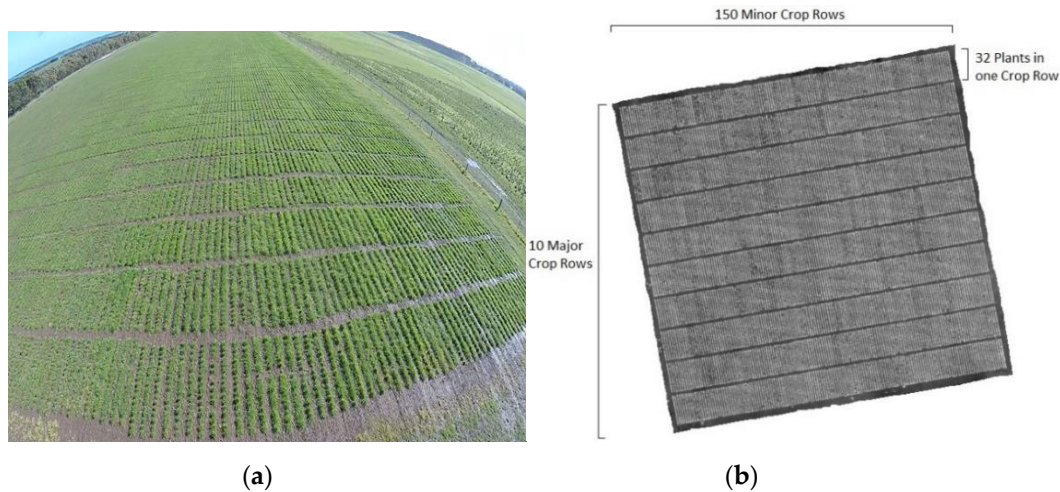

(**a**) (**b**)

Figure 1. (**a**) An example of field trial in RGB form and (**b**) a grey scale image of the perennial ryegrass field trial stitched together from aerial images.
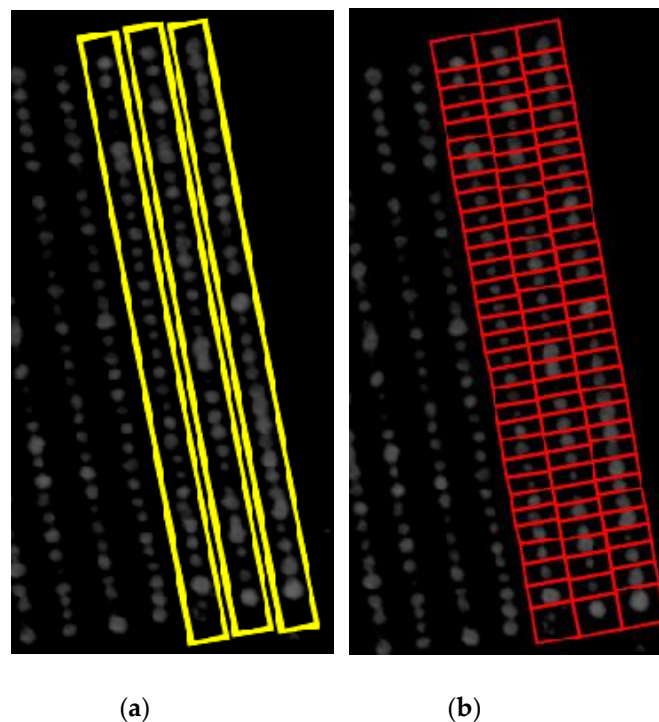

(**a**) (**b**)

Figure 2. Bounding Boxes of (**a**) 3 plant-row boxes and (**b**) their individual plant boxes.

In images where there is moderate amount of plant growth (Figure 2), the extraction of phenomics is relatively simple. The plants are almost entirely confined in their individual bounding boxes, referred to as plant boxes, and therefore, the area and mean NDVI value can be calculated easily. However, there are bounding boxes where plants have not grown at all, but due to encroachment of adjacent plants, their bounding boxes contain some image pixels that show NDVI signals, as shown in Figure 3.

A bounding box where no plant is grown.
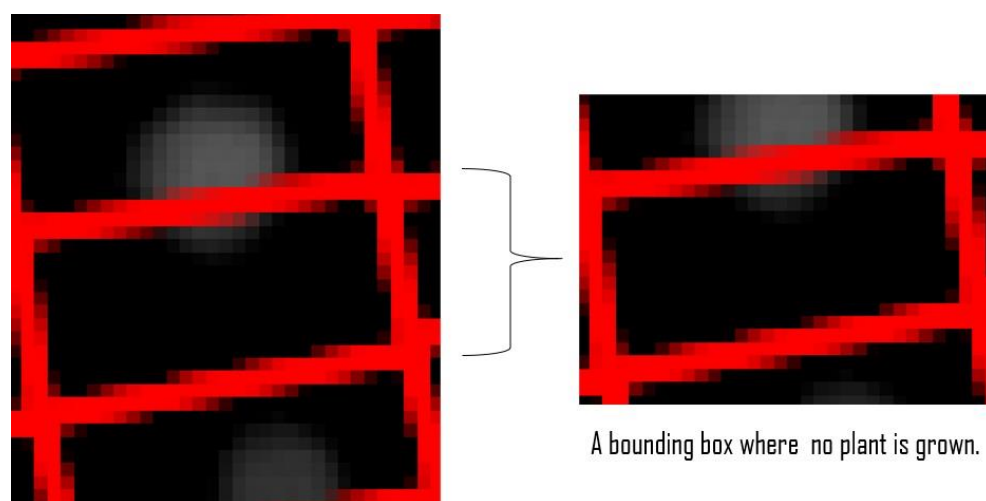
Figure 3. A bounding box without a plant, but due to the overlapping of the top plant, the bounding box contains some image pixels that are erroneously classified as plants.

These NDVI values can be mistaken for a plant in the box which has either died or not grown at all, when it was in fact the neighboring plant. Additionally, the plants can overgrow and overlap into adjacent plants (Figure 4a). In such cases, calculating the area by counting the number of non-zero pixels in that bounding box (Figure 4b) will not be accurate. Therefore, a potentially more accurate area is hypothesized in Figure 4c of the same plant, by highlighting a circular plant region. In summary, these problems are the main objectives of our work, aimed at identifying the accurate area of individual plants, and includes the following sub-objectives:

1. to identify bounding boxes with no plants;
2. to calculate accurate individual plant areas, despite overlapping adjacent plants;
3. to calculate accurate individual plant NDVI values, despite overlapping adjacent plants;
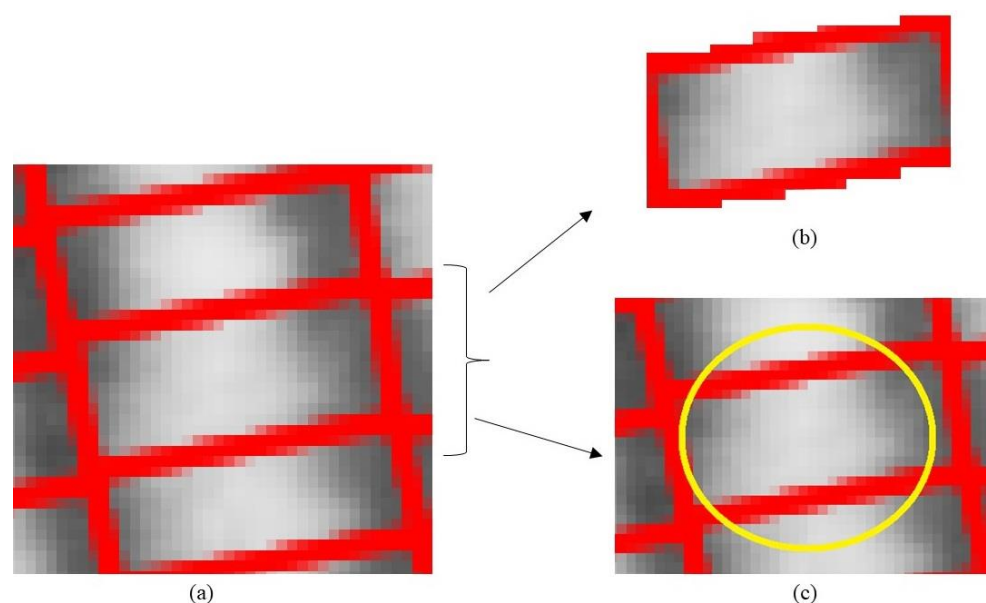

Figure 4. (**a**) Plants overgrow from their bounding boxes and overlapping with adjacent plants. (**b**) Rectangular bounding box of a plant; the area equal to the bounding box is not accurate as plant is overgrown from the bounding box. (**c**) A potentially more accurate representation of the area is illustrated with the circular plant region.

3. Methods

The use of machine vision in phenotyping started almost three decades ago, for the extraction of NDVI values [24]. Since then, there has been huge progress in monitoring large fields using sensor technologies. However, the applications involve simple digital data, which are usually extracted in controlled environments. In the previous proposals [25–31], the examined plants were captured in very controlled and simplistic environments; either there was only one plant per digital image, or the plants did not overlap.

To detect circles in images, Circular Hough Transform (CHT) [32] and its variants [33] have become common methods in numerous image processing applications. CHT is very effective in detecting circles in digital images, even with somewhat irregular circular shapes. However, it performs poorly when circles are merged and overlap with each other, just as in the case of our research problem.

These existing studies do not provide solutions that are relevant to our mentioned problems; therefore, we have developed a new and effective image-based phenotyping method. The proposed algorithm was developed and implemented on a field trial image dataset, in which images were taken from the top view. A sample of a single crop row image from the field trial, taken at four time points, is shown in Figure 5a–d. We employed MATLAB version R2019a for the simulations and analyses of our work. In the next subsections, the proposed algorithm is explained, and images are shown to aid the reader's understanding.
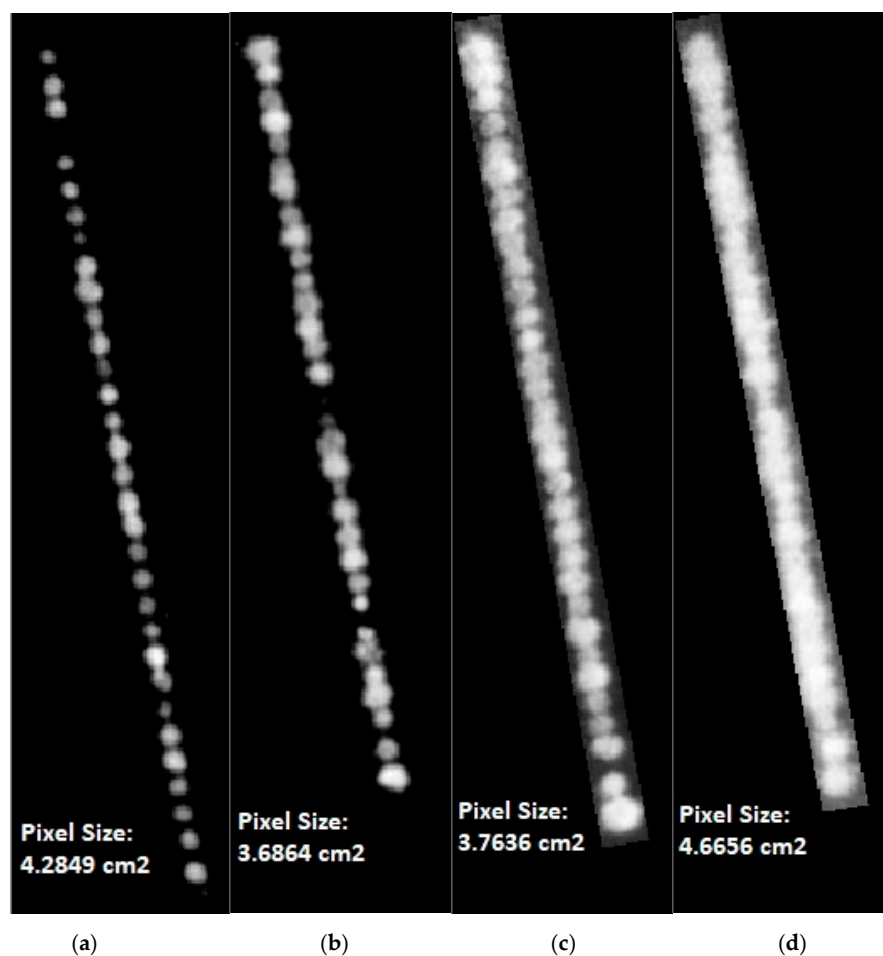

Figure 5. (**a**–**d**) A small set of different crop rows extracted from four field trial images taken on (**a**) 9 May 2017, (**b**) 5 July 2017, (**c**) 11 September 2017 and (**d**) 20 November 2017. Note: that the rows at different time points are not exactly the same length as pixel size varied slightly from expected 2 cm. Values were converted to metric units to standardize between capture dates.

3.1. Background Correction

Let I be the two-dimensional matrix for a single plant box image with size r, c, where r is the total number of image rows and c is the total number of image columns. It should be noted that the plants are at a specific angle, but we did not rotate them for the analysis. As the plant's geometry is somewhat circular, the rotation will not affect the extraction of the center point and radius, as explained below. I is considered for one individual plant and there are 32 such plants in one crop row, as shown in Figure 5a. Moreover, let $I(i,j)$ represent the NDVI value of the image pixel at the ith row and j^{th} column of I, and $I(i,j) \in [-1, 1]$. The first step was to remove any background values, which did not contain plant pixels. To remove the unnecessary background, Otsu binary thresholding [19] was employed to automatically perform clustering-based image thresholding, returning a threshold value of th_{Otsu}. The background corrected image of a single plant, I^b is obtained using the following:

$$I^b(i,j) = \begin{cases} I(i,j) & if \quad I(i,j) > th_{Otsu}, \\ 0 & otherwise. \end{cases} \tag{1}$$

The Otsu image thresholding for background correction was applied in Figure 5a–d and the results are shown in Figure 6a–d.
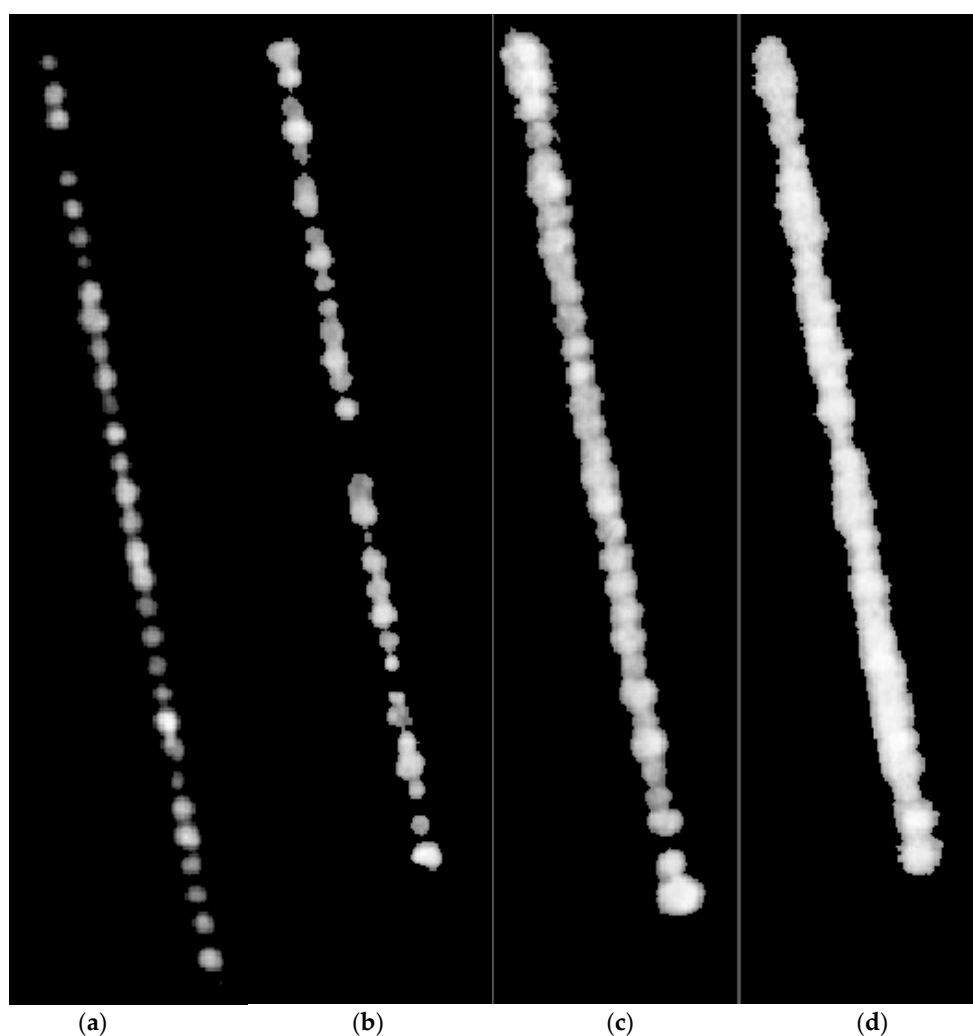

(a)   (b)   (c)   (d)

Figure 6. (**a–d**) Background corrected images obtained from applying Otsu thresholding on images shown in Figure 5a–d, respectively. Grey pixels represent normalized difference vegetation index (NDVI) intensity and black pixels represent the background.

3.2. Center Point Calculation

　　Whether a rectangular plant bounding box contained a plant or not was determined by identifying the center point of the plant. If there was a center point in a bounding box, then it was determined as containing a plant and vice-versa. As mentioned in the problem statement, bounding boxes were defined based on row layouts and the expected plant number and spacing per row, following [22]. The distribution of greenness or NDVI values in an individual plant, assists in finding the plant centers (Figure 7). The greenness is likely to be at a maximum in the center of plant and gradually decreases towards the plant's edges. Therefore, the center point should correspond to, or near, a location of an image pixel with the maximum NDVI value. However, there can be more than one pixel whose values correspond to the maximum NDVI and they can be in different places. Another solution could consider the middle point of the bounding box as the plant centers. However, this assumption is not always justified, as plant locations could deviate from bounding box centers. Our approach combines these two methods. This allows for the correction of NDVI maxima that are at bounding box edges but have false values due to encroaching neighboring plants. The centered positions of a plant image are determined as follows:

$$\left\{ (i,\, j) \,\middle|\, I^b(i,j) \,\geq\, 0.6 * I_{max}; \forall\, i \,\epsilon\, [0.2r,\, 0.8r]; \forall\, j \,\epsilon\, [1,\, c] \right\} \tag{2}$$

where I_{max} is the maximum value of I^b. Without loss of generality, the above equation specifies a set of image positions within a given plant-box, as shown in Figure 4b, with its origin specified at (1,1) and with r rows and c columns that have intensity values that satisfy $I^b(i,j) \,\geq\, 0.6 * I_{max}$. The optimization value of 0.6 is based on trial and error and was chosen based on visual inspection. Increasing the value beyond 0.6 will result in more centered image pixels and vice-versa. We recommend investigating this threshold when applying the algorithm to new datasets. This set will be empty if there is no center point, otherwise the average i, Θ_r and average j, Θ_c, location (Θ_r, Θ_c) is used to define a plant's center point within its corresponding plant-box. The goal is to locate a center point of the plant which cannot be at the top or bottom of the image. Therefore, the search row domain in each plant-box is constrained to not include the top and bottom 20% of the rows. In our study, plants were generally planted at equal distances, justifying this assumption. In field data where this is not the case, further development of the algorithm may be needed. This process was then applied to all plant-boxes within each field image.
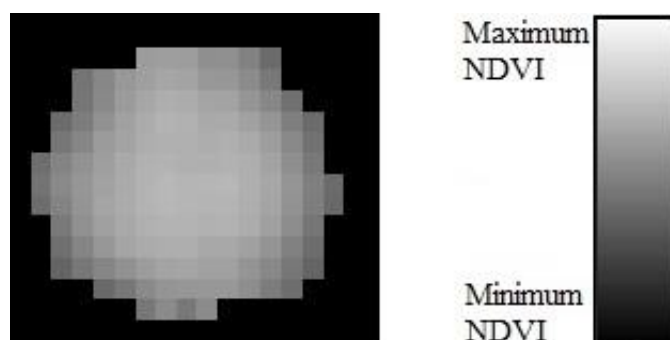

Figure 7. Distribution of image pixels in terms of greenness or NDVI values in an individual plant.

　　The results of this step, applied to the images shown in Figure 6a–d, are shown in Figure 8a–d. The center points are represented by a red plus symbol. The algorithm correctly identified the number of plants in a crop row. For instance, Figure 8a has only 31 plants with center points labelled and Figure 8b only has 30 plants. The identification of center points indicates that the first research problem has been solved, that is, the bounding boxes with no plants have been identified.
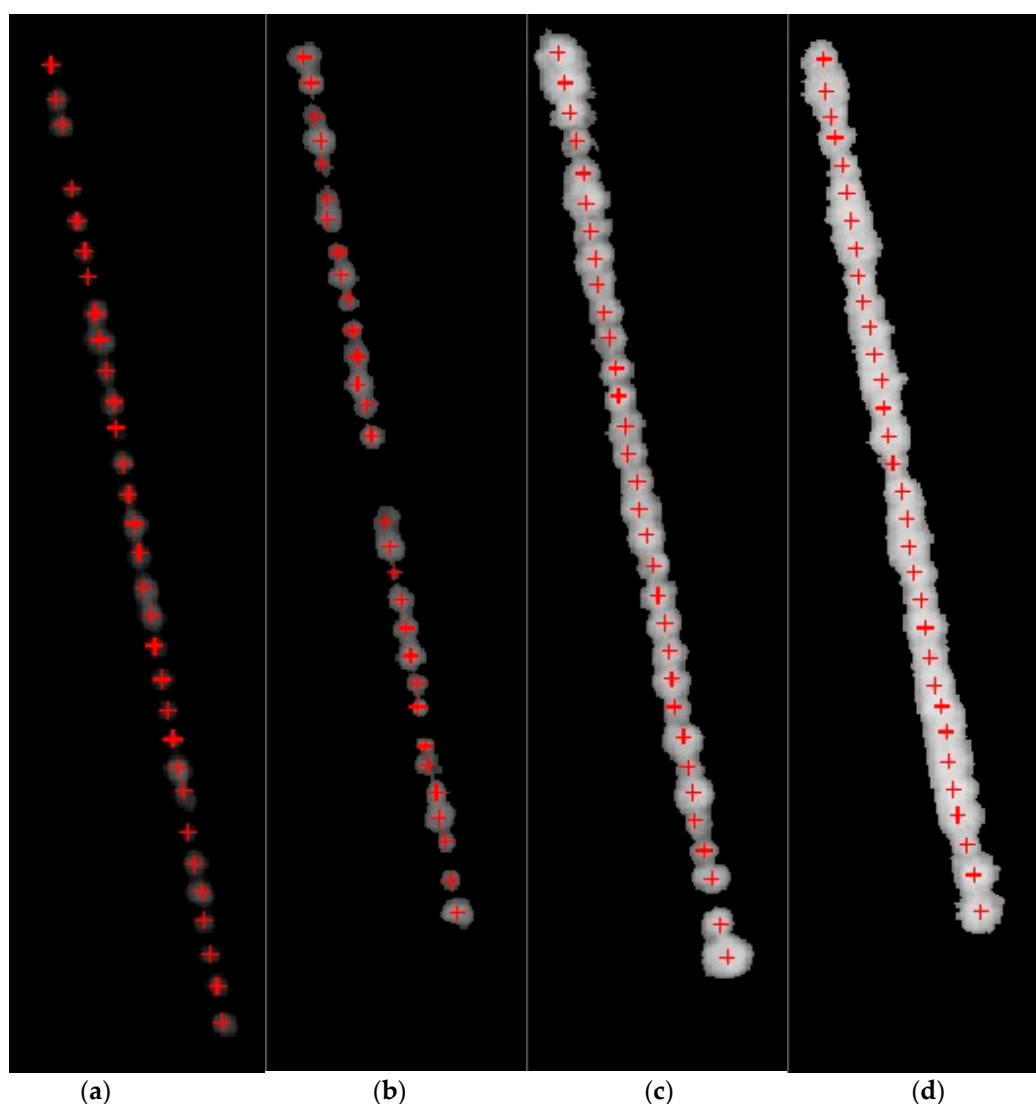
(a)   (b)   (c)   (d)

Figure 8. (**a**–**d**) Identification of center points using Algorithm 1.

3.3. Extraction of Plant Areas

The next goal is to extract the individual plant areas. The distribution of plant pixels is somewhat circular and symmetrical (Figure 7). To define the circular plant region associated with each plant-box containing a plant requires only a center point and a corresponding radius. The center points were calculated in the previous step and the radius was calculated by measuring the distance in terms of number of non-zero image pixels from the center point to the horizontal extreme. Figure 9 shows the same plant illustrated in Figure 7, with labelling of the center point, center row and horizontal distances from the center point to the horizontal extremes. These horizontal distances give the possible radius of the plant. The vertical distances are not taken into consideration, as the adjacent plants may overlap at the vertical (at both top and bottom; except the 1st and 32nd plant of the row) positions. For each center pixel defined above (Θ_r, Θ_c), let its corresponding radius be defined by:

$$radius = \max\left\{ \mathrm{abs}(\Theta_c - j) \,\middle|\, I^b(\Theta_r, \mathrm{j}) \geq 0.6 * I_{max} \right\} \tag{3}$$

Using the radii and center points, the circular plant regions of each plant were extracted (Figure 10a–d). The extraction of radii and the circular plant regions resulted in the second research problem being solved, that is, the accurate area of the individual plants has been calculated, despite the overlapping of adjacent plants. Furthermore, the area is calculated

by taking the product of the number of non-zero pixels with the area of one pixel in cm^2 within that region.
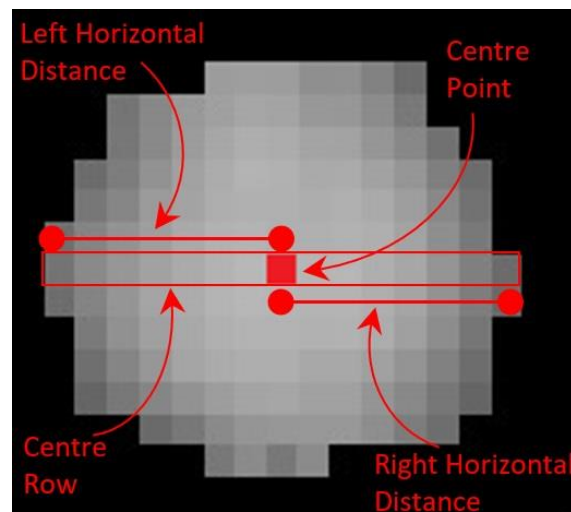

Figure 9. Distribution of image pixels with labelling of center point, center row and horizontal distances from center point to the horizontal extremes.
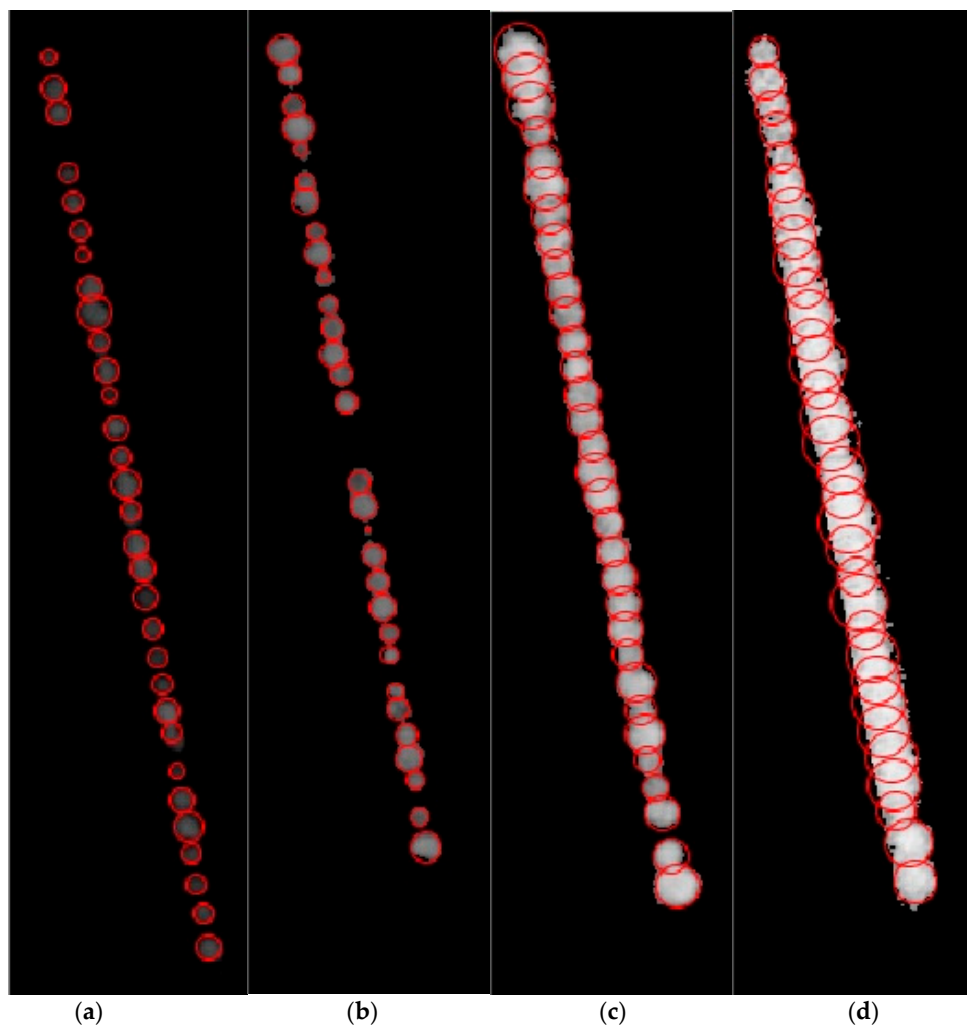

Figure 10. (**a**–**d**) Extraction of circular plant regions and accurate area of individual plants from Figure 8 using Algorithm 2.

3.4. Extraction of NDVI Values

As mentioned earlier, due to the overlapping of the adjacent plants, the NDVI values can be inflated at the top and bottom positions, as depicted in Figure 10c,d. Therefore, the overlapping pixels rows at top and bottom positions must be identified and adjusted.

3.4.1. Finding the Overlapping Pixel Rows

Considering a single crop row (32 plants), the overlapping pixels rows for each plant can be extracted using the center points and radii calculated earlier. Let P_x, $x \in [1, 2, \ldots, 32]$ be a plant whose overlapping rows are to be extracted. The center point and radius for P_x are calculated earlier and let be denoted as (Θ_r^x, Θ_c^x) and R_x, respectively. The number of overlapping rows at the bottom position ρ_{bottom}^x of the plant P_x are extracted as:

$$\rho_{bottom}^x = (\Theta_r^x + R_x) - \left(\Theta_r^{x+1} - R_{x+1}\right) - 1 \tag{4}$$

Similarly, the number of overlapping rows at the top position ρ_{top}^x of the plant P_x is extracted as:

$$\rho_{top}^x = \left(\Theta_r^{x-1} + R_{x-1}\right) - (\Theta_r^x - R_x) - 1 \tag{5}$$

It should be noted that ρ_{bottom}^x for P_x at the bottom position is the same as ρ_{top}^x for P_{x+1} at the top position.

This is illustrated in Figure 11, with three plants and their center points and radii. Moreover, the first plant is overlapping with the second plant at the bottom position and the reverse is true for the second plant. Similarly, the second plant overlaps with the third plant at the bottom position and vice-versa. Using Equations (4) and (5), it can be calculated that $\rho_{bottom}^1 = \rho_{top}^2 = 2$ and $\rho_{bottom}^2 = \rho_{top}^3 = 3$. These are the number of pixel rows where the NDVI values are likely inflated and should be adjusted before consideration. Note: that $\rho^x > 0$, if there is overlap, otherwise there is no overlap and, therefore, no adjustment needed.
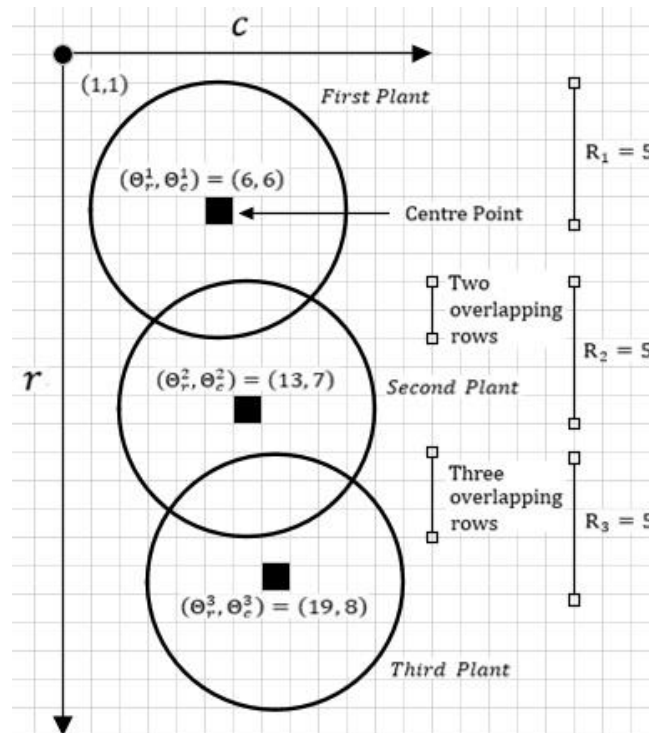

Figure 11. Three plants in a crop row overlapping at top and bottom positions. The center points and radii are also mentioned, which assist in extracting overlapping rows.

3.4.2. Adjusting NDVI Values at Overlapping Pixel Rows

The symmetrical distribution of plant NDVI values with center maxima and a gradual decrease towards the boundary of plant informs the adjustment procedure for overlapping pixel rows (Figure 7).

Care must be taken to exclude overlapping areas from the determination of maximum and minimum NDVI values. The use of the center row avoids overlapping areas and increases the accuracy of maxima and minima. There are three steps described as follows:

1. the maximum and minimum NDVI values of the plant are first calculated, labelled as I_{max}^b and I_{min}^b; respectively;
2. the whole center row is updated and will be used as a reference for the adjustment of plant pixels at overlapping rows. The step size, which is the difference of NDVI values between two adjacent pixels, is calculated as:

$$I_{step} = \frac{I_{max}^b - I_{min}^b}{R - 1} \tag{6}$$

The center row is then updated with the following values:

$$I^b(\Theta_r, :) = [I_{min}^b, I_{min}^b + I_{step}, I_{min}^b + 2 * I_{step}, \ldots \ldots, I_{max}^b, \ldots \ldots, I_{min}^b \\ +2 * I_{step}, I_{min}^b + I_{step}, I_{min}^b]_{1 \times (2R-1)}. \tag{7}$$

1. Let us take a symmetric reference vector, V_{sym}, such that $V_{sym} = [1, 2, 3, \ldots, R-2, R-1, R, R-2, R-1, \ldots, 3, 2, 1]$. The NDVI values are adjusted as following:

$$I^b(i, j) = \begin{cases} I^b(\Theta_r, i + j - R) \text{ if } \left[(V_{sym}(i) + V_{sym}(j)) > R+1\right] \& [i \text{ is an overlapping row}], \\ I^b(\Theta_r, 1) \text{ if } \left[(V_{sym}(i) + V_{sym}(j)) \leq R+1\right] \& [i \text{ is an overlapping row}], \\ I^b(i, j) \text{ otherwise, } \forall i \, \epsilon \, [1, r], \, \forall j \, \epsilon \, [1, c]. \end{cases} \tag{8}$$

As an example, after adjustment, the plant matrix I^b will look similar to the following two-dimensional matrix if each pixel of I^b is adjusted, considering the plant has seven rows and seven columns.

$$I^b = \begin{bmatrix} I_{min}^b & I_{min}^b & I_{min}^b & I_{min}^b & I_{min}^b & I_{min}^b & I_{min}^b \\ I_{min}^b & I_{min}^b & I_{min}^b & I_{min}^b + I_{step} & I_{min}^b & I_{min}^b & I_{min}^b \\ I_{min}^b & I_{min}^b & I_{min}^b + I_{step} & I_{min}^b + 2 * I_{step} & I_{min}^b + I_{step} & I_{min}^b & I_{min}^b \\ I_{min}^b & I_{min}^b + I_{step} & I_{min}^b + 2 * I_{step} & I_{max}^b & I_{min}^b + 2 * I_{step} & I_{min}^b + I_{step} & I_{min}^b \\ I_{min}^b & I_{min}^b & I_{min}^b + I_{step} & I_{min}^b + 2 * I_{step} & I_{min}^b + I_{step} & I_{min}^b & I_{min}^b \\ I_{min}^b & I_{min}^b & I_{min}^b & I_{min}^b + I_{step} & I_{min}^b & I_{min}^b & I_{min}^b \\ I_{min}^b & I_{min}^b & I_{min}^b & I_{min}^b & I_{min}^b & I_{min}^b & I_{min}^b \end{bmatrix}_{7 \times 7}$$

To validate the results obtained from the digital adjusted plants, the phenomics of these plants were correlated with the manually harvested fresh weights. The higher value of correlation confirms the accuracy of extracted phenomics of the adjusted plants. The results were obtained by considering two phenomic bio-characteristics: (1) area and (2) mean NDVI values of adjusted plants.

After the adjustment of NDVI values and the extraction of circular plant regions, the next aim was to extract the area and mean NDVI value of each plant for each field trial image. The individual plant area was calculated as the product of number of non-zero pixels with the area of one pixel in cm^2 within the circular plant region. Mean NDVI was tabulated by calculating the mean NDVI values of non-zero pixels with the bounding box. The area provides information about the size of the plant and the mean NDVI value indicates how dense the plant canopy is. Note that the area and mean NDVI values may not be correlated, e.g., a plant with small area can have a similar mean NDVI value as a plant occupying a large area.

3.5. Testing of the Algorithm

Fresh biomass weights were collected for a subset of 480 perennial ryegrass plants to measure their individual biomass yield. The field trial was located and operated by Agriculture Victoria Research, Hamilton, Victoria, Australia (37.8464°S, 142.0737°E). The Hamilton region is in the Victorian high rainfall zone, generally receiving >600 mm per year of rain. Fresh weights were available for four harvesting dates (9 May 2017, 5 July 2017, 11 September 2017 and 20 November 2017) in different seasons of 2017 [34]. Harvest dates were determined by the growth stage of the individual plants, in which the two to three leaf stage was considered as a standard simulated grazing stage. The above-ground biomass was harvested manually at 5 cm height.

The following phenomics metrics were compared via Pearson correlations (*r*) [35]: mean NDVI of rectangular bounding boxes, area of rectangular bounding boxes, unadjusted mean NDVI of circular plant regions, adjusted mean NDVI of circular plant regions and area of circular plant regions.

4. Results and Discussions

The robustness of the proposed algorithm was tested by correlating extracted phenomics metrics with harvest fresh weights. Metrics included the area calculated from rectangular bounding boxes and their mean unadjusted and adjusted NDVI. The fresh biomass weight value per individually harvested plant (82.48–127.18 g) varied across seasons in 2017. Moreover, measured seasonal fresh biomass weight in 2017 indicated a wide variability of biomass values (~1.41–428 g) for each measurement season for the individual plants [34]. This suggests that biomass yield had sufficient variation to use to correlate the NDVI and plant phenomics.

The Pearson correlation coefficients (*r*) between the area of circular plant regions and fresh weights for four field trial images from four timepoints are shown in Table 1 and Figure 12a–d. The values of *r* for these four images demonstrate a good relationship between fresh weight and circular area (0.63–0.75). The correlation could likely be further improved by including height measures [22]. Areas extracted from the circular plant regions were more closely correlated with fresh weights than those from rectangular boxes (Table 1). The advantage of the circular areas was less pronounced at the May 2017 time point, which also had the lowest number of plants overlapping across boxes. However, for the other timepoints with higher degrees of plant overlap, the correlation for circular plant regions was substantially higher than the rectangular boxes. There are two main reasons for this: (1) most plants in these three field trial images had overgrown across bounding boxes and merged with adjacent plants, thus, rectangular bounding boxes will not provide an accurate measure of the area; (2) rectangular boxes may show an area that is entirely due to the overlapping of neighboring plants, leading to an area or NDVI being attributed to missing plants. These factors erode the accuracy of rectangular bounding boxes, especially when there is substantial biomass.

Table 1. Values of ř calculated for the area extracted from rectangular and circular plant regions with the fresh weights of subset of 480 perennial ryegrass plants.

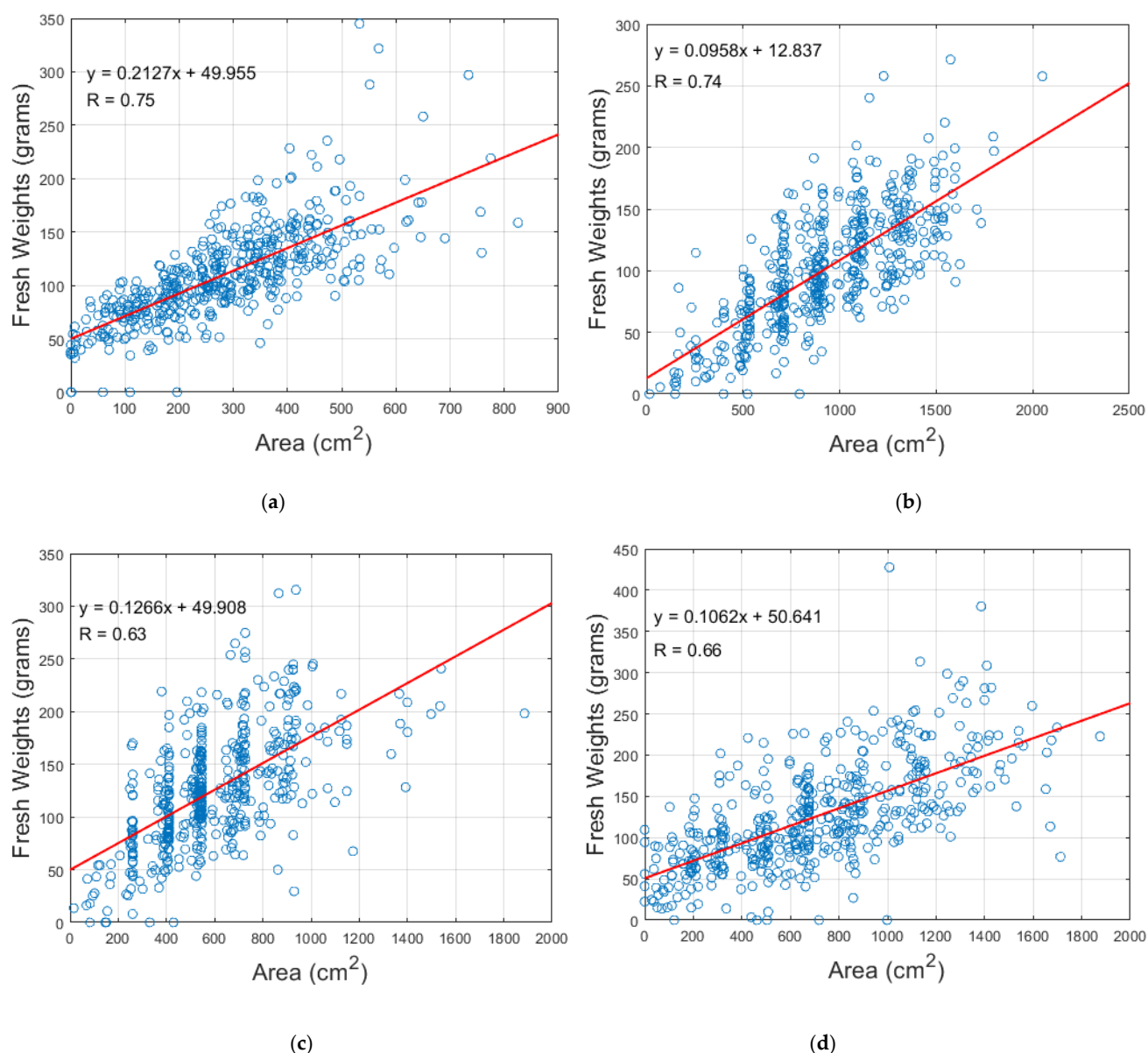| Image Time Point	Correlation	
	Area of Rectangular Bounding Boxes	**Area of Circular Plant Regions**
9 May 2017	0.74	0.75
5 July 2017	0.30	0.74
11 September 2017	0.28	0.63
20 November 2017	0.30	0.66

Figure 12. Correlation coefficients between fresh weight of subset of 480 perennial ryegrass plants and circular area for field trial images taken on (**a**) 9 May 2017, (**b**) 5 July 2017, (**c**) 11 September 2017 and (**d**) 20 November 2017.

To see the trends of individual plant's values of fresh weight and extracted phenomics, the ranges of fresh weight and area were normalized to a single range of [0, 100] and plotted as a comparison, shown in Figure 13, which shows that plant fresh weight and area follow a very similar pattern on 9 May 2017. This pattern is consistent with the other time points (Supplementary Material, Figure S1–S3).

We further compared the mean adjusted and unadjusted plant NDVI of circular plant regions and unadjusted NDVI of rectangular boxes to fresh weights (Table 2). The correlations were moderate for rectangular boxes and ranged between 0.51 and 0.56. Circular plant regions slightly improved in terms of correlations to 0.53 and 0.58. The relatively low level of improvement is due to NDVI values being similar for both types of bounding boxes, despite large differences in area. Further small correlation improvements (range 0.55–0.59) were achieved by adjusting NDVI values for circular plant regions by accounting for plant overlap. While the improvement observed from adjusting NDVI, here, was minor, the adjustment methods applied could be useful for other trials, crops or even data types (e.g., point clouds).
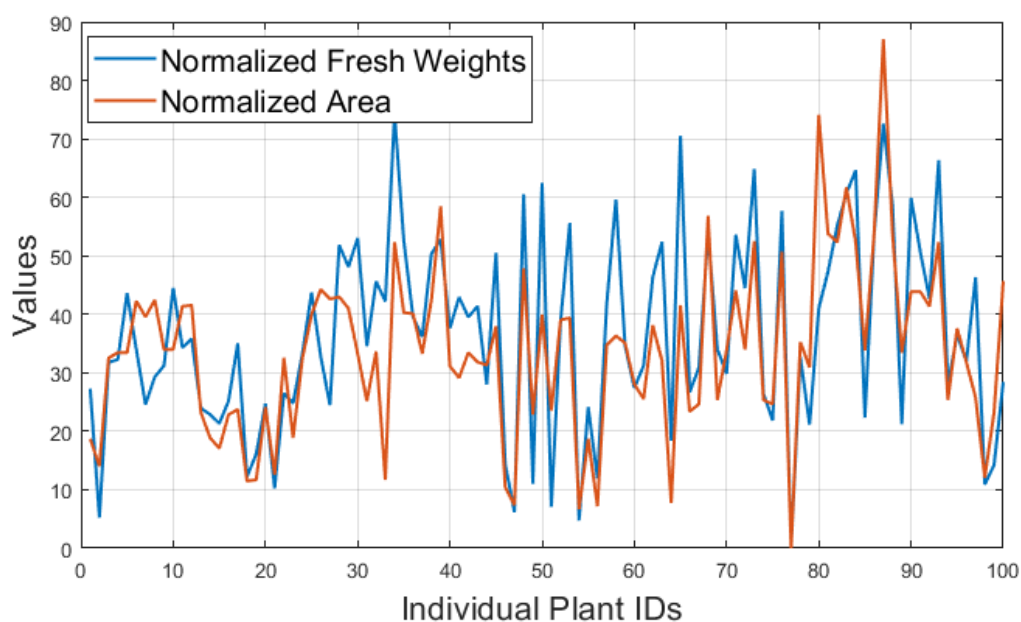
Figure 13. Comparisons between the individual plant values of normalized values of fresh weights and areas for first 100 plants in a same range of [0, 100] for the field trial image taken on 5 July 2017.

Table 2. Correlations of mean NDVI and fresh weights of subset of 480 perennial ryegrass plants for rectangular boxes and proposed circular plant regions: with unadjusted and adjusted NDVI values.

Image Time Point	Correlation		
	Unadjusted NDVI from Rectangular Boxes	Unadjusted NDVI from Circular Plant Regions	Adjusted NDVI from Circular Plant Regions
9 May 2017	0.56	0.56	0.57
5 July 2017	0.55	0.58	0.59
11 September 2017	0.52	0.54	0.55
20 November 2017	0.51	0.53	0.56

The multi-spectral images used in this study had a pixel size of approximately 2cm. This was sufficient to distinguish single perennial ryegrass plants. The successful application of our algorithm to other image datasets depends on their relative pixel and plant size. Furthermore, we set a numerical threshold for NDVI intensity and the search space within the bounding box to detect plant centers. In part, these values are expected to be dataset specific and could depend on achieving relatively uniform plant spacing, and, therefore, should be revisited during application. Finally, further improvements may be needed to the determination of radii, especially when plants are large and overlap substantially (Table 1, timepoints three and four), which adds noise and causes some overestimation.

The correlation of our phenomic bio-characteristics (plant areas and adjusted NDVI) found in our study is at a level that is useful to provide proxy phenotypes of individual biomass in the field. Plant breeding, with or without genomics, requires the phenotypic screening of many breeding lines to select the best for commercialization or as parents for the next breeding cycle. Furthermore, methods such as genomic selection require a large training population of phenotype lines with genome-wide DNA markers [36]. The advantage of sensor-based methods is that they are non-destructive and take less time to be conducted, which makes them suitable to be used at multiple time points during the growing season. In pasture grasses, growth rate and recovery after harvest are key properties that only non-destructive sensor-based methods can investigate at a sufficient scale to be useful for plant breeding. Further, as pasture grasses are generally outbreeding (i.e., they cannot self-pollinate making each plant genetically unique), it can be of importance to measure single plants for research and selection purposes. Of particular

interest, is the genetic predisposition of individual plants to compete with plants in close proximity in the field because highly competitive plants will lead to non-uniform growth patterns in the paddock, which is undesirable. The bio-characteristics defined in our study provide crucial information at the individual plant level to better understand the phenome-to-genome relationships of biomass production and other important traits.

5. Conclusions

Here, we present an efficient and effective solution to develop a machine-vision mathematical model that can extract plant phenomic bio-characteristics with sufficient accuracy, despite the overlapping of adjacent plants. The estimation of plant areas when plants are very large and overlap substantially could potentially be improved in future studies. The mathematical model consisted of three parts: locating center points, extracting the area by means of radius and center point, and extracting of mean NDVI via adjustment of overlapping plant regions. Overall, correlations of phenomic metrics with fresh weights were moderate, with plant areas derived from circular plant regions being more strongly correlated than the NDVI derived measures. The proposed NDVI adjustment for overlapping plant portions increased correlations with fresh weights slightly. As is the case with all new proposals, we strongly encourage the evaluation of the algorithm performance before deployment. The algorithms presented in this study can be applied to a wide variety of crops and to other field trial designs.

References

1. Tester, M.; Langridge, P. Breeding Technologies to Increase Crop Production in a Changing World. *Science* **2010**, *327*, 818–822. [CrossRef]
2. Long, S.P.; Marshall-Colon, A.; Zhu, X.-G. Meeting the Global Food Demand of the Future by Engineering Crop Photosynthesis and Yield Potential. *Cell* **2015**, *161*, 56–66. [CrossRef]
3. Brown, T.B.; Cheng, R.; Sirault, X.R.R.; Rungrat, T.; Murray, K.D.; Trtilek, M.; Furbank, R.T.; Badger, M.; Pogson, B.J.; O Borevitz, J. TraitCapture: Genomic and environment modelling of plant phenomic data. *Curr. Opin. Plant Biol.* **2014**, *18*, 73–79. [CrossRef]

4.　Kumar, J.; Pratap, A.; Kumar, S. Plant Phenomics: An Overview. In *Phenomics in Crop Plants: Trends, Options and Limitations*; Springer: New Delhi, India, 2015; pp. 1–10.

5.　Sticklen, M.B. Feedstock Crop Genetic Engineering for Alcohol Fuels. *Crop. Sci.* **2007**, *47*, 2238–2248. [CrossRef]

6.　Van der Kooi, C.J.; Reich, M.; Löw, M.; De Kok, L.J.; Tausz, M. Growth and yield stimulation under elevated CO_2 and drought: A meta-analysis on crops. *Environ. Exp. Bot.* **2017**, *122*, 150–157. [CrossRef]

7.　O'Malley, R.C.; Ecker, J.R. Linking genotype to phenotype using the Arabidopsis unimutant collection. *Plant J.* **2010**, *61*, 928–940. [CrossRef]

8.　Weigel, D.; Richard, M. The 1001 Genomes Project for Arabidopsis thaliana. *Genome Biol.* **2009**, *10*, 1–5. [CrossRef]

9.　Cannon, S.B.; May, G.D.; Jackson, S.A. Three Sequenced Legume Genomes and Many Crop Species: Rich Opportunities for Translational Genomics. *Plant Physiol.* **2009**, *151*, 970–977. [CrossRef]

10.　International Brachypodium Initiative. Genome sequencing and analysis of the model grass Brachypodium distachyon. *Nature* **2011**, *463*, 763–770.

11.　Atwell, S.; Huang, Y.S.; Vilhjálmsson, B.J.; Willems, G.; Horton, M.W.; Li, Y.; Meng, D.; Platt, A.; Tarone, A.M.; Hu, T.T.; et al. Genome-wide association study of 107 phenotypes in Arabidopsis thaliana inbred lines. *Nat. Cell Biol.* **2010**, *465*, 627–631. [CrossRef]

12.　Wang, M.; Jiang, N.; Jia, T.; Leach, L.; Cockram, J.; Comadran, J.; Shaw, P.; Waugh, R.; Luo, Z. Genome-wide association mapping of agronomic and morphologic traits in highly structured populations of barley cultivars. *Theor. Appl. Genet.* **2012**, *124*, 233–246. [CrossRef] [PubMed]

13.　Lucocq, J.M. Efficient quantitative morphological phenotyping of genetically altered organisms using stereology. *Transgenic Res.* **2007**, *16*, 133–145. [CrossRef] [PubMed]

14.　Chung, K.; Crane, M.M.; Lu, H. Automated on-chip rapid microscopy, phenotyping and sorting of C. elegans. *Nat. Methods* **2008**, *5*, 637–643. [CrossRef] [PubMed]

15.　Sozzani, R.; Benfey, P.N. High-throughput phenotyping of multicellular organisms: Finding the link between genotype and phenotype. *Genome Biol.* **2011**, *12*, 219. [CrossRef] [PubMed]

16.　De Souza, N. High-throughput phenotyping. *Nat. Methods* **2010**, *7*, 1. [CrossRef]

17.　P-Sanz, F.; Navarro, P.J.; E-Cortines, M. Plant phenomics: An overview of image acquisition technologies and image data analysis algorithms. *Gigascience* **2017**, *6*, 1–18.

18.　Badrinarayanan, V.; Kendall, A.; Cipolla, R. SegNet: A Deep Convolutional Encoder-Decoder Architecture for Image Segmentation. *IEEE Trans. Pattern Anal. Mach. Intell.* **2017**, *39*, 2481–2495. [CrossRef] [PubMed]

19.　Otsu, N. A threshold selection method from gray-level histograms. *IEEE Trans. Syst. Man, Cybern.* **1979**, *9*, 62–66. [CrossRef]

20.　Vincent, L.; Soille, P. Watersheds in digital spaces: An efficient algorithm based on immersion simulations. *IEEE Trans. Pattern Anal. Mach. Intell.* **1991**, *13*, 583–598. [CrossRef]

21.　Banerjee, B.P.; Spangenberg, G.; Kant, S. Fusion of Spectral and Structural Information from Aerial Images for Improved Biomass Estimation. *Remote Sens.* **2020**, *12*, 3164. [CrossRef]

22.　Gebremedhin, A.; Badenhorst, P.; Wang, J.; Shi, F.; Breen, E.; Giri, K.; Spangenberg, G.C.; Smith, K. Development and Validation of a Phenotyping Computational Workflow to Predict the Biomass Yield of a Large Perennial Ryegrass Breeding Field Trial. *Front. Plant Sci.* **2020**, *11*. [CrossRef]

23.　Silva, J.C.E.; Kerr, R.J. Accounting for competition in genetic analysis, with particular emphasis on forest genetic trials. *Tree Genet. Genomes* **2012**, *9*, 1–17. [CrossRef]

24.　Tucker, C.J. Red and photographic infrared linear combinations for monitoring vegetation. *Remote Sens. Environ.* **1979**, *8*, 127–150. [CrossRef]

25.　Neumann, K.; Klukas, C.; Friedel, S.; Rischbeck, P.; Chen, D.; Entzian, A.; Stein, N.; Graner, A.; Kilian, B. Dissecting spatiotemporal biomass accumulation in barley under different water regimes using high-throughput image analysis. *Plant Cell Environ.* **2015**, *38*, 1980–1996. [CrossRef]

26.　Tackenberg, O. A New Method for Non-destructive Measurement of Biomass, Growth Rates, Vertical Biomass Distribution and Dry Matter Content Based on Digital Image Analysis. *Ann. Bot.* **2006**, *99*, 777–783. [CrossRef]

27.　Chen, D.; Neumann, K.; Friedel, S.; Kilian, B.; Chen, M.; Altmann, T.; Klukas, C. Dissecting the Phenotypic Components of Crop Plant Growth and Drought Responses Based on High-Throughput Image Analysis. *Plant Cell* **2014**, *26*, 4636–4655. [CrossRef]

28.　Hartmann, A.; Czauderna, T.; Hoffmann, R.; Stein, N.; Schreiber, F. HTPheno: An image analysis pipeline for high-throughput plant phenotyping. *BMC Bioinform.* **2011**, *12*, 148. [CrossRef] [PubMed]

29.　Subramanian, R.; Spalding, E.P.; Ferrier, N.J. A high throughput robot system for machine vision based plant phenotype studies. *Mach. Vis. Appl.* **2012**, *24*, 619–636. [CrossRef]

30.　Miller, N.D.; Parks, B.M.; Spalding, E.P. Computer-vision analysis of seedling responses to light and gravity. *Plant J.* **2007**, *52*, 374–381. [CrossRef]

31.　Clark, R.T.; MacCurdy, R.B.; Jung, J.K.; Shaff, J.E.; McCouch, S.R.; Aneshansley, D.J.; Kochian, L.V. Three-Dimensional Root Phenotyping with a Novel Imaging and Software Platform. *Plant Physiol.* **2011**, *156*, 455–465. [CrossRef] [PubMed]

32.　Atherton, T.; Kerbyson, D. Size invariant circle detection. *Image Vis. Comput.* **1999**, *17*, 795–803. [CrossRef]

33.　Yuen, H.K.; Princen, J.; Dlingworth, J.; Kittler, J. A Comparative Study of Hough Transform Methods for Circle Finding. *Image Vis. Comput.* **1989**, *8*, 71–77. [CrossRef]

34. Gebremedhin, A.; Badenhorst, P.; Wang, J.; Giri, K.; Spangenberg, G.; Smith, K. Development and Validation of a Model to Combine NDVI and Plant Height for High-Throughput Phenotyping of Herbage Yield in a Perennial Ryegrass Breeding Program. *Remote Sens.* **2019**, *11*, 2494. [CrossRef]
35. Rodgers, J.L.; Nicewander, W.A. Thirteen Ways to Look at the Correlation Coefficient. *Am. Stat.* **1988**, *42*, 59. [CrossRef]
36. Daetwyler, H.D.; Villanueva, B.; Woolliams, J.A. Accuracy of Predicting the Genetic Risk of Disease Using a Genome-Wide Approach. *PLoS ONE* **2008**, *3*, e3395. [CrossRef] [PubMed]